LUND UNIVERSITY

Design and Implementation of RF Kickers in MAX IV

Olsson, David

2017

Citation for published version (APA):
Olsson, D. (2017). *Design and Implementation of RF Kickers in MAX IV* (1 ed.). [Doctoral Thesis (compilation), Department of Electrical and Information Technology]. MAX-lab, Lund University.

LUND UNIVERSITY

PO Box 117
221 00 Lund
+46 46-222 00 00

DESIGN AND IMPLEMENTATION OF RF KICKERS IN MAX IV

David Olsson

Doctoral Thesis
2017

Cover: The interior of the waveguide overloaded cavity kicker in the MAX IV 3 GeV ring.

DESIGN AND IMPLEMENTATION OF RF KICKERS IN MAX IV

Printed in Sweden by Tryckeriet i E-huset, Lund, 2017

Department of Electrical and Information Technology
Lund University
Box 118
SE-221 00 LUND
Sweden

http://www.eit.lth.se

Series of licentiate and doctoral theses
No. 105
ISSN: 1654-790X
ISBN: 978-91-7753-349-8 (printed version)
ISBN: 978-91-7753-350-4 (electronic version)

To my parents, Anna and Gert

ABSTRACT

The MAX IV facility in Lund, Sweden, consists of two storage rings for production of synchrotron radiation, and a full-energy LINAC for top-up injections. The LINAC also delivers short high-intensity electron bunches to a short pulse facility. MAX IV was inaugurated in June 2016, and the larger 3 GeV ring has been delivering light to users since November 2016. In this thesis, the design and implementation of RF kickers for different systems in MAX IV are presented.

The first system is the chopper which is located in the so called thermionic pre-injector that delivers the electron pulses to the main LINAC during ring injections. The electron source is here a thermionic S-band RF gun. All electrons that enter the chopper can not be captured by the rings during injection. These undesired electrons are deflected and dumped by the chopper before they reach the first accelerating structure in the LINAC. The RF kickers in the chopper system are two planar striplines.

The second system is the bunch-by-bunch feedback system in the 3 GeV ring. The system is mainly used to suppress coupled-bunch mode instabilities. These instabilities drive coherent oscillations of the electron bunches. The oscillations have a degrading effect on the beam quality since they increase the effective emittance and the energy spread. By sampling the beam motion, the bunch-by-bunch feedback system suppresses the oscillations by corrective kicks to the bunches in all three planes via RF kickers. The system is also a comprehensive diagnostic tool that can be used to characterize many different parameters of the ring. This far, two striplines have been operating as RF kickers in the three planes. A waveguide overloaded cavity kicker has been designed, and this device will operate as a dedicated kicker in the longitudinal plane after the 2017 summer shut-down.

The third system is a diagnostic stripline with switching networks that is mainly used for betatron tune measurements in the two MAX IV storage rings and in the SOLARIS storage ring. This stripline can be used for many different applications.

POPULÄRVETENSKAPLIG SAMMANFATTNING

MAX IV-laboratoriet är en forskningsanläggning i Lund som består av en 300 meter lång linjäraccelerator och två lagringsringar för elektroner. Den större lagringsringen har en omkrets på 528 meter och den mindre en omkrets på 96 meter. Lagringsringarna fylls på (injiceras) med elektroner som först har accelererats till hastigheter nära ljusets i linjäracceleratorn. Elektronerna bildar klungor med 3 m avstånd och dessa cirkulerar i ringarna. I ringarna finns undulatorer, vilka består av ett hundratal permanentmagneter med växlande polarisation som sitter i rader under och över elektronstrålen. Magneterna gör att elektronstrålen svänger fram och tillbaka i sidled när den passerar genom undulatorn och därigenom alstras synkrotronljus. Detta synkrotronljus är mycket intensivt och dess våglängd kan variera från infrarött till hårt röntgenljus, beroende på vilken ring och undulator som används. Extremt korta ljuspulser kan även skapas i en undulator i den så kallade kortpulsanläggningen i slutet av linjäracceleratorn. Synkrotronljuset leds ut via strålrör till experimentstationer där forskare inom områden som t.ex. biologi, fysik, kemi, miljö, geologi, teknik och medicin använder det för att studera molekylära strukturer och ytor.

Inom vissa acceleratorapplikation krävs det att man kan ändra de accelererade partiklarnas bana eller energi, och då används ibland RF- (Radio Frekvens) kickers (från engelskans "kick"). En RF-kicker kan ses som en vakuumkammare vars insida exciteras av elektromagnetiska fält då den matas med en extern RF-signal. Då de laddade partiklarna färdas genom RF-kickern växelverkar de med de elektromagnetiska fälten och deras rörelsemängd ändras. Som RF-kickers i acceleratorer används oftast mikrovågskaviteter eller striplines. Mikrovågskaviteter är metallstrukturer med hålrum där elektromagnetisk energi kan lagras. Striplines är vakuumkammare med en eller flera elektroder som omges av elektromagnetiska fält då de matas med en RF-signal. Tre olika system med RF-kickers som används på MAX IV presenteras i denna avhandling.

Det första systemet är choppern (från engelskans "chop") som finns i början av linjäracceleratorn. Under injektion genereras elektronerna av en så kallad RF-kanon. De flesta av dessa elektroner har en tidsstruktur som gör att de inte kan lagras i ringarna om de accelereras vidare. Choppern sparkar ut dessa oönskade elektroner med hjälp av RF-kickers så att de dumpas på en metallskiva innan de hinner bli accelererade av själva linjäracceleratorn. Genom att dumpa de oönskade elektronerna när de har låg energi istället för att förlora dem när de har full energi så minimeras strålningsnivåerna i anläggning. Detta skyddar både personal och känslig elektronisk utrustning.

När de laddade elektronklungorna cirkulerar i ringarna omges de av elektromagnetiska fält. Under speciella resonansförhållande kan elektronklungorna påverka varandra via dessa elektromagnetiska fält (även kallade wakefields) och driva koherenta oscillationer i elektronstrålen. När sådana oscillationer är exciterade säger man att strålen är instabil. Resultatet blir att den effektiva strålstorleken och energispridningen ökar. För att hålla strålen stabil är så kallade bunch-by-bunch feedbacksystem installerade i båda ringarna. Dessa system mäter elektronklungornas positioner i alla tre planen och applicerar därefter korrigerande signaler till strålen via RF-kickers som dämpar dess oscillationer. Bunch-by-bunch feedbacksystemen presenteras även i denna avhandling.

Ett tredje system som presenteras i denna avhandling är diagnostikstriplines med tillhörande utrustning. Dessa är RF-kickers som är installerade i båda lagringsringarna och de används främst för att excitera elektronstrålen i det horisontella och vertikala planet. Denna excitation gör att man kan mäta elektronstrålens respons och därmed bestämma många av dess egenskaper.

LIST OF PUBLICATIONS

This thesis is based on the following papers, which will be referred to by their Roman numerals in the text.

I **A Chopper System for the MAX IV Thermionic pre-Injector**
D. Olsson, F. Lindau, M. Eriksson, J. Andersson and L. Malmgren.
Nuclear Inst. And Methods A **759**, 29-35 (2014).

II **New Features of the MAX IV Thermionic pre-Injector**
J. Andersson, D. Olsson, F. Curbis, L. Malmgren and S. Werin.
Nuclear Inst. And Methods A **855**, 65-88 (2017).

III **Commissioning Status of the Chopper System for the MAX IV Injector**
D. Olsson, J. Andersson, F. Curbis, L. Isaksson, L. Malmgren,
E. Mansten and S. Thorin.
pp MOP106015 (2008) *Proceedings of LINAC16, East Lansing, USA.*

IV **The Bunch-by-Bunch Feedback System for the MAX IV 3 GeV Ring**
D. Olsson, A. Karlsson and L. Malmgren.
LUTEDX/(TEAT-7253)/(2017) *Technical Report, Department of Electromagnetic Theory, Lund University.*

V **Design and Implementation of Stripline Feedback Kickers in the MAX IV 3 GeV Ring**
D. Olsson, L. Malmgren and K. Åhnberg.
pp THPIK086 (2017) *Proceedings of IPAC17, Copenhagen, Denmark.*

VI **A Waveguide Overloaded Cavity Kicker for the MAX IV Bunch-by-Bunch Feedback System**
D. Olsson, L. Malmgren and K. Åhnberg.
pp THPIK087 (2017) *Proceedings of IPAC17, Copenhagen, Denmark.*

VII **Design of Striplines for the MAX IV and SOLARIS Storage Rings**
D. Olsson, A. Karlsson and L. Malmgren.
LUTEDX/(TEAT-7254)/(2017) *Technical Report, Department of Electromagnetic Theory, Lund University.*

VIII **Design of Stripline Kicker for Tune Measurements in the MAX IV 3 GeV Ring**
D. Olsson.
(2013) *Proceedings of PIERS13, Stockholm, Sweden.*

CONTENTS

Papers

CHAPTER 1

INTRODUCTION

I started working in the MAX IV RF group in August 2011. During that time, the three storage rings, MAX I-III, at the old MAX-lab facility were still in operation, and the construction workers had just started to dig in the ground at the location what is now the MAX IV facility. Today, MAX IV is in operation and delivers light to external users. It has been exciting to take part in the commissioning of the LINAC and the two storage rings, as well as designing and installing subsystems that are now used in the accelerator. After a year at MAX IV, I was given the opportunity to do PhD studies and to write a thesis about the projects that I was working on. Since I wanted to specialize in RF technology and electromagnetic field theory, I chose to register as a PhD student at the department of Electrical and Information Technology. I include three projects that I have been working on in this thesis; the chopper system, the bunch-by-bunch feedback system, and a diagnostic stripline. What these systems have in common is that some of their key components are RF kickers. The scope of this thesis is therefore on the design and implementation of RF kickers in MAX IV.

MAX IV consists of two electron storage rings that are injected from a full-energy LINAC. In order to reduce the radiation levels in the facility, only electrons that can be captured in the rings during injection are accelerated in the LINAC. The electron source during injection is a thermionic RF gun. Most of the electrons emitted by the gun are lost if they are accelerated further since they have the wrong time structure. The purpose of the chopper system is to deflect and dump these undesired electrons before they reach the first accelerating structure in the LINAC.

The electron beams that are circulating the two rings are bunched with a 100 MHz structure. During certain resonance conditions, the bunches can couple to each other via wakefields and drive so called coupled-bunch mode instabilities. These instabilities have a degrading effect on the beam quality since they increase the effective emittance and the energy spread. The bunch-by-bunch feedback system damps these instabilities by sampling the motion of each single bunch and then applying correcting kicks to them via feedback kickers.

Several diagnostic devices are needed for stable operation of electron storage rings. One such diagnostic device is a stripline that can be used as a passive device that monitors the beam motion. It can also operate as an RF kicker and excite the beam so that some of the beam parameters can be measured. The diagnostic stripline has mainly been used to excite coherent oscillations of the beam during so called betatron tune measurements in the two storage rings.

An overview of the MAX IV facility is presented in Chapter 2. The basic physics of RF kickers are explained in Chapter 3. In that chapter, some examples of typical applications for RF kickers in accelerators are also presented. A brief overview of the RF kickers in MAX IV are given in Chapter 4. The papers included in this thesis give a detailed descriptions of the projects.

Chapter 2

MAX IV

The MAX IV Laboratory is a Swedish national research facility located in Lund. MAX IV was inaugurated in June 2016, and consists of two electron storage rings for production of synchrotron radiation, and a Linear Accelerator (LINAC) [1]. Figure 2.1 shows an overview of MAX IV.

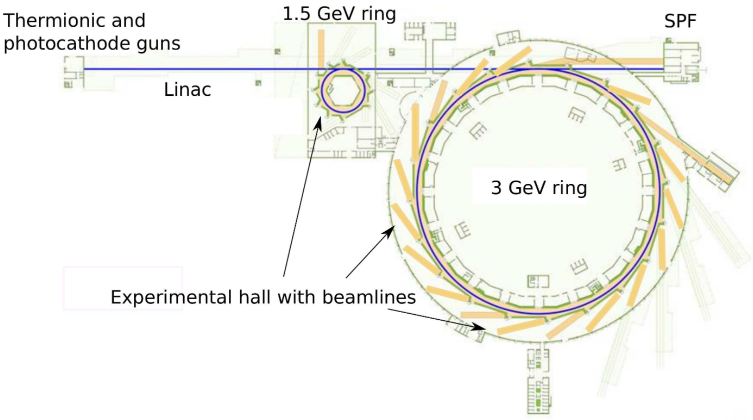

Figure 2.1: An overview of the MAX IV facility. Drawing by Johnny Kvistholm.

2.1 Storage Rings

The purpose of the two MAX IV storage rings is to produce synchrotron radiation in the spectral range from UV to hard X-ray. Scientists in areas such as biology, chemistry, engineering, environment, geology, medicine, and physics can use this light to examine molecular structures and surfaces.

A charged relativistic particle emits synchrotron radiation in its propagation direction when it is accelerated radially. As an example, a charged particle beam emits a burst of radiation when it is deflected by a dipole magnet (the acceleration is here perpendicular to the propagation vector), as illustrated in Figure 2.2 (a). This dipole light can be extracted to an experimental station and used for scientific measurements. The downside with dipole light is that the emitted light cone is very wide in the horizontal plane. If the particle beam instead passes a so called Insertion Device (ID), as shown in Figure 2.2 (b), the emitted light cone becomes more compact and intense. An ID consists of a periodic array of dipole magnets, and the intensity of the emitted light is built up as the beam wiggles through the structure. The two types of IDs are wigglers and undulators. The wiggler has a higher bending strength and by that the emitted spectra becomes broad and similar to that of a dipole, while the undulator spectra consists of a fundamental spectral line and its harmonics.

The MAX IV storage rings have been designed for low emittance and high brilliance (especially the 3 GeV ring). The emittance measures the beam size in phase space, and can be seen as the "temperature" of the beam. In the horizontal plane, the emittance is defined as $\epsilon_x = \sigma_x \sigma'_x$, where σ_x and σ'_x are the horizontal beam size and divergence, respectively at a given position. Similar, the vertical emittance is defined as $\epsilon_y = \sigma_y \sigma'_y$. The unit of emittance is meter radians.

The brilliance, B, is a measure of the quality of the synchrotron light, and it is given by

$$B = \frac{F}{4\pi^2 \epsilon_x \epsilon_y} \tag{2.1}$$

Here F is the photon flux, which is the number of photons emitted per second normalized to a ring current of 1 A. F is often defined over a photon energy bandwidth of 0.1 %. The brilliance is proportional to the inverse of the horizontal and vertical emittance and hence it is crucial to obtain a low emittance in synchrotron light sources.

2.1.1 3 GeV Ring

The 3 GeV ring has a circumference of 528 m, and is optimized for production of high-brightness hard X-ray light. This ring has an ultra-low emittance. At the maximum design current of 500 mA the emittance in the horizontal plane will vary between $\epsilon_x = 221$ pm rad and $\epsilon_x = 372$ pm rad, depending on the number of installed IDs (the extra radiation losses introduced by the IDs decrease the emittance) [3]. The vertical emittance varies between $\epsilon_y = 2$ pm rad and $\epsilon_y = 8$ pm rad depending on the demands from the users. The low emittance is obtained mainly thanks to the designs of the magnets and RF systems. The beam commissioning of the 3 GeV ring started in the autumn of 2015.

The 3 GeV ring has a 20 fold symmetry, and the magnet layout in each such section (achromat) is shown in Figure 2.3. The emittance in a storage ring scales roughly as $\epsilon \propto M^{-3}$, where M is the number of bending magnets (dipoles). For that reason, the 3 GeV ring employs so called multibend achromats, where each achromat has seven dipoles (see Figure 2.3). By increasing the number of dipoles, the number of higher order magnets, such as focusing quadrupole magnets, must also increase. This requires a very compact magnet design, and this is achieved by using very small beam pipes (the inner diameter of the circular beam pipe is only 21 mm at the magnet blocks) [4]. The magnets are integrated into larger iron blocks.

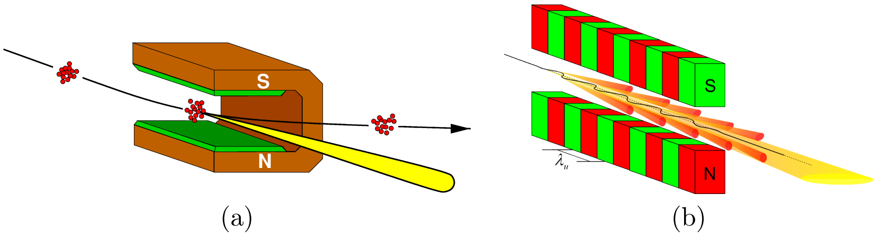

Figure 2.2: Synchrotron radiation emitted when a charged particle beam passes a dipole magnet (a), and an ID (b). The figures are take from [2].

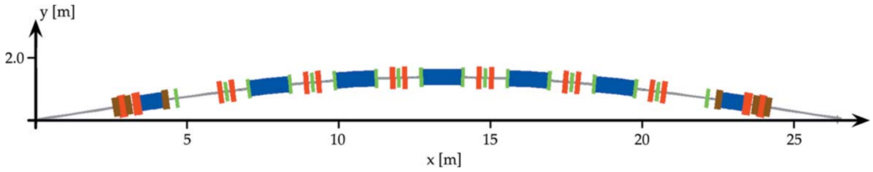

Figure 2.3: A magnet diagram showing one of the 20 achromats in the 3 GeV ring. The blue blocks are the bending dipoles, and the red blocks are focusing quadrupoles. The function of the sextupoles (green) and octupoles (brown) are to compensate for non-linear effects. The figure is taken from [3].

The electrons lose energy when they emit synchrotron radiation. The 3 GeV ring will in its final configuration be equipped with six accelerating RF cavities to compensate for the radiation losses and to keep the beam energy constant [5]. The cavities operate at a relatively low frequency of 100 MHz, and commercial solid-state FM transmitters provide them with RF power. Due to the RF system, the electron beam is bunched with a 100 MHz structure. Thus, there are 176 electron bunches, with an intermediate distance of 3 m, in the ring. In addition to the accelerating cavities, there are three harmonic (Landau) cavities that operate at 300 MHz. Unlike the acceleration cavities, the Landau cavities are passive, and the accelerating fields are excited by the beam itself, and not by external RF sources. When introducing the Landau cavities, the accelerating field gradient seen by the bunches is reduced (during ideal conditions, the gradient is zero) which increases the bunch length. By elongating the bunches, the particle density decreases and that reduces the effects of intrabeam scattering, which is particle collisions that blows up the transverse emittance. The longer bunches also reduce the growth rates of so called coupled-bunch mode instabilities (see Paper **IV**).

The 3 GeV ring has currently four undulators and one wiggler. Three of the undulators have delivered light to external users since the spring of 2017. The ring will host 19 IDs when fully equipped.

2.1.2 1.5 GeV Ring

The 1.5 GeV ring is optimized for production of light in the IR to the soft X-ray spectral range. It will mainly serve the same type of users that were doing experiments at the old MAX II and MAX III rings. The circumference of this ring is 96 m, and the maximum design current is 500 mA, i.e. the same as in the 3 GeV ring. Beam commissioning started in the autumn of 2016. A replica of the MAX IV 1.5 GeV ring has been built at the SOLARIS facility in Krakow, Poland [6].

This ring also has a compact magnet design with multiple magnets integrated into iron blocks. There is a 12-fold symmetry, and each achromat has two dipoles [4]. The horizontal and vertical emittance is around $\epsilon_x = 6$ nm rad and $\epsilon_y = 60$ pm rad, respectively. The RF system is similar to that in the 3 GeV ring, but due to the lower radiation losses in this ring, only two acceleration cavities and two Landau cavities are installed. The 1.5 GeV ring has not yet delivered light to any users, and the commissioning of the first three undulators will start in the autumn of 2017. When fully equipped, this ring can host 10 IDs.

2.2 LINAC

The MAX IV LINAC is approximately 300 m long, and can accelerate electrons to energies above 3 GeV. It operates both as an injector for the two storage rings and as a source of short electron bunches [7]. The acceleration occurs in 39 5.2m long multi-cell copper structures. The structures are fed with 4 μs long 3 GHz pulses that are delivered by 20 klystron amplifiers. These RF pulses are compressed in so called SLED systems before they are fed to the accelerator structures. The maximum rms RF power in a pulse can reach values above 200 MW. An overview of the LINAC is shown in Figure 2.4.

When injecting into the rings, the electron source is a so called thermionic RF gun that generates 1 μs long electron pulses at a heated cathode. Before entering the first accelerator structure, most of that charge is removed by a chopper system and an energy filter, so that the remaining electron pulse has a time structure that matches the ring it is to be injected in (see Paper **II**). The remaining electron pulse is then accelerated until it has an energy of 1.5 GeV or 3 GeV, and then injected into the corresponding storage ring from its extraction point (see Figure 2.4). During ring injections, the LINAC is pulsed with a maximum repetition frequency of 10 Hz.

When not injecting, the LINAC delivers short high-intensity electron bunches to the Short Pulse Facility (SPF) that is located at the end of the LINAC (see Figure 2.4). The SPF contains an undulator that is able to generate very short and intense X-ray pulses that can be used for time-resolved measurements at its experimental station. This is a great complement to the synchrotron light that is produced in the two storage rings. When delivering to the SPF, the electron source is a so called photo-cathode RF gun, where a single high-intensity electron bunch is generated by a laser pulse that hits a copper surface [8]. Before reaching the SPF, the bunch is compressed in two magnetic bunch compressors (see Figure 2.4), and it will be possible to produce light pulses that are shorter than 100 fs at the SPF. After future upgrades, the LINAC can operate with a maximum repetition frequency of 100 Hz when delivering beam to the SPF.

There are plans to construct a Free Electron Laser (FEL) parallel to the SPF [9]. In a FEL, the electrons in a single bunch are energy modulated until a micro bunch structure within the bunch appears. When a bunch with randomly distributed electrons propagates in an undulator, the emitted light will be (almost) monochromatic, but the fields emitted by the electrons along the bunch do not add up coherently. The power of the emitted light is therefore proportional to the number of electrons within the bunch, N. The electrons in a bunch with the micro bunch structure will however emit radiation coherently, and the power of the emitted light is therefore proportional to N^2. This is illustrated in Figure 2.5.

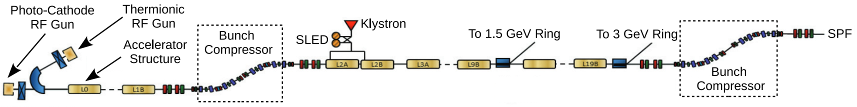

Figure 2.4: A simplified overview of the MAX IV LINAC. The picture is taken from [7].

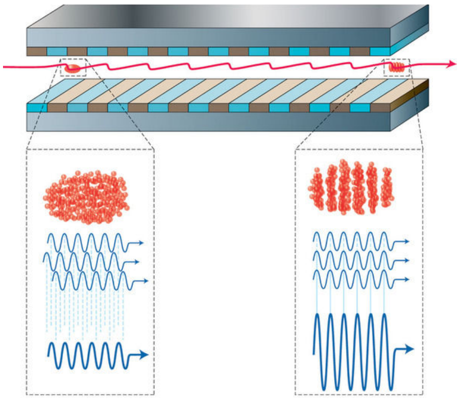

Figure 2.5: The incoherent undulator radiation emitted from a bunch with randomly distributed electrons (left), and the coherent radiation from a bunch with a micro bunch structure (right). The picture is taken from [10].

Chapter 3

RF Kickers in Accelerators

In this chapter, the basics physics of an RF kicker is explained. Some examples of common applications for RF kickers in accelerators are also presented. A more detailed report on kicker properties is given by [11].

3.1 Basic Working Principles of an RF Kicker

An RF kicker can be seen as a black box with a beam inlet and outlet, as shown in Figure 3.1. An RF signal with the rms power P is applied to the kicker via a waveguide. The signal induces electromagnetic fields within the kicker boundaries.

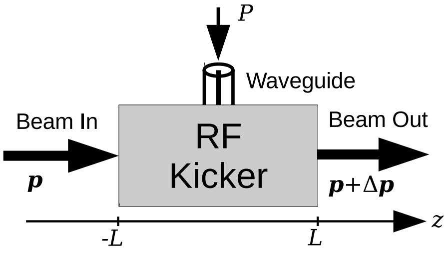

Figure 3.1: A black box model of an RF kicker.

The momentum of a particle is given by $\boldsymbol{p} = m_0\gamma\boldsymbol{v}$, where m_0 is the rest mass of the particle, $\boldsymbol{v}$ its velocity, $\gamma = 1/\sqrt{1-(v/c_0)^2}$ is the Lorentz factor, and c_0 is the speed of light. When a particle with charge q passes through a kicker it experiences the Lorentz force

$$\boldsymbol{F} = \frac{\mathrm{d}\boldsymbol{p}}{\mathrm{d}t} = q(\boldsymbol{E} + \boldsymbol{v} \times \boldsymbol{B}) \tag{3.1}$$

where $\boldsymbol{E}$ and $\boldsymbol{B}$ are the electric field and magnetic flux density inside the kicker, respectively. If we assume that the electromagnetic fields of the kicker are contained in the volume where $-L < z < L$ (see Figure 3.1), the total momentum gain of the particle when it passes the cavity is

$$\Delta \boldsymbol{p} = q \int_{t_{-L}}^{t_{+L}} (\boldsymbol{E} + \boldsymbol{v} \times \boldsymbol{B}) \mathrm{d}t \tag{3.2}$$

Here t_{-L} and t_{+L} are the times when the particle passes $z = -L$ and $z = L$, respectively. It is often convenient to separate longitudinal kickers from transverse kickers. For the longitudinal and transverse kicker, $\Delta \boldsymbol{p}$ corresponds to changes $\Delta p_{||}$ of the longitudinal momentum and $\Delta \boldsymbol{p}_{\perp}$ of the transverse momentum. In reality, purely longitudinal or transverse kickers do not exist due to mechanical tolerances of the kicker, fringing fields, and misalignments of the vacuum chamber and the particle beam, etc. In a real accelerator, the beam will therefore experience a momentum change in all three planes when passing the kicker.

In electron accelerators, one can in most applications assume that the beam is ultrarelativistic and propagates along the z-axis with a velocity $\boldsymbol{v} = \beta c_0 \hat{\boldsymbol{z}}$, where $\beta \approx 1$. The analysis can be simplified further by using a constant-velocity and a straight-line motion approximation. This implies that the momentum change introduced by the kicker is relatively small, thus $|\Delta \boldsymbol{p}| \ll |\boldsymbol{p}|$. It is often convenient to work with phasors when analysing RF component so that the electromagnetic fields have a $e^{\mathrm{j}\omega t}$ time dependence, where ω is the angular frequency of the sinusoidal input RF signal. The longitudinal and transverse voltage gain of an electron when passing a kicker are then defined as

$$V_{||} = \int_{-L}^{L} E_z(z) e^{\mathrm{j}kz} \mathrm{d}z \tag{3.3}$$

$$V_{\perp} = \int_{-L}^{L} (\boldsymbol{E}_{\perp}(z) + \beta c_0 \hat{\boldsymbol{z}} \times \boldsymbol{B}_{\perp}(z)) e^{\mathrm{j}kz} \mathrm{d}z \tag{3.4}$$

Here $k = \omega/\beta c_0$ is the wavenumber of the beam, and $\boldsymbol{E(z)}$ and $\boldsymbol{B(z)}$ are the electromagnetic fields along the z axis at the time when the ultrarelativistic electron reaches $z = 0$. Note that both $\boldsymbol{E}(z)$ and $\boldsymbol{B}(z)$ are complex vectors, and they can for example have their own $e^{\mathrm{j}k_z z}$ dependency if the kicker is a travelling wave structure, where k_z is the wavenumber of the propagating fields. Also note that $V_{\perp}$ is not a voltage strictly speaking, but the transverse work per unit charge since some of the forces come from a magnetic field. The longitudinal and transverse momentum gain can now simply be obtained as $\Delta p_{||} = q_e \Re(V_{||})/\beta c_0$ and $\Delta \boldsymbol{p}_{\perp} = \hat{\boldsymbol{e}}_{\perp} q_e \Re(V_{\perp})/\beta c_0$, respectively, where q_e is the electron charge, and $\hat{\boldsymbol{e}}_{\perp}$ is the unit vector of the transverse momentum change. For a longitudinal kicker, it is sometimes more convenient to use energy instead of momentum, and the energy change is then $\Delta W = q_e \Re(V_{||})$. Similar, the deflection angle is often a parameter used for a transverse kicker which is given by $\Theta = q_e \Re(V_{\perp})/W$, where $W = m_0 \gamma c_0^2$ is the energy of the electron.

A figure of merit of the kicker is its shunt impedance, which measures the effectiveness to produce a voltage for a given input power, P. The longitudinal and transverse shunt impedances, $R_{||}$ and $R_{\perp}$, are given by (3.5) and (3.6), respectively[1]. The shunt impedance is often (but not always) a parameter that should be maximized when designing an RF kicker.

$$R_{||} = \frac{|V_{||}|^2}{2P} \tag{3.5}$$

$$R_{\perp} = \frac{|V_{\perp}|^2}{2P} \tag{3.6}$$

The two most common types of RF kickers that are used in accelerators are striplines and microwave cavities. Other types exist, but the focus of this theses is on these two types.

In the accelerator community, a vacuum chamber with one or more electrodes (also called strips) that can interact with the beam is often referred to as a stripline. For stripline kickers, one end of each electrode is fed with an input signal, and the other electrode end is normally terminated with the reference impedance of the RF system (often 50 Ω). The electromagnetic fields that interact with the beam propagate in parallel with the electrodes, as illustrated in Figure 3.2 (a). From a circuit perspective, a stripline electrode can be seen as an extension of the coaxial waveguides at the upstream and downstream ends. Therefore, a stripline can be made very broadband as long as no significant impedance mismatch exists between the coaxial waveguides and the electrodes. Striplines are often used as transverse kickers, but they can also operate as weak longitudinal kickers, as shown in Paper **IV**.

Microwave cavities that are used as RF kickers are resonance structures enclosed by metal walls that confine the electromagnetic fields inside the cavity. Unlike striplines, microwave cavities are narrowbanded devices that can only be excited at their resonance frequencies. To each resonance frequency belongs an electromagnetic field that can be determined by solving Maxwell's equations in the confined volume. We refer to the electromagnetic field of a resonance as the eigenmode. The eigenmode is excited by an external source via a coupler (typically a loop, a waveguide slot, or a probe). When the charged particles pass through the cavity volume via beam pipes, they interact with the stored electromagnetic fields, as illustrated in Figure 3.2 (b). There exist many different cavity types in the accelerator community, and they can be single-cell or multi-cell, normal conducting or superconducting. Microwave cavities are used both as longitudinal and transverse kickers, and their stored fields can provide much higher shunt impedances than striplines. One drawback with cavities compared to striplines is the much longer rise and fall times of the fields, and cavities are therefore not suitable for applications that require very short rise and fall times.

---

[1] There exist several definitions of the shunt impedance in the literature. For cavities, it is common to define the longitudinal shunt impedance as $|V_0|^2/2P$, where $V_0 = \int_{-L}^{L} E_z(z)\mathrm{d}z$ is the instantaneously voltage. With this definition, the transit-time of the particle is not considered. V_0 relates to $R_{||}$ in (3.5) as $R_{||} = |V_0 T|^2/2P$, where $T = |V_{||}/V_0|$ is called the transit-time factor, and $V_{||}$ is the longitudinal voltage as it is defined in (3.3). For LINAC structures, the shunt impedance (sometimes called the "effective shunt impedance") is often defined as $|V_{||}|^2/P$, thus a factor 2 greater than in (3.5) [12]. For LINAC structures, it is also common to use the definition shunt impedance per unit length. Similar definitions exist for the transverse shunt impedance.

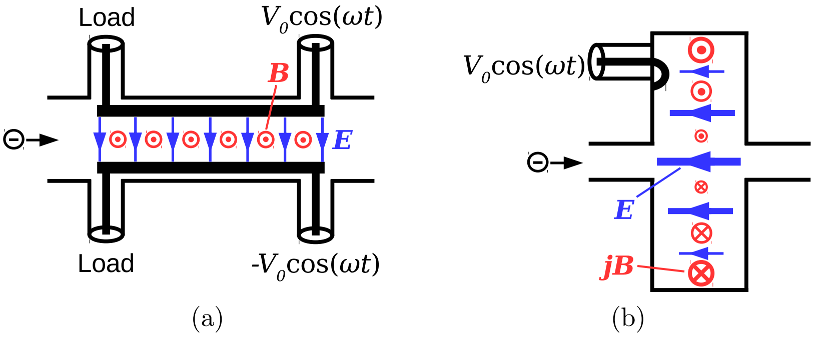

Figure 3.2: A stripline that is operating as a vertical kicker (a), and a microwave pillbox cavity that is operating at its TM_{010} mode as a longitudinal kicker (b).

3.2 Applications for RF Kickers

Some common applications for RF kickers in accelerators are listed in this chapter. Note that RF cavities that are used for acceleration and for bunching charged particle beams are normally not considered RF kickers, even though they provide a longitudinal kick, $\Delta p_{||}$, as described above.

3.2.1 Transverse RF Separators

Transverse RF separators can be used to separate the bunches in a bunched beam to different beamlines or to combine two (or more) bunched beams into a single beam. A good example of such an application is the Compact Linear Collider (CLIC) project [13], where the drive beam is initially bunched with a 0.5 GHz structure, and then split up and recombined in several steps so that the final drive beam has a 12 GHz structure. Figure 3.3 shows the CLIC delay loop where the bunch structure of the drive beam is increased from 0.5 GHz to 1 GHz.

Another application for transverse RF separators is to separate particles of different masses in a secondary beam during experiments in nuclear physics [14] [15]. The secondary beam can for example be the product when a (primary) charged particle beam hits a target. This collision results in a burst of particles with different masses that are deflected differently by the kicker fields.

Many chopper systems can also be considered to be transverse RF separators since they dump charged particles that are outside a preferred time window and/or have undesired energies. In the MAX IV chopper, S-band bunches that can not be captured in the ring buckets during injection are vertically deflected and dumped before they enter the main LINAC, as described in Papers **I**, **II**, and **III**.

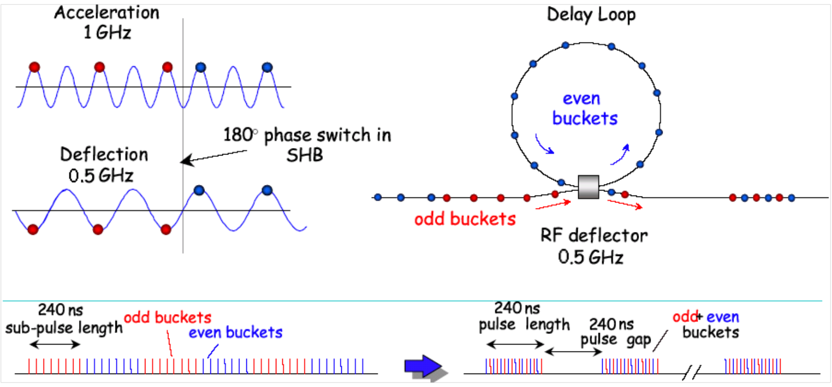

Figure 3.3: An overview of the CLIC delay line where the bunch structure is increased from 0.5 GHz to 1 GHz by using deflecting cavities. The figure is taken from [13].

3.2.2 Bunch Length Diagnostics

A transverse RF kicker can be used as a diagnostic tool for bunch length measurement if the bunch is deflected off-crest so that its centroid experiences a net deflecting kick that is zero. The head and tail of the bunch will then obtain transverse kicks in opposite directions. The chirped bunch is then projected on a downstream located screen, as illustrated in Figure 3.4. As seen, the transverse size of the projected beam is proportional to its bunch length. This set-up makes it possible to measure time-correlated parameters, such as the longitudinal bunch profile and the transverse slice emittance of the bunch. Measuring these parameters is especially useful in free electron lasers, where it is important to produce short high-intensity bunches with low emittance. In order to achieve a high temporal resolution in the measurements, the required transverse voltage of the kicker is often relatively high. Multi-cell transverse deflecting cavities are therefore commonly used due to their high shunt impedances. A transverse deflecting cavity for bunch length diagnostics in the MAX IV LINAC is currently being developed.

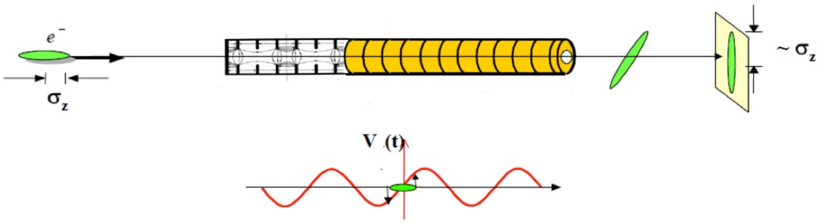

Figure 3.4: The working principle of a transverse deflecting cavity that is used for bunch length diagnostics. The figure is taken from [16].

3.2.3 Feedback Kickers

RF kickers can also be used as feedback kickers to correct the motion of a particle beam. A good example of such an application is a Bunch-By-Bunch (BBB) feedback system that is used in many electron storage rings to suppress coupled-bunch mode instabilities. Here, it must be possible to provide a corrective kick to a single bunch, while affecting the motion of the neighbouring bunches as little as possible. Fast kickers (also known as actuators) with low rise/fall times are therefore used. Typically, striplines provide the feedback in the transverse plane, while overloaded cavities are providing feedback in the longitudinal plane. The BBB feedback systems at MAX IV are described in Chapter 4.2 and in Paper **IV**.

3.2.4 Bunch Excitation in Storage Rings

The beam in a storage ring can be excited by RF kickers in order to study the beam response. It is then common to measure the betatron and synchrotron tunes of the beam, which are the number of transverse and longitudinal oscillations the particles perform per revolution, respectively. In its most simple measurement set-up, the excitation signal is swept at the RF kicker (often a stripline), and the magnitude response from a beam pick-up is monitored with a spectrum analyzer. When the excitation signal is swept over the betatron/synchrotron frequency, the magnitude response is maximized, as described in Paper **VII**. If instead a vector network analyzer is used to both generate the excitation signal and to monitor the beam, the phase response can also be obtained. With this information available, the beam transfer function can be calculated, which enables measurements of other parameters such as the beam impedance, as described in [17]. The tunes and beam transfer function can also be obtained by exciting and monitoring the beam with most modern digital BBB feedback systems.

Another application where an RF kicker is exciting the ring bunches is Pulse Picking by Resonant Excitation (PPRE), that was developed at BESSY-II [18]. In PPRE, an RF kicker excites the electrons in a single bunch close to the betatron frequency. This drives incoherent oscillations of the electrons, which increases the emittance and thereby the divergence of the light emitted by the excited bunch. By using an adjustable knife-edge aperture at the beamlines, one can dump the light emitted by the non-excited bunches while a fraction of the light emitted by the excited bunch enters the experimental stations. This is illustrated in Figure 3.5. The beamlines with inserted apertures enables time resolved experiments that require pulsed synchrotron light with a repetition rate that is lower than the bunch repetition frequency. The other can still benefit from the much higher photon flux that multi-bunch experiments offer. The average brilliance for the users that are performing multi-bunch experiments during PPRE operation is only slightly decreased since only the emittance in one single bunch is increased. There are plans to implement PPRE in the MAX IV 1.5 GeV ring, and initial PPRE experiments have already been performed where the BBB feedback system in the 3 GeV ring excites the bunches [19].

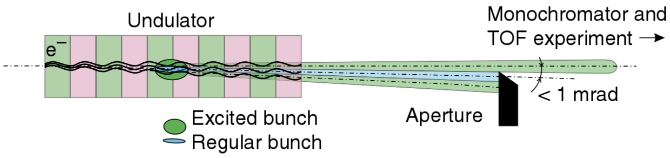

Figure 3.5: The light cone emitted by an excited and non-excited (regular) bunch that passes an undulator during PPRE operation. The light from the non-excited bunches is dumped by an adjustable knife-edge aperture. The figure is taken from [18].

3.2.5 Crab Cavities in Colliders

In circular colliders, such as the Large Hadron Collider (LHC), two counter-rotating particle beams are propagating in two separate chambers. The two beams cross each other with a crossing angle at one or more interactions regions (IRs), where the collisions occur. It is possible to rotate the bunches of the two beams around their barycentres with so called crab cavities before and after the IRs, as illustrated in Figure 3.6 (a). By doing so, the overlap of the two beams is maximised at the collision points, and that increases the luminosity of the collider. Crab cavities will be installed around the IRs of the ATLAS and CMS detectors in the High-Luminosity LHC (HL-LHC), which is the future upgrade of LHC. Two different cavity designs, the Double Quarter Wave (DQW) and the RF Dipole (RFD), are here being evaluated in parallel, and they can both be seen in Figure 3.6 (b). Both designs are superconducting single-cell cavities made of niobium.

Crab cavities can also be used in linear colliders to increase the efficiency of the head-on collision. For example, the crab cavities in CLIC will be normal conducting travelling wave multi-cell structures [20].

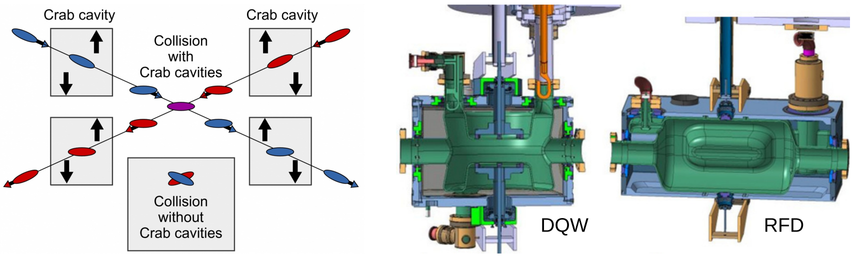

(a) (b)

Figure 3.6: (a) shows how the overlap between two beams at the collision point can be increased by using crab cavities. (b) shows the two superconducting crab cavity designs that are being evaluated for the HL-LHC upgrade. The figures are taken from [21] and [22].

Chapter 4

RF Kickers in MAX IV

This chapter describes the RF kickers, and their corresponding systems, that are installed in MAX IV.

4.1 The Chopper System

As mentioned in Chapter 2, the electron source during ring injections is a thermionic RF gun. The gun delivers an electron pulse with a length of $\approx 1\ \mu$s that is bunched with an S-band (3 GHz) temporal structure. However, only a fraction of that charge can be captured in the ring buckets during injection since most of the electrons have too low energies and/or are within the wrong time structure. The undesired electrons are therefore dumped in the thermionic pre-injector before they reach the main LINAC, where they are accelerated to their final energy. The advantage of dumping the undesired electrons in the thermionic pre-injector, where they have energies below 3 MeV, is that the radiation levels in the facility is reduced compared to the case where they would have been dumped at higher energies. The undesired electrons are dumped by a chopper system in combination with an energy filter, as described in Papers **I**, **II**, and **III**. The basic components of the chopper system can be seen in Figure 4.1.

In order to achieve a high injection efficiency, the electron pulse that enters the main LINAC must have a 100 MHz time structure that is synchronized to the buckets of the ring. The 100 MHz structure is created by a stripline that is fed with a superposed signal consisting of one 100 MHz, one 300 MHz, and one 700 MHz signal. By adjusting the amplitudes and phases of these three signals, it is possible to change the number of S-band bunches that are injected into each ring bucket. The undesired electrons are deflected and dumped at a downstream located collimator scraper. The second chopper stripline is fed with two high-voltage pulses that determine the length of the electron pulse that is accelerated in the main LINAC, i.e. the number of ring buckets that are injected. Figure 4.2 (a) shows the striplines in the thermionic pre-injector, and Figure 4.2 (b) shows the bi-polar BPM signal when injecting into ten ring buckets. An identical copy of the chopper system is installed in the SOLARIS LINAC, and they are currently commissioning their system.

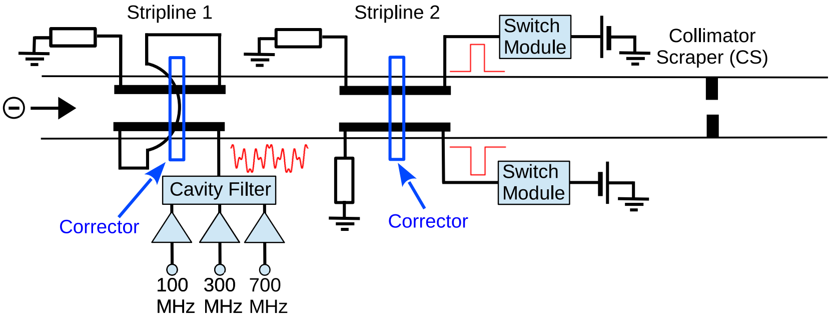

Figure 4.1: The basic components of the chopper system.

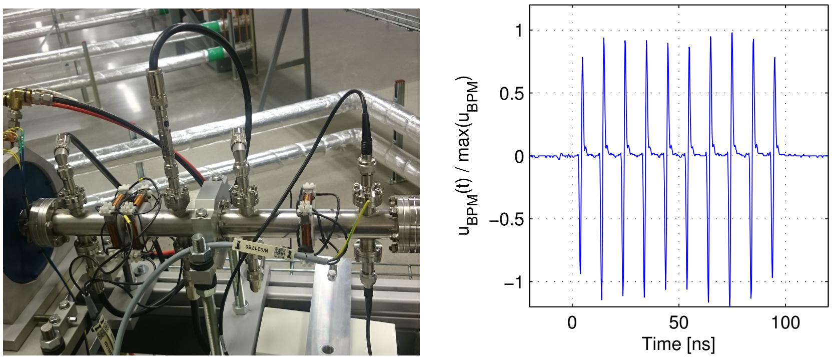

(a)

(b)

Figure 4.2: (a) shows the chopper striplines in the MAX IV thermionic pre-injector. (b) shows the bi-polar BPM signal, $u_{\mathrm{BPM}}(t)$, obtained in the end of the LINAC when injecting into ten ring buckets. Note the 100 MHz structure in the electron pulse.

4.2 The Bunch-By-Bunch Feedback System

In order to provide high-brightness synchrotron light to the users, the stored electron beam has to be stable in all three planes. Since the electron bunches couple to each other via wakefields, they can under certain resonance conditions drive coherent coupled-bunch oscillations. Such phenomena are known as Coupled-Bunch Mode Instabilities (CBMIs). They can both increase the effective emittance and the energy spread of the beam. This decreases the brilliance of the produced light. The oscillations driven by CBMIs are damped with negative feedback applied by a Bunch-By-Bunch (BBB) feedback system. The BBB feedback system in the 3 GeV ring is currently in operation, while the feedback system in the 1.5 GeV ring will be commissioned in the autumn of 2017. Figure 4.3 shows a simplified block diagram of a BBB feedback system that is operating in the vertical plane. The displacement of each individual bunch from its ideal orbit is measured at a Beam Position Monitor (BPM). This displacement signal is sampled by a signal processing unit that calculates the correction signal for each bunch. The correction signals are then amplified and sent to the bunches via kickers.

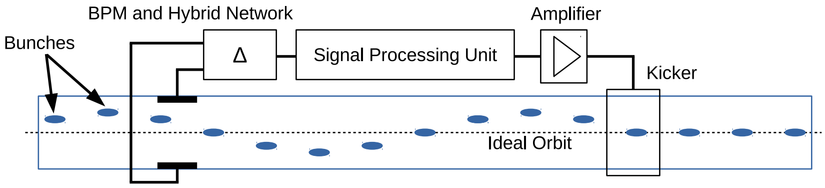

Figure 4.3: A simplified block diagram of a digital BBB feedback system.

The kickers in the BBB feedback system are also known as actuators. Two striplines are used in the 3 GeV ring to provide feedback in the horizontal, vertical, and longitudinal plane. After the 2017 summer shut-down, the feedback in the longitudinal plane will instead be provided via a waveguide overloaded cavity kicker. Figure 4.4 shows the striplines and the overloaded cavity when they are installed in the 3 GeV ring. The design of the actuators and the layout of the BBB feedback system in the 3 GeV ring are described in Papers **IV**, **V**, and **VI**. Here, it is also shown that CBMIs have a degrading effect on the quality of the light at the beamlines, and that the BBB feedback system can suppress the CBMIs.

4.3 Diagnostic Striplines

Striplines can both excite and monitor the beam. Therefore, they can be used for several applications. The two MAX IV storage rings and the SOLARIS ring are equipped with one diagnostic stripline each. At MAX IV, these striplines have mainly been used for betatron tune measurements. Figure 4.5 shows the stripline that is installed in the 1.5 GeV ring. The number of horizontal/vertical betatron oscillations that an electron perform around its ideal orbit during one revolution in a circular accelerator is called the horizontal/vertical betatron tune. It is important to monitor the tunes regularly since deviations from their operation values indicate that the properties of the accelerator have changed. This can for example be caused by a faulty magnet power supply. If the beam is stable, the electrons perform betatron oscillations incoherently. Therefore, the stripline excites the beam so that the electrons oscillate coherently at their betatron frequencies, and the tunes can now be measured by using the signal from a BPM. Unlike the striplines in the BBB feedback system, the diagnos-

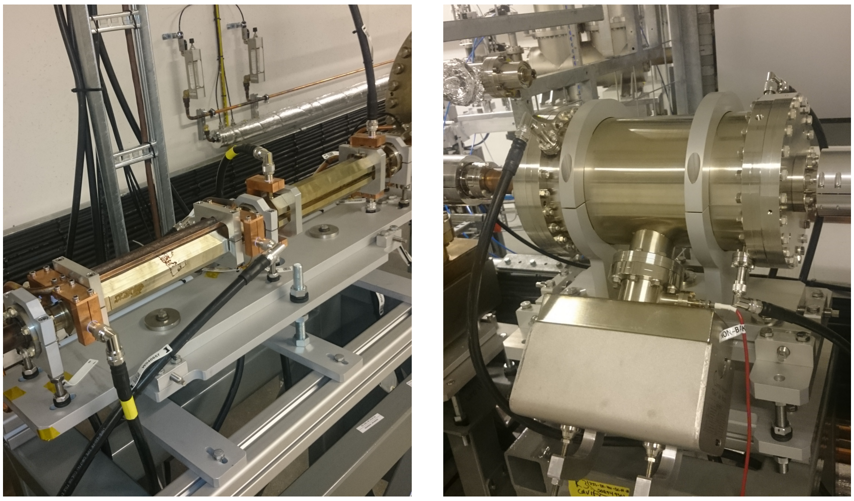

(a) (b)

Figure 4.4: The actuators for the BBB feedback system. (a) shows the two striplines in Achromat 08, and (b) shows the overloaded cavity in Achromat 11.

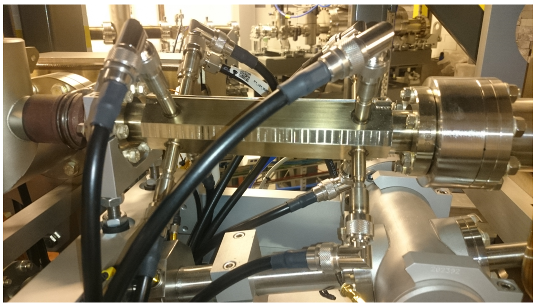

Figure 4.5: The diagnostic stripline in the MAX IV 1.5 GeV ring.

tic striplines have four electrodes each. This makes it possible to change the polarization of their deflecting fields by adjusting the amplitudes and phases of the RF signals that are fed to the electrodes. This is for example useful when monitoring the transverse tunes since it becomes easy to separate the two planes from each other. The diagnostic stripline in the 1.5 GeV ring will also be used as an actuator in all three planes for its BBB feedback system after the 2017 summer shut-down. The design of the diagnostic striplines are presented in Papers **VII** and **VIII**.

COMMENTS ON THE PAPERS

I **A Chopper System for the MAX IV Thermionic pre-Injector**
In this paper, the initial design of the chopper system is presented. The injection requirements and the advantages of a chopper system are explained. The design and measurements of the chopper striplines are presented, as well as the set-up of the chopper system and two stripline driving schemes. Measurements of the electron pulses and charge projections when operating with the chopper system are also shown here. These measurements were obtained at a test set-up at the old MAX-lab facility.
My contributions: I have done the design and analysis of the stripline kickers, the implementation of the chopper system, and all the presented measurements. I am the main author of this paper and I wrote the manuscript. The co-authors were part of the commissioning team of the pre-injector, and they have served as advisories.

II **New Features of the MAX IV Thermionic pre-Injector**
This paper presents the complete MAX IV thermionic pre-injector which delivers the electron pulses to the main LINAC during ring injections. Compared to the paper above, the analysis and versatility of the chopper system are extended and all the measurements are now performed in the actual MAX IV LINAC.
My contributions: The first authorship of this paper is shared with my colleague Joel Andersson. Joel has mainly been focusing on simulations of the electron beam, the gun, and the optics, while I have focused on the chopper and the surrounding RF systems. I have investigated different driving schemes of the chopper that allow us to adjust the number of ring buckets that are injected and how many S-band bunches that are injected into each ring bucket during a LINAC shot. Here, I show that the driving schemes can be optimized analytically by assuming that the transverse charge distribution of the S-band bunches that pass the energy filter is Gaussian. I have also verified the driving schemes with measurements of the current throughput and charge projections on YAG screens. The measurements of the RF pulses from the klystron and in the gun have been done together with Joel. I have written more than half of the manuscript, and Joel the rest. The other co-authors served as advisories.

III **Commissioning Status of the Chopper System for the MAX IV Injector**
This paper describes how the chopper system has operated during beam commissioning of the storage rings. The charge distribution of the injected electron pulses are measured in the LINAC by using BPM signals and YAG screens.
My contributions: I have done the analysis, the measurements, and written the manuscript. The co-authors are part of the LINAC commissioning team, and they served as advisories. I presented this work at a conference.

IV **The Bunch-by-Bunch Feedback System for the MAX IV 3 GeV Ring**
In this technical report, the bunch-by-bunch feedback system in the 3 GeV ring is described. The actuators of the feedback system are two striplines and a waveguide overloaded cavity. The design, as well as measurements, of these components are presented. A short introduction to the physics of coupled-bunch mode instabilities, and how a digital bunch-by-bunch feedback system works are also given. Finally, some measurements are presented that show the degrading effect coupled-bunch mode instabilities have on the beam quality, and how the feedback system can suppress them.
My contributions: I have done the RF design and analysis of the striplines and the cavity, the design and construction of the stripline back-end, all the presented measurements, and written the manuscript. The mechanical design of the striplines and the cavity was made by Karl Åhnberg. The measurements at BioMAX and the diagnostic beam line presented in Section 6.3.2 were assisted. The commissioning of the bunch-by-bunch feedback system has been a long process, and has mainly been done together with Åke Andersson, Francis Cullinan, Pedro Fernandes Tavares, and Dmitry Teytelman. The co-authors of this paper served as advisories.

V **Design and Implementation of Stripline Feedback Kickers in the MAX IV 3 GeV Ring**
This paper explains how bunch-by-bunch feedback is applied in all three planes via two stripline kickers in the 3 GeV ring. The stripline design is discussed, and simulation results are compared to measurements. Initial results from instability studies in the 3 GeV ring are also discussed.
My contributions: I have done the analysis, RF design and simulations of the stripline kickers, and all the presented measurements. I have also written the manuscript. With the exception of the mechanical design of the striplines, which was made by Karl Åhnberg, the paper is entirely my own work. Lars Malmgren served as an advisory. I presented this work at a conference.

VI **A Waveguide Overloaded Cavity Kicker for the MAX IV Bunch-by-Bunch Feedback System**
This paper describes the design of the waveguide overloaded cavity kicker for the 3 GeV ring that will provide feedback in the longitudinal plane. The requirements of the kicker are explained, and simulation results are presented.
My contributions: I have done the analysis, RF design and simulations of the overloaded cavity. I have also written the manuscript. With the exception of the mechanical design of the cavtiy, which was made by Karl Åhnberg, the paper is entirely my own work. Lars Malmgren served as an advisory. I presented this work at a conference.

VII **Design of Striplines for the MAX IV and SOLARIS Storage Rings**
This is a detailed technical report on the diagnostic striplines that are being used in the two MAX IV storage rings and in SOLARIS. Parameters such as kick efficiency, pick-up characteristics and beam impedance are derived analytically and compared to numerical results. It is shown that the electromagnetic fields inside the stripline can be obtained with high accuracy by solving Laplace equation over a 2D cross section. The design and measurements of two RF networks that are used to change the excitation polarization of a stripline, and to change the plane that is being monitored at a BPM chamber are also presented. Initial measurements on the beam spectrum are also shown, where the beam is excited and monitored in the transverse plane.
My contributions: I have done the RF design and analysis of the striplines, the design/construction of the RF networks, all the presented measurements, and written the manuscript. With the exception of the mechanical design of the striplines, which was made by Johnny Ahlbäck, the paper is entirely my own work. The co-authors served as advisories.

VIII **Design of Stripline Kicker for Tune Measurements in the MAX IV 3 GeV Ring**
This paper presents the initial RF design of the diagnostic stripline. The kicker and pick-up performances are here obtained analytically, and then compared to simulations.
My contributions: The paper is entirely my own work. I presented this work at a conference

ACKNOWLEDGMENTS

The work in this thesis would not have been possible without the help from the skilled staff at the MAX IV Laboratory. MAX IV is truly a workplace with a lot of knowledgeable people within several different disciplines. I want to thank all my colleagues in the accelerator development, engineering, operation, radiation safety, and RF group who have helped me during these years. In the RF group, a special thanks to Robert Lindvall and Sven-Olof Heed for your help and expertise on everything from matching circuits to microcontroller programming.

Big thanks to Åke Anderson, Pedro Fernandes Tavares, and Sara Thorin for all your input, and for reading and correcting this thesis.

I would like to thank my supervisor Anders Karlsson for your guidance and for allowing me to do PhD studies at the department of Electrical and Information Technology. Also big thanks to my co-supervisor and group manager Lars Malmgren for giving me the opportunity to do PhD studies and to work independently with several different projects.

Thanks to my good friends, Victoria Olsson and Jens Sundberg for cheering and encouragements me during these years.

Finally, the greatest thanks to my family. To my parents, Anna and Gert for believing in me and for always being there for me, and to my brothers, Simon and Adam.

REFERENCES

1. MAX IV Laboratory website, `https://www.maxiv.lu.se/`.
2. DESY website, `http://www.desy.de/`.
3. P. F. Tavares et al, "The MAX IV storage ring project", *Journal of Synchrotron Radiation 21* , 862-877 (2014).
4. MAX IV detailed design report website, `https://www.maxiv.lu.se/accelerators-beamlines/accelerators/accelerator-documentation/max-iv-ddr/`.
5. Å. Andersson et al, "The 100 MHz RF System for the MAX IV Storage Rings", pp MOPC051, *Proceedings of IPAC11, San Sebastian, Spain* , 2011.
6. SOLARIS website, `http://www.synchrotron.uj.edu.pl/`.
7. S. Thorin et al, "The MAX IV Linac", pp TUIOA03, *Proceedings of LINAC16, Geneva, Switzerland* , 2014.
8. F. Lindau et al, "MAXIV Photocathode Gun Laser System Specification and Diagnostics", pp TUPAB097, *Proceedings of IPAC17, Copenhagen, Denmark* , 2017.
9. S. Werin et al, "The Soft X-Ray Laser Project at MAX IV", pp WEPAB077, *Proceedings of IPAC17, Copenhagen, Denmark* , 2017.
10. B. W. J. McNeil and N. R. Thompson, "X-ray free-electron lasers", *Nature Photonics 4* , 814-821 (2010).
11. D. A. Goldberg and G. R. Lambertson, "Dynamic Devices A Primer on Pickups and Kickers", *AIP Conference Proceedings Series - Physics of Particle Accelerators*, 1992.
12. T. P. Wangler, "RF Linear Accelerators", 2nd printing (2008), Ch 2.
13. CLIC website, `http://home.cern/about/accelerators/compact-linear-collider`.
14. W. Chao and M. Tigner, "Handbook of Accelerator Physics and Engineering", 3rd printing (2009), Ch 7.2.

15. G. Burt, "Transverse deflecting cavities", In: *CAS - CERN Accelerator School: Specialised Course on RF for Accelerators*, 2012.

16. R. Akre et al, "Bunch Length Measurements Using a Transverse RF Deflecting Structure in the SLAC LINAC", *SLAC-PUB-9241*, 2002.

17. P. J. Chou and G. Jackson, "Beam transfer function and transverse impedance measurements in the Fermilab Main Ring", *Proceedings of PAC1995, Dallas, Texas, USA* , 1995.

18. K. Holldack et al, "Single bunch X-ray pulses on demand from a multi-bunch synchrotron radiation source", *Nature Communications 5* , 1-6 (2014).

19. T. Olsson et al, "First Measurements of Pulse Picking by Resonant Excitation (PPRE) at the MAX IV 3 GeV Storage Ring", pp WEPAB073, *Proceedings of IPAC17, Copenhagen, Denmark* , 2017.

20. G. Burt et al, "Prototype Development of the CLIC Crab Cavities", pp THPP013, *Proceedings of LINAC16, Geneva, Switzerland* , 2014.

21. HL-LHC website, `http://home.cern/topics/high-luminosity-lhc`.

22. F. Carra et al, "Crab Cavity and Cryomodule Development for HL-LHC", pp FRBA02, *Proceedings of SRF2015, Whistler, BC, Canada* , 2015.

PAPERS

PAPER I

A Chopper System for the MAX IV Thermionic pre-Injector

D. Olsson, F. Lindau, M. Eriksson, J. Andersson and L. Malmgren.

Nuclear Inst. And Methods A **759**, 29-35 (2014).

Nuclear Instruments and Methods in Physics Research A 759 (2014) 29–35

Contents lists available at ScienceDirect

Nuclear Instruments and Methods in Physics Research A

journal homepage: www.elsevier.com/locate/nima

A chopper system for the MAX IV thermionic pre-injector

D. Olsson*, F. Lindau, M. Eriksson, J. Andersson, L. Malmgren

MAX IV Laboratory, Lund University, P.O. Box 118, SE-221 00 Lund, Sweden

ARTICLE INFO

Article history:
Received 18 March 2014
Received in revised form
28 April 2014
Accepted 8 May 2014
Available online 22 May 2014

Keywords:
Chopper
Stripline
Kicker
Electron gun
LINAC

ABSTRACT

The MAX IV pre-injector will have one thermionic and one photocathode S-band RF gun, where the former will be used for ring injections. During ring injections, the bunches leaving the pre-injector have a structure that consists of ten 10 ns bunch trains, each containing three bunches. A chopper system consisting of two striplines and an adjustable aperture is used, where the desired bunch structure is obtained by superposing RF signals. The design of the chopper system and the initial tests of the thermionic pre-injector are presented in this paper.

1. Introduction

MAX IV will be Sweden's next-generation synchrotron radiation light source and will consist of two storage rings. MAX IV will be operational and open for users in June 2016. The larger 3 GeV ring has a circumference of 528 m and the smaller 1.5 GeV ring a circumference of 96 m. A Short Pulse Facility (SPF) is located at the end of the injector, and the design also includes an option for a Free Electron Laser (FEL). The FEL would be a second development stage of the facility. The injector consists of 39 constant-gradient traveling-wave S-band LINAC structures that are fed by klystrons via SLED systems [1]. During ring injections, the electrons are injected at full energy, i.e. no ramp-up is needed.

The pre-injector consists of one thermionic and one photocathode S-band RF gun [2] where the former is used during ring injections, and the latter is generating the high-charge and low-emittance bunches required for the SPF and FEL. The maximum repetition rate is 10 Hz during ring injection and 100 Hz during SPF and FEL operation. Initially, the plan was also to generate bunches for ring injections in the photocathode gun, but the thermionic gun was added to the pre-injector since it was considered as a simpler and more reliable system. Another reason for the change of design was that MAX-lab already has years of experience of a nearly identical thermionic gun [3]. A chopper system is needed after the thermionic gun in order to create the desired bunch structure for ring injections.

2. Bunch structure

Table 1 lists the design parameters of the thermionic pre-injector, and Fig. 1 shows the desired bunch structure for ring injections. These parameters are based on the requirements for injections to the 3 GeV ring which are more narrow than for the 1.5 GeV ring. The electrons are generated in an in-house developed thermionic RF gun and have a bunch frequency of $f_{gun} = 2.9985$ GHz. The buckets in the rings have a frequency of $f_{ring} = 99.931 \pm 0.5$ MHz, and an average of three bunches are injected into each bucket at a time. During this 1 ns time window (3×333 ps), the ring buckets have a high electron capture efficiency. Ten bunch trains of $1/f_{ring} \approx 10$ ns, each containing three bunches, are injected in each LINAC shot, thus the current pulse in each shot is 100 ns long. The frequency of the bunch trains is locked to f_{ring}, which needs to be variable in order to compensate for temperature contractions/expansions and other phenomena in the rings. However, f_{gun} is fixed and locked to the master frequency of the LINAC. That gives rise to a variation of the distribution of the bunches within the 1 ns time window. Due to the SLEDs, there is an energy chirp within the LINAC shot, and by injecting a 100 ns long current pulse, the energy chirp becomes less than 1.3%. A longer pulse results in a higher energy chirp and this is the main reason why a longer current pulse is not injected [1]. The thermionic injector has a maximum repetition frequency of 10 Hz.

The full-energy injector enables top-up injection which means that by continuous injections the current in the rings can be kept at a nearly constant level. This is in contrast to the present MAX-lab where the rings are filled at a lower energy and then ramped up to the energy of operation. The rings are then dumped and re-filled when too much of the ring current has been lost. Top-up

---

* Corresponding author. Tel.: +46 733952704.
E-mail address: david.olsson@maxlab.lu.se (D. Olsson).
URL: http://www.maxlab.lu.se.

http://dx.doi.org/10.1016/j.nima.2014.05.052
0168-9002/

Table 1
Design parameters of the MAX IV thermionic pre-injector.

Beam kinetic energy	2–2.5 MeV
Bunch frequency before chopper, f_{gun}	2.9985 GHz
Bunch train frequency, f_{ring}	99.931 ± 0.5 MHz
Number of bunches per bunch train	3
Number of bunch trains per LINAC shot	1 or 10
LINAC shot repetition frequency	10 Hz
Total injected charge per top-up injection	9.0 nC

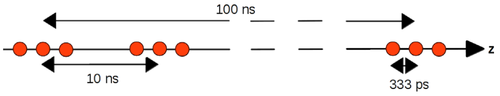

Fig. 1. The desired bunch structure after the chopper (note that the scale is not proportional).

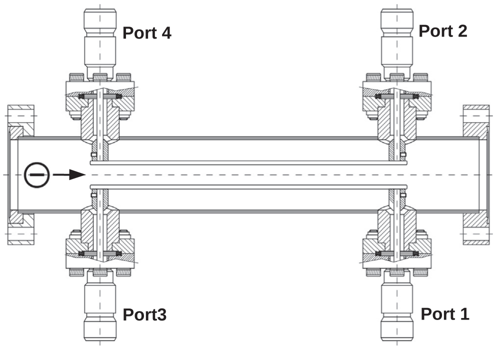

Fig. 2. Cut through and port numbering of the stripline.

injection has several benefits, such as constant heat loading in the vacuum chambers, constant signal levels detected by the Beam Position Monitors (BPMs) and the ability to use more exotic filling patterns than homogeneous filling. The users would also benefit from top-up injection since the current is constantly kept at a high level, which means maximum light flux for their experiments. An algorithm determines which parts of the rings that require refilling in order to maintain a constant current and the desired charge distribution over the buckets. Many modern light sources are in the meantime operating with top-up injection [4]. A total charge of 9 nC is injected every 6 min during regular top-up operation [5].

Even though homogeneous filling with a 100 MHz bucket structure is the standard mode of operation, other more exotic filling patterns have been considered. One possible option is to run the 3 GeV ring in a so-called camshaft mode. That benefits experimental stations that require high time resolution. The filling pattern and bucket distribution in this mode can be made in different ways, with the common factor that there exists at least one high-charge bucket that is well separated from the neighboring buckets. Hence, this requires the ability to also inject a single bunch train with three bunches per LINAC shot. However, it has not yet been decided if the camshaft mode option will be implemented into MAX IV.

Keeping three bunches in a 10 ns bunch train also has the advantage that it maximizes the 500 MHz Fourier component detected by the BPM system. This is optimal for the spatial resolution since 500 MHz is the operating frequency of the BPM electronics.

Another purpose of the chopper is to reduce the radiation level in the facility since it removes electrons that otherwise would be lost at much higher kinetic energy, i.e. removing electrons that cannot be collected by the ring buckets. This also reduces the overall beamloading in the LINACs.

3. Stripline design

A design with two planar stripline electrodes (strips) is chosen since it simplifies the manufacturing process and offers good field homogeneity, when the separation of the strips is small. Each strip has a length $L = 150$ mm, a width $w = 15.8$ mm, and a thickness $h = 2$ mm. They are separated by a distance $d = 10$ mm, and attached to N-type coaxial feedthroughs by screws, as seen in Fig. 2. The pipe chamber is made of stainless steel and the strips of copper. Both components are manufactured in-house. The strips are oriented so that the shaking of the beam occurs in the vertical direction. This is because the allowed vertical emittance is higher than the horizontal one during ring injections, and the latter should not be further increased.

The deflecting electric field $\boldsymbol{E}_{\perp}(\boldsymbol{r})$ for a TEM mode corresponds to the transverse field $\boldsymbol{E}_{\perp}(\boldsymbol{r}) = -\nabla\Phi(\boldsymbol{r})$ for the two-dimensional geometry in electrostatics. Thus, the scalar potential $\Phi(\boldsymbol{r})$ can be obtained by solving the Laplace equation over a cross-section of the stripline. Here, COMSOL Multiphysics is used to optimize the design and match it to the line impedance of 50 Ω for the odd TEM mode. The characteristic impedance of the even TEM mode is 88 Ω. Fig. 3 shows $\Phi(\boldsymbol{r})$ of the two TEM modes obtained in COMSOL. The transverse geometry factor, $g_{\perp} = |\boldsymbol{E}_{\perp}(\rho = 0)|d/2$, for the odd TEM mode is defined as the product of the transverse electric field in the center and the distance to the strips that are held at ±1 V [6]. In this design, $g_{\perp} = 0.99$, thus the field in the center is close to that between two infinitely long conducting planes.

The stripline is fed at Port 1 (see Fig. 2 for port numbering) which is a downstream port. The RF signal is circulated from Port 3 to Port 2 via a cable and an adjustable coaxial phase shifter. These are tuned to a phase difference of 180° between the incoming signals at Port 1 and Port 2 at the frequency $f_0 = 100$ MHz. Hence, the propagating mode is an odd TEM mode at frequencies $f = (1+2n)f_0,\ n \in \mathbb{N}$, i.e. odd harmonics of 100 MHz. The propagating mode is an even TEM mode when $f = 2nf_0,\ n \in \mathbb{N}$. Port 4 is terminated with a high-power load. The main advantage of this setup, compared to a more traditional solution with a 3 dB 180 degree hybrid coupler (splitter) after the amplifier, is that the required power is reduced by almost a factor of two at low frequencies. A drawback is that the potential at the upper strip will be somewhat lower due to the extra attenuation in the cable and the coaxial feedthroughs. This reduces the kick efficiency, the 50 Ω matching of the strips and the field homogeneity, especially at higher frequencies. However, these effects are minor at frequencies up to 700 MHz, which can be seen in Fig. 4 where the measured S-parameters of the stripline are shown.

Since the stripline is pulsed during a couple of microseconds with the same repetition frequency, 10 Hz, as the gun, the time average of the resistive losses is low.

4. Creating the bunch structure

Since the RF signal is circulated through both strips, the ideal voltage function at Port 1, $U(t)$, is

$$U(t) = U_0 \sum_{n=-\infty}^{\infty} [\theta(t + \tau/2 + nT_0)$$

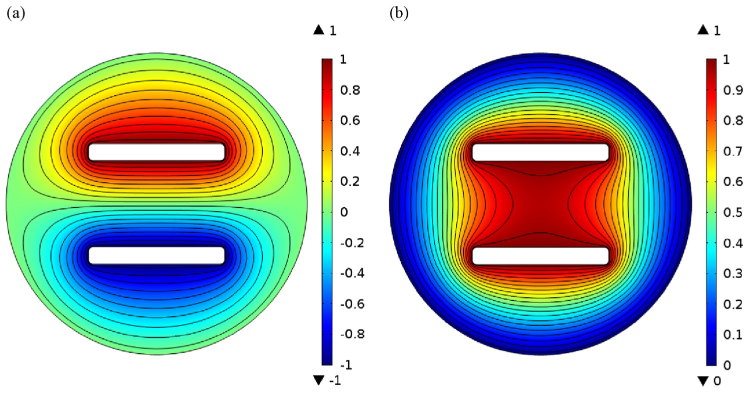

Fig. 3. The scalar potential $\Phi(\mathbf{r})$ of the odd (a) and even (b) TEM mode.

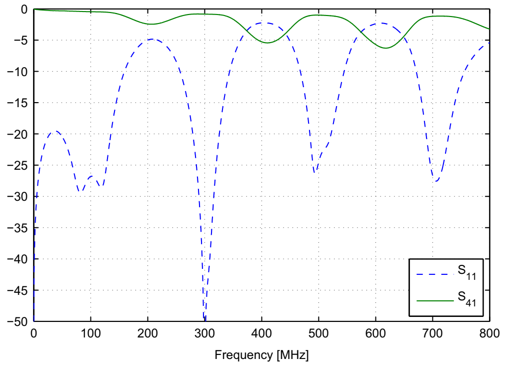

Fig. 4. Measured S-parameters (reflection and transmission) of the stripline. Note the 50 Ω matching of the strips at odd harmonics of 100 MHz.

$$
\begin{aligned}
&-\theta(t-\tau/2+nT_0)\\
&-\theta(t+\tau/2+(n+1/2)T_0)\\
&+\theta(t-\tau/2+(n+1/2)T_0)]
\end{aligned}
\tag{1}
$$

where U_0 is a constant, $\theta(t)$ is the Heaviside step function and T_0 is the period of the bunch train. $\tau = 2L/c_0 + t_w$ is the sum of the stripline rise time and the time window t_w where we want to keep the electrons. In our case, $T_0 = 1/f_{\text{ring}} \approx 10$ ns, and $t_w \approx 3 \times 333$ ps ≈ 1 ns (see Fig. 1). The dominant Fourier components of this function have the frequencies 100 MHz, 300 MHz and 700 MHz. One can obtain the voltage function shown in Fig. 5 by superposing these three frequency signals, where the 700 MHz signal is phase shifted 180° relative to the other two. The ideal voltage function in Eq. (1) is shown in the same figure.

If N different RF signals are combined and fed into Port 1, the total transverse voltage gain of the beam, $V_\perp(t)$, has the time dependence

$$V_\perp(t) \approx \frac{40 c_0 g_\perp}{d} \sum_{n=1}^{N} \frac{\sqrt{P_n}\,\sin(\omega_n L/c_0)}{\omega_n} \cos(\omega_n t + \varphi_n) \tag{2}$$

where P_n, ω_n and φ_n are the rms input power, angular frequency and relative phase of the nth RF signal, respectively. Note that losses in the stripline are not included in Eq. (2). The vertical deflection Δy at a distance Δz away from the center of the stripline is determined by

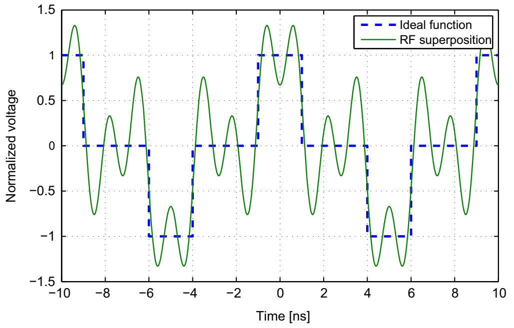

Fig. 5. The ideal voltage signal from Eq. (1) together with a combined signal of 100 MHz, 300 MHz and 700 MHz.

$$\Delta y(t) \approx \Delta\alpha(t)\Delta z + y_0 \approx \frac{eV_\perp(t)}{W_{tot}}\Delta z + y_0 \tag{3}$$

where $\Delta\alpha(t)$ is the angular deflection, e is the elementary charge, W_{tot} is the total electron energy and y_0 is the vertical offset. The vertical offset y_0 can be adjusted by corrector magnets. If the signal in Fig. 5 is fed to the first stripline with powers $P_{100\text{ MHz}} = 210$ W, $P_{300\text{ MHz}} = 490$ W, $P_{700\text{ MHz}} = 140$ W, and if the total electron energy is $W_{tot} = 3$ MeV, the vertical deviation of the bunch train at the aperture is the one in Fig. 6. As seen, three bunches in each bunch train are located on a flat top, and by using correctors, these bunches can pass the pre-injector centered in the pipe, while the rest of the bunches are dumped at an aperture. In this example, it must be possible to focus the beam within a circle with a diameter of 1 mm, otherwise some of the neighboring bunches would also pass. Cavity band pass filters are used for insulation between the three signals combined in this set-up. The cavity filters are similar to those used to combine multiple channels in the broadcast industry and customized for our application.

An alternative is to feed a 300 MHz signal to the first stripline and a 100 MHz signal to the second. Then, if $P_{100\text{ MHz}} = 310$ W and $P_{300\text{ MHz}} = 295$ W, the vertical deviation at the aperture can be seen in Fig. 7. The advantage of this set-up is that a larger aperture can be used since the vertical separation to the undesired bunches outside the time window is larger. However, the three bunches are

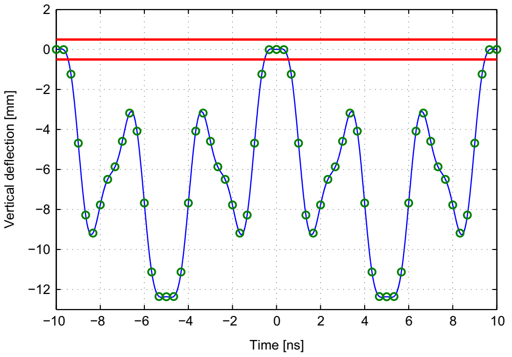

Fig. 6. The vertical deviation as a function of time at the aperture when three signals are combined at the first stripline. Here, $P_{100\ \mathrm{MHz}} = 210$ W, $P_{300\ \mathrm{MHz}} = 490$ W and $P_{700\ \mathrm{MHz}} = 140$ W. The circles show the distribution of the bunches, and the area enclosed by the two straight lines corresponds to the aperture. In this case, the aperture has a diameter of 1 mm.

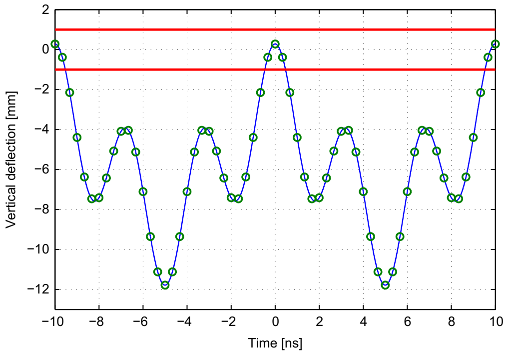

Fig. 7. The vertical deviation as a function of time at the aperture when a 300 MHz signal is fed to the first stripline, and a 100 MHz signal is fed to the second. Here, $P_{100\ \mathrm{MHz}} = 310$ W and $P_{300\ \mathrm{MHz}} = 295$ W. The circles show the distribution of the bunches, and the area enclosed by the two straight lines corresponds to the aperture. In this case, the aperture has a diameter of 2 mm.

now diverging relative each other and the emittance within the bunch train is higher.

To achieve a bunch structure that is 100 ns long, when the signals are combined at the first stripline, two pulsed DC generators are used to deflect the beam during this period. The two DC generators have opposite polarities, $\pm\hat{U}$, and are connected to the downstream ports (Port 1 and Port 2) of the second stripline, while the upstream ports (Port 3 and Port 4) are terminated. Thus, no cable is used to circulate the signal when using the DC generators. The required voltage to deflect the beam Δy at a distance Δz away from the center of the stripline is given by Eq. (4). In this case, the distance to the aperture is $\Delta z = 84$ cm, and with a transverse deflection of $\Delta y = 3$ mm, a voltage of $\hat{U} = 180$ V is required

$$\Delta y \approx \frac{4 e g_{\perp} \hat{U} L}{W_{tot} d} \Delta z + y_0 \tag{4}$$

When running the 3 GeV ring in camshaft mode, i.e. only injecting one bunch train per LINAC shot to a specific ring bucket, the pulse width of the two DC generators is adjusted to a couple of nanoseconds.

If the set-up is chosen where each stripline is fed with a single frequency, the amplifiers can be pulsed to define the start of the bunch structure, while the end of the 3 GHz pulse to the gun defines the end of the bunch structure. Note that this is not possible if the signals are first combined using the cavity filters, since the rise time would be too long. This solution is simpler than using two pulsed DC generators to feed the second stripline, but the start of the bunch structure will not be as well defined since the amplifiers have a longer rise time. Fig. 8 shows the driving schemes of the two set-ups mentioned above. Note that a hybrid scheme is also possible where 100 MHz and 300 MHz are combined and fed to the first stripline, and the DC pulses are fed to the second. By doing that, a wider aperture can be used, and the 100 ns bunch structure is well defined.

In the early phase of commissioning of the new facility when the ring RF cavities are not in operation, a single 500 MHz signal can be fed to the first stripline while half of the bunches in each 500 MHz period are dumped. This would maximize the BPM signal levels, both in the LINAC and in the ring, and thereby maximize the spatial resolution.

5. Test set-up

The test set-up is almost identical to the planned MAX IV thermionic pre-injector, and can be seen in Fig. 9. The divergent beam leaving the gun is focused at the aperture by the first solenoid, and then re-focused at the center of an Energy Filter (EF) by the second solenoid. The first solenoid was actually placed 40 cm closer to the gun in the simulations, and will also probably be so in the final set-up. The aperture consists of a movable plate with two circular holes with diameters 1 mm and 2 mm. Thus, one can select the obstacle by adjusting the plate. The plate can also be removed from the beam pipe. Correctors are placed along the beam pipe to keep the desired bunches centered. Since the bunches leaving the gun have a low-energy tail, the EF is included in the design in order to remove this tail and the low-energy bunches that are generated in the first part of the 3 GHz RF pulse. The EF is a copy of the one used in the present MAX-lab injector, and consists of five quadrupoles, two bending magnets, and a scraper [3]. The energy discrimination of the EF is adjustable around a couple of percent. The exiting beam has zero dispersion. Movable YAG screens with cameras, Current Transformers (CTs) and a Faraday cup at the pre-injector end are used for beam diagnostics.

A stripline BPM and a standard button BPM are mounted at the end of the set-up. These two components are used for diagnostics in the LINAC and in the rings, and the reason for including them in the test set-up is to confirm that the BPM electronics can detect signals strong enough for early commissioning.

6. Results

The tests were performed when the gun was not fully conditioned, and the delivered power level was therefore very low (5.4 MW compared to a maximum estimated power of 7 MW). This resulted in a relatively low beam current. Fig. 10 shows the bunch distribution projected on the YAG screen directly after the aperture (the plate is not inserted) when using the driving schemes equivalent to those in Figs. 6 and 7. Here, the exposure time is longer than the 3 GHz pulse to the gun. Table 2 shows the peak current, before and after the EF, for different apertures and stripline driving schemes. The current after the EF measured by a

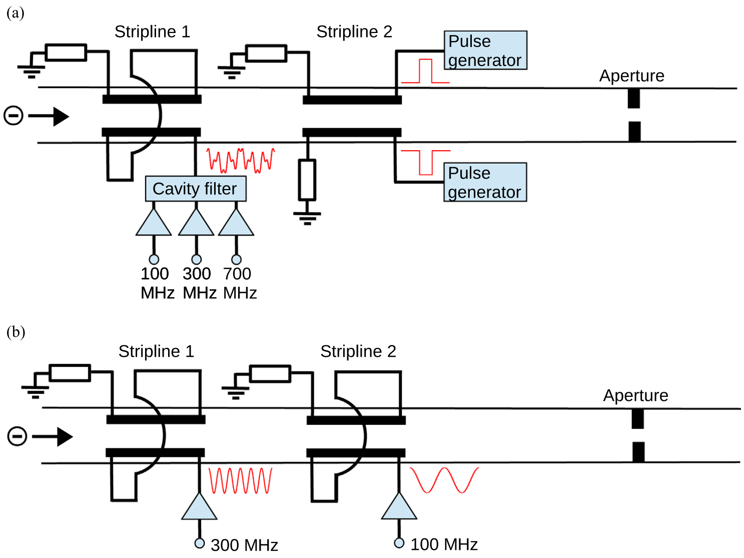

Fig. 8. Two different driving schemes for the striplines. In (a), three frequencies are combined and fed to the first stripline to create the 10 ns bunch trains, while two DC pulses with a width of 100 ns fed to the second stripline define the start and end of the bunch structure. In (b), the two striplines are fed with one frequency each to create the 10 ns bunch trains. Here, the RF amplifiers are pulsed to define the start and end of the 100 ns bunch structure.

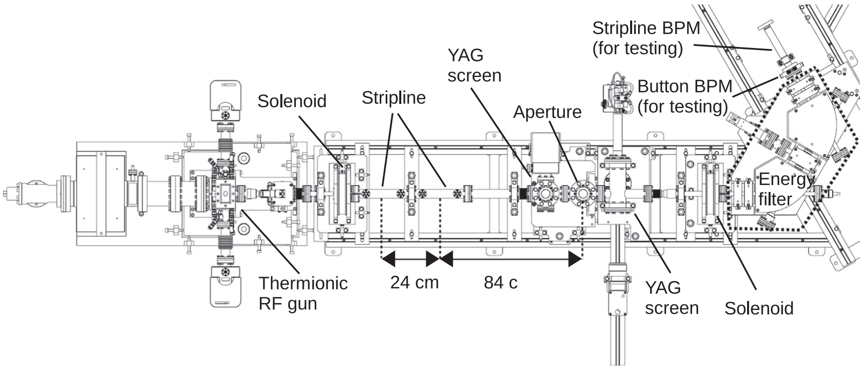

Fig. 9. The layout of the thermionic pre-injector during the tests. The first solenoid will be moved 40 cm closer to the gun in the final set-up.

CT is seen in Fig. 11. Note that physical and digital LP filters are used to obtain a clean DC signal, so the real fall/rise time is actually somewhat shorter. As seen in Table 2, the current loss after the EF is roughly 3% when using the 2 mm hole, and 31% when using the 1 mm hole, compared to when no aperture is used. Ideally, the current after the EF when using the chopper should be 10% compared to the case with no chopper (3 of 30 bunches per bunch train should pass). These ratios are lower in Table 2 for the two driving schemes (7% and 8%) and might be improved by optimizing the focusing optics. However, parts of the two neighboring bunches are leaking through the aperture when using three frequencies and the 1 mm hole.

The design target is to inject a total charge of 9 nC during each top-up injection. With a current of 2 mA after the chopper and EF, the required injection time becomes 4.5 s at a LINAC shot repetition rate of 10 Hz. Two more seconds are required for ramping the injection magnets including the EF. This results in a total injection time of 6.5 s. The current output during the initial tests is somewhat low, and based on simulations and experience with the gun at the present MAX-lab, it should be possible to increase the peak current output after the chopper and EF at least by a factor three by increasing the input power and by adjusting the optics. By doing so, the injection time is reduced to below 4 s.

The pulsed DC supplies that are needed to cut the beam current when using the cavity filter were not available at the time of the measurements. However, the two amplifiers were pulsed when running with the driving scheme presented in Fig. 8(b). It works well and the result can be seen in Fig. 11. The measurements on the stripline BPM and standard button BPM show that the detected 500 MHz single-shot signal is strong enough for early commissioning.

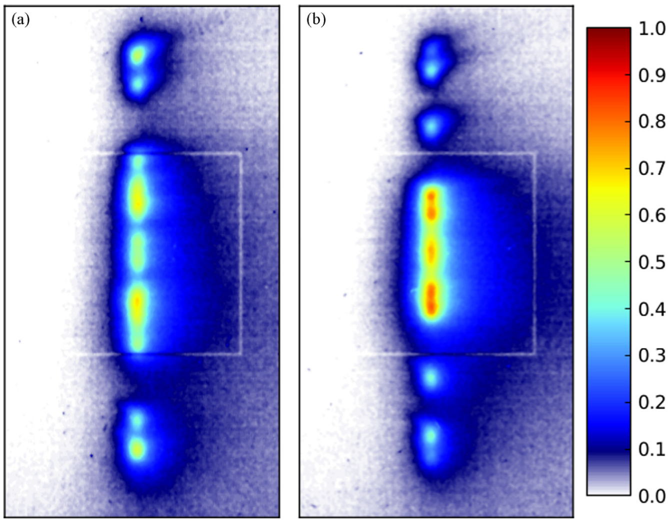

Fig. 10. The bunch distribution projected on the YAG screen directly after the aperture (the plate is removed) when three kicker frequencies are used (a), and when two frequencies are used (b). The square in the middle of the screen has the size 5×5 mm. It is seen that the bunch distributions correspond to the vertical deviations in Figs. 6 and 7.

Table 2
Peak current before and after the EF for different apertures and stripline driving schemes.

Stripline driving scheme	Aperture	Current before EF (mA)	Current after EF (mA)
–	Open	202	29
–	2 mm	80	28
–	1 mm	46	20
100 MHz, 300 MHz	2 mm	9.1	2.0
100 MHz, 300 MHz, 700 MHz	1 mm	5.3	1.7

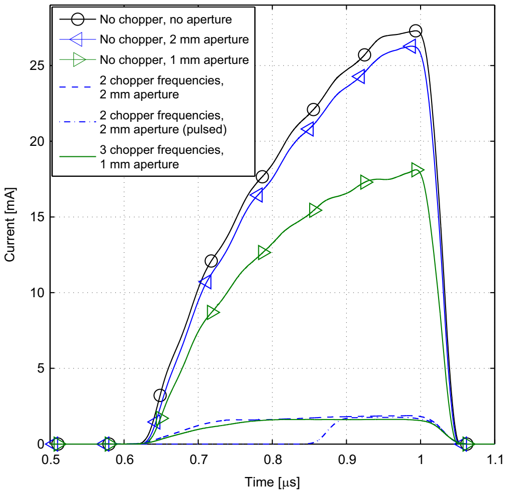

Fig. 11. The beam current after the EF for different apertures and stripline driving schemes. Here, the 3 GHz pulse to the gun starts at $t=0$.

During alignment it was discovered that the horizontal position of the beam moved as the beam energy was swept. This should not be the case for a symmetric gun. It is believed that this is a result of an interfering magnetic field originating from the ion pumps. By applying a vertical magnetic field from an electromagnet over the cathode cell, this phenomenon can be partly compensated for.

7. Future work

More conditioning and optimization of the gun and the pre-injector optics will be performed during the spring/summer of 2014. Initial tests and simulations show that by increasing the input power, the beam current can be increased further. The current loss in the aperture might also be decreased by moving the first solenoid. New ion pumps that are better shielded will also be installed in order to decrease the interfering magnetic field in the cathode area.

8. Conclusions

Initial tests of the thermionic pre-injector and the chopper system show that the desired bunch structure can be created. The overall performance is sufficient for MAX IV, both for normal ring injection and for the spatial resolution of the BPM diagnostics, during early commissioning. The current output is still somewhat low, and we expect it to increase as the testing and conditioning of the gun proceed.

Acknowledgments

The authors would like to thank R. Andersson, Å. Andersson, A. Karlsson, D. Kumbaro, S.C. Leemann, E. Mansten, A. Mitrovic, R. Nilsson, H. Svensson, S. Thorin, and S. Werin for their help during the process.

References

[1] Z.D. Farcas, H.A. Hogg, G.A. Loew, P.B. Wilson, SLED: A Method of doubling SLAC's Energy, SLAC-PUB-1453, June 1974.
[2] E. Elafifi, M. Eriksson, D. Kumbaro, F. Lindau, E. Mansten, S. Thorin, S. Werin, An electron gun test stand to prepare for the MAX IV Project, in: Proceedings of IPAC 2012, New Orleans, Louisiana, USA.
[3] B. Anderberg, Å. Andersson, M. Demirkan, M. Eriksson, L. Malmgren, S. Werin, Nuclear Instruments and Methods in Physics Research A 491 (2002) 307.
[4] H. Ohkuma, Top-up operation in light sources, in: Proceedings of EPAC 2008, Genoa, Italy.
[5] S.C. Leemann, Physical Review Special Topics—Accelerators and Beams 15 (2012) 050705.
[6] D.A. Goldberg, G.R. Lambertson, Dynamic Devices – A Primer on Pickups and Kickers, Lawrence Berkeley Laboratory, URL: 〈https://www.bnl.gov/edm/review/files/references/Goldberg_Lambertson_aip_249_537.pdf〉.

Paper II

New Features of the MAX IV Thermionic pre-Injector

J. Andersson, D. Olsson, F. Curbis, L. Malmgren and S. Werin.

Nuclear Inst. And Methods A **855**, 65-88 (2017).

Nuclear Instruments and Methods in Physics Research A 855 (2017) 65–80

Contents lists available at ScienceDirect

Nuclear Instruments and Methods in Physics Research A

journal homepage: www.elsevier.com/locate/nima

New features of the MAX IV thermionic pre-injector

J. Andersson*, D. Olsson*, F. Curbis, L. Malmgren, S. Werin

MAX IV Laboratory, Lund University, P.O. Box 118, SE-221 00 Lund, Sweden

ARTICLE INFO

Keywords:
Chopper
Electron gun
Energy filter
LINAC
Stripline
Top-up injection

ABSTRACT

The MAX IV facility in Lund, Sweden consists of two storage rings for production of synchrotron radiation. The smaller 1.5 GeV ring is presently under construction, while the larger 3 GeV ring is being commissioned. Both rings will be operating with top-up injections from a full-energy injector. During injection, the electron beam is first delivered to the main injector from a thermionic pre-injector which consists of a thermionic RF gun, a chopper system, and an energy filter. In order to reduce losses of high-energy electrons along the injector and in the rings, the electron beam provided by the thermionic pre-injector should have the correct time structure and energy distribution. In this paper, the design of the MAX IV thermionic pre-injector with all its sub components is presented. The electron beam delivered by the pre-injector and its dependence on parameters such as optics, cathode temperature, and RF power are studied. Measurements are here compared with simulation results obtained by particle tracking and electromagnetic codes. The chopper system is described in detail, and different driving schemes that optimize the injection efficiency for the two storage rings are investigated. During operation, it was discovered that the structure of the beam delivered by the gun is affected by mode beating between the accelerating and a low-order mode. This mode beating is also studied in detail. Finally, initial measurements of the electron beam delivered to the 3 GeV ring during commissioning are presented.

1. Introduction

The MAX IV facility in Lund, Sweden consists of two electron storage rings that will be operating at 3 GeV and 1.5 GeV, respectively, where the former is designed for production of high-brilliance hard X-ray synchrotron light, and the latter will produce light in the IR to the soft X-ray spectral range [1]. The 3 GeV ring is currently undergoing beam commissioning, while the 1.5 GeV ring is being constructed. MAX IV also includes a short-pulse facility (SPF) for experiments with short X-ray pulses with high peak brilliance [2]. For injection into the two storage rings, the electron beam is generated from a thermionic cathode in the thermionic pre-injector and then accelerated in the main injector. For SPF operations the electron beam is generated by photoemission from a copper cathode in the photocathode pre-injector and then accelerated in the main injector. In this paper the MAX IV thermionic pre-injector is described both from a system and from a performance perspective. The photocathode pre-injector, SPF and main injector are not covered in detail, there are only some brief references to the first LINAC section. The thermionic pre-injector is based on the design of the pre-injector at the old MAX-Lab facility [3]. The major improvement is the chopper system, explained in Section 6, used to create the correct bunch structure of the electron beam and to properly time the bunches to the two storage rings. An overview of the injector is found in Section 2, followed by a more detailed overview of the pre-injector and the requirements of the chopper system in Section 3. The sub-systems of the pre-injector are then described in Sections 4–6. Through analytical solutions and simulations the expected performance of the system is investigated with respect to the optics and emittance as well as the chopper system and bunch structure. During 2015 and early 2016, a series of measurements were made to characterize the system, both on optics, gun performance and the chopper system. These measurements are reported in Section 4.7 for the electron beam, and Section 7 covers the complete system performance. Finally, a conclusion is made on the system performance, followed by topics of interests where investigations will continue.

2. The MAX IV Injector

The two storage rings will be operating with top-up injections from the MAX IV injector, a full-energy injector which consists of 39 traveling-wave S-band LINAC structures that are fed by klystrons via SLED systems [4]. A schematic overview of the MAX IV injector can be seen in Fig. 1. There are two bunch compressors in the injector to compress bunches for SPF operations, one at 275 MeV and one at 3 GeV. The electron beam can be extracted from the injector at three different points. The first point is the extraction to the 1.5 GeV ring, it

---

* Corresponding authors. Both authors contributed equally to the article.
E-mail addresses: joel.andersson@maxiv.lu.se (J. Andersson), david.olsson@maxiv.lu.se (D. Olsson).

http://dx.doi.org/10.1016/j.nima.2016.10.051
Received 12 July 2016; Received in revised form 25 October 2016; Accepted 28 October 2016

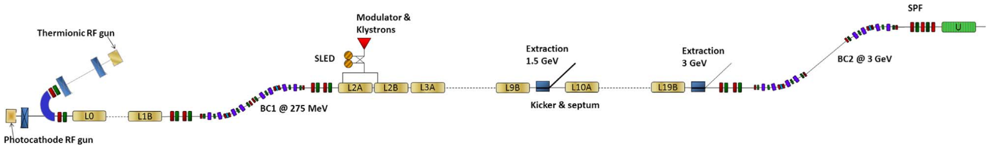

Fig. 1. Schematic overview of the MAX IV injector.

is located after 19 LINAC structures, and the two other points are the extraction to the 3 GeV ring and to the SPF, and they are both located after 39 structures. Commissioning of the injector was carried out during 2014–2015, and initial results are presented in [5]. The electron beam is delivered to the main injector by two separate pre-injectors, and the electron sources in these are a photocathode and a thermionic RF gun, respectively. For SPF operation, the photocathode pre-injector is used, where the high-charge electron bunch is accelerated in the injector in combination with the two bunch compressors. The photocathode gun might also be the electron source in a future free-electron laser (FEL) [6]. The thermionic pre-injector is solely used for ring injections, and is further described in Section 3.

3. The thermionic pre-injector system overview

For reliable operation of the injector system a thermionic RF gun system similar to the well experienced solution at MAX-lab was chosen for the thermionic pre-injector. The electrons are generated from a thermionic cathode and then accelerated and bunched in the RF gun cavities. The thermionic RF gun provides electrons at 2.5 MeV, but due to the non-triggered emission from the cathode, the bunch contains an energy tail. This tail should by preference be removed as early as possible, which is achieved in an energy filter (EF). The requirements of the temporal bunch structure of the electron bunches delivered by the thermionic pre-injector depends on several parameters, such as available RF voltage and radiation losses in the ring that is about to be filled (see Section 3.1). To create the correct temporal bunch structure and to match the 3 GHz structure of the gun and injector to the 100 MHz of the storage rings, a chopper system placed between the gun and the EF is used. It streaks the low energy beam across an aperture. There are two solenoids for focusing, one close to the gun exit used to focus the beam onto the aperture, and a second solenoid after the aperture to collimate the beam into the EF. A set of quadrupoles at the EF entrance puts a double focus at the center of the EF, and a set of quadrupoles after the EF matches the electron beam into the first LINAC section of the injector.

3.1. Injection requirements

Both storage rings will be operating with top-up injections that are as transparent to the users as possible, i.e., the perturbation of the stored beam that occurs during injection is minimized. Unlike many 3:rd generation light sources that use closed four-kicker injection bumps, pulsed nonlinear injection kickers will be used in the MAX IV storage rings [7,8].

During normal operation, the thermionic RF gun delivers a current pulse with a length of hundreds of nanoseconds that consists of S-band bunches, and most of that charge can not be accumulated in the ring buckets during injection. Therefore, a chopper system is needed to create the desired time structure of the injected current pulse. The chopper is installed in the thermionic pre-injector, and the unwanted electrons are dumped before they reach the first LINAC structure. The advantage of dumping them in the pre-injector where they have energies below 3 MeV is that the electron losses at high energies are minimized and thereby also the radiation emitted via bremsstrahlung. Apart from protecting personnel and sensitive electronic equipment from radiation, it also reduces radiation-induced demagnetization of the permanent magnets in insertion devices (IDs).

Table 1 shows the number of S-band bunches that can be accumulated in each ring bucket during an injection for different values of the RF momentum acceptance (MA) resulting from a chosen total RF cavity voltage in the two rings [9,10]. Note that Table 1 is valid when injecting with the non-linear kicker, and only for the bare lattice. The RF MA will decrease once IDs are added. As seen, the number of S-band bunches that can be accumulated in the 3 GeV ring increases when lowering the RF voltage since this results in a larger phase acceptance of the separatrix. The reasons for the much larger phase acceptance in the 1.5 GeV ring compared to the 3 GeV ring are that the former has a larger MA for injected bunches, i.e. for bunches with large amplitudes. Also note that the number of S-band bunches that can be accumulated in each ring bucket actually decreases when lowering the RF voltage in this ring. This is because the injection energy acceptance extends all the way to the maximum RF acceptance in this ring. Hence, when increasing the RF voltage, the MA increases and thereby the number of S-band bunches that can be accumulated.

The RF acceptance and the life time will vary during a typical user shift due to different ID gaps (assuming that this is not compensated for by adjusting the RF voltage). This also changes the phase acceptance and therefore the number of S-band bunches that can be accumulated in each ring bucket during an injection. In the 3 GeV ring, these variations might be considerable since the total radiation losses from IDs and damping wigglers are large compared to the losses in the bare lattice. Here, the radiation loss of the bare lattice is 364 keV/turn while the total loss in the fully equipped ring is estimated to be approximately 1 MeV/turn [10].

Since the LINAC structures are fed via SLED systems, the energy gain is a function of the electron release time. This results in an energy chirp within each LINAC shot [11]. This energy chirp limits the number of ring buckets that can be filled during each shot since the transfer lines that connect the extraction points of the injector with the two rings each have a MA of $\pm 0.8\%$. It is possible to reduce the chirp by phase modulating the RF pulse to the SLED cavities, and thereby to

Table 1
The number of S-band bunches that can be accumulated during injection in the 3 GeV ring (a), and in the 1.5 GeV ring (b) for different RF MA, δ_{RF}, resulting from a chosen total cavity voltage, U_{cav}. Here, it is assumed that the electrons in the injected S-band bunches have the same momentum as the synchronous particle in the ring, and the table is only valid for the bare lattice (no added IDs).

U_{cav} [MV]	δ_{RF} [%]	# S-band bunches
1.80	± 7.1	4
1.00	± 4.4	5
0.60	± 2.4	7

(a)

U_{cav} [MV]	δ_{RF} [%]	# S-band bunches
0.56	± 4.0	19
0.37	± 3.0	18
0.28	± 2.3	16

(b)

increase the injection efficiency further. This feature is however not yet implemented into the LLRF system. The beam loading in the LINAC structures depends on the injected current and has to be taken into consideration since it affects the gain function. Note that the energy spread in each LINAC shot scales down the phase window of the buckets where the charges can be accumulated due to the rotation in phase space. Aside from operating the two rings with uniform filling patterns, the injector should also be able to fill the rings with other exotic patterns with gaps [12].

The total lifetime in each ring is estimated to be at least 10 h, and if one allows a deadband of 1% for this lifetime, one injection every 6 min is required [7]. If smaller deadbands are desired, more frequently injections are of course also possible. Note that more frequent injections results in less experimental time for the SPF and future FEL due to the rise and fall times of the extraction magnets. The timing system that synchronizes the injector to the two rings has filling pattern feedback and is further described in Section 5.2.

In order to fulfill the injection requirements, the chopper has to be dynamic and able to adjust the number of S-band bunches that are injected into each ring bucket and the number of ring buckets that are filled in each LINAC shot. This is explained in detail in Section 6.

4. Design and performance of the electron gun and electron beam

An overview of the pre-injector can be seen in Fig. 7, where the different components are included. Current transformers (CT2-4) are used for the thermionic pre-injector, CT1 is used for the photocathode gun and is not included here.

4.1. Thermionic RF gun

The electron gun used for storage ring injection is an S-band RF gun with a thermionic cathode. The design of the gun has been covered before [3] and a short review is given here. A cut-through of the gun can be seen in Fig. 2, where some of the dimensions are included. The TM_{010} mode at 2.9985 GHz ($\pi/2$ mode) is used for acceleration, and the magnitude of the electric field is roughly 50% in the cathode cell compared to the coupled cell. The resonance frequency is tuned by using a cooling/heating water system that can control the temperature with an accuracy better than 0.1 °C. The gun currently in operation is operated at 60.8 °C to have the correct resonance frequency at the extracted charge levels.

Electrons are emitted from a 3 mm diameter thermionic barium oxide on tungsten cathode produced by Spectramat [13]. The temperature of the cathode filament is controlled using a heater wire, where the current through the heating wire is supplied from a power supply with a current accuracy of 0.2%. The emission from the cathode depends on the temperature and the electric field at the cathode surface through the Schottky effect. An additional effect that can have impact on the emission is back bombardment, i.e. electrons that are emitted at a point in the RF cycle so that they are accelerated backwards and hit the cathode. This has not been studied in detail for the current thermionic gun. The electron beam emitted from the gun is bunched by the 3 GHz RF field, where each of these S-band bunches has a high energy head and a long low energy tail. Due to the filling time of the gun, the emitted charge and energy of each bunch increase over time as the stored energy in the cavity increases, and thus the amplitude of the electric field increases. To ensure an effective injection, the emitted and accelerated charge needs to be as high as possible, while still keeping beam quality parameters through the pre-injector at values to match the beam to the subsequent accelerating systems.

The electromagnetic properties of the gun are simulated using COMSOL Multiphysics [14] and SUPERFISH [15]. SUPERFISH can only simulate 2D rotationally symmetric structures, but its field data output is more suitable for the particle tracking code PARMELA [16]. COMSOL does full 3D simulations and is used to obtain the electromagnetic properties of the complete gun structure, including the vacuum ports and the waveguide. The electric field output from COMSOL is used together with the field output from SUPERFISH to cross-check the simulation results. The field from COMSOL is also used in ASTRA [17] for particle simulations.

The resonant structure contains three separate cells and there are three resonant TM_{010} modes with different phase advances between the cells. From the COMSOL simulations, the 0, $\pi/2$ and π modes are found at 2.9822 GHz, 2.9985 GHz and 3.1673 GHz, respectively. The mode separation between the $\pi/2$ mode and 0 mode is 16.3 MHz which should help to minimize excitation of the 0 mode.

The unloaded quality factor, Q_0, of the structure obtained from COMSOL is 12,830 and the coupling factor β is 2.0. COMSOL is also used to simulate the maximum on-axis field amplitude based on input power at the waveguide port. The simulated case corresponds to the steady state solution, i.e. the field amplitude when the length of the RF pulse is long enough to reach the maximum possible stored energy in the cavity. Fig. 3 shows the maximum accelerating field amplitude in the full cell for different input powers.

The filling time for the cavity is $T_c = Q_0/\omega(\beta + 1)$, where ω is the angular frequency. T_c= 220 ns for the simulated cavity. The length of the RF pulse for the current mode of operation is 1.1 μs, and the field amplitude reaches around 90% of the maximum value for this pulse length without beam loading. The actual maximum field amplitude is then 90% of the data in Fig. 3. At the current time, it is not foreseen

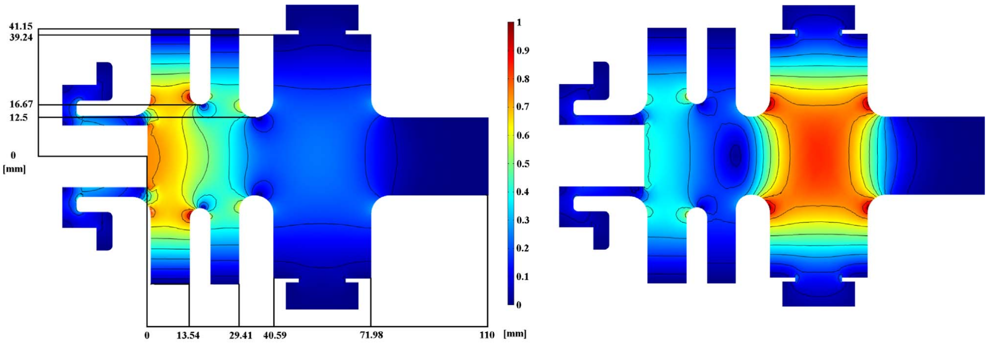

(a) (b)

Fig. 2. Normalized electric field contour plot from COMSOL for the 0 mode (a) and the $\pi/2$ mode (b).

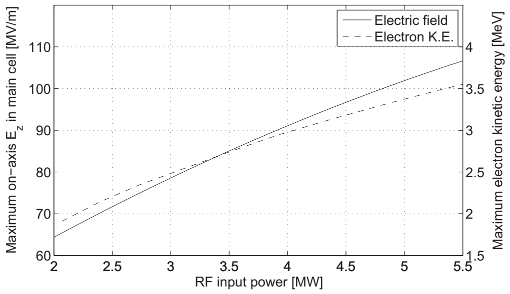

Fig. 3. Maximum on-axis accelerating field in the full cell as function of input power based on the steady-state COMSOL simulations. The maximum electron kinetic energy from ASTRA is based on the input power.

that the gun will be operated at higher on-axis fields than approximately 100 MV/m in the full cell.

4.2. *Gun RF measurements*

Q_0 and β were measured using a vector network analyzer, and their values were 11,872 and 2.0, respectively. As seen, the measured Q_0 is slightly lower than the simulated one obtained from COMSOL, while β agrees well with the simulations.

The bead-pull technique was used to obtain the accelerating field inside the gun cavities. A small metallic sphere (1.1 mm in radius) is moved through the center axis of the gun. The Slater theorem [18] can be used to calculate the electric field, $E_z(z)$, along the central axis of the cavity. Since the radial and azimuthal electric field components as well as the magnetic field in the vicinity of the central axis are close to zero, the theorem simplifies into the following form

$$|E_z(z)| \propto \sqrt{\frac{\omega_0^2 - \omega^2(z)}{4\pi\epsilon_0 a^3}} \qquad (1)$$

where ϵ_0 is the vacuum permittivity, and a is the radius of the metallic ball. ω and ω_0 are the angular frequencies with and without any field perturbation, respectively. The results from this measurement are shown in Fig. 4 together with $E_z(z)$ obtained from COMSOL. The fields correspond well, but there is a small discrepancy to the field amplitude in the cathode cell. This might be caused by small errors in the physical dimensions of the gun from the brazing procedure, since the coupling of the electric field between the cells in the gun is less effective than in the simulated model. The first data points in the measurement that form the sharp peak are when the bead is very close to the cathode surface, and these points should be ignored. Particle simulations, using the same codes as in Section 4.6 are used to investigate if the difference on the electric field properties would have a significant effect on the beam properties. The difference in field amplitude is about 4% close to the cathode surface, and it does change the beam properties but within acceptable limits. Simulations shows that it is possible to operate with the same settings in the pre-injector for up to 5% field difference at the cathode. Larger field amplitude differences requires adjustments along the pre-injector, however it has not been investigated in detail how large differences that are acceptable with adjustments.

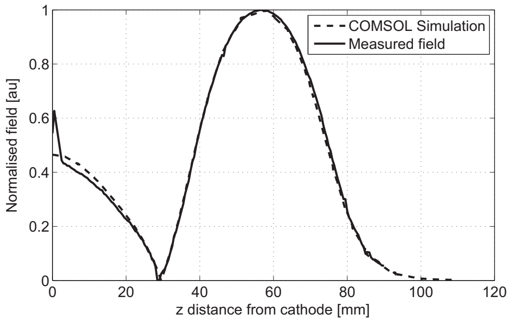

Fig. 4. $E_z(z)$ along the gun center axis obtained from COMSOL and from the bead-pull measurement.

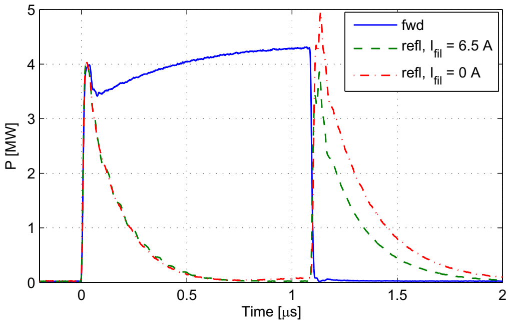

Fig. 5. The measured forward and reflected power obtained by diode peak detectors at the gun input port.

Fig. 5 shows the forward and reflected power measured with diode peak detectors at a wave guide directional coupler at the gun input. As seen, the 1.1 µs long forward RF pulse is not perfectly rectangular due to limitations of the klystron and its modulator. This is the RF pulse that is fed to the gun during ring commissioning, and the peak power, P_{peak}, defined as the average power within the RF pulse is 4.02 MW. The two reflected RF pulses in the figure were obtained at two different cathode filament currents and will be further explained in Section 4.3.

4.3. *Beam loading*

In the absence of beam loading, the filling time of the electric field should be the same for different emitted currents, i.e. for different I_{fil}. It can be seen in Fig. 6 for P_{peak} = 4.02 MW that the effects of beam loading became visible for values of I_{fil} over 5.5 A, where the filling time and maximum field amplitude start to decrease.

The effects of beam loading can also be seen when studying the reflected power in Fig. 5. When beam loading is present, the coupling to the gun goes from over coupled (β=2.0) to a coupling that is closer to matched (β=1.0). As seen, the transient of the reflected power after the

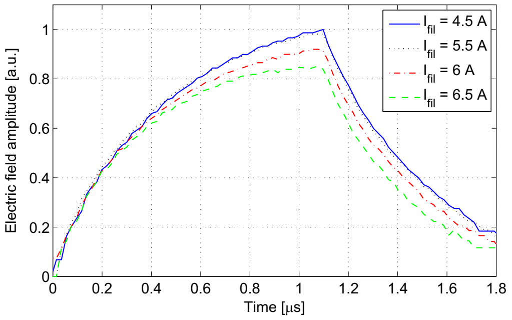

Fig. 6. The measured amplitude of the accelerating electric field inside the gun cavities for different cathode filament currents.

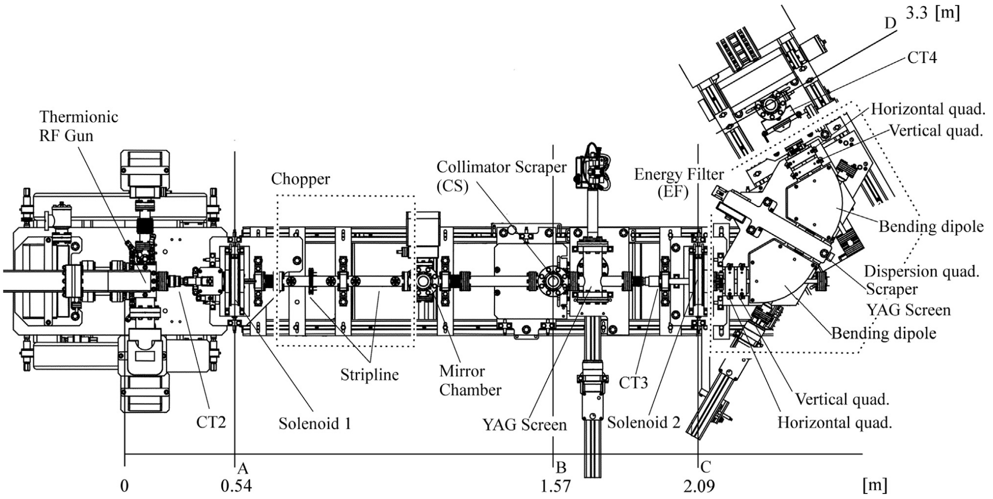

Fig. 7. Schematic overview of the pre-injector.

end of the forward RF pulse at 1.1 µs is higher when I_{fil}=0 A compared to the case when I_{fil}=6.5 A. This shows that the over coupling is higher in the former case. The reflected transient is emitted from the gun cavity which still has electromagnetic energy stored after the end of the forward RF pulse. The beam loading has therefore a significant effect on the matching between the RF power source and the gun.

4.4. Optics and energy filter

There are two different focusing sections, the first section consists of two solenoids and the second of five quadrupoles in the energy filter. When the electron beam exits the gun it is divergent, and the first solenoid at 0.5 m (position A in Fig. 7) from the cathode focuses the beam for the high energy electrons onto an adjustable collimator scraper (CS), 1.6 m from the cathode (position B in Fig. 7). The CS has different types of obstacles that can be inserted into the beam path.

Before the beam reaches the CS, it passes two planar striplines and two vertical corrector magnets. These components are part of the chopper system, and are further described in Section 6.1. The vertical deflection of the chopper makes it possible to create the correct bunch structure of the electron beam. Electrons that are not selected by the chopper are dumped before they reach the first LINAC structure. After the focus at the CS, the beam becomes divergent, and the second solenoid (at position C in Fig. 7) is used to collimate the beam before it passes into the first quadrupole of the EF, 2.2 m from the cathode.

There are two quadrupoles at the entrance to the EF, focusing in the horizontal and vertical planes, respectively. These quadrupoles create a double focus at the central plane of the EF. The EF has two bending dipoles with a dispersion correction quadrupole in the middle. This quadrupole is mechanically split to make it possible to insert a scraper into the beam at the middle plane of the EF. There is also a possibility to insert a YAG screen at this position. The scraper is at the dispersive plane of the EF, and can be moved through the beam in the direction towards higher energy electrons. By combining the dipole settings with the scraper edge position, the EF is tuneable both in respect to the accepted energy and energy spread. The mechanical energy acceptance of the energy filter is approximately 200 keV due to the size of the beam pipe. After the second bending dipole there are two quadrupoles for focusing in the horizontal and vertical plane, respectively. These quadrupoles are used to refocus the beam to properly match it into the first LINAC structure, 3.3 m from the cathode (position D in Fig. 7).

4.5. Particle emission

The electron source for the pre-injector is a thermionic cathode in the first cell of the gun. There are diagnostic possibilities to measure the cathode temperature with a pyrometer. The temperature was measured for a set of different cathode filament currents, I_{fil}, and the measured cathode temperatures were $T_{\text{fil}} = 1060\,^{\circ}\text{C}$ for $I_{\text{fil}} = 6.0$ A, $T_{\text{fil}} = 1130\,^{\circ}\text{C}$ for $I_{\text{fil}} = 6.5$ A and $T_{\text{fil}} = 1220\,^{\circ}\text{C}$ for $I_{\text{fil}} = 7.0$ A.

The initial electron beam properties depend on the emission process. For a thermionic cathode it is possible to show that the transverse emittance, ϵ, depends on the temperature T of the cathode as

$$\epsilon = \sigma\sqrt{\frac{k_B T}{mc_0^2}} \tag{2}$$

where k_B is the Boltzmann constant, σ is the rms size of the emitting area, m the electron mass and c_0 the speed of light. It is assumed that the emission is radially uniform, so σ is half the cathode radius. Using the temperature range obtained from the measurements, it is possible to estimate that the thermal emittance is 0.35 − 0.37 mm mrad for the emitted electrons during operating conditions. A value for the initial transverse emittance of 0.37 mm mrad will thus be used for the initial particle distribution in simulations.

4.6. Particle Tracking

To investigate the electron beam properties at the exit of the gun and through the focusing systems, two different particle tracking codes were used, ASTRA and PARMELA. ASTRA is used to simulate the first part of the pre-injector from the cathode in the gun, acceleration in the gun and beam propagation through the first solenoid. The beam optics for this part of the pre-injector verify the results from PARMELA which simulate the propagation through the full pre-injector, cathode to LINAC entrance. The simulations are based on a maximum on-axis electric field amplitude of 80 MV/m and a total extracted charge per S-band bunch of 200 pC, unless otherwise specified. The full bunch

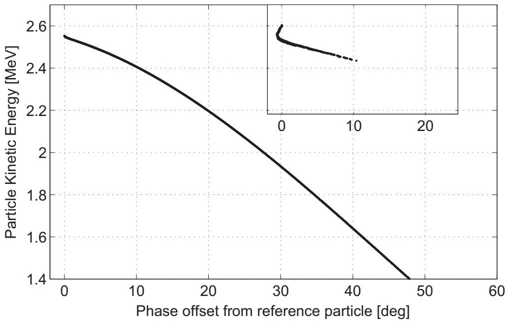

Fig. 8. Simulated electron kinetic energy as a function of phase offset from PARMELA. The subplot in the figure is for the bunch after it passes the EF and low energy electrons have been dumped.

length is 100 ps, corresponding to emission times where electrons are accelerated out of the gun.

4.6.1. Beam energy and energy spread

The maximum electron energy can be found using ASTRA, with the electric field amplitude and electric field distribution as obtained from COMSOL, see Section 4.1. Fig. 3 shows the simulated maximum electron energy as a function of input power from ASTRA at steady state, where the electric field as function of the input power is also found from COMSOL.

Fig. 8 shows the energy-phase distribution of the bunch from PARMELA, as can be seen there is a large energy spread within the S-band bunch. In the same figure the subplot shows the energy-phase distribution of the bunch after it passes through the CS and EF where the low energy tail has been dumped. Space charge effects during the transport are visible as an energy expansion in the subplot.

4.6.2. Emittance and optics

From ASTRA the charge distribution in the bunch and the normalized transverse rms emittance are found. Approximately 20%, or 40 pC, of the bunch charge is in the top 100 keV of the bunch energy distribution (2.45 – 2.55 MeV), and the emittance for this part of the bunch is approximately 1 mm mrad. The emittance decreases to 0.7 mm mrad for electron energies of 2.2 MeV, and then increases rapidly with lower electron energy. However, the next 20% of the bunch charge has an energy spread of 300 keV which is outside the acceptance of the EF, and in order to keep the maximum charge possible the top 100 keV of the bunch is kept through the EF.

From PARMELA the beam optics can be extracted, as well as how much of the charge that is transported through the pre-injector. The optics and transported charge for the pre-injector are shown in Figs. 9 and 10. As can be seen for the operating parameters, there is a double focus in the energy filter at 2.5 m from the cathode. This simulation does not include correctors or the chopper system. From this result it is can also be seen that the S-band bunch charge at the entrance of the first LINAC structure is approximately 40 pC (about 20% of the initial S-band bunch charge). From the simulation it can be seen that the final energy spread after the EF is roughly 150 keV (also illustrated in the subplot in Fig. 8) and the emittance is around 3 mm mrad, which verifies that the EF can be used to dump the low-energy electrons.

As mentioned, each S-band bunch from the gun has a high energy head and a long low energy tail. Due to the chromatic properties of solenoid 1, different parts of the beam have different focal points and transverse positions at the CS. The CS has an aperture of 1 or 2 mm and cut some of the beam depending on the beam properties. From simulations in PARMELA, the acceptance of this additional energy filtering can be estimated. Simulations show that for $P_{\mathrm{peak}} = 4.02$ MW the energy acceptance is 200 keV with the 1 mm aperture, and 300 keV with the 2 mm aperture. It is also seen that the energy acceptance depends on the divergence of the beam at the gun exit. A less divergent beam leads to a higher energy acceptance through the CS.

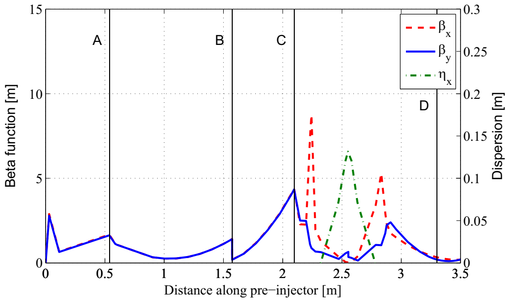

Fig. 9. Simulated optics for the operating parameters where beta functions and the dispersion along the pre-injector are shown. The four vertical lines correspond to positions A, B, C and D as in Fig. 7.

The chopper system can be included in the ASTRA simulation by using MATLAB to include the change of particle momentum through the striplines. For a single 500 MHz signal fed to first the stripline, the projected charge distribution at the YAG screen directly after the CS can be seen in Fig. 22 (c), and compared to the measured projection it is seen that the results agree well.

4.7. Measured electron beam properties

The EF can be used as a spectrometer by observing the beam at the YAG screen that can be inserted at the position of the scraper. To estimate the beam energy, the first solenoid focuses the beam onto the YAG screen. The electron energy was then obtained by scanning the current to the EF dipoles, placing the beam edge at the reference trajectory through the EF and then using data on the dipole current to kinetic energy for this reference trajectory. The results from these measurements are seen in Fig. 11.

It is possible to compare these values to the simulations in Section 4.6.1 using the measured input power data. For $P_{\mathrm{peak}} = 4.02$ MW and $I_{\mathrm{fil}} = 6.0$ A it was found that the electric field amplitude is 83.5 MV/m. For $P_{\mathrm{peak}} = 4.02$ MW and $I_{\mathrm{fil}} = 6.5$ A the electric field amplitude was 79 MV/m. The measured data however shows a lower maximum electron energy for higher emitted currents, which is expected if beam loading is taken into account.

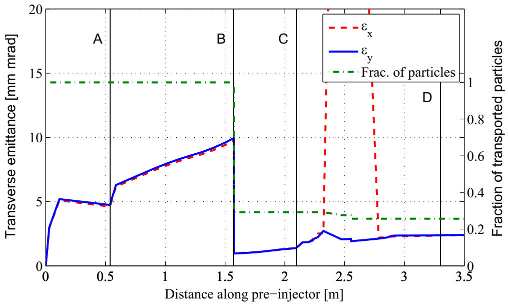

Fig. 10. Simulated transverse normalized rms emittance and the fraction of transported electrons along the pre-injector. The four vertical lines correspond to positions A, B, C and D as in Fig. 7.

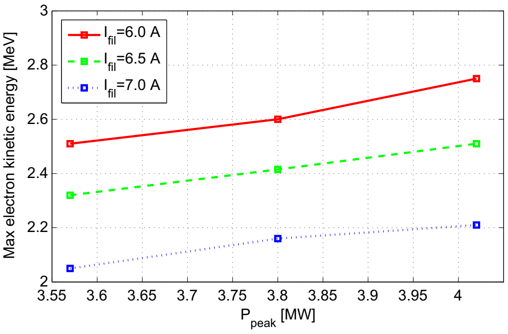

Fig. 11. The measured electron energy as a function of input power for three different filament currents.

For the two cases above the field amplitude ratio, i.e. the maximum electric field amplitude at the end of the RF pulse compared to the maximum electric field of the steady state simulation, was found. Then the relative maximum amplitude compared to the maximum amplitude in the cavity at absence of beam loading, i.e. at $I_{\rm fil}$ = 4.0 A, was found for each measurement settings. The relative maximum amplitude for each setting was then multiplied by 83.5 MV/m and 79 MV/m, respectively to find the electric field at steady state with no beam loading. The steady state amplitudes are found to be 95.6 MV/m and 96.1 MV/m. Compared to the results from the simulations this correspond to a input power of 4.3–4.4 MW, fairly well in agreement with the measured input power.

In Section 4.6.2 it was described that the combination of the first solenoid and CS becomes an energy filter. By adjusting the dipoles in the EF and observing the beam on the YAG screen in the center of the EF, the energy spread of the beam when entering the EF can be estimated. For the operating parameters with $P_{\rm peak}$ = 4.02 MW and $I_{\rm fil}$ = 6.5 A, the energy spread at the EF was 1.3 MeV when the CS was extracted. With the 2 mm aperture at the CS, the energy spread was approximately 500 keV. For the same input power but $I_{\rm fil}$ = 7.0 A, the energy spread at the EF was approximately 300 keV. These measured values are in the same order as the simulated results, but they do not match exactly. In Section 4.3 it was shown that the accelerating gradient is lowered for higher emitted beam currents due to beam loading. For $I_{\rm fil}$ = 7.0 A, a higher emitted current is expected, leading to a lower accelerating gradient and a more divergent electron beam out from the gun. The beam is not as focused onto the CS as for the higher gradient case, and less electrons are accepted through the CS.

The measured current at CT2 during operating conditions is shown in Fig. 22 (a). It was expected that this curve would rise smoothly over the RF pulse duration, but in the measurement result an oscillating component can be seen. The oscillation has a frequency of 16.6 MHz, which is close to the mode separation between the $\pi/2$ mode and the 0 mode. The oscillating structure of the emitted current is therefore believed to come from mode beating between the $\pi/2$ mode and the 0 mode. This will be further discussed in Section 4.8.

The emitted current from the gun at operating conditions was measured to maximum 670 mA, which corresponds to approximately 220 pC emitted per S-band bunch. A series of measurements of the emitted current (1 mV on u_2=1 mA) as a function of input power and filament current were made, and the results are shown in Table 2.

From these measurements it can be observed that the increase in filament current does increase the emitted current as expected.

Table 2
Measured CT voltage and bunch charge at the gun exit for different input power and filament currents.

$P_{\rm peak}$ [MW]	$I_{\rm fil}$ [A]	max ($u_2(t)$) [mV]	max (Q_b) [pC]
4.02	7	1251	417
3.80	7	1180	393
3.57	7	1080	360
4.02	6.5	687	229
3.80	6.5	641	214
3.57	6.5	612	204
4.02	6	244	81
3.80	6	247	82
3.57	6	245	82

4.8. Mode beating

As mentioned in Section 4.7 it was observed that the emitted current out from the gun had an oscillation with a frequency of 16.6 MHz. Since this is close to the measured mode separation between the 0 mode and the $\pi/2$ mode, it is suspected that this could be caused by excitation of the 0 mode. Fig. 22 (a) shows the measured beam current out from the gun where the oscillation is clearly visible in the $u_2(t)$ signal (CT2). By simulating the charge out from the gun assuming an excitation of the 0 mode, it is possible to show that this will create an oscillation similar to the one observed in the beam current. Fig. 12 shows the simulated beam current from ASTRA with both the 0 mode and the $\pi/2$ mode excited, at an electric field amplitude for the 0 mode that is 5% of the $\pi/2$ mode. The value of 5% excitation was found to produce similar amplitudes for the oscillation in the simulations as in the measured beam current. Further work is being carried out to fully be able to simulate the oscillation.

From the simulations it can also be seen that the energy difference during the mode beating can be as high as 300 keV, which is outside the acceptance of the EF. The mode beating also affects the divergence of the beam out from the gun and the energy spread, and more particles will be lost on the CS. This might have a significant impact on the injection efficiency, but further measurements are needed to fully characterize the impact.

A real-time spectrum analyzer was used to measure the power density spectrum of the 1.1 µs output RF pulse from the klystron, seen in Fig. 13. The spectrum of an ideal 1.1 µs long RF pulse of 2.9985 GHz can also be seen in the same figure. As seen, the shape and magnitude of the klystron spectrum do not differ much from the spectrum of the ideal pulse, and no signs of any excited buncher cavities inside the klystron can be seen in the spectrum in the vicinity of the 0 mode. However, the power density close to this mode is of course not zero.

Fig. 14 shows the power density spectrum of the accelerating field inside the gun obtained via the pick-up hook antenna. The spectrum at three different cathode filament currents are plotted, and one can

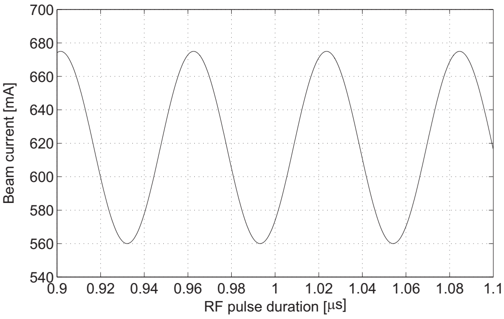

Fig. 12. Simulated emitted current from the thermionic gun with excitation of both the 0 and the $\pi/2$ mode.

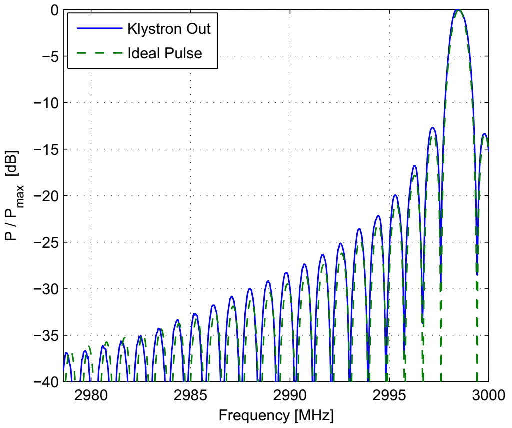

Fig. 13. The measured power density spectrum of the 1.1 μs long RF pulse from the klystron output and the spectrum of an ideal RF pulse.

clearly see that the 0 mode around 2.982 GHz is excited. As seen, the excitation exists even when the cathode is not heated (I_{fil} = 0 A) which indicates that the unwanted mode excitation is driven by the RF pulse from the klystron. A very small peak current of 3 mA can however still be measured at CT2 when I_{fil} = 0 A. This is cold-emitted dark current, and might partly explain the mode excitation in this case. However, since the magnitude of the cold-emitted dark current is very low compared to the emitted current when I_{fil} = 6 A even though the magnitude of the measured mode excitation is roughly the same in the two cases, it is assumed that the mode excitation when I_{fil} = 0 A is mainly driven by the RF pulse. The mode excitation is much stronger when I_{fil} = 5 A compared to when I_{fil} = 6 A. One can therefore draw the conclusion that the unwanted mode excitation is partly driven by the beam since different values of I_{fil} result in different beam loading and therefore different time-dependent magnitudes of the accelerating electric field. Even though the charges that can drive the mode excitation are more numerous when I_{fil} = 6 A, the field properties of the accelerating $\pi/2$ mode seems to be more ideal for excitation of the 0 mode during the 1.1 μs pulse when I_{fil} = 5 A.

Hence, the unwanted mode excitation seems to be a result of both a non-zero power density in the vicinity of the 0 mode in the klystron pulse, and an excitation by the emitted current via wakefields. One way of reducing the impact of former is to amplitude modulate the rising flank of the RF pulse in several steps and thereby making the power spectrum more narrow. The latter can be reduced by finding a suitable combination of the RF input power and the I_{fil} that minimizes the wakefield excitation of the mode.

5. Design of the RF system

5.1. RF distribution

The 2.9985 GHz CW master signal of the injector originates from a signal generator and is distributed to all the S-band structures. For the thermionic gun, the master signal is distributed to a LLRF box, where the pulse shaping of the CW signal is done using a fast GaAs switch, and the phase relative to the other S-band structures is adjusted by a voltage controlled varactor diode based phase shifter. The low-power pulsed signal is then amplified, first by a solid state pre-amplifier and then by a klystron which is driven by a solid state modulator. In order to minimize amplitude jitter, the klystron is operated in saturation. Therefore, the pulsed power delivered to the gun has to be adjusted by adjusting the voltage in the modulator. The high-power RF pulse is then fed to the gun via a waveguide system. A circulator is protecting the klystron from the reflected field from the standing wave cavities of the gun, and the waveguide system in the vicinity of the circulator is filled with sulfur hexafluoride (SF_6). Unlike the other S-band structures (including the photocathode gun), the thermionic gun is not fed via a SLED system. The forwarded and reflected pulses are monitored along the RF chain from several directional couplers. The accelerating field in the gun cavities is monitored via a hook antenna that is located inside one of the pipes that are used for vacuum pumping. The cut-off frequency of the TE_{11} mode in the pipe is well above 3 GHz, and the antenna is only intercepting a small fraction via the leaking field.

Fig. 15 shows a block diagram of the RF distribution to the gun.

5.2. Timing and synchronization

As described in Section 6.2, the superposed RF signal that is fed to the first stripline is always frequency synchronized to the ring that is about to be filled. However, the synchronous phase will vary during operation due to several parameters. Since the phase window where charges can be accumulated during injection follows the drift of the synchronous phase, the superposed signal in the chopper has to follow the same phase drift. This will simply be accomplished by measuring the synchronous phase and then adjusting the phases in each branch line in Fig. 17.

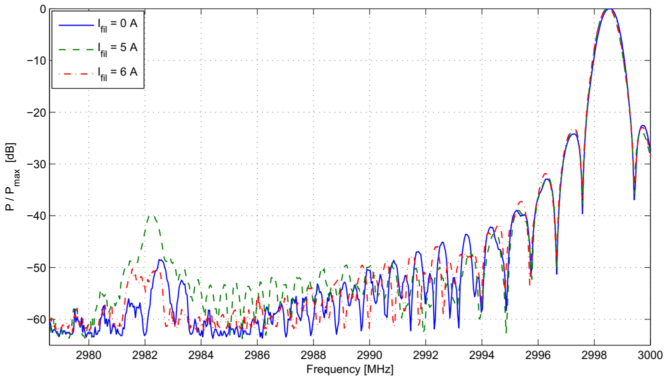

Fig. 14. The measured power density spectrum of field inside the gun obtained via the pick-up hook antenna for three different cathode filament currents, I_{fil}. Note that the (normalized) noise floor is just below −60 dB.

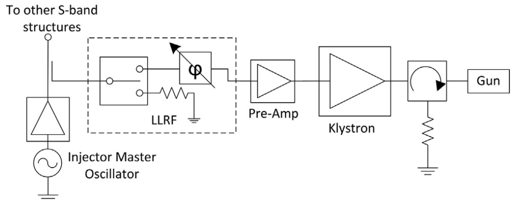

Fig. 15. The RF distribution to the thermionic gun.

Since the LINAC RF and the main RF in the two rings are drifting relative to each other, the vertical deflection of the S-band bunches within the desired time window vary (they will drift along the trajectory lines in the left plots in Figs. 20–21) from shot to shot. This phase drift results in small variations in the total injected charge of the LINAC shots over time. One way of reducing these variations of the injected charge is to implement a coincident detector that is able to monitor the beating between the frequency of the LINAC RF and the main RF of the ring that is about to be filled. By doing so, the trig signals to the injector are only generated when the phase difference is within an acceptable interval. This coincident detector will be a future upgrade to the timing system.

The top-up operation starts by injecting into ten successive ring buckets. In order to decide which buckets to refill, a quantitative bunch charge measurement is needed. This is done by measuring the sum signal from one BPM head or by measuring the signal from a photodiode at a diagnostic beamline using an oscilloscope. The oscilloscope is triggered by the machine clock, and the waveforms of all the buckets (176 in the 3 GeV ring and 32 in the 1.5 GeV ring) are collected and read into the control system. An estimation of the relative charge can then be determined for each bucket by data analysis. The individual buckets that are refilled during each LINAC shot are then selected by the control system by using the chopper.

6. Design and performance of the chopper system

6.1. Layout

As mentioned above, the main components of the chopper system are two planar striplines, two vertical corrector magnets and a collimator scraper (CS). Fig. 16 shows the basic set-up of the chopper system. The first stripline is fed by a superposed RF signal that consists of 100 MHz, 300 MHz and 700 MHz components (see Section 6.2), and the second stripline is fed by two DC pulses of different polarities. The superposed RF signal in the first stripline is circulated as shown in Fig. 16, and the propagating mode is an odd (differential) TEM mode at frequencies $f = (1 + 2n)f_0$, $n \in \mathbb{N}$, i.e. odd harmonics of $f_0 = 100$ MHz. The stripline design is further described in [19].

The electrons within the desired time structure experience a deflecting net force that is zero (or close to zero) when passing each stripline. This is because the Lorentz forces induced by the horizontal magnetic field of the two correctors are canceled out by the forces induced by the counter propagating TEM waves in the striplines.

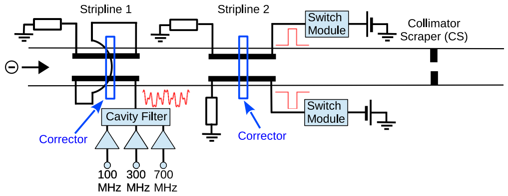

Fig. 16. The basic components of the chopper system.

Electrons outside the desired time structure are dumped at the CS which is basically an adjustable plate. Three different obstacles can be selected at this plate: a 1 mm aperture hole, a 2 mm aperture hole, or a knife edge. Note that it is actually possible for some electrons to pass the CS if they are outside the desired time structure, even if one of the holes are inserted and centered in the beam pipe. These are electrons with significantly lower energies than those in the head of the bunch that are focused at the CS (see Section 4.6.1), and in order to pass they need to approach the first stripline with a significant vertical angle. However, even if some of these electrons manage to pass the CS, they can not pass the energy discrepancy of the EF due to their lower energy. This is shown in Section 7.1. With the 2 mm aperture inserted, it is possible to find more efficient driving schemes for different phase acceptances compared to the case when the 1 mm aperture is inserted. From a radiation safety perspective, it is also an advantage to use the 2 mm aperture over the knife edge since the latter obstacle could result in a higher current throughput with undesired time structure if wrong settings are applied to the correctors and/or to the chopper (this can for example be caused by a faulty power supply or amplifier). Therefore, the chopper optimization and measurement results presented in this report are obtained when the 2 mm aperture is inserted.

The chopper is a critical component in the radiation safety system, which should prevent that an electron current that is too high accidentally enters the injector. In order to do that, the current levels delivered to the two corrector magnets that are placed around the striplines are monitored by a surveillance system that is separated from the machine control system. The position of the CS is also monitored by the same system, and an interlock occurs if the corrector current are below a threshold level and/or if the plate of the CS is not located within a certain interval. This prevents any electrons from entering the first LINAC structure in case the chopper is not activated. The total charge per shot before and after the EF is also monitored, and an interlock also occur if the total charge exceeds a certain threshold.

6.2. RF and high-voltage distribution

As explained in [19], three signals of 100 MHz, 300 MHz, and 700 MHz were chosen to feed the first stripline since these are the dominant Fourier frequency components of the ideal combined signal when injecting 3 S-band bunches per ring bucket. This was the only injection scheme that the chopper was initially designed for. By adding more frequencies that are odd harmonics of 100 MHz to the superposed signal, it is possible to generate signals that are better optimized for different phase acceptances of the ring buckets. However, this is at the cost of a more complex feeding network, and it will be shown in Section 6.5 that it is possible to obtain quite good driving schemes, even with three frequencies.

It would be possible to synchronize and frequency lock the injector master oscillator to the 30:th harmonic of the ring main RF frequency by adjusting the temperature of the injector S-band structures as the ring main RF frequency varies. However, this becomes unrealistic since there are two storage rings whose main RF frequencies are set independently of each other due to different thermal contractions/expansions of the circumferences over time. Such continuous temperature adjustments in the injector would also have a negative effect on the phase stability, which is crucial for the SPF and for the future FEL. Instead, only the RF signals in the chopper system are phase and frequency locked to the ring that is about to be filled. This is achieved by distributing the main RF frequencies of the two rings to a switch unit in the pre-injector. The RF signal of the ring that is about to be filled is then fed to a comb generator which produces harmonics of the original 100 MHz signal. The new signal is then split into four branch lines, where each line is filtered with band pass filters. The frequencies that are kept in the branch lines are 100 MHz, 300 MHz, 500 MHz, and 700 MHz respectively. Each branch line has its individual IQ modulator that operates as a vector modulator, and a fast switch. This

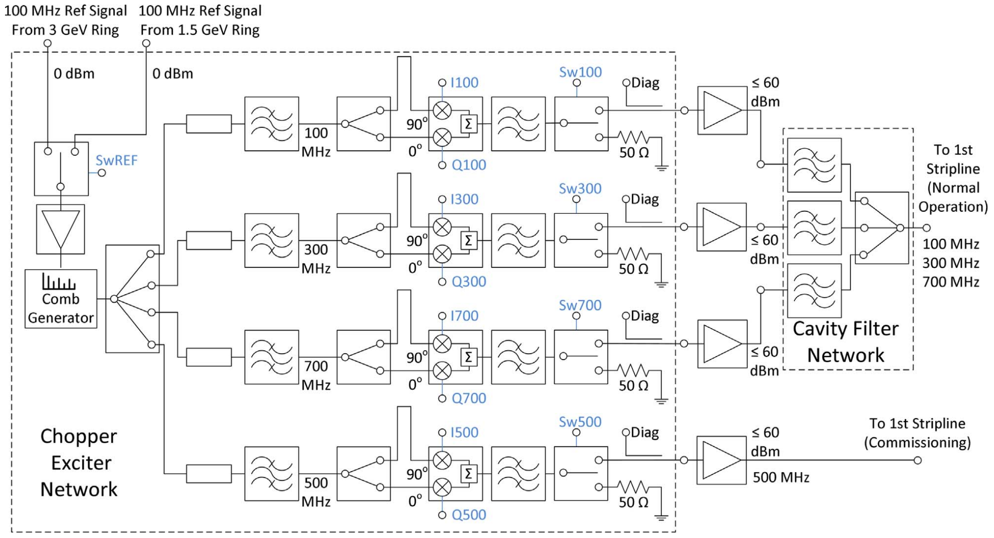

Fig. 17. A somewhat simplified block diagram of the RF distribution to the first stripline.

enables control of the phase and amplitude of each individual branch line, but also fast pulse shaping of the output signals. The 100 MHz, 300 MHz and 700 MHz signals are then amplified and fed to a cavity combiner filter where the superposing RF signal that is fed to the first stripline is created.

Note that the fourth branch line, which distributes the 500 MHz signal, is only used for commissioning purposes in the injector and in the rings since it maximizes the sensitivity of the BPM system. This is because the BPM electronics [20] is sampling an oscillation in a 500 MHz band pass filter that is excited by the beam. During commissioning, 1 or 2 S-band bunches per 500 MHz cycle are kept. The signal from this branch line is not fed to the cavity combiner. However, it is possible to also implement a 500 MHz cavity into the combiner filter in the future. This would make it possible to create a more complex superposed RF signal which makes the chopper system more flexible.

Fig. 17 shows the RF distribution network for the first stripline. The Sw*x*00 signals control the pulse shaping, I*x*00 and Q*x*00 control the phase/amplitude of each branch line, while SwREF selects the source of the RF harmonics. As seen, it is an analog system that eliminates the need for creating each individual RF signal with digital signal generators.

The two DC pulses that are fed to the second stripline are generated by two commercial switch modules. Basically, each such module consists of a capacitor bank with a fast solid-state switch that is gated by a trig signal. Each module is fed by a variable voltage supply which can be seen in Fig. 16.

6.3. Deflection and current throughput

A particle, with charge q and a total kinetic energy W, that propagates at the speed of light along the center of the beam pipe at the entrance of the chopper, has a transverse displacement $\mathbf{r}_0(t) = x_0\hat{\mathbf{x}} + (y_s(t) + y_0)\hat{\mathbf{y}}$ at the CS, where x_0 and y_0 are the static displacements caused by the two corrector magnets. The vertical time dependent displacement $y_s(t)$, caused by the counter propagating TEM waves in the two striplines, is given by

$$y_s(t) \approx \frac{q}{W}\left\{\sqrt{2}L_1\sum_{n=1}^{N}\sqrt{P_n Z_\perp(\omega_n)}\cos\left(\omega_n\left(t-\frac{L_1}{c_0}\right)+\varphi_n\right) - \frac{L_2\sqrt{Z_0 Z_\perp(\omega=0)}}{L_s}\int_{-L_s/2}^{L_s/2} i_{DC}\left(t+\frac{2z-L_2}{c_0}\right)\mathrm{d}z\right\} \tag{3}$$

Here $Z_0 = 50\ \Omega$ is the characteristic impedance of a single strip for the odd (differential) TEM mode, $i_{DC}(t)$ is the current pulse delivered to the upper strip of the second stripline, c_0 is the speed of light in vacuum, and $L_s = 15$ cm is the length of a single strip. L_1 is the distance between the center of the first stripline and the CS, and L_2 is the distance between the center of the second stripline and the CS. P_n, ω_n, and φ_n are the rms input power, angular frequency, and relative phase of the n:th RF signal that is combined into the superposed signal and fed to the first stripline, respectively. $Z_\perp(\omega)$ is the stripline transverse shunt impedance and is given by

$$Z_\perp(\omega) = Z_0\left(\frac{4g_\perp c_0}{\omega d}\right)^2 \sin^2\left(\frac{\omega L_s}{c_0}\right) \tag{4}$$

where d= 10 mm is the spacing between the two strips, and $g_\perp = 0.99$ is the transverse geometry factor of the stripline defined in [21]. Note that $Z_\perp(\omega)$ in (4) is a factor two greater than the shunt impedance found in most literature, since the RF signal is circulating through both strips (see [19]). Hence, the required power for a given kick is reduced by a factor two compared to a more traditional system where the RF signal is split using a 3 dB 180 degree hybrid coupler and then fed to the two downstream ports. Note that this is a low-frequency approximation and only valid when the losses in the ceramic feedthroughs are low. In (3), it is assumed that the current pulse that is applied to the lower strip of the second stripline is identical but has the opposite sign compared to the current pulse applied to the upper electrode $i_{DC}(t)$.

Assume that the charges are ultra-relativistic, and that the current $i_{CS}(t)$ that reaches the CS at time t, has a normalized transverse projected charge distribution in the transverse plane $\lambda_\perp(\mathbf{r}, t)$ so that $\int\lambda_\perp(\mathbf{r}, t)\mathrm{d}a = 1$. Then if the energy acceptance of the EF is $W^- \leq W \leq W^+$, the current that passes the EF, $i_{EF}(t)$, can be written as

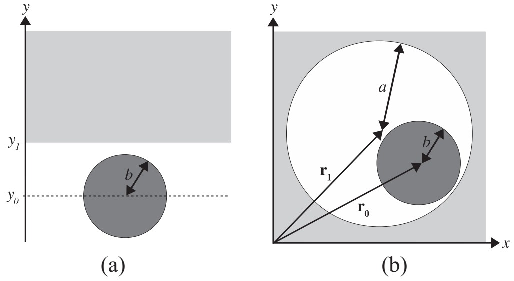

Fig. 18. The projected beam spot at the CS together with the geometry of the knife edge (a), and the aperture hole (b).

$$i_{\mathrm{EF}}(t - L_3/c_0) \approx \int_{W^-}^{W^+} i_{\mathrm{CS}}(t) \int_S \lambda_\perp(\mathbf{r}, t)\mathrm{d}a\mathrm{d}W \tag{5}$$

Here S is the surface of the opening area bounded by the CS, and L_3 is the distance in orbit between the CS and the scraper in the EF. S is illustrated in Fig. 18, where (a) shows the knife edge and (b) shows the aperture hole. The plate is inserted from above, so $S \in (x, y < y_1)$ when using the knife edge obstacle, where y_1 is the vertical position of the edge.

During the time window where the electron current is injected, the fields in the gun cavities have reached a state that is very close to steady state. One can therefore consider the transversely deflected particle flow from the gun to be a T_0-periodic function within this time window, where $T_0 = 10$ ns is the fundamental period of the superposed signal. Hence, $i_{\mathrm{CS/EF}}(t) = i_{\mathrm{CS/EF}}(t + nT_0)$ and $\lambda_\perp(t) = \lambda_\perp(t + nT_0)$, where $n \in \mathbb{Z}$.

The total charge, Q_w, injected to each ring bucket during its phase acceptance window t_w is given by (6). Consequently, one can define the total charge Q_f during a 10 ns period that passes the EF but is injected outside t_w as in (7). Q_f will be lost in the ring or somewhere in the injector.

$$Q_w = \int_{-t_w/2}^{t_w/2} i_{\mathrm{EF}}(t)\mathrm{d}t \tag{6}$$

$$Q_f = \int_{-T_f2}^{-t_w/2} i_{\mathrm{EF}}(t)\mathrm{d}t + \int_{t_w/2}^{T_0/2} i_{\mathrm{EF}}(t)\mathrm{d}t \tag{7}$$

The total injected charge during one LINAC shot, Q_{inj}, and the total charge that is lost after the EF, Q_{loss}, is given by (8) and (9), respectively. Here, N is the number of ring buckets that are filled in each shot, and $\mathbb{T}_{\mathrm{inj}}$ is the time interval where the injection should occur during each shot. Note that if the time interval within $\mathbb{T}_{\mathrm{inj}}$ is shorter than the time interval that is limited by the MA in the transport, charges that are injected in the vicinity of $\mathbb{T}_{\mathrm{inj}}$ can be collected by neighboring buckets and are therefore not necessarily lost. However, since the goal is to dump them in the pre-injector, they are included in Q_{loss} in the analysis. In (6)–(9) the simplification that there are no electron losses along the injector, and that the capture efficiency of the ring buckets is 100%, is used.

$$Q_{\mathrm{inj}} = N \cdot Q_w \tag{8}$$

$$Q_{\mathrm{loss}} = N \cdot Q_f + \int\limits_{t \notin \mathbb{T}_{\mathrm{inj}}} i_{\mathrm{EF}}(t)\mathrm{d}t \tag{9}$$

6.4. Optimizing the chopper driving schemes

Here, the driving scheme of the superposed signal that is fed to the first stripline is optimized for different phase acceptances of the ring buckets. These optimization schemes are valid during the time window when the switch modules are gated, i.e. when the vertical net force experienced by the electrons in the second stripline is zero.

Only the electrons that are within the MA of the EF are considered (electrons outside this MA will be dumped anyway). Assume that these electrons have the same energy (they obtain the same kick), and that each S-band bunch has the longitudinal $\delta(z - c_0 t)$ distribution and a transverse Gaussian distribution $\lambda_\perp(\mathbf{r}, \mathbf{r_0})$ when they reach the CS. The displacement of the distribution center is $\mathbf{r} = \mathbf{r_0}$ (see Fig. 18 (b)). If the aperture hole is inserted, then for the Gaussian distribution the throughput of $\lambda_\perp(\mathbf{r}, \mathbf{r_0})$ becomes

$$\begin{aligned}\int_S \lambda_\perp(\mathbf{r}, \mathbf{r}_0)\mathrm{d}a &= \frac{1}{\sigma^2} e^{\frac{-|\mathbf{r}_1-\mathbf{r}_0|^2}{2\sigma^2}} \int_0^a \rho e^{-\frac{\rho^2}{2\sigma^2}} I_0\left(\frac{|\mathbf{r}_1 - \mathbf{r}_0|}{\sigma^2}\rho\right)\mathrm{d}\rho \\ &= 1 - e^{-\frac{|\mathbf{r}_1-\mathbf{r}_0|^2+a^2}{\sigma^2}} \sum_{n=0}^{\infty} \left(\frac{|\mathbf{r}_1 - \mathbf{r}_0|}{a}\right)^n I_n\left(\frac{a|\mathbf{r}_1 - \mathbf{r}_0|}{\sigma^2}\right)\end{aligned} \tag{10}$$

where σ is the standard deviation of the transverse charge distribution, and I_n is the modified Bessel function of the first kind of order n. Note that (10) can be expressed using the Marcum Q-function which is available in many numerical libraries. If instead the knife edge is inserted, the throughput of $\lambda_\perp(\mathbf{r}, \mathbf{r_0})$ becomes

$$\int_S \lambda_\perp(\mathbf{r}, \mathbf{r}_0)\mathrm{d}a = \frac{1}{2}\left(1 + \mathrm{erf}\left(\frac{y_1 - y_0}{\sqrt{2}\sigma}\right)\right) \tag{11}$$

where erf is the error function. It is also assumed that the beam has no horizontal displacement ($x_0 = 0$), and thus the time dependent displacement becomes $\mathbf{r}_0(t) = y(t)\hat{\mathbf{y}}$. With the three RF signals and the vertical corrector at the first stripline, the displacement of the bunches at the CS becomes

$$y(t) = y_0 + \sum_{n=1}^{3} y_n \cos(\omega_n t + \varphi_n) \tag{12}$$

where f_1, f_2 and f_3 are 100 MHz, 300 MHz, and 700 MHz, respectively. φ_n is the phase of each signal, and y_0 is the vertical offset introduced by the corrector. With the assumption mentioned above, the time dependent electron current that passes the EF is given by

$$i_{\mathrm{EF}}(t - L_3/c_0) = q_b \sum_{n=-\infty}^{\infty} \delta(t - nT_b) \int_S \lambda_\perp(\mathbf{r}, y(t)\hat{\mathbf{y}})\mathrm{d}a \tag{13}$$

where q_b is the total charge in each S-band bunch that will pass the EF when the CS is extracted, and T_b=333 ps is the period of the S-band bunches.

6.5. Chopper driving schemes

By using the approach presented in Section 6.4, a measurement series was performed where 7 different driving schemes were compared. Here, the injection window was optimized for 3, 5, 7, 9, 11, 13, and 15 S-band bunches per ring bucket. It is shown in the Section 4.6.1 that approximating the longitudinal charge distribution of an S-band bunch as a Dirac function as in (10) is not entirely true since an S-band bunch that passes the EF has a total length of approximately 10 ps. This results in a streak at the CS which is proportional to the gradient of the deflecting fields in the chopper. The maximum streak is less than a factor 1/10 of the total transverse beam size at the CS for the driving schemes that are presented in this section. One can compensate for this streak by using a larger σ in the optimizations of the driving schemes. By doing so, Q_f in (7) becomes overestimated which result in more conservative schemes. In the optimizations of the driving schemes, σ is set to 0.5 mm, and the 2 mm aperture ($a = 1$ mm) is used which origin was set to $\mathbf{r_1} = \mathbf{0}$. During the measurements, the fundamental chopper frequency, f_1, was set to a fractional of the LINAC main RF frequency $f_L = 2.9985$ GHz, thus $f_1 = f_L/30 = 99.95$ MHz. f_2 and f_3 were as usually generated as harmonics of f_1, and all three signals were phase locked to the LINAC RF.

The maximum allowed total charge to pass outside the phase acceptance window during a 10 ns period was set to $Q_f = 0.05 \cdot q_b$. During the optimizations, the two harmonic signals set to be in phase

Table 3
Different driving schemes for different ring bucket phase acceptances, and the measured average current after the EF. Negative values of y_n means that the n: th signal is in antiphase with the fundamental signal, thus $\varphi_n = \pi$.

# S-band bunches	y_0 [mm]	y_1 [mm]	y_2 [mm]	y_3 [mm]	i_{avg} after EF [mA]
3	−8	3.75	5.25	−0.75	3.5
5	−4	2.5	2.25	−1	5.8
7	−4.5	4.5	0.25	−0.5	7.8
9	−4.5	5	0	0	8.8
11	−4	4.75	−1	0.25	11.9
13	−3	3.75	−1	0	12.9
15	−1.5	2	−0.75	−0.25	14.7
30	0	0	0	0	35

or antiphase with the fundamental one, thus $\varphi_1 = 0$ and $\varphi_{2,3} \in \{0, \pi\}$. The optimized values of $y_0 - y_3$ in (12) for different phase acceptance windows are listed in Table 3.

The average current within the desired time window, i_{avg}, after the EF for the different driving schemes was measured using CT4, is also listed in Table 3. Of course, since $\mathbf{r_1} = \mathbf{0}$, $i_{\text{EF}}(t)$ in (13) would be identical if one would change the sign of all the y_n parameters in each driving scheme. As seen, $i_{\text{avg}} = 35$ mA when the beam is passing the CS and the EF with the chopper system turned off. When the CS was extracted, the average current in this case did not drop, thus the transverse beam size is significantly smaller than the 2 mm aperture. The current 35 mA with the chopper disabled, corresponds to a transported charge of 12 pC per S-band bunch. It is shown in Section 7.1 that it is possible to transport up to 20 pC per S-band bunch to the first LINAC structure, but this measurement series was performed before that was possible.

Fig. 19 shows the measured current after the EF compared to the current obtained from the analysis. As seen, a beam size of $\sigma = 0.4$ mm shows a better agreement with the measurements compared to the more conservative $\sigma = 0.5$ mm. In the analysis, q_b is set to 12 pC. The vertical displacements in time domain and the projections of the S-band bunches for the different driving schemes are shown in Figs. 20–21.

7. Overall performance and operation

7.1. Performance during ring commissioning

Fig. 22 (a) shows the induced signals at CT2-4 that are shown in Fig. 7. The set-up is typical for commissioning where a single 500 MHz signal is applied to the first stripline in order to maximize the BPM response. The HV pulses that are fed to the second stripline are 100 ns long, and the electron pulse that is accelerated starts at t=0. Fig. 22 (b) shows the projected charge distribution on the YAG screen directly after the CS (see Fig. 7). Since the YAG screen is located before the EF, electrons within a large energy span are projected here. However, one can obtain a quite clear picture of the charge distribution in the high-energy span by adjusting the first solenoid so that the low-energy electrons are over-focused at the screen. The 500 MHz signal was here generated as the sixth fraction of the LINAC master signal, and there are 2 S-band bunches in each projected population per 500 MHz cycle. For illustration purposes, the CS was extracted in Fig. 22 (b), and the HV pulses at the second stripline are not applied (when applying the HV pulses, two overlapping projections can be seen on the screen, each containing 3 populations). Note that there is a 5×5 mm etched square on the surface of the YAG screen. The contour of this square has been enhanced in the figure. However, the HV pulses are applied and the 2 mm aperture is inserted when obtaining the CT signals in Fig. 22 (a), and only the upper population passes the CS, thus 1/3 of the S-band bunches are transported to the first LINAC section.

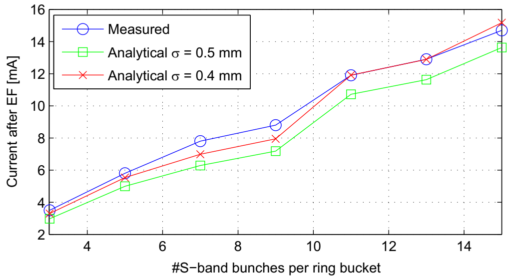

Fig. 19. Measured and analytical average current after the EF for the driving schemes listed in Table 3.

One can see that the average current at CT4 in the 100 ns electron pulse that reaches the first LINAC section was approximately 20 mA. This corresponds to a transported charge of 20 pC per S-band bunch since 2 out of 6 S-band bunches pass during a 500 MHz cycle. With the presented settings, the total charge in the 100 ns pulse can be transported to the two extraction points at 1.5 GeV and 3.0 GeV, respectively with very small losses. Note that both analog and digital filters are applied to the three signals which makes the plotted rise and fall times longer.

As mentioned in Section 6.1, it is possible for some low-energy electrons to pass the CS when they are outside the desired time window if they have a combination of low energy and a certain angle. This can be seen as a small amplitude outside the desired time window in $u_3(t)$. However, these charges are dumped downstream in the pre-injector due to their lower energy, and they can not be seen in $u_4(t)$.

The voltage $u_2(t)$ is the induced CT signal close to the exit of the gun, and the average current output within the desired time window was more than 600 mA. Thus, roughly 10% of the output charges (20 pC per S-band bunch) within the time window have such high energy that they can be transported to the extraction points.

Initial measurements of the pre-injector were reported in [19]. As seen, the current throughput after the EF has been improved since the previous measurements results were published. This was achieved by doing more RF conditioning of the gun, and by further optimizations of the optics. It was also reported that an interfering vertical magnetic field was detected in the vicinity of the gun cavities. This altered the horizontal trajectory of the beam when its energy was swept. The interfering field originates from the nearby located ion pumps, and the pumps have now been shielded with sheets of mu-metal. After the sheets were applied, the interfering field was no longer detected, and the alignment of the gun was done without taking the beam energy into consideration.

7.2. Length of the injected current pulse

The chopper system proved to be adequate for defining the start and stop of the injected current pulse and thereby selecting the number of ring buckets that are filled during each LINAC shot. During the tests, the number of injected ring buckets could easily be adjusted between one and ten. Fig. 23 shows the induced signals at an upstream BPM strip port during injection to one (a) and to ten (b) ring buckets.

In January 2016, some initial single-bunch experiments were performed in the 3 GeV ring. Here, only one of the 176 ring buckets was filled by injecting with the bunch train shown in Fig. 23 (b). The maximum charge that could be accumulated in the single ring bucket during the experiments was 15 nC with a total charge contamination of ≈2% in the neighboring ring buckets. The contamination can probably be further decreased by adjusting the optics and timing in the injector.

This charge contamination is not a problem when shortening the length of the injected current pulse in order to obtain a more even charge distribution in the ring when operating with a uniform filling pattern. This is because the additional charge injected into the

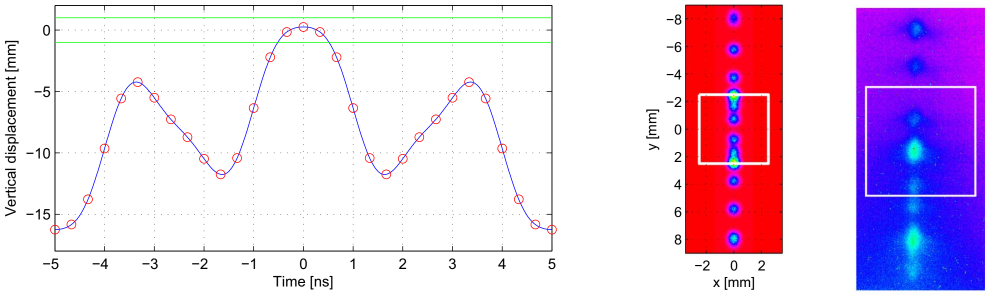

3 S-band bunches per ring bucket

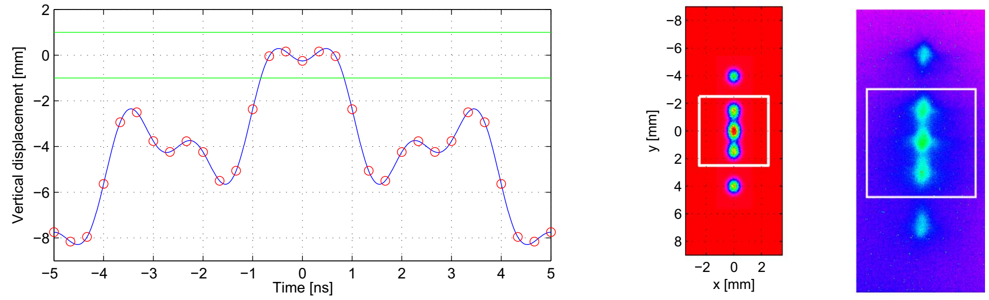

5 S-band bunches per ring bucket

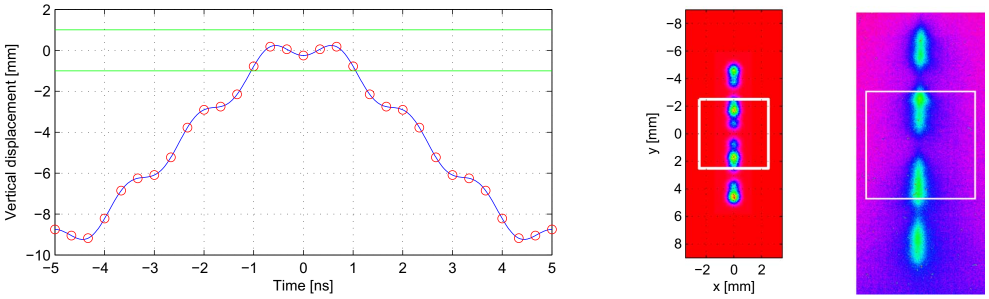

7 S-band bunches per ring bucket

Fig. 20. The vertical displacements of the driving schemes with 3, 5, and 7 S-band bunches per ring bucket listed in Table 3. The left figures show the simulated vertical displacements in time domain during one 10 ns period. Here, each circle is one of the S-band bunches, and the horizontal lines are the boundaries of the 2 mm aperture in the CS. The middle and right figures show the simulated and measured projected charge distributions on the YAG screen directly after the CS. Note that the CS is extracted in these figures, and that there is no static offset ($y_0 = 0$) except for the upper right figure for the 3 S-band bunches per ring bucket where an offset of approximately −3 mm is applied. The reason for applying an offset to this figure is that the projection is larger than the screen itself, and the top population on the YAG screen corresponds here to the top population in the simulation. There is an etched square of size 5×5 mm on the screen, and its contours have been enhanced in the measured projections in the right figures. As a reference, the same square is plotted in the middle figures.

neighboring ring buckets is much smaller than the charge injected into the targeted ring bucket. However, the charge contamination is suboptimal when operating with exotic (non-uniform) filling patterns with gaps. This contamination can be removed with bunch cleaning by using RF-knockout. Transverse (and longitudinal) bunch-by-bunch feedback systems are currently being developed for both rings, and these systems will also be suitable for bunch cleaning as described in [22].

Another way of injecting into a single ring buckets with high precision and with low charge contamination would be to use the photocathode gun. Preparations are ongoing where the laser and timing systems are modified to allow ring injections using that gun too. By doing so, one also gain redundancy in case the thermionic pre-injector starts to malfunction.

8. Conclusions and future work

In this paper, the MAX IV thermionic pre-injector design is presented. To fulfill the injection requirements, an electron beam with the correct time structure needs to be injected into the two storage rings, and the electrons outside this time structure must be dumped before they reach the first LINAC structure. A thermionic RF gun is the electron source during injections, and it produces an electron beam containing S-band bunches with a large energy spread. The low-energy

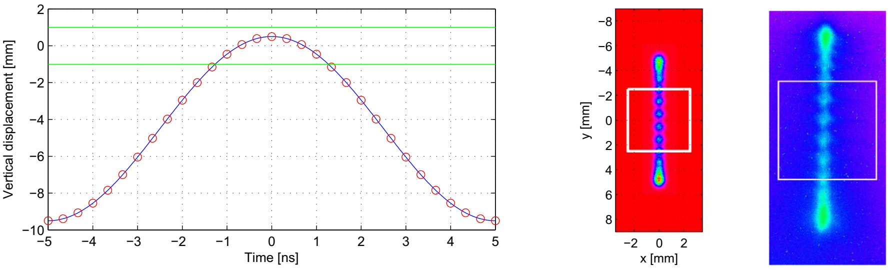

9 S-band bunches per ring bucket

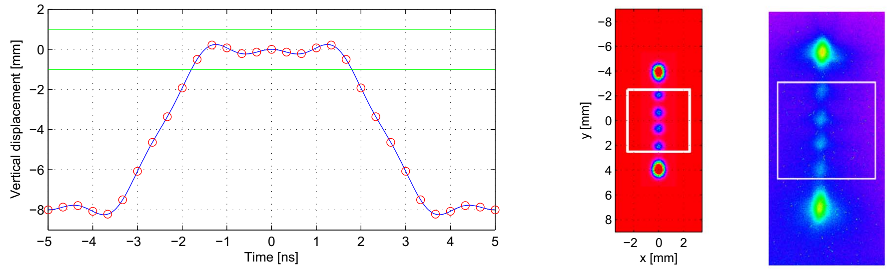

11 S-band bunches per ring bucket

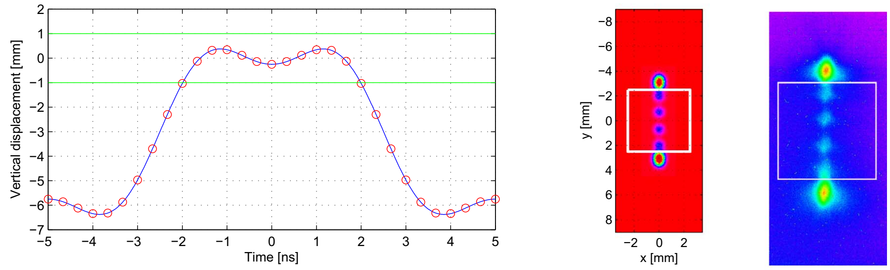

13 S-band bunches per ring bucket

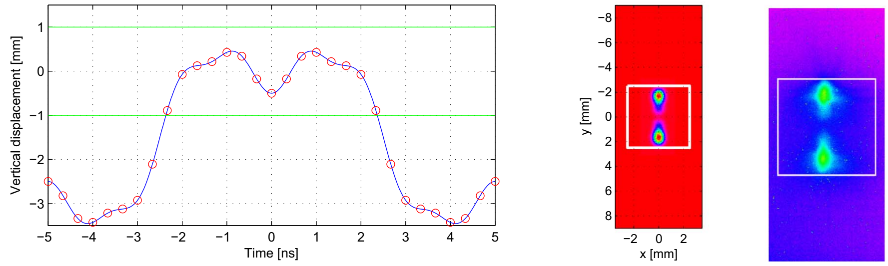

15 S-band bunches per ring bucket

Fig. 21. The vertical displacements of the driving schemes with 9, 11, 13, and 15 S-band bunches per ring bucket listed in Table 3. The layout of the figures is the same as in Fig. 20.

electrons can not be captured in the injector and must be dumped. A chopper system and an energy filter are used to dump the unwanted electrons, where the former creates the correct time structure of the beam, and the latter removes the low-energy tail of the S-band bunches. Analytical solutions and simulation tools were used to investigate the thermionic gun structure and the downstream components to investigate the electron beam properties out from the gun and through the pre-injector.

Using COMSOL Multiphysics and SUPERFISH, the electromagnetic properties for the different modes in the thermionic gun were simulated. Subsequent measurements of the manufactured gun show that the achieved values are close to the simulated ones.

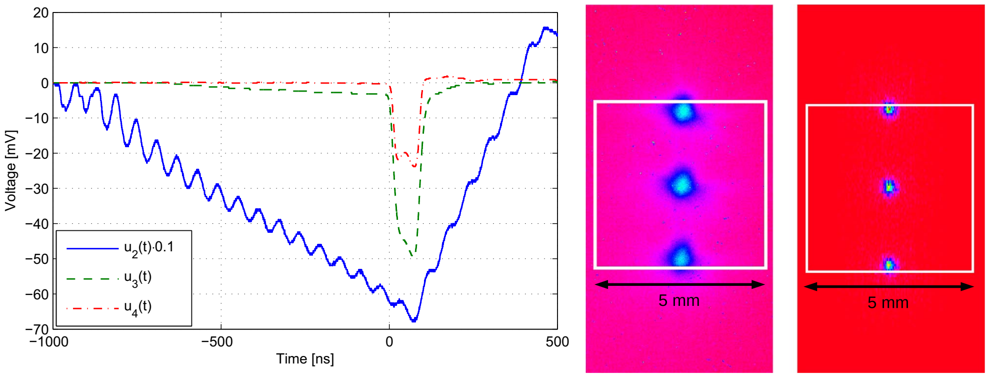

(a) (b) (c)

Fig. 22. (a) shows the induced signals, $u_{2-4}(t)$ at CT2-4, respectively. Each CT has a transfer impedance of $1\ \Omega$. Here, 2 out of 6 S-band bunches are kept, and the electron pulse that enters the first LINAC structure is 100 ns long. Note that $u_2(t)$ is a factor 10 greater than illustrated in the plot. (b) shows the measured projected charge distribution on the YAG screen directly after the CS, where the latter is extracted for illustration purposes. The etched 5×5 mm square that is seen on the screen has been enhanced. Only the electrons in the upper population are kept when the CS is inserted. (c) shows the same projected charge distribution obtained from particle tracking in ASTRA as described in Section 4.6.2 at the position of the YAG screen.

Simulations using ASTRA and PARMELA give an indication of the electron beam parameters in terms of maximum achieved energy, transported charge and emittance of the beam. In PARMELA, the complete pre-injector was described including the EF but not the chopper system. At the entrance to the first LINAC structure the electron beam has a simulated emittance of about 3 mm mrad and a kinetic energy of 2.5 MeV. Simulations show that up to 40 pC of each S-band bunch can be transportable with good beam quality all the way to the first LINAC structure. During the measurements it was shown that 20 pC of each S-band bunch were transported through the system with an energy setting for the EF corresponding to 2.5 MeV.

By distributing the 100 MHz RF signals of the two rings into an exciter network that produces harmonics of the input signals, it is possible to obtain 100 MHz, 300 MHz, and 700 MHz signals that are phase locked to the ring that is about to be injected. These three signals are then combined and fed to a stripline. Through a series of measurements, it was shown that the number of S-band bunches that are injected into each ring bucket can be altered by adjusting the amplitudes and phases of the three signals. During commissioning of the injector and during early beam commissioning of the 3 GeV ring, the chopper has produced an electron beam with a 500 MHz structure in order to maximize the BPM response along the accelerator. The number of ring buckets that are filled during each LINAC shot can also be adjusted, and in early 2016 it was shown that injecting into single ring bucket in the 3 GeV ring is possible with an acceptable charge contamination in the neighboring ring buckets. Together with the filling pattern feedback system, this will make it possible to fill both rings with arbitrary filling patterns, and to obtain an even charge distribution among the ring buckets during top-up injection. Overall, it was shown that the chopper system is versatile and able to create an electron beam with an arbitrary bunch structure to adapt to the future injection requirements of MAX IV.

Measurements on the emitted electron beam current showed behaviour deviant from the simulated current. It was discovered that there is an oscillating component of the emitted current, believed to have its source from excitation of the 0 mode in the electron gun.

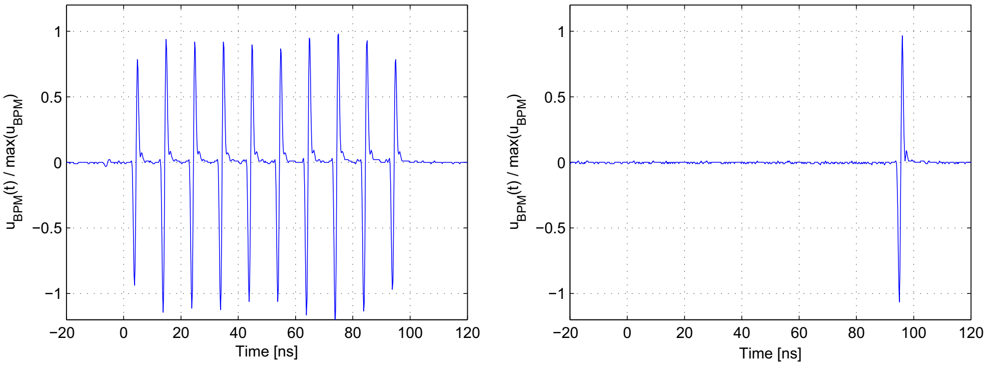

(a) (b)

Fig. 23. The induced voltage, $u_{\mathrm{BPM}}(t)$, at an upstream BPM stripline port that is located after 32 LINAC structures ($W_e \approx 2.6$ GeV). (a) shows the signal during injection into ten ring buckets, and (b) shows the signal during injection into one ring bucket. Note that the magnitude of the induced voltage vary inside the 100 ns shot in (a). This signal variation is a result of the current variation due to the mode beating in the gun, and the same magnitude variations within the 100 ns pulse can be seen in $u_4(t)$ in Fig. 22 (a). 3 S-band bunches per ring bucket are injected in both figures.

Simulations on this show that a 5% excitation of the 0 mode would produce an oscillation as observed, and that it also will affect the injection efficiency. Initial measurements indicate that the mode beating in the gun is affecting the performance of the pre-injector negatively, work will continue to fully investigate why the mode beating appear with the aim to be able to either remove it or limit its impact.

Beam commissioning of the 3 GeV ring is currently ongoing. During this process, the phase and momentum acceptance of the ring bucket are studied, and how the dispersion in the transport line limits the length of the injected current pulse. This will provide valuable information on how the injection efficiency can be optimized for different modes of top-up operation.

Acknowledgments

The authors would like to thank Robert Andersson, Lars Christiansson, ElSayed ElAfifi, Mikael Eriksson, Dionis Kumbaro, Johnny Kvistholm, Filip Lindau, Erik Mansten, Aleksandar Mitrovic, and Sara Thorin for their help during the process. Big thanks to Simon C. Leemann for the input and for all the stimulating discussions on the injection requirements. Also thanks to Anders Karlsson at the department of Electrical and Information Technology. Finally, a special thanks to Sven-Olof Heed and Robert Lindvall in the RF group for constructing the chopper exciter network and the amplifiers.

References

[1] P.F. Tavares, S.C. Leemann, M. Sjöström, Å. Andersson, The MAX IV storage ring project, J. Synchrotron Rad. 21 (2014) 862–877.
[2] S. Werin, et al., Short pulse facility for MAX-lab, Nucl. Instr. Meth. A 601 (2009) 98–107.
[3] B. Anderberg, et al., The Design of a 3 GHz Thermionic RF-gun and energy filter for MAX-lab, Nucl. Instr. Meth. A 491 (2002) 307–313.
[4] S. Thorin et al., The MAX IV Linac, in: Proceedings of LINAC 2014, Geneva, Switzerland, 2014, pp. 400–403.
[5] J. Andersson et al., Initial Commissioning Results of the MAX IV Injector, in: Proceedings of Free Electron Laser Conference, Daejeon, Korea, 2015.
[6] F. Curbis et al., Extension of the MAX IV Linac for a Free Electron Laser in the X-Ray Region, in: Proceedings of IPAC 2013, Shanghai, China, 2013, pp. 1244–1246.
[7] S.C. Leemann, Pulsed sextupole injection for Sweden's new Light Source MAX IV, Phys. Rev. ST. B 15, 050705.
[8] S.C. Leemann, et al., Progress on Pulsed Multipole Injection for the MAX IV Storage Rings, in: Proceedings of PAC 2013, Pasadena, CA, USA, 2013, pp. 1052–1054.
[9] S. C. Leemann, priv. comm (Nov 2015).
[10] S.C. Leemann, Interplay of Touschek Scattering, Intrabeam Scattering, and RF Cavities in Ultralow-emittance Storage Rings, Phys. Rev. ST. B 17 050705.
[11] Z. Farcas, H. Hogg, G. Loew, P. Wilson, SLED: A Method of Doubling SLAC's Energy, SLAC-PUB-1453.
[12] C. Stråhlman, T. Olsson, et al., Preparing the MAX IV Storage Rings for Timing-based Experiments, in: Proceedings of SRI 2015, New York City, USA, 2015.
[13] Spectra-mat, inc. URL ⟨http://http://www.spectramat.com/⟩.
[14] COMSOL Multiphysics(R) by COMSOL AB. URL ⟨https://www.comsol.com/⟩.
[15] K. H. et al., SUPERFISH - A Computer Program for Evaluation of RF Cavities with Cylindrical Symmetry.
[16] Parmela. ⟨http://laacg.lanl.gov/laacg/services/serv_codes.phtml⟩.
[17] K. Floettmann. - ASTRA - A Space Charge Tracking Algorithm, DESY.
[18] J.C.S.L.C. Maier, Field strength measurements in resonant cavities, J. Appl. Phys. 23 (68) (1952) 68–77.
[19] D. Olsson, et al., A chopper system for the MAX IV thermionic pre-injector, Nucl. Instr. Meth. A 759 (2014) 29–35.
[20] Libera Single Pass E. ⟨http://www.i-tech.si/accelerators-instrumentation/single-pass-e/benefits_13⟩.
[21] D.A. Goldberg, G.R. Lambertson, Dynamic Devices A Primer on Pickups and Kickers, in: AIP Conference Proceedings Series - Physics of Particle Accelerators, 1992.
[22] W. Cheng, et al., Commissioning of Bunch-by-Bunch Feedback System for NSLS2 Storage Ring, in: Proceedings of IBIC 2014, Monterey, CA, USA, 2014, pp. 707–711.

Paper III

Commissioning Status of the Chopper System for the MAX IV Injector

D. Olsson, J. Andersson, F. Curbis, L. Isaksson, L. Malmgren,
E. Mansten and S. Thorin.

pp MOP106015 (2008) *Proceedings of LINAC16, East Lansing, USA.*

MOP106015 **Proceedings of LINAC2016, East Lansing, MI, USA**

COMMISSIONING STATUS OF THE CHOPPER SYSTEM FOR THE MAX IV INJECTOR

D. Olsson*, J. Andersson, F. Curbis, L. Isaksson, L. Malmgren, E. Mansten, S. Thorin
MAX IV Laboratory, Lund, Sweden

Abstract

The MAX IV facility in Lund, Sweden consists of two storage rings for production of synchrotron radiation, and a short-pulse-facility (SPF). The two rings are designed for 3 GeV and 1.5 GeV, respectively, where the initial beam commissioning of the former has recently been completed, and commissioning of the latter was started in September 2016. Both rings will be operating with top-up injections delivered by a full-energy injector. In order to reduce losses of high-energy electrons along the injector and in the rings during injection, only electrons that are within a time structure where they can be accumulated in the ring buckets are accelerated. Electrons outside this time structure are dumped before they reach the first LINAC structure by a chopper system. The performance of the chopper system during commissioning of the 3 GeV ring is presented in this paper.

INTRODUCTION

The MAX IV injector consists of 39 travelling-wave S-band LINAC structures that are fed via SLED systems [1]. It provides top-up injections for two storage rings at 3 GeV and 1.5 GeV, respectively. The injector also operates as a driver for a short-pulse-facility (SPF) [2], and might be the driver for a future free-electron laser (FEL) [3]. Initial beam commissioning of the 3 GeV ring was completed in the summer of 2016, and the facility will soon open up for the user community. The beam commission of the 1.5 GeV was started in September 2016.

For ring injections, the electron source is a thermionic S-band RF gun that delivers an electron pulse with a length of ≈ 1 μs [4]. This electron pulse is bunched with an S-band structure, and only a fraction of its charge can be accumulated in the rings during injection. The RF systems in both rings are operating at 100 MHz, and the number of S-band bunches that can be accumulated in each ring bucket depends on parameters such as available RF voltage and the radiation losses. In its final state, the number of S-band bunches that can be accumulated in each bucket in the 3 GeV ring might vary between 4 and 7, while the number might be as high as 19 in the 1.5 GeV ring [5]. Due to the SLED systems, the accelerated electron pulse has an energy chirp [6] which limits the number of ring buckets that can be injected during each LINAC shot because of the finite momentum acceptance in the transport lines to the rings [7].

Electrons that can not be accumulated during injection are dumped before they reach the first LINAC structure by a chopper system. The electron losses at high energies, as well as the emitted bremsstrahlung, are by that minimized. Apart from protecting personnel and sensitive electronic equipment from radiation, it also reduces radiation-induced demagnetization of the permanent magnets in insertion devices (IDs). Such magnet degradation does not only reduce the undulator/wiggler parameter, K, but does also result in an extra broadening of the spectral lines since the demagnetization is often non-uniform along the IDs [8] [9].

THE CHOPPER SYSTEM

The chopper system consists of two planar striplines with corrector magnets placed around them, as seen in the schematic overview in Figure 1. By adjusting the strengths of the correctors and the shape of the counter propagating TEM waves that are fed to the striplines, only the S-band bunches within the desired time structure experience a net deflecting force that is zero when passing each stripline. S-band bunches that are outside this time structure are vertically deflected and dumped at a downstream located adjustable aperture.

The first stripline is fed with a superposed signal consisting of one 100 MHz, one 300 MHz, and one 700 MHz signal. These three signals can be generated as harmonics (in a comb generator) from any of the 100 MHz main RF signals of the two rings. By doing so, the superposed signal is always phase locked to the RF system of the ring that is being injected. After the three signals have been generated, they are amplified and combined in a cavity filter and fed to the first stripline, as shown in Figure 1. Note that the combined signal is circulated through both stripline electrodes, and the total electrical length is adjusted so that the propagating mode in the stripline is an odd (differential) TEM mode at odd harmonics of 100 MHz. By adjusting the amplitudes of the three signals, it is possible to change the number of S-band bunches per 10 ns period that enters the main injector, i.e. the number of S-band bunches that are injected into each ring bucket. This is illustrated in Figure 2, where the vertical displacement at the position of the aperture is shown for the driving scheme that has been used during commissioning of the 3 GeV ring. With this driving scheme, only 3 S-band bunches per 10 ns period pass the boundaries of the aperture, while the rest are dumped. In [5], other driving schemes are presented where up to 15 S-band bunches per ring bucket are injected.

By feeding two high-voltage pulses with different polarities to the second stripline, the total length of the electron pulse that enters the main injector can be adjusted, i.e. the number of ring buckets that are injected during each LINAC shot. These pulses are generated by commercial switch

---

* email: david.olsson@maxiv.lu.se

ISBN 978-3-95450-169-4

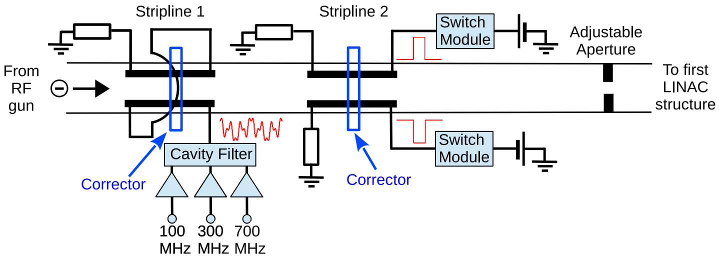

Figure 1: The basic components of the chopper system.

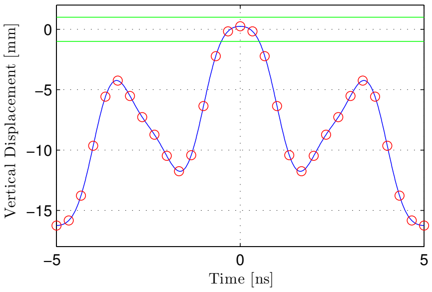

Figure 2: The vertical displacement of the beam at the position of the adjustable aperture in Figure 1 during one 10 ns period. The red circles are the S-band bunches, and the green lines represent the boundaries when a 2 mm aperture is inserted.

modules consisting of fast solid-state switches and capacitor banks.

The chopper system and the other component in the thermionic pre-injector are described in further details in [5] and in [10].

PERFORMANCE DURING RING COMMISSIONING

The structure of the electron pulse that passes the chopper can be studied at several BPM striplines situated throughout the injector. For the chopper operations described above, the induced voltage $u(t)$ at a single upstream port of an ideal BPM stripline is given by

$$u(t) = \frac{g_{||} Z_s}{8} q_b \sum_{n=0}^{N-1} \sum_{m=0}^{M-1} \Big\{ i_b(t - m \cdot T_b - n \cdot T_{\mathrm{RF}}) - i_b(t - m \cdot T_b - n \cdot T_{\mathrm{RF}} - 2L/c_0) \Big\} \qquad (1)$$

where c_0 is the speed of light in vacuum, q_b the total charge in each S-band bunch, $Z_s \approx 50\ \Omega$ the characteristic impedance of a single BPM stripline electrode (in sum mode), L =

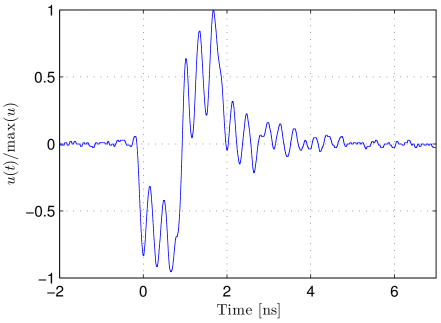

Figure 3: The induced voltage, $u(t)$, at a BPM stripline port that is located at the end of the injector obtained with a 4 GHz oscilloscope. 3 S-band bunches per ring bucket are injected ($M = 3$).

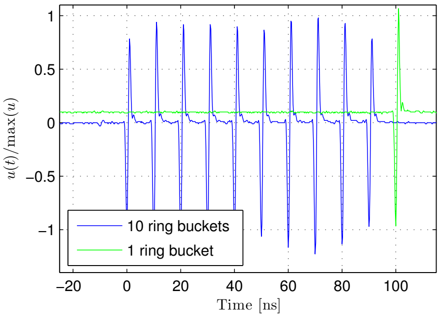

Figure 4: The induced voltage, $u(t)$, at a BPM stripline port at the end of the injector when injecting into 10 and into 1 ring buckets ($N = 10$ and 1). In both cases, 3 S-band bunches are injected into each ring bucket ($M = 3$), but this oscilloscope does not have high enough resolution to resolve individual S-band bunches. Note that the horizontal and vertical offsets in the green curve are 100 ns and 0.1 units, respectively.

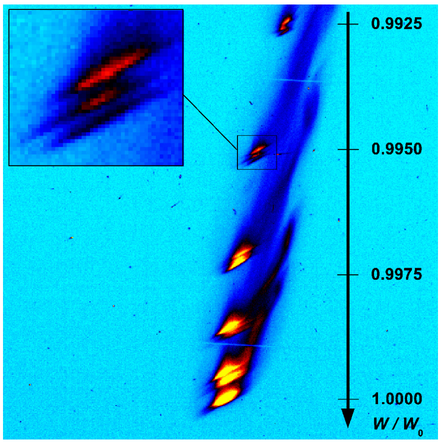

Figure 5: The projected beam of a single LINAC shot at a YAG screen in the transport line to the 3 GeV ring. The vertical dispersion is here $\eta_y = -1$ m, and the axis shows the corresponding relative beam energy W/W_0. Ten ring buckets are here injected as in Figure 4. One can distinguish the electrons that are being injected into the first six ring buckets as distinctive populations due to their larger energy spread, while the electrons that are injected into the last four ring buckets are located in the lower population. As seen, it is even possible to distinguish the three S-band bunches in the upper low-energy populations. These are clearly visible in the zoomed area of the 2nd upper population.

15 cm the length of an electrode, and $g_{||}$ the longitudinal geometry factor defined in [11]. $T_b = 333$ ps and $T_{\mathrm{RF}} = 30T_b = 10$ ns are the period of the S-band bunches, and the period of the ring RF systems, respectively. M and N are the number of S-band bunches that are injected into each ring bucket, and the number of ring buckets that are injected, respectively. $i_b(t)$ is the longitudinal (normalized) charge distribution of a single S-band bunch centered at $t = 0$. The bunch length of an S-band bunch is tens of picoseconds, i.e. small compared to the operating frequencies of the chopper. In (1), it is assumed that the S-band bunches are ultrarelativistic and propagate in the center of the beam pipe.

Figure 3 shows $u(t)$ induced by the driving scheme illustrated in Figure 2 ($M = 3$). Here, three bipolar pulses (one for each S-band bunch) can be seen whose negative and positive parts are separated by $2L/c_0 = 1$ ns. The remaining oscillations are mainly caused by reflections due to the fact that the BPM stripline is far from perfectly matched to 50 Ω for the wideband spectrum of a single S-band bunch.

The blue curve in Figure 4 shows $u(t)$ when injecting into ten successive ring buckets thus $(M, N) = (3, 10)$. This is the injection scheme that has been used so far during normal beam commissioning of the 3 GeV ring. It has been possible to transport a total charge of 290 pC per LINAC shot to the injection point with a capture efficiency in the ring that is above 90 %. As seen, there is a small variation in amplitude among the ten bipolar pulses which is caused by mode beating the thermionic RF gun. The frequency of this mode beating is 16.6 MHz, and it is further described in [5].

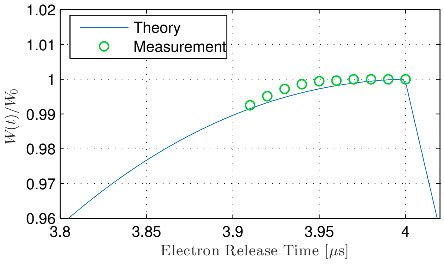

Figure 6: The relative energy gain, $W(t)/W_0$, of the MAX IV injector as a function of the electron release time. The blue curve shows the theoretical gain, while the green circles show the relative energy of the ten populations in Figure 5.

The green curve in Figure 4 shows $u(t)$ when injecting into a single ring bucket, thus $(M, N) = (3, 1)$. In January 2016, some initial single-bunch experiments were performed in the 3 GeV ring, where only one of the 176 ring buckets was filled using this injection scheme. The maximum charge that could be accumulated in the single ring bucket during the experiments was 15 nC, while the total charge contamination in the neighbouring ring buckets was ≈ 2 %. Since then, a transverse bunch-by-bunch feedback system has been commissioned which makes it possible to perform bunch cleaning that eliminates this charge contamination by RF-knockout [12].

YAG screens located at dispersive sections along the injector can be used as spectrometers and therefore to correlate the bunch train from the chopper to the energy chirp caused by the SLED systems. Figure 5 shows the charge distribution for a single LINAC shot projected at a YAG screen, and Figure 6 shows the theoretical and measured energy spread along the injected electron pulse. As seen, the measured energy chirp is ≈ 0.75 %. The small deviation from the theoretical curve is partly due to a measurement error originating from the mode beating.

CONCLUSIONS AND FUTURE WORK

During the commissioning of the 3 GeV ring, the chopper system and the main injector delivered an electron beam with the correct time structure for injection. Apart from further optimization of the injection efficiency in this ring, the commissioning of the 1.5 GeV ring has recently started. Since the latter ring has a significantly higher phase acceptance during injection, other chopper driving schemes with higher current throughput can be used to increase the injection rate.

REFERENCES

[1] S. Thorin *et al.*, "The MAX IV LINAC", in *Proc. 27:th Linear Acc. Conf. (LINAC'14)*, Geneva, Switzerland, Sep. 2014, paper TUIOA03, pp. 400–403.

[2] S. Werin *et al.*, "Short pulse facility for MAX-lab", *Nucl. Instr. Meth.*, vol. 601, pp. 98–107, 2009.

[3] F. Curbis *et al.*, "Extension of the MAX IV Linac for a Free Electron Laser in the X-ray Region", in *Proc. 4:th Int. Part. Acc. Conf. (IPAC'13)*, Shanghai, China, May. 2013, paper TUPEA050, pp. 1244–1246.

[4] B. Anderberg *et al.*, "The design of a 3 GHz thermionic RF-gun and energy filter for MAX-lab", *Nucl. Instr. Meth.*, vol. 491, pp. 307–313, 2002.

[5] J. Andersson and D. Olsson *et al.*, "New features of the MAX IV thermionic pre-injector", *Nucl. Instr. Meth.*, to be published.

[6] Z. Farcas *et al.*, "SLED: A Method of Doubling SLAC's Energy", in *SLAC-PUB-1453*, 1974.

[7] S.C. Leemann, "Pulsed sextupole injection for Sweden's new light source MAX IV", *Phys. Rev. ST Acc. Beams*, 15, 050707, 2012.

[8] S. Sasaki *et al.*, "Radiation damage to advanced photon source undulators", in *Proc. Part. Acc. Conf. (PAC'05)*, Knoxville, Tennessee, USA, May. 2005, pp. 4126–4128.

[9] P. Vagin *et al.*, "Radiation damage of undulators at PETRA III", in *Proc. 5:th Int. Part. Acc. Conf. (IPAC'14)*, Dresden, Germany, June. 2014, paper WEPRO035, pp. 2019–2021.

[10] D. Olsson *et al.*, "A chopper system for the MAX IV thermionic pre-injector", *Nucl. Instr. Meth.*, vol. 759, pp. 29–35, 2014.

[11] D. A. Goldberg and G. R. Lambertson, "Dynamic Devices A Primer on Pickups and Kickers", in *AIP Conf. Proc. Series - Phys. of Part. Acc.*, 1992.

[12] W. Cheng *et al.*, "Commissioning of bunch-by-bunch feedback system for NSLS2 storage ring", in *Proc. 3:rd Int. Beam Inst. Conf. (IBIC'14)*, Monteray, CA, USA, Sep. 2014, paper WEPD27, pp. 707–711.

ISBN 978-3-95450-169-4

Paper IV

The Bunch-by-Bunch Feedback System for the MAX IV 3 GeV Ring

D. Olsson, A. Karlsson and L. Malmgren.

LUTEDX/(TEAT-7253)/(2017) *Technical Report, Department of Electromagnetic Theory, Lund University.*

(TEAT-7253)/1-51/(2017): D. Olsson *et al.*, The Bunch-by-Bunch Feedback System in the MAX IV 3 GeV Ring

CODEN:LUTEDX/(TEAT-7253)/1-51/(2017)

The Bunch-by-Bunch Feedback System in the MAX IV 3 GeV Ring

David Olsson, Lars Malmgren, and Anders Karlsson

Electromagnetic Theory
Department of Electrical and Information Technology
Lund University
Sweden

David Olsson
david.olsson@maxiv.lu.se

MAX IV Laboratory
Lund University
P.O. Box 118
SE-221 00 Lund
Sweden

Lars Malmgren
lars.malmgren@maxiv.lu.se

MAX IV Laboratory
Lund University
P.O. Box 118
SE-221 00 Lund
Sweden

Anders Karlsson
anders.karlsson@eit.lth.se

Department of Electrical and Information Technology
Electromagnetic Theory
Lund University
P.O. Box 118
SE-221 00 Lund
Sweden

This is an author produced preprint version as part of a technical report series from the Electromagnetic Theory group at Lund University, Sweden. Homepage `http://www.eit.lth.se/teat`

Editor: Mats Gustafsson

Abstract

The MAX IV facility in Lund, Sweden consists of two storage rings for production of synchrotron radiation. The larger 3 GeV ring has been delivering light to the first users since November 2016, while the smaller 1.5 GeV ring is being commissioned. Coupled-Bunch Mode Instabilities (CBMIs) have been observed in both rings, and they have a degrading effect on the beam quality since they increase the effective emittance and the energy spread. In order to suppress CBMIs, a digital Bunch-By-Bunch (BBB) feedback system has been commissioned in the 3 GeV ring. The feedback in the three planes has this far been two provided by two striplines kickers. A waveguide overloaded cavity kicker, dedicated for feedback in the longitudinal plane, will soon be commissioned. Apart from applying negative feedback, the BBB feedback system is a comprehensive diagnostic tool. The design of the feedback kickers and the implementation of the BBB feedback system in the 3 GeV ring are presented in this report. Initial results from instability studies are also discussed.

Contents

1 Introduction

The MAX IV facility in Lund, Sweden consists of two storage rings, where the larger 3 GeV ring is designed for production of high-brilliance hard X-ray synchrotron light, and the smaller 1.5 GeV ring will produce light in the IR to the soft X-ray spectral range [26]. The 3 GeV has currently five beamlines in operation, and this ring has delivered light to the first users since November 2016, while the first beamlines in the 1.5 GeV ring will be commissioned in the autumn of 2017.

In order to provide high-brightness synchrotron light to the users, the electron beam has to be stable in all three planes. Since the electron bunches couple to each other via wakefields, they can under certain resonance conditions drive coherent coupled-bunch oscillations. Such oscillations are called Coupled-Bunch Mode Instabilities (CBMIs). They can increase the effective emittance and the energy spread of the beam which thereby decreases the brilliance at the beamlines. In order to suppress these CBMIs, both rings will operate with Bunch-By-Bunch (BBB) feedback systems. The commissioning of the BBB feedback system in the 3 GeV ring started in early 2016, while the commissioning in the 1.5 GeV ring will start in the autumn of 2017. The focus of this report is therefore on the 3 GeV BBB feedback system and on the beam measurements performed there.

A brief introduction to CBMIs and their effect on the electron beam is given in Section 2. The driving sources of the CBMIs and different ways to suppress them are also discussed in that section. The feedback signal is applied via kickers (actuators), and striplines have this far been used as actuators in all three planes.

The stripline design is presented in Section 3. Section 4 describes the design of a waveguide overloaded cavity that will soon be the dedicated actuators in the longitudinal plane (the two striplines will still provide feedback in the horizontal and in the vertical plane). The basic principles and the layout of the BBB feedback system in the 3 GeV ring is described in Section 5. Finally, some measurements on how the BBB feedback system affects the beam properties are presented in Section 6. In this section, it is shown how the quality of the light seen at the beamlines is affected by CBMIs and that they can be suppressed by the BBB feedback system.

2 Coupled-bunch Mode Instabilities

The main purpose of the BBB feedback system is to damp CBMIs since they have a degrading effect on the quality of the synchrotron light seen at the beamlines. CBMIs and the collective effects that are driving them is a vast and complex topic, and only a brief introduction to the physics necessary to understand the basic concept of CBMIs and BBB feedback systems is therefore presented in this section. A more comprehensive and very intuitive guide on bunch-by-bunch feedback systems can be found in the Cern Accelerator School material provided by M. Lonza [17]. For more in-depth information on CBMIs and other collective effects, [19] is recommended.

2.1 Beam Dynamics in a Storage Ring

In circular accelerators, the displacement of a particle from its ideal orbit is described by the equation of motion

$$x''(t) + 2Dx'(t) + \omega^2 x(t) = 0 \tag{2.1}$$

where $D = \tau_D^{-1}$ is the radiation damping, and τ_D is the radiation damping time. Since the particle emits synchrotron radiation, $D > 0$ and then the excited oscillations are damped. $x(t)$ can describe the displacement in any of the three planes. When (2.1) describes the horizontal/vertical motion, then ω is the horizontal/vertical betatron angular frequency, and when it describes the motion in the the longitudinal plane, then ω is the synchrotron angular frequency. If we assume that $\omega >> D$, the solution to (2.1) is approximated by an exponentially damped sinusoidal oscillation

$$x(t) = Ae^{-Dt}\cos(\omega t + \phi) \tag{2.2}$$

where A and ϕ are an arbitrary amplitude and phase, respectively. In reality, the displacement of a single electron is not entirely damped until it propagates along its ideal orbit since it experiences smaller excitations continuously due to quantum excitations when emitting light. Quantum excitations of the electrons is the main contributor to the finite energy spread (also known as the natural energy spread) of the beam, and appears because synchrotron radiation is emitted in discrete packets of photons. Excitations do also occur due to collisions between the electrons. This is knowns as intrabeam scattering, and becomes more notable at higher beam currents.

The size of a stable beam is therefore not zero, and its average size in phase space is given by its emittance.

In, (2.1), all oscillations are damped, and the electrons in a single bunch are oscillating around their ideal orbit incoherently. However, there is an electromagnetic coupling between the bunches via wakefields. Under certain resonance conditions, the wakefields might drive the electrons in a single bunch so that they oscillate coherently around their ideal orbit. These oscillations are known as coupled-bunch oscillations. That modifies the equation of motion to

$$x''(t) + 2(D - G)x'(t) + \omega^2 x(t) = 0 \tag{2.3}$$

with the solution

$$x(t) = Ae^{-(D-G)t}\cos(\omega t + \phi) \tag{2.4}$$

where G is the growth rate driven by the wakefields, and $\tau_G = G^{-1}$ is the growth time. If $G > D$, the beam becomes unstable, and the oscillations grow exponentially, which leads to an excited CBMI. If the oscillations grow larger than what is allowed by the acceptance of the storage ring, then the exponential growth can result in beam loss. For smaller values of G, the CBMI might not result in beam loss since non-linear effects saturate the amplitude of the oscillations before they grow so large that the beam is lost. If this is the case, the effects of transverse CBMIs can be seen as an increased transverse beam size and thereby as an increase of the effective emittance. Longitudinal CBMIs result in an increased energy spread which also increases the beam size due to dispersion. It will be shown in Section 6.3 that CBMIs have a degrading effect on the quality of the beam and the brightness of the light seen at the beamlines. Since G is proportional to the beam current, it is always possible to keep the beam stable below the current threshold where the CBMI is excited.

The number of Coupled-Bunch Modes (CBMs) that can be excited depends on the filling pattern in the storage ring. If all the ring buckets are filled, the number of possible CBMIs is the same as the number of bunches, i.e., the same as the harmonic number of the accelerator. As mentioned above, the electrons oscillate coherently at their betatron/synchrotron frequency when a CBMI is excited. The index of the CBM that is excited determines how the centroids of the bunches oscillate relative to each other, i.e., the phase advance $\Delta\phi$ of the oscillations between each bunch. If all the M buckets in the storage ring are filled (as in normal operation at MAX IV), $\Delta\phi$ is given by

$$\Delta\phi = m\frac{2\pi}{M} \tag{2.5}$$

where $m = 0, 1, \cdots, M - 1$ is the index of the CBM. Each excited CBM appears in the beam spectrum as an infinite number at resonance peaks at

$$f = pf_{\mathrm{RF}} \pm (m + \nu)f_0 \tag{2.6}$$

where $f_{\mathrm{RF}} = Mf_0$ is the frequency of the RF system, f_0 is the revolution frequency, ν is the fractional betatron/synchrotron tune, and $p \in \mathbb{Z}$. One important observation from (2.6) is that it is sufficient to monitor a frequency span of $f_{\mathrm{RF}}/2$ centred around $f = f_{\mathrm{RF}}(1/4 + n/2)$, $n \in \mathbb{N}$ in order to observe an excited CBMI. To illustrate this, assume that we have a storage ring with $M = 8$ equally spaced bunches, the circumference L, and a vertical fractional tune of $\nu = 0.33$. Then, Figure 1 (a) shows the vertical displacement of the 8 bunches at a given time when the vertical CBM #1 ($m = 1$) and CBM #5 ($m = 5$) are excited compared to a stable beam. Figure 1 (b) shows the corresponding beam spectrum in the span $0 \leq f \leq f_{\mathrm{RF}}$ for the three cases.

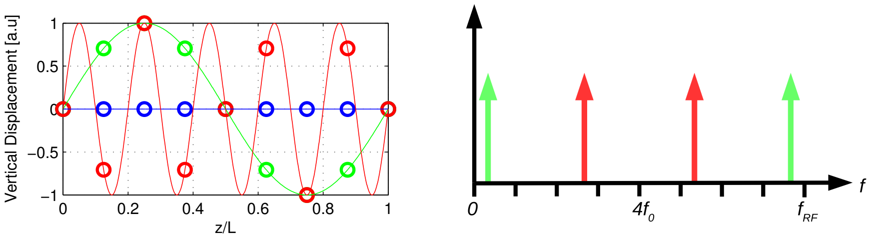

(a)

(b)

Figure 1: (a) shows the maximum vertical displacement of the 8 bunches at a given time for a stable beam (blue circles), when CBM #1 ($m = 1$, green circles) is excited, and when CBM #5 ($m = 5$, red circles) is excited. Here, $M = 8$, $\nu = 0.33$, z is the longitudinal position, and L is the circumference of the storage ring. (b) shows the corresponding vertical beam spectrum lines for CBM #1 (green) and CBM #5 (red).

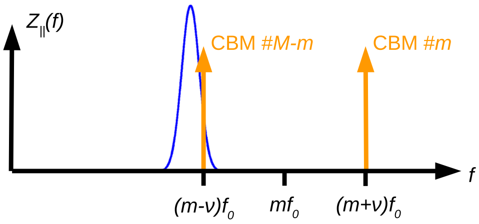

Figure 2: The longitudinal beam impedance, $Z_{||}(f)$, around a cavity HOM (blue line). The two orange lines are the spectrum lines of CBM number m and $M - m$ ($p = 0$). As seen, the spectrum line of the latter overlaps with the impedance response of the HOM, and that CBM can therefore be excited.

2.2 Drivers of CBMIs

As mentioned in the previous section, CBMIs are driven by wakefields. Below we list the sources of the wakefields that give a coupling between bunches.

2.2.1 Vacuum Chamber Discontinuities

Wakefields from a single bunch can be reflected at discontinuities in the vacuum chambers and affect the motion of succeeding bunches. This can be the driving source of both transverse and longitudinal CBMIs. Examples of such discontinuities are tapers, BPM buttons, bellows, RF fingers, pumping ports, and accelerator cavities.

In the longitudinal plane, the instabilities are often driven by high-Q eigenmodes trapped in the vacuum chambers since the stored energy in these eigenmodes can grow quite large due to coherent multi-turn wakefield superposition. At MAX IV, many of the Higher-Order Modes (HOMs) in the main and in the Landau cavities are such high-Q eigenmodes. These HOMs can drive CBMIs if their beam impedance spectrum overlaps with the frequencies of the CBMs in (2.6), as illustrated in Figure 2. Since these eigenmodes are very narrowbanded, it is sometimes possible to shift them in frequency and thereby avoid excitations of CBMIs as described in Section 2.3.4.

2.2.2 Resistive Wall Instabilities

The beam induces mirror currents on the inside of the vacuum chambers as it propagates in the accelerator. Since the beam chambers are made of materials with a finite conductivity, the mirror currents experience resistive losses. These losses assert a decelerating force on the bunches which is proportional to the beam current. The decelerating forces can drive CBMIs, and they are especially strong in low-gap chambers (such as in-vacuum undulators/wigglers). One of the reasons for using copper (a high-conductivity material) chambers in the 3 GeV ring is to reduce the risks of resistive wall instabilities. Resistive wall instabilities can appear both in the longitudinal and in the transverse plane, but is often a problem in the latter.

2.2.3 Ion-induced Instabilities

Ions in the vacuum chambers can drive ion-electron coherent oscillations that result in transverse CBMIs. The ions, which are created when the beam is colliding with gas molecules in the non-perfect vacuum, are trapped in the negative potential of the beam and they are accumulated over several beam passages. Normally, the beam current threshold, where the ion-induced instabilities appear, increases with time as the vacuum improves. This was a also observed at MAX IV which is reported in Section 6.3.1.

2.3 Methods to Suppress CBMIs

In the early design phase of an accelerator, one should reduce the risks of CBMIs. By carefully designing the vacuum chambers, one can make sure that the geometrical wake impedance is minimized. It is then important to redice the impact of high-Q eigenmodes that are trapped in the structures. As already mentioned, materials with low resistivity in the walls of the vacuum cambers reduce the impact of resistive-wall instabilities, and a good quality of the vacuum suppresses ion-induced instabilities. However, once the accelerator is running and the "damage has been done", there are several ways to suppress the CBMIs that hopefully makes it possible to operate the storage ring with a stable beam at the nominal beam current. Some methods that are used or considered at MAX IV are listed below.

2.3.1 Negative Feedback

The most straightforward way to suppress a CBMI is to damp the coherent oscillations with negative feedback. A BBB feedback system is here applying a kick to each single bunch for every revolution. The kick signal is sinusoidal and proportional to the derivative of the coherent oscillation so that the equation of motion from Section 2.1 becomes

$$x''(t) + 2(D + D_{\text{fb}} - G)x'(t) + \omega^2 x(t) = 0 \tag{2.7}$$

where D_{fb} is the damping term from the feedback. We see that stability is achieved if $(D + D_{\text{fb}} - G) > 0$. As mentioned in Section 2.1, it is sufficient to monitor a carefully chosen span of $f_{\text{RF}}/2$ in order to observe all the CBMs in the beam spectrum. The same goes for the feedback signal, i.e., the feedback kickers should have a bandwidth (BW) of at least $f_{\text{RF}}/2$ in order to suppress all the CBMIs. The BBB feedback system in MAX IV is presented in detail in Section 5.

2.3.2 Harmonic Cavities

Both MAX IV storage rings are equipped with passive 3:rd harmonic (Landau) cavities that provide bunch lengthening up to a factor five compared to a single 100 MHz RF system [2]. The bunch lengthening decouples the high-frequency part of the impedance spectrum of the machine from the beam, i.e., the impedance spectrum at higher frequencies has little effect on the beam since the spectrum of each bunch becomes more narrow as the bunch length increases. For example, the loss factor $\kappa_{||}$ in (4.9) is reduced as $\lambda(\omega)$ becomes more narrow. A very important consequence of the bunch lengthening is that it reduces the excitation of the cavity HOMs that are driving longitudinal CBMIs, and thereby increases the current threshold where the beam becomes unstable.

The Landau cavities also increase the spread of the synchrotron frequency (tune spread) among the electrons in a single bunch. The tune spread increases with the non-linearity of the RF waveform [19]. With a single RF system, the RF waveform is sinusoidal and is quite linear at the synchronous phase unless the total maximum voltage provided by the RF system per turn is close to the voltage lost by the electrons as synchrotron radiation per turn. When the Landau cavities are excited for optimum bunch lengthening, the superposed RF waveform forms a plateau (the derivative is zero) at the synchronous phase and is therefore more non-linear. The tune spread has a damping effect on CBMIs since it reduces the coherency of the driven bunch oscillations. This is also known as Landau damping.

Simulation model	f_c [MHz]	Q
No HOM damper	101.91	21502
	407.18	34786
	460.38	36920
One HOM damper	101.90	21370
	406.99	1299
	459.38	746

Table 1: The resonance frequencies f_c and quality factors Q of the first three main cavity eigenmodes, with and without HOM dampers. The simulations are done in COMSOL [9].

Apart from reducing the impacts of collective effects, the bunch lengthening also decreases the electron density which increases the Touschek lifetime and reduces the transverse emittance.

2.3.3 Damping of HOMs

In the early design phase of MAX IV, there were plans to attach at least one HOM damper to each main cavity. The purpose of the dampers is to increase the external loading of the unwanted HOMs and thereby to decrease their quality factors as described in [16]. By doing so, the growth rates of the CBMs driven by the HOMs are reduced.

An in-air HOM damper prototype for the MAX IV main cavities has been developed. The prototype consists of a coaxial structure that forms a notch filter (rejection filter) around 100 MHz (around the cavity fundamental mode). The coaxial structure is inserted into the cavity lateral surface, and it couples to the cavity magnetic fields via a loop antenna. The other end of the structure is terminated with a 50 Ω load. Figure 3 (a) shows a simulation model of the HOM damper inserted into a main cavity, and (b) shows the prototype inserted into a vented cavity. By tuning the notch filter to the frequency of the fundamental mode, many of the HOMs can be damped, while the coupling to the fundamental mode is negligible. Table 1 shows the resonance frequency and quality factors of the fundamental and the first two HOMs in a main cavity, with and without the prototype HOM damper. As seen, the fundamental mode is quite unaffected by the HOM damper, while the two HOMs are heavily damped. Note that the input coupling loop for the 100 MHz RF power is not included in the model. The plan to implement HOM dampers is currently on hold, and it will be evaluated if the combination of Landau cavities and a BBB feedback system is sufficient to suppress all the longitudinal CBMIs up to the design current of 500 mA.

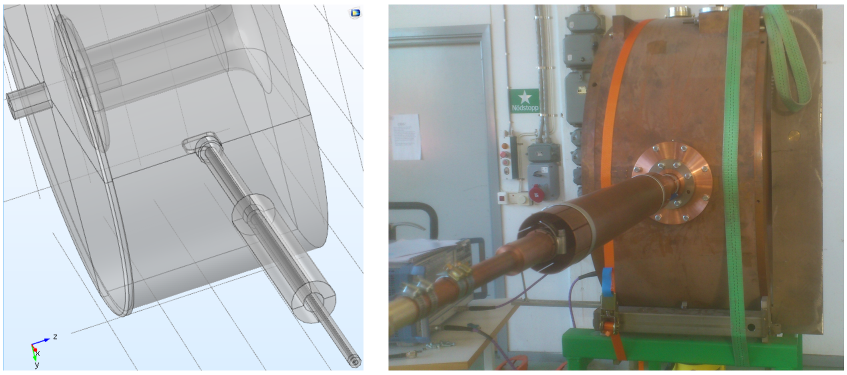

(a) (b)

Figure 3: (a) shows the HOM damper prototype together with a MAX IV main cavity in COMSOL, and (b) shows the prototype when it is inserted into a vented cavity.

2.3.4 Shifting Cavity HOMs in Frequency

Another passive way to decrease the impact of CBMs is to shift the frequencies of the cavity HOMs and move them away from the spectrum lines of any harmful CBMs (see Figure 2). There are two ways to shift the frequencies of the cavity eigenmodes. The first method is to move the position of the cavity end plates with a mechanical tuning system. The second method is to change the temperature of the cavity with the cooling water, and thereby change the cavity volume due to the expansion/contraction of the copper. When tuning the cavities, the aim is to keep the frequency of the fundamental modes constant, and shift frequencies of the HOMs. Thus for every new cavity temperature (within the operational span), there exists an end plate position where the frequency of the fundamental mode is unchanged. Since the HOMs are responding differently to mechanical and temperature tuning compared to the fundamental mode, the new combination of end plate position and temperature will shift the HOMs in frequency. An extensive study on how the eigenmodes in the main and Landau cavities respond to mechanical and temperature tuning can be found in [6].

This method is being used together with negative feedback in the longitudinal plane in order to continuously increase the beam current threshold where the beam becomes unstable. With the BBB feedback system it is possible to perform grow/damp transient measurements (see Section 6.1) just below the current threshold were the stability is lost and to see which CBM that has the highest growth rate. That particular CBM is then the reason why stability is lost at a slightly higher current. The next step is to identify which cavity the HOM that is driving the CBM is originating from by tuning the end plates and the temperature of the cavities. When the problematic cavity is found (for some reason, it is always the last cavity you investigate...), the HOMs of that cavity are shifted in frequency, and it is now hopefully possible to keep the beam stable at higher currents. The procedure is then repeated just below the new threshold where the beam goes unstable. These studies are often very time consuming.

2.3.5 Non-uniform Filling Patterns

There are some advantages of operating a storage ring with non-uniform filling patterns. For example, if ion-induced CBMIs are a problem, one can introduce a gap in the filling pattern. By doing so, the negative potential of the beam is distorted, and it might prevent trapping of ions if the gap is large enough. Such gap is also known as an ion-clearing gap. The effects on the beam performance after introducing an ion-clearing gap is reported in [25].

Since the bunches couple to each other via wakefields, it is also possible to increase the longitudinal tune spread by introducing gaps in the filling pattern. Note that we are here mainly increasing the tune spread among the bunches, and not among electrons in each bunch as in the case with harmonic cavities. This technique has been used at MAX IV at lower currents in order to keep the beam stable.

Non-uniform filling patterns can be achieved in MAX IV by selecting the ring buckets that are injected by adjusting the chopper [3] or by doing bunch cleaning with the BBB feedback system (see Section 6.2).

2.3.6 Phase Modulation

One active method to suppress longitudinal CBMIs that is being used with success at LNLS is to phase modulate the RF fields in the main cavities [1]. With the phase modulation activated, the signal delivered to a main cavity, $V_{\mathrm{RF}}(t)$, becomes

$$V_{\mathrm{RF}}(t) = \hat{V}\cos(\omega_{\mathrm{RF}}t + \hat{\phi}_{\mathrm{mod}}\cos(\omega_{\mathrm{mod}}t + \varphi_{\mathrm{mod}}) + \varphi_{\mathrm{RF}}) \tag{2.8}$$

where $\hat{V}$ and $\hat{\phi}_{\mathrm{mod}}$ are the amplitude of the RF voltage and the phase modulation respectively. φ_{RF} and φ_{mod} are arbitrary phases, and ω_{RF} and ω_{mod} are the frequencies of the main RF system and the phase modulation, respectively. At LNLS, ω_{mod} is set to a value close to twice that of the synchrotron frequency, and the effect of phase modulation is that the electrons in each bunch are split up into two (or three) bunchlets, each with slightly different synchrotron frequencies. The phase modulation increases the Landau damping by an increase of the longitudinal tune spread in the bunches.

This far, LNLS has been operating with a single-RF system (no bunch lengthening with harmonic cavities), and this is when phase modulation is most advantageous. However, one drawback with phase modulating the main RF signal is that it increases the energy spread within the bunches. At MAX IV, phase modulation is therefore a tool that might be useful at lower beam currents to keep the beam stable where there are no significant Landau damping due to bunch lengthening. At date, it is not possible to phase modulate the main RF signal, but the required modifications to the LLRF system would be rather small [21].

3 Design of Striplines

As mentioned, stripline kickers are used as actuators when applying transverse feedback. Two striplines for the BBB feedback system are installed in the 3 GeV ring, one for excitation in each plane. Striplines offer several advantages such as, high transverse shunt impedance, simple design, short rise and fall times, and they can be operated directly in the baseband (BB) span of 0-50 MHz, which is where the signal processing units operate (see Section 5.1.2). The striplines can also simultaneously be used as weak actuators for feedback in the longitudinal plane. This is possible by upconverting the BB signal to a frequency range where the striplines have higher longitudinal shunt impedance (see Section 5.1.3).

Since the in-vacuum parts of the two striplines are identical (they are only rotated 90 degrees relative to each other during installation), only the horizontal stripline is analysed. The electromagnetic properties of a stripline are covered in detail in [20], and no detailed analysis is therefore given in this report.

3.1 Geometry

The design of the striplines for the BBB feedback system is a modified version of the design in [20]. Except for the dimensions, the two major differences are that the new striplines only have two strips each, and that they have tapering sections at the ends of the strips.

The main chamber, the strips, and the flanges are made of stainless steel 316. Figure 4 (a) shows a 3D model of the chamber. Figure 4 (b) shows a 2D cross section of the stripline mid section, where $a = 13.5$ mm, $a_g = 25.2$ mm, $\phi_s = 107.20$ degrees, and $\phi_g = 12.75$ degrees. The length of each strip (feedthrough-to-feedthrough) is $L = 300$ mm, and the total length of the vacuum chamber (flange-to-flange) is 400 mm. Each strip has two tapered sections that make the transition between the feedthroughs and the stripline mid section in Figure 4 (b) less abrupt. The length of each tapered section is $L_t = 25$ mm, and they are visible in Figure 4 (a). Asides from improving the transmission line impedance matching, the tapers also reduce the beam impedance of the stripline at higher frequencies, as shown in Section 3.2. Figure 5 shows one of the manufactured striplines.

3.2 Electromagnetic Properties

The electric scalar potential, $\Phi(\rho, \phi)$, can be obtained analytically by solving Laplace equation over a transverse cross section of the geometry, which is shown in [20]. $\Phi(\rho, \phi)$ is here limited to the region where $0 \leq \rho \leq a$ and requires that the stripline is evaluated far away from its end-gaps. $\boldsymbol{E}(\rho, \phi)$ and $\boldsymbol{H}(\rho, \phi)$ are then obtained as $-\nabla\Phi(\rho, \phi)$ and $\frac{j}{\mu_0\omega}\nabla \times \boldsymbol{E}(\rho, \phi)$, respectively.

The first propagating TEM modes are the odd (differential) and even (common) modes. The potentials of the two strips have the same magnitudes but different polarities in odd mode ($U_1 = V_0$ and $U_2 = -V_0$ in Figure 4 (b)), and the scalar

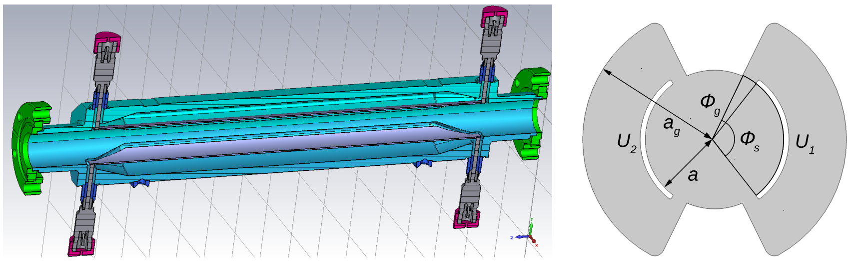

(a) (b)

Figure 4: (a) shows a 3D cross section of the stripline, and (b) shows a 2D cross section with some of its dimensions.

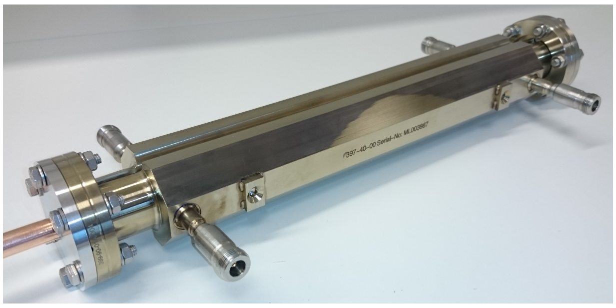

Figure 5: The manufactured vacuum chamber of the vertical stripline.

potential $\Phi_\perp(\rho,\phi)$ for this mode can be expanded in a Fourier series

$$\Phi_\perp(\rho,\phi) = \frac{8V_0}{\pi\phi_g} \sum_{n=1,3,5,\ldots}^{\infty} \left(\frac{\rho}{a}\right)^n \frac{\sin\left(n\frac{\phi_g}{2}\right)\sin\left(n\frac{\phi_s+\phi_g}{2}\right)}{n^2}\cos(n\phi) \tag{3.1}$$

In the even mode, the two strips both have the same potential ($U_1 = U_2 = V_0$), and the Fourier series $\Phi_{||}(\rho,\phi)$ becomes

$$\Phi_{||}(\rho,\phi) = V_0\frac{\phi_g+\phi_s}{\pi} + \frac{8V_0}{\pi\phi_g} \sum_{n=2,4,6,\ldots}^{\infty} \left(\frac{\rho}{a}\right)^n \frac{\sin\left(n\frac{\phi_g}{2}\right)\sin\left(n\frac{\phi_s+\phi_g}{2}\right)}{n^2}\cos(n\phi) \tag{3.2}$$

Figure 6 shows $\Phi(\rho,\phi)$ obtained in (3.1) and (3.2) (upper figure), together with electrostatic simulations of the same modes in COMSOL (lower figure). The longitudinal and transverse geometry factors, $g_{||}$ and $g_\perp$, defined in [14] are

$$g_{||} = \frac{\Phi_{||}(\rho=0)}{V_0} = \frac{\phi_s+\phi_g}{\pi} = 0.67 \tag{3.3}$$

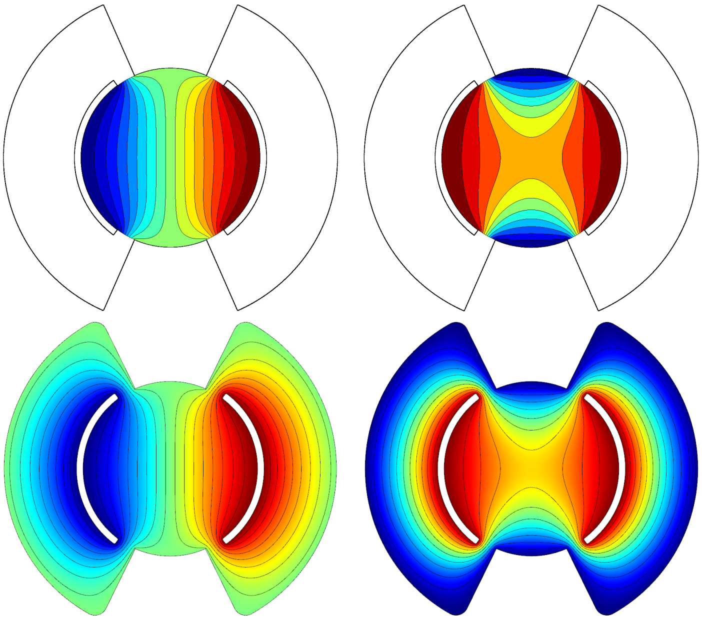

Figure 6: $\Phi(\rho, \phi)$ obtained analytically in (3.1) and (3.2) (upper), and numerically in COMSOL (lower). The left figures show the odd mode, and the right ones show the even mode.

$$g_\perp = \frac{a|E_x(\rho = 0)|}{V_0} = \frac{8}{\phi_g \pi} \sin\left(\frac{\phi_g}{2}\right) \sin\left(\frac{\phi_s + \phi_g}{2}\right) = 1.10 \tag{3.4}$$

A design goal is to make the deflecting field as homogeneous as possible in the vicinity of the beam. Figure 7 shows $E_x(x, y = 0)/E_x(\rho = 0)$ and $E_x(x = 0, y)/E_x(\rho = 0)$ for different values of ϕ_s. As seen, a quite good homogeneity is obtained when $\phi_s = 107.2$ degrees.

Since the characteristic impedance of the surrounding RF system is $Z_0 = 50\ \Omega$, each strip should be matched to this impedance in order to avoid reflections when the strips are excited by the amplifiers and/or by the beam itself. The strips are loaded differently in the odd and even mode which results in different impedances. An optimization approach that can be found in the literature is $Z_0 \approx \sqrt{Z_{0,\perp} Z_{0,||}}$, where $Z_{0,\perp}$ and $Z_{0,||}$ are the characteristic impedance of a single strip in the odd and even mode, respectively. The gap at the outer side of the strips are therefore adjusted to fulfil this relationship. With the stripline dimensions mentioned above, $Z_{0,\perp} = 47.2\ \Omega$ and $Z_{0,||} = 52.9\ \Omega$.

As mentioned, the transmission line impedance matching is improved by implementing the two tapered sections to each strip. The geometry of the tapers and the grounded regions close to the them are optimized for the best possible S-parameters, both when the stripline is fed in common and in differential-mode. There are also

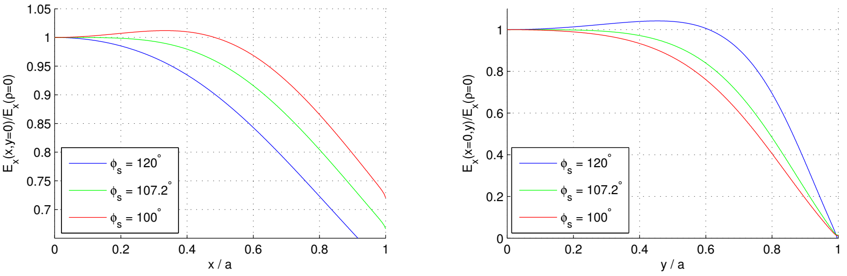

(a) (b)

Figure 7: $E_x(x, y = 0)/E_x(\rho = 0)$ (a) and $E_x(x = 0, y)/E_x(\rho = 0)$ (b) obtained as $-\nabla\Phi(\rho, \phi)$ from (3.1) for different ϕ_s. Here, ϕ_g and a are set to 12.75 degrees and 13.5 mm, respectively.

some production limits that must be considered such as the minimum radius of the tools and the milling angle. In Section 3.3, the simulated S-parameters are compared with the measured S-parameters for one of the manufactured striplines.

The low-frequency approximation of the longitudinal and transverse (horizontal) beam impedance, $Z_{||}(\omega)$ and $Z_x(\omega)$, are give by (3.5) and (3.6), respectively. As seen, the last term makes the beam impedance converge to zero at higher frequencies due to the tapers [4]. Figure 8 shows $Z_{||}(\omega)$ and $Z_x(\omega)$ obtained in GdfidL [13] up to 10 GHz. Note that the ceramic feedthroughs are simplified as simple coaxial lines in these simulations. The loss factor, $\kappa_{||}$, and the dissipated power, P_{loss}, due to the beam impedance are listed in Table 2. Almost all of the beam induced power is dissipating in the coaxial high-power loads that are connected to the upstream stripline ports.

$$Z_{||}(\omega) = \frac{Z_{0,||}g_{||}^2}{4}\left(2\sin^2\left(\frac{\omega(L-L_t)}{c_0}\right) + j\sin\left(\frac{2\omega(L-L_t)}{c_0}\right)\right)\frac{\sin^2\left(\frac{\omega L_t}{c_0}\right)}{\left(\frac{\omega L_t}{c_0}\right)^2} \tag{3.5}$$

$$Z_x(\omega) = \frac{c_0 Z_{0,\perp}}{2}\left(\frac{g_\perp}{a}\right)^2\frac{1}{\omega}\left(2\sin^2\left(\frac{\omega(L-L_t)}{c_0}\right) + j\sin\left(\frac{2\omega(L-L_t)}{c_0}\right)\right)\frac{\sin^2\left(\frac{\omega L_t}{c_0}\right)}{\left(\frac{\omega L_t}{c_0}\right)^2} \tag{3.6}$$

An approximation of the transverse and longitudinal shunt impedances , $R_\perp(\omega)$ and $R_{||}(\omega)$, are given by (3.7) and (3.8). In these two equations, it is assumed that the stripline is fed in differential and common-mode, respectively. Figure 9 shows $R_\perp(\omega)$ and $R_{||}(\omega)$ obtained analytically and from frequency domain simulations in COMSOL. In the simulations, the ceramic and dielectric losses in the chamber are included, and all the sub components of the coaxial feedthroughs are included as well.

$$R_\perp(\omega) = 2Z_{0,\perp}\left(\frac{g_\perp c_0}{a}\right)^2 \frac{\sin^2\left(\frac{\omega(L-L_t)}{c_0}\right)}{\omega^2}\,\frac{\sin^2\left(\frac{\omega L_t}{c_0}\right)}{\left(\frac{\omega L_t}{c_0}\right)^2} \tag{3.7}$$

$$R_{||}(\omega) = 4\,\mathrm{Re}(Z_{||}(\omega)) = 2Z_{0,||}g_{||}^2\sin^2\left(\frac{\omega(L-L_t)}{c_0}\right)\frac{\sin^2\left(\frac{\omega L_t}{c_0}\right)}{\left(\frac{\omega L_t}{c_0}\right)^2} \tag{3.8}$$

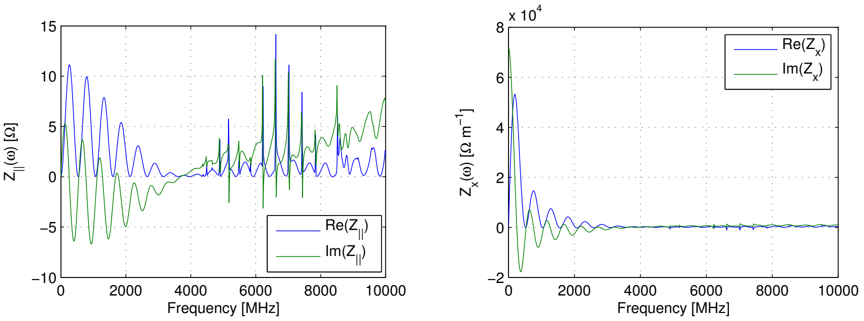

(a) (b)

Figure 8: $Z_{||}(\omega)$ (a) and $Z_x(\omega)$ (b) of the stripline obtained in GdfidL.

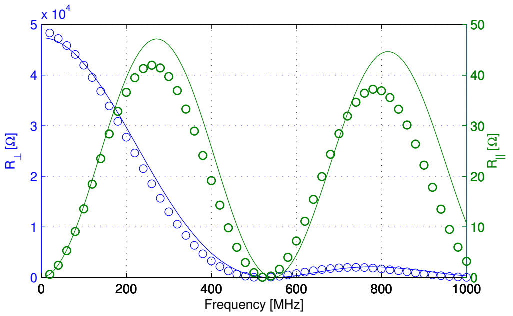

Figure 9: $R_\perp(\omega)$ and $R_{||}(\omega)$ obtained from (3.7)-(3.8) (solid lines) and from COMSOL (circles).

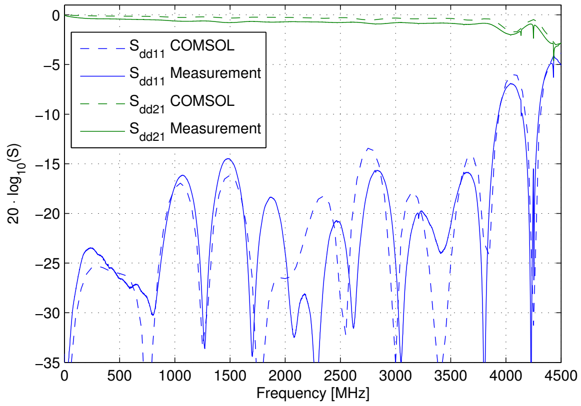

Figure 10: S_{dd11} and S_{dd21} of a stripline obtained from COMSOL and from a measurement.

Guassian $\sigma = 40$ mm		Quartic $\sigma = 56$ mm	
$\kappa_{\|\|}$ [mV/pC]	P_{loss} [W]	$\kappa_{\|\|}$ [mV/pC]	P_{loss} [W]
10.5	26.3	7.70	19.3

Table 2: The loss factor, $\kappa_{||}$, and the dissipated power, P_{loss}, in a stripline due to the beam impedance for two different bunch profiles. P_{loss} is obtained for a uniform filling pattern at a total beam current of 500 mA.

3.3 Measurements

The simulated differential and common-mode S-parameters are shown in Figure 10 and 11, respectively. The simulations are performed with the frequency domain solver in COMSOL with all the details and material parameters of the coaxial feedthroughs included. Dielectric losses in the ceramic and the resistive losses in the metal walls are also included in the simulations. The differential-mode parameters, S_{dd11} and S_{dd21}, are the reflection and transmission parameters, respectively when applying transverse feedback in BB, i.e., feeding the two strips with opposite polarities. Similar, the common-mode parameters, S_{cc11} and S_{cc21} correspond to the S-parameters when applying longitudinal feedback via the stripline back-end, as described in 5.1.3. The same S-parameters obtained from measurements of the vertical stripline are also shown in the figures. Here, a 4-port VNA is used, and the set-up during the mixed-mode measurements is the same as described in [20]. As seen, there is a quite good agreement to the simulations, even though the simulations slightly underestimate the transmission losses (up to 0.25 dB in the stripline operational range). The complete result from the mixed-mode measurements of both striplines are shown in Figure 50-57 in Appendix A.

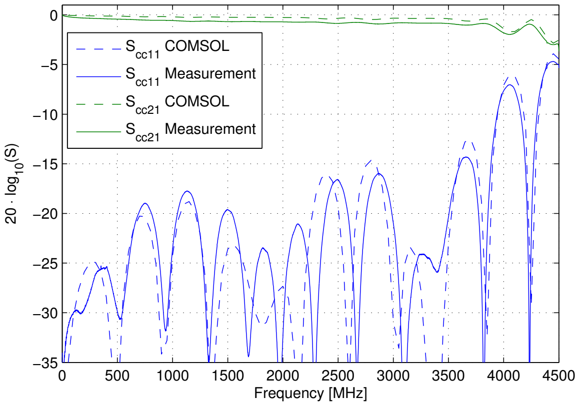

Figure 11: S_{cc11} and S_{cc21} of a stripline obtained from COMSOL and from a measurement.

There are some visible narrow-banded notches above 4 GHz in the measured data in Figure 10. These notches are trapped eigenmodes, similar to those described in [20]. The eigenmodes are not studied further since they are considered too weak and located too high up in frequency in order to have any notable effect on the beam quality.

4 Design of a Waveguide Overloaded Cavity

As explained in Section 3, the two striplines were initially used both as longitudinal and transverse actuators. A waveguide (WG) overloaded cavity was designed as a designated longitudinal actuator, and it was installed in the 3 GeV ring in July 2017. Overloaded cavities are used as longitudinal actuators at several facilities, and most of them are based on the DAΦNE design which was developed in the mid 90's [7]. The main advantage of an overloaded cavity compared to a stripline is its much higher longitudinal shunt impedance in the former.

4.1 Geometry

The basic components of the cavity are a standard stainless steel pipe and two copper bodies. Figure 12 shows a 3D model of the assembled cavity. The steel pipe has an inner radius of 100 mm, and four smaller pipes with CF16 flanges are attached to its lateral surface. Coaxial N-type feedthroughs are attached to the CF16 flanges. The steel pipe also has one attached pipe with a CF75 flange for an ion pump. Cavity nose cones and four ridged WGs are milled into the copper bodies. Each copper body is braced to a steel flange and then attached to the flanges that are welded to

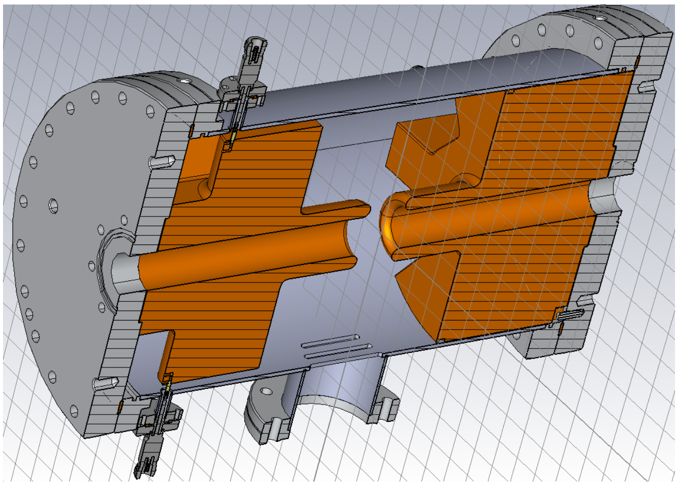

Figure 12: A 3D model of the assembled cavity.

the outer steel pipe. Proper electrical contact between the steel pipe and the copper bodies are provided by silver plated CuBe contact springs as in the ELSA design [15], where the springs are placed in grooves in the copper body as shown in Figure 13 (a). Electrical contact between the inner conductor of the coaxial feedthrough and the copper body is provided by gold plated socket connectors that are screwed to the latter as seen in Figure 13 (b). These socket connectors are the same type as the female inner pin at the N-type connector of the feedthroughs. The cavity is manufactured by FMB Berlin [12].

(a)

(b)

Figure 13: (a) shows the silver plated contact springs that provide electrical contact between the copper bodies and the steel pipe. (b) shows the gold plated socket connectors where the inner conductor of the feedthroughs are inserted.

4.2 Cavity Requirements

The first step when designing the cavity is to determine its center frequency f_c and its bandwidth (BW). As explained in Section 2.3.1, the minimum required BW in order to suppress all CBMIs is $f_{\mathrm{RF}}/2 = 50$ MHz if f_c is chosen so that $f_c = f_{\mathrm{RF}}(1/4 + n/2),\ n \in \mathbb{N}$. f_c in similar cavities might vary between 900 MHz [29] and 1900 MHz [18], and is often carefully chosen and optimized for the conditions at the facility where it is installed. Choosing a higher f_c has several advantages such as a more compact cavity and a higher achievable shunt impedance, $R_{||}$. Another advantage with a higher f_c is that all the potentially harmful HOMs are shifted upwards as well. The most important figure of merit when designing a cavity is the longitudinal shunt impedance, $R_{||}$, which is given by

$$R_{||} = \frac{V_{||}{V_{||}}^*}{2P} \tag{4.1}$$

where P is the input power, $V_{||}$ is the gap voltage seen by an ultra-relativistic particle, and $V_{||}^*$ its complex conjugate. $V_{||}$ is obtained from the longitudinal electric field along the center of the cavity $E_z(z)$, and is given by (4.2) where $k = \omega/c_0$ is the wavenumber and φ an arbitrary phase. Here, the integral length L is large enough so that $E_z(|z| > L) \approx 0$ [1].

$$V_{||} = \int_{-L}^{L} E_z(z) e^{j(kz+\varphi)}\,\mathrm{d}z \tag{4.2}$$

It is also useful to define the geometrical factor ($R_{||}/Q_0$) in order to compare the performance of different geometries without taking the conductivity of the materials and external loading into account. $Q_0 = \omega W/P$ is the unloaded quality factor, where W is the total stored electromagnetic energy inside the structure.

When selecting f_c, one also has to consider the relatively long bunches at MAX IV. Currently, both rings have double RF systems, where the accelerating cavities operate at $f_{\mathrm{RF}} = 100$ MHz and the passive Landau cavities operate at $3 \cdot f_{\mathrm{RF}}$. With optimum bunch lengthening, each bunch has a quartic (super Gaussian) distribution with $\sigma = 187$ ps $\equiv 56$ mm (FWHM $= 562$ ps $\equiv 169$ mm). There are future plans to operate with a triple RF system in the 3 GeV ring in order to increase the bunch lengthening further by adding 5:th harmonic cavities as well. Figure 14 shows the normalized charge distribution of a single bunch in TD, $\lambda(t)$, and in FD, $\lambda(\omega)$, during ideal bunch lengthening with a double and a triple RF system [2]. The issue with the long bunches is that the head of the bunch obtains a kick with the opposite direction compared to its tail if f_c is chosen too high due to the time varying fields. To illustrate this, assume that each bunch has a normalized spatial distribution $\lambda_z(z)$ so that $\int \lambda_z(z)\,\mathrm{d}z = 1$, and $\lambda_z(c_0 t)c_0 = \lambda(t)$. Then, a single electron at position z'

---

[1] Note that the gap voltage is sometimes defined as $\int |E_z(z)|\,\mathrm{d}z$ in the literature. Thus, with that definition, $V_{||}$ is a real value and the transit time of the particle is not taken into account.

[2] TD data provided by Pedro F. Tavares

will experience the voltage $V_{\mathrm{e}}(z')$

$$V_{\mathrm{e}}(z') = \int_{-L}^{L} E_z(z) e^{j(k(z-z')+\varphi)}\,\mathrm{d}z = V_{||} e^{-jkz'} \tag{4.3}$$

The average voltage gain over the normalized electron bunch V_{avg} is then

$$\begin{aligned} V_{\mathrm{avg}} &= \int_{-L}^{L} \lambda_z(z') V_{\mathrm{e}}(z')\,\mathrm{d}z' = V_{||} \int_{-L}^{L} \lambda_z(z') e^{-jkz'}\,\mathrm{d}z' \\ &= V_{||} \int_{-L/c_0}^{L/c_0} \lambda_z(c_0 t') e^{-j\omega t'} c_0\,\mathrm{d}t' = V_{||}\lambda(\omega) \end{aligned} \tag{4.4}$$

Note that the Fourier transform of $\lambda(t)$ in (4.4) is only a valid approximation when $\lambda(z) \approx 0$ for $|z| > L$. Consequently, one can define the effective geometrical factor $(R_{||}/Q_0)_{\mathrm{eff}}$ as

$$(R_{||}/Q_0)_{\mathrm{eff}} = \frac{V_{\mathrm{avg}} {V_{\mathrm{avg}}}^*}{2P_{\mathrm{rms}}} \frac{1}{Q_0} = (R_{||}/Q_0) \cdot |\lambda(\omega)|^2 = \frac{2}{\omega}\kappa_{||,1} \tag{4.5}$$

where $\kappa_{||,1}$ is the (longitudinal) modal loss factor of the fundamental mode ($n = 1$ in (4.11)). Note that $(R_{||}/Q_0)_{\mathrm{eff}} \to R_{||}/Q_0$ when $\lambda(t) \to \delta(t)$, where $\delta(t)$ is the Dirac delta distribution. As seen in Figure 14 (b), we have to select an f_c that is considerable lower than for other similar cavities in order not to lose the kick efficiency when operating with a triple RF system. A good compromise between a compact cavity geometry and fairly high $(R_{||}/Q_0)_{\mathrm{eff}}$ is to set $f_c = 625$ MHz. Here, $|\lambda(f_c = 625 \text{ MHz})|$ is 0.77 and 0.40 for a double and for a triple RF system, respectively. This frequency is also well within the terrestrial UHF band which makes it easier to find suitable commercial RF amplifiers and other high-power RF component for the distribution network.

4.3 Cavity Body

Once f_c was decided, the geometry of the unloaded (no attached WGs) cavity body was designed. Some mechanical restrictions were set on the cavity body. The first restriction was that the cavity beam pipe should have a circular cross section with a radius of 15 mm which is the same cross section as the neighbouring vacuum chambers. Secondly, the initial plan was to manufacture the cavity in-house, and the restriction was that the largest allowed inner radius of the cavity was 103.5 mm in order for the metal pieces to fit the milling machine. The goal is to maximize $R_{||}/Q_0$ of the fundamental mode and at the same time to minimize $R_{||}/Q_0$ of the first longitudinal HOMs. By minimizing $R_{||}/Q_0$ of the HOMs, their coupling to the beam is decreased. The radius of a simple pillbox cavity with $f_c = 625$ MHz is $(c_0\eta_{0,1})/(2\pi f_c) = 184$ mm which is larger than the design restriction of 103.5 mm. Therefore, f_c is shifted with a coaxially loaded structure. In order to simplify the manufacturing process, simple nose cones are added. Thus, no mushroom structures (as in the main and Landau cavities) are investigated. The nose cones also

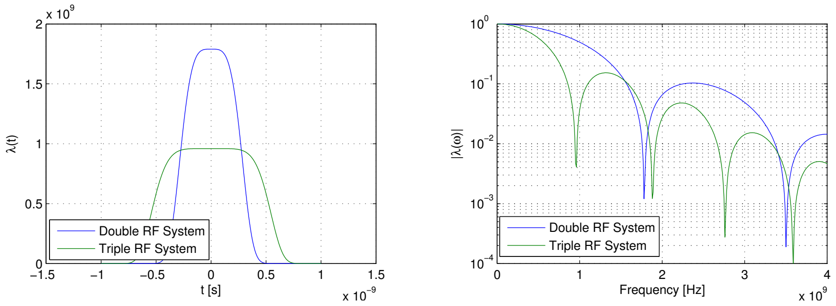

(a) (b)

Figure 14: (a) shows the normalized charge distribution of a bunch in TD, $\lambda(t)$, and (b) shows the distribution in FD, $|\lambda(\omega)|$. The charge distributions are for a double (100 MHz + 300 MHz) and for a triple (100 MHz + 300 MHz + 500 MHz) RF system during ideal bunch lengthening.

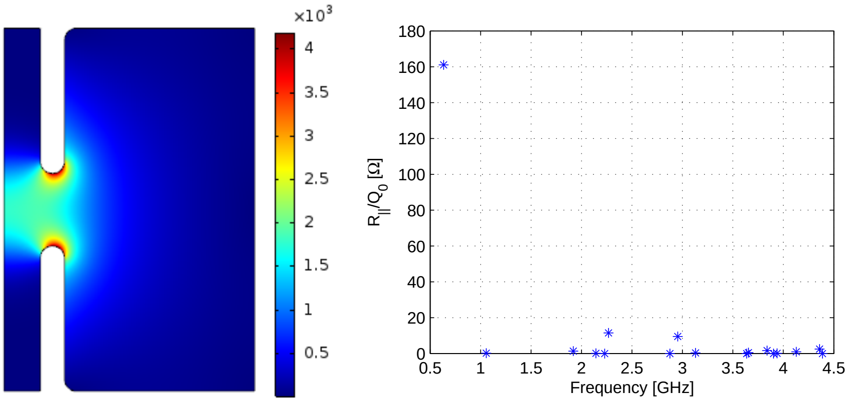

(a) (b)

Figure 15: (a) shows $|\boldsymbol{E}(\boldsymbol{r})|$ of the optimized rotation-symmetrical fundamental mode of the unloaded cavity in COMSOL. The scale of $|\boldsymbol{E}(\boldsymbol{r})|$ is arbitrary. (b) shows $R_{||}/Q_0$ of the rotation-symmetrical eigenmodes in the same cavity up to 4.5 GHz.

increase the field focusing and thereby increase $R_{||}/Q_0$. The optimization of the 2D rotation-symmetrical cavity body was performed in a MATLAB script with livelink to COMSOL. Note that the geometry of the cavity has to be slightly modified when the WGs are added since they perturb the fields and thereby shift f_c. The fundamental mode of the optimized unloaded cavity has $R_{||}/Q_0 = 162\ \Omega$. Figure 15 (a) shows $|\boldsymbol{E}(\boldsymbol{r})|$of the fundamental mode obtained in COMSOL, and Figure 15 (b) shows $R_{||}/Q_0$ of the rotation-symmetrical eigenmodes up to 4.5 GHz. As a comparison, $R_{||}/Q_0$ of the main and Landau cavities are 86 Ω and 133 Ω, respectively.

4.4 Cavity Matching

As mentioned above, the required BW of the cavity is 50 MHz, centred around f_c. Here, the BW is define as the 3 dB BW of the common-mode transmission coefficient S_{cc21} (see below). Note that it would also be possible to define the BW from $R_{||}(\omega)$. However, a somewhat larger BW of 70 MHz is chosen, and the cavity is matched so that the 3 dB limits of S_{cc21} are located at 590 MHz and 660 MHz. Of course, a larger BW lowers the peak $R_{||}$, but it results in a better gain flatness and makes the mechanical tolerances less critical in the manufacturing process. The required BW gives a loaded quality factor of $Q_L = f_c/f_{\text{BW}} = 8.9$. The BW is simply increased by increasing the power losses in the cavity system, and this is achieved by adding four ridged WGs to the pillbox cavity as seen in Figure 16. The WGs are optimized to have a good transmission to the cavity in a span from ≈ 500 MHz to ≈ 2500 MHz. The large BW of the WGs also ensures that the first HOMs are damped, which make them less likely to drive any CBMIs. Each WG is terminated with 50 Ω via a coax-to-waveguide transition. The two pair of WGs at each side are rotated 90° relative to each other in order to make the fields of the fundamental mode as symmetric as possible. This orientation also improves the damping of dipole HOMs. Consequently, almost all the power delivered to the cavity by the amplifier and by the beam is lost in the external loads, and this also removes the need for water cooling of the cavity. No tuning mechanism is added to the cavity since the mechanical tolerances in the manufacturing process are relatively low due to the rather large BW.

The fundamental mode is excited when the two WGs at the upstream (or downstream) end are driven with the same amplitudes and phases (common-mode), while the other two WGs are terminated as shown in the driving scheme in Figure 17. The amplifiers that feed the two WGs are protected via circulators from reflected waves and from backward travelling waves that are excited in the cavity by the beam itself. Figure 18 shows the S-parameters obtained in COMSOL where the physical ports 1 and 3 in Figure 17 form the logical mixed-mode port 1, and the physical ports 2 and 4 form the logical mixed-mode port 2. As seen $S_{cc11}(f = 590\ \ \text{MHz}) \approx S_{cc11}(f = 660\ \ \text{MHz}) \approx -3$ dB. Also note that f_c is shifted to 621 MHz in order to keep the BW in the 590 - 660 MHz range.

One can represent the cavity with the two identical (but orthogonal) upstream and downstream WG pairs as the resonant circuit in Figure 20 (a), where the resonance frequency is given by $\omega_c^2 = (LC)^{-1}$. Here, each WG pair is modelled as a

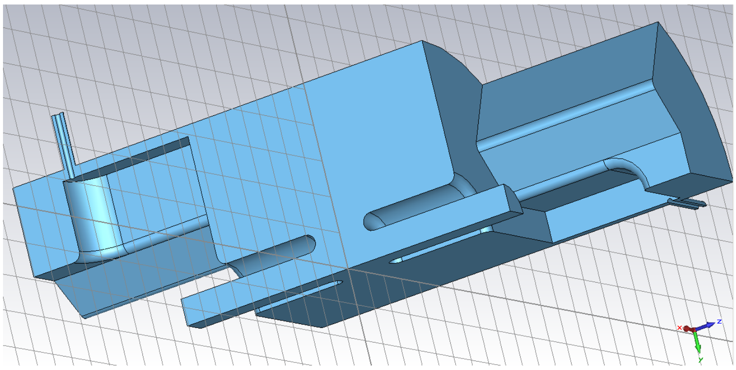

Figure 16: 1/4 of the cavity vacuum body when the four ridged WGs are added.

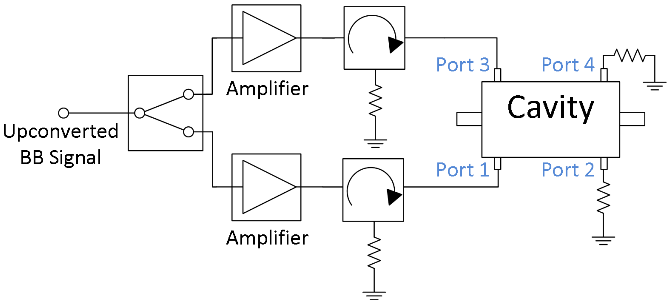

Figure 17: The driving scheme of the cavity.

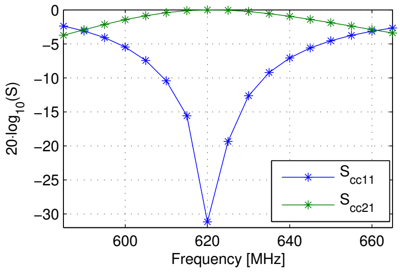

Figure 18: The common-mode S-parameters of the cavity.

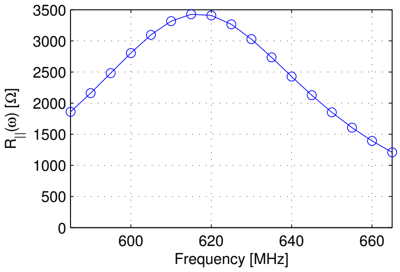

Figure 19: $R_{||}(\omega)$ of the cavity around its span of operation.

coupler transformer with the turns ratio $1 : n$. Each transformer is terminated with a load with the impedance $Z_0 = 50\ \Omega$ via a transmission line with a characteristic impedance of Z_0. The RF source corresponds to the drive amplifiers. The cavity itself corresponds to the RLC circuit in the middle, with the circuit shunt resistance $R \gg Z_0$. The circuit in Figure 20 (a) can be transformed into the RF source circuit, as in Figure 20 (b). Now, assume that a voltage $V(t) = \hat{V}\cos(\omega_c t)$ is applied over the circuit, then the total energy that is stored in the system is $W = n^2 C\hat{V}^2/2$. The unloaded quality factor of the cavity itself becomes $Q_0 = \omega_c W/P_c = \omega_c RC$, where $P_c = n^2\hat{V}^2/(2R)$ is the power dissipated in the cavity walls. The quality factors of the two external circuits (the two waveguides) are $Q_{\mathrm{e1}} = Q_{\mathrm{e2}} = \omega_c W/P_{\mathrm{e1}} = \omega_c n^2 Z_0 C$, where $P_{\mathrm{e1}} = \hat{V}^2/(2Z_0)$ is the power dissipated in the circuit of the RF source. The loaded Q factor, Q_L, is then obtained as

$$\frac{1}{Q_L} = \frac{1}{Q_0} + \frac{1}{Q_{\mathrm{e1}}} + \frac{1}{Q_{\mathrm{e2}}} = \frac{1}{Q_0} + \frac{2}{Q_{\mathrm{e1}}} \tag{4.6}$$

If the interior material of the unloaded cavity is made of copper or SS316L, Q_0 is 16808 and 2514, respectively. Since $Q_L = 8.9 \ll Q_0$, we have that $Q_L \approx Q_{\mathrm{e1}}/2$, thus the choice of material has an insignificant effect on the cavity BW.

One drawback with the circuit model described above is that it is only accurate for a cavity system with high Q_L where it is assumed that the coupler(s) have the same transmission/reflection coefficients to the cavity within the narrow BW of the resonator. This is not true in the case of overloaded cavity which can be seen in the slightly asymmetrical S-parameters in the 3 dB BW span around f_c in Figure 18. Despite this, the circuit model is an intuitive way to understand the overloaded cavity, and it provides a good approximation of the power dissipation in the cavity system.

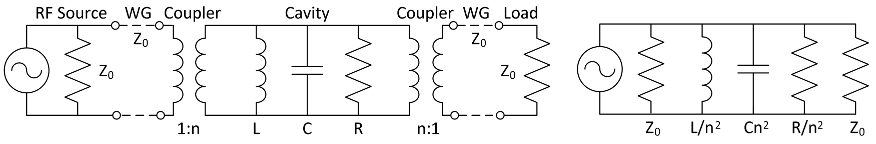

(a) (b)

Figure 20: (a) shows an equivalent circuit model of the cavity with two identical couplers, where the first one is connected to the RF source and the second to an external load. (b) shows the same circuit transformed into the RF source.

The shunt impedance, $R_{||}(\omega) = |V_{||}(\omega)|^2/(2P_{\mathrm{in}}(\omega))$, around the frequency span of operation can be seen in Figure 19. Here, $P_{\mathrm{in}}(\omega)$ is the total input power at Port 1 and 3, as shown in Figure 17. $V_{||}(\omega)$ is obtained from $E_z(z,\omega)$ in the 3D model. As seen, $R_{||}(\omega)$ is lower in the upper half of the operational span than in the lower half. This is mainly because the transit time factor decreases with frequency. It would be possible to make the shunt impedance more symmetrical in the span of operation by shifting the port matching to a higher frequency, but it was decided to keep the -3 dB S-parameter BW as it is.

The shunt impedance at the resonance frequency f_c can also be roughly estimated from the circuit model. If we feed the cavity as in Figure 17, almost all the power is lost in the two loads that are connected to Port 2 and 4 which correspond to the right Z_0 resistor in Figure 20 (b). Thus, with this set-up, the quality factor of the complete system is $\approx Q_{e2}$. By using $R_{||}/Q_0 = 162\ \Omega$ obtained from the unloaded cavity in the 2D simulations, $R_{||}(\omega_c)$ can be estimated as in (4.7). The maximum value of $R_{|}|(\omega)$ in Figure 19 is ≈ 3.4 kΩ.

$$R_{||}(\omega_c) \approx (R_{||}/Q_0) \cdot Q_{e2} \approx 2.9\ \text{k}\Omega \tag{4.7}$$

4.5 Wakefields and Heat Load

The wakefields in the structure are simulated in GdfidL [13], where the mesh size and wake length are set to 0.4 mm and 40 m, respectively. Here, the feedthroughs are simulated as simple coaxial waveguides that are terminated with several layers of perfectly matched layers, i.e., the sub components of the feedthroughs are not included. The longitudinal beam impedance $Z_{||}(\omega)$ is shown in Figures 21-22, while the transverse beam impedance $Z_{\perp}(\omega)$ is shown in Figure 24. When inspecting $\text{Re}(Z_{||}(\omega))$ in Figure 21, one can distinguish three different regions. In the first region, where $f \lesssim 3$ GHz, the eigenmodes are heavily damped by the WGs, and they are quite wideband. In the region where 3 GHz $\lesssim f \lesssim$ 8 GHz, the eigenmodes do not couple as much to the WGs due to the finite BW of the WGs and/or due to the fact that these eigenmodes do not have field distributions that couple to the geometrical cross sections of the WGs. Therefore, the eigenmodes in this regions are narrowbanded compared to those in the first region. The broad-band impedance region appears when 8 GHz $\lesssim f$ which is above the TM_{01} cut-off frequency of the beam pipe which is 7.6 GHz. Here, the longitudinal modes with field components in the beam pipe center are not trapped, but are propagating or semi-propagating.

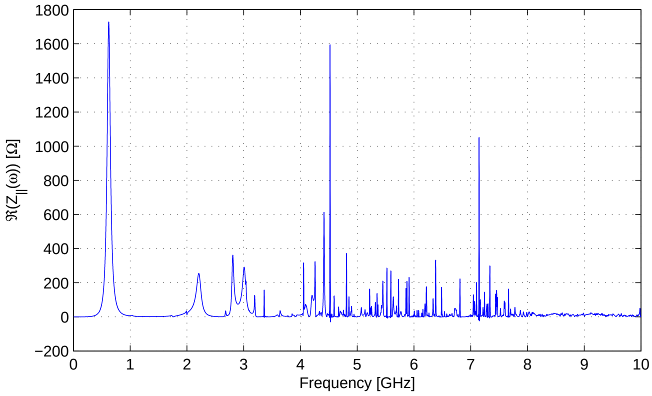

Figure 21: $\text{Re}(Z_{||}(\omega))$ of the cavity up to 10 GHz.

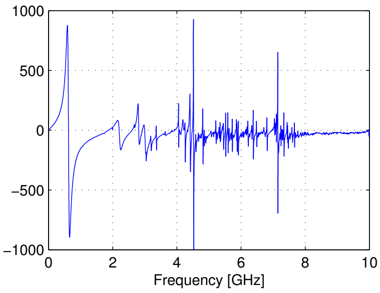

Figure 22: $\mathrm{Im}(Z_{||}(\omega))$ of the cavity up to 10 GHz.

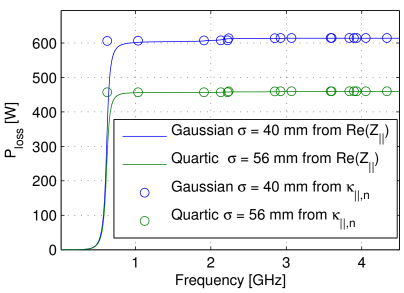

Figure 23: $\int_0^{\omega} \mathrm{d}P_{\mathrm{loss}}(\omega')\,\mathrm{d}\omega'$ calculated from $\kappa_{||}$ in (4.10) and from $\kappa_{||,n}$ in (4.12) for two different bunch profiles at 500 mA.

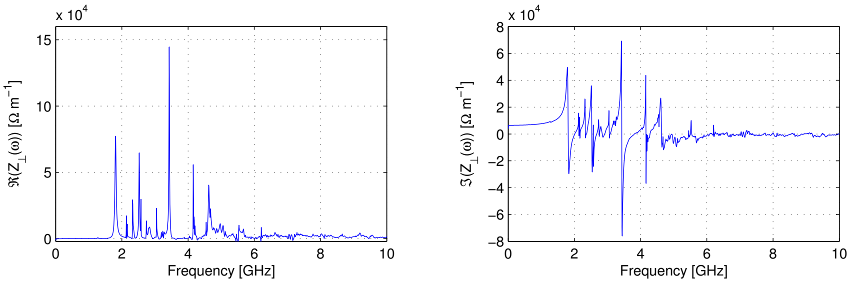

(a) (b)

Figure 24: $\mathrm{Re}(Z_{\perp}(\omega))$ (a) and $\mathrm{Im}(Z_{\perp}(\omega))$ (b) of the cavity up to 10 GHz.

Since the fundamental mode has a quite high $(R_{||}/Q_0)_{\mathrm{eff}}$, the beam induced power, P_{loss}, in the cavity is considerable. However, as explained above, almost all beam induced power dissipates in the external loads, which is shown in (4.8). P_{loss} is obtained from the longitudinal loss factor $\kappa_{||}$ as in (4.9)-(4.10), where I_0 is the total beam current. Note that (4.10) is only valid for a uniform filling pattern and has to be modified if other filling patterns are used. A conservative way to estimate P_{loss} is to calculate it for Gaussian bunches with $\sigma = 40$ mm at the maximum design current of 500 mA. Table 3 shows $\kappa_{||}$ and P_{loss} obtained from (4.9)-(4.10) for Gaussian bunches and for the quartic $\sigma = 56$ mm bunches (double RF system). Unlike the striplines, the cavity is a non-directional device, and P_{loss} is distributed almost equally among the four external loads. These loads have to be able to handle P_{loss} plus the additional power from by the feedback system.

$$P_{\mathrm{loss}} = P_c + P_{\mathrm{e1}} + P_{\mathrm{e2}} = P_c(1 + 2Q_0/Q_{\mathrm{e1}}) \Rightarrow P_c = P_{\mathrm{loss}}/(1 + 2Q_0/Q_{\mathrm{e1}}) \tag{4.8}$$

$$\kappa_{||} = \frac{1}{\pi} \int_0^{\infty} \mathrm{Re}(Z_{||}(\omega))\lambda(\omega)\lambda^*(\omega)\,\mathrm{d}\omega \tag{4.9}$$

$$P_{\mathrm{loss}} = \frac{I_0^2}{f_{\mathrm{RF}}}\kappa_{||} \tag{4.10}$$

P_{loss} can also be estimated from the modal loss factors $\kappa_{||,n}$ as seen from (4.11)-(4.12). Here, $\omega_{c,n}$ and $(R_{||}/Q_0)_n$ are the angular resonance frequency and the geometrical factor of the n:th eigenmode, respectively. This estimation is of course more accurate when the modes are more narrow (higher Q) since the variations in $\lambda(\omega)$ are smaller over the BW of the modes.

$$\kappa_{||,n} = \frac{\omega_{c,n}}{2}\left(\frac{R_{||}}{Q_0}\right)_n \lambda(\omega_{c,n})\lambda^*(\omega_{c,n}) \tag{4.11}$$

$$P_{\mathrm{loss}} = \frac{I_0^2}{f_{\mathrm{RF}}}\sum_{n=1}^{\infty}\kappa_{||,n} \tag{4.12}$$

To show how P_{loss} is distributed among the eigenmodes, $\int_0^{\omega} \mathrm{d}P_{\mathrm{loss}}(\omega')\,\mathrm{d}\omega'$ obtained from (4.10) and (4.12) is plotted in Figure 23. Here, the modal loss factors are obtained directly from the rotational-symmetric 2D simulations of the unloaded cavity. Even though the WGs have shifted the eigenmodes and perturbed the fields, there is a quite good agreement between the two methods. It is easy to see that almost all the beam induced power couples to the fundamental mode.

In the calculations of P_{loss} above, it is assumed that the power lost by the beam is incoherent, i.e., that there is no coherent multi-turn wakefield superposition. Such coherent power loss appears when the multi-turn spectrum of the beam coincides with peaks in $\mathrm{Re}(Z_{||}(\omega))$ that are caused by eigenmodes with considerable Q-factors. Thus, with a uniform fill pattern, this occurs if the spectrum of the eigenmodes overlap with any harmonic of f_{RF}. As seen in Figure 21, the lower part of the beam

Guassian $\sigma = 40$ mm		Quartic $\sigma = 56$ mm	
$\kappa_{\|\|}$ [mV/pC]	P_{loss} [W]	$\kappa_{\|\|}$ [mV/pC]	P_{loss} [W]
245	614	183	457

Table 3: $\kappa_{||}$ and P_{loss} in the cavity obtained from (4.9)-(4.10) for two different bunch profiles. P_{loss} is obtained for a uniform filling pattern at a total beam current of 500 mA.

spectrum of the fundamental mode overlaps with $6 \cdot f_{\text{RF}}$ due to the high BW, but a Q_L of 8.9 is considered too low to cause any notable coherent power loss [24]. As a comparison, the fall time of the voltage in the eigenmode is $\tau_f = 2Q_L/\omega_c \approx$ 4.5 ns, while the bunch separation is 10 ns. Such coherent multi-turn wakefield superposition is by the way the working principle of the passive Landau cavities, but Q_L in those structures is above 10000.

4.6 Vacuum Port

Since the inner volume of the cavity chamber is quite large compared to the cross section of the beam pipe, it was decided to add an ion pump to the design in order to improve the vacuum quality inside the cavity and in its surrounding chambers. The pipe that is connecting the ion pump to its CF75 flange is welded to the mid part of the cavity lateral surface. In order to perturb the cavity fields as little as possible, the pumping slits are milled so that they are oriented parallel to the surface currents $\boldsymbol{J} = \hat{\boldsymbol{n}} \times \boldsymbol{H}$. For the TM$_{010}$ mode in a pillbox cavity, $\boldsymbol{J}$ is oriented in the $\pm z$ direction at the lateral surface. The four WGs do however perturb the fields and add an azimuthal component of $\boldsymbol{J}$ on the lateral surface, as shown in Figure 25 (a). The slits are therefore milled where J_ϕ is small, which is shown in Figure 25 (b). Simulations show that the introduction of the ion pump has an insignificant effect on the field distribution and on the port matching.

4.7 Measurements

The mixed-mode measurements were performed with a 4-port VNA, and Figure 26 shows the measurement set-up. The port indices correspond to those in the driving scheme in Figure 17. The measured and simulated common-mode S-parameters around the fundamental mode can be seen in Figure 27. The simulation results are here obtained in COMSOL, and the full details of the ceramic feedthroughs are included, unlike the evaluation of S-parameters in Figure 18. Resistive and dielectric losses of the complete cavity are also included in the model. The measured 3 dB BW obtained from S_{cc21} is 74 MHz (590 MHz - 664 MHz), which is acceptable. The main reason why the measured S_{cc11} resonance is wider than the simulated is that the losses in the ceramic feedthroughs are lower in the latter. The interior of the feedthroughs is the same as in the striplines, and the simulations of these components do also underestimate the losses (see Section 3.3), despite using all

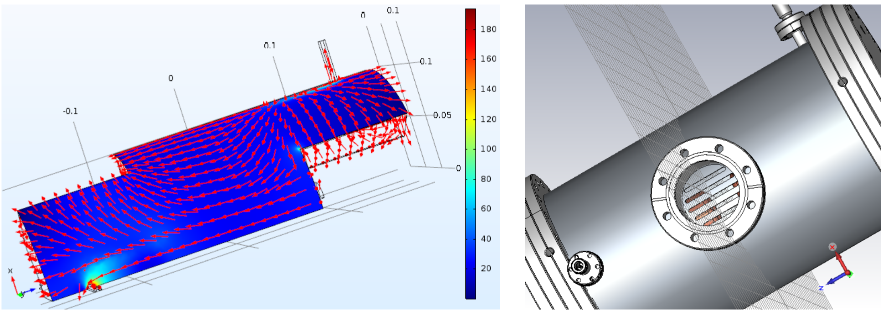

(a) (b)

Figure 25: (a) shows the surface currents $\boldsymbol{J}$ (arrows) and its magnitude $|\boldsymbol{J}|$ (color scheme) at the cavity lateral surface. (b) shows the pipe that is added for the ion pump and the orientation of the pumping slits at the lateral surface.

the dimensions and material parameters provided by the supplier. The measured resonance frequency of the fundamental mode is $f_c = 621$ MHz, and agrees well with the simulations.

The volume around the feedthroughs and the ridged WGs were considered critical from a tolerance perspective since proper electrical contact here is important for the matching of the cavity. In order to verify the matching of each WG, a single-ended measurement of each port was performed. Here, the reflection parameter of each physical port was measured, while the other three ports were terminated. Figure 28 shows the results and one can see that the matching is slightly different for each port. The variations are acceptable, and no further investigations were made to find if the variations were caused by mechanical variations in the cavity or in the feedthroughs.

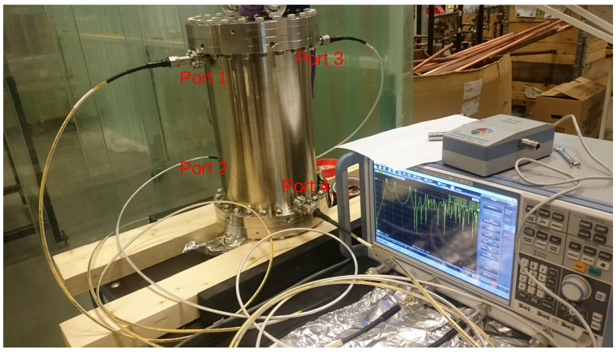

Figure 26: The set-up during the mixed-mode S-parameters measurements of the cavity.

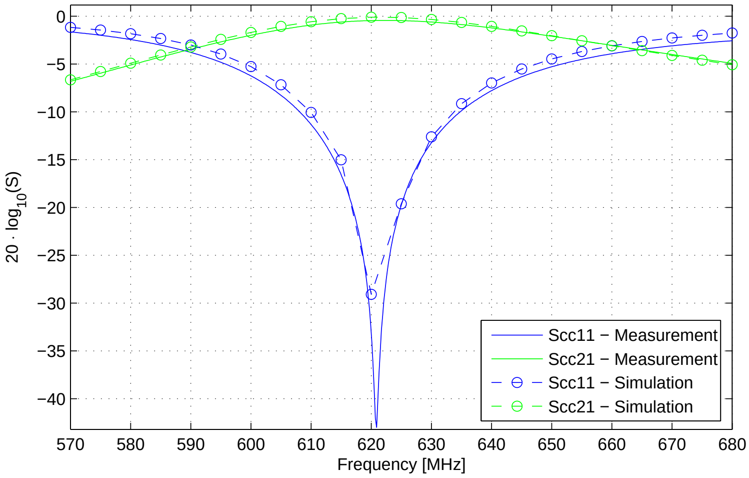

Figure 27: The measured and simulated common-mode S-parameters of the cavity around the fundamental mode.

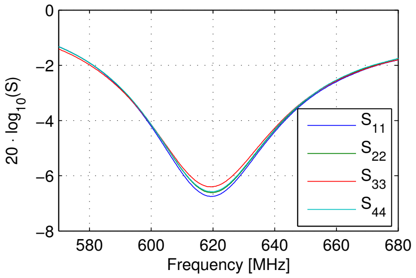

Figure 28: The measured single-ended reflection parameters of the cavity around the fundamental mode.

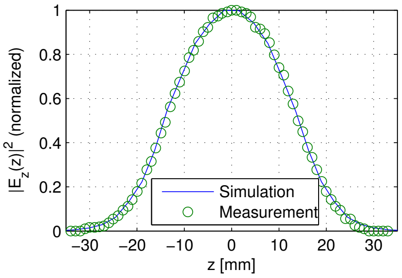

Figure 29: The measured and simulated electric field in the cavity along its center axis ($x = y = 0$).

A bead-pull measurement was also performed to characterize E_z along the cavity center axis. Here, the bead was a steel ball (taken from a ball bearing) with a radius of $a = 4$ mm. The ball was translated along the center axis via a 0.15 mm thick fishing line, and the shift of the resonance frequency was measured from S_{cc11} as the metal ball moved along the cavity. The Slater perturbation theorem describes the shift in resonance frequency when a small volume is removed from a resonance cavity. If the reduced volume is caused by a metallic ball, the relationship between the frequency shift, $\Delta\omega(z)$, and the magnitude of the longitudinal electric field,

Parameter	Measurement	Simulation
f_c	621 MHz	621 MHz
BW (from S_{cc21})	74 MHz	70 MHz
Q_L	8.4	8.9
$R_{\|\|}(f = f_c)$	3.31 kΩ	3.35 kΩ

Table 4: The cavity parameters obtained from the measurements. The results are compared with simulation results obtained in COMSOL, where the resistive and dielectric losses from the cavity walls and from the feedthroughs are included.

$|E_z(z)|$, when the ball is at position z is given by

$$\frac{\Delta\omega(z)}{\omega_c} = -\frac{\epsilon_0 \pi a^3}{W}|E_z(z)|^2 \tag{4.13}$$

where ϵ_0 is the permittivity of free space, ω_c the resonance frequency of the unperturbed cavity, and W is the time average of the stored energy inside the cavity [27]. In (4.13), it is assumed that the magnetic field is close to zero and that the derivative $\boldsymbol{E}$ is small compared to a in the vicinity of the metal ball, which is true in the gap between the nose cones. E_z also extends somewhat into the beam pipes, and the approximation is less accurate here (the beam pipe has a radius of 15 mm), and a larger discrepancy can here be seen in the measurement results. However, the fields are quite low in these regions and contribute little to $R_{||}$. Figure 29 shows the measured and simulated $|E_z(z)|^2$ along the center axis. As seen, there is a good agreement. The voltage gain, $V_{||}$, at the resonance frequency can now be calculated as

$$V_{||} = \int_{-L}^{L} |E_z(z)|e^{jkz}\,\mathrm{d}z = \sqrt{\frac{W}{\omega_c\epsilon_0\pi a^3}}\int_{-L}^{L}\sqrt{-\Delta\omega(z)}e^{jkz}\,\mathrm{d}z \tag{4.14}$$

where k is the wavenumber, and $2L$ is the total integration length. The shunt impedance, $R_{||}$, at the resonance frequency can then be obtained as

$$R_{||} = \frac{|V_{||}|^2}{2P} = \frac{Q_L}{\omega_c^2\epsilon_0\pi a^3}\left(\int_{-L}^{L}\sqrt{-\Delta\omega(z)}e^{jkz}\,\mathrm{d}z\right)^2 \tag{4.15}$$

where P is the total power fed to Port 1 and 3 in common-mode. In (4.15), we are using the relationship between stored energy and power which is $W/P \approx Q_{e2}/\omega_c \approx 2Q_L/\omega_c$ since almost all the input power is dissipating in the terminations at Port 2 and 4 (thus in the second external port as described in Section 4.4). The measurement gives $R_{||}(\omega_c) = 3.31$ kΩ, which is close to the simulated value of 3.35 kΩ (the losses in the metal walls and in this feedthroughs are included in this simulation). The measured and simulated parameters are summarized in Table 4.

5 The BBB Feedback System

As mentioned, the focus of this report is on the BBB feedback system in the 3 GeV ring, and Section 5.1 describes the layout of that system. A short summary on the current status of the BBB feedback system in the 1.5 GeV ring is given in Section 5.2.

5.1 BBB Feedback in the 3 GeV Ring

The commissioning of the BBB feedback system in the 3 GeV started in the beginning of 2016. This far, it has been possible to keep the beam stable in all three planes at beam currents that are above 100 mA. The largest challenge has been to keep the beam stable in the longitudinal plane. As mentioned, the longitudinal feedback has been provided by the striplines. It will hopefully be possible to reach the maximum design current of 500 mA once the overloaded cavity is installed after the 2017 summer shut-down. At higher currents, we can also tune in the Landau cavities which would suppress the CBMs further due to the increased bunch lengthening and Landau damping.

5.1.1 Front-End

The first part of the BBB feedback system is the detector-end, also known as the front-end. The beam signal is here monitored at the standard 4-button BPM chamber, depicted in Figure 30 (a). In order to create the horizontal and vertical differential, as well as the sum signal from the four buttons, a hybrid network was constructed which can be seen in Figure 30 (b). This network is basically the same as the "receiving network" described in [20], except there are no electromechanical switches. Figure 5 shows the phase and amplitude balance of the hybrid network obtained from its S-parameters.

	Horizontal		Vertical		Sum	
BPM Port, x	$20{\cdot}\log_{10}(S_{5x})$	$\arg(S_{5x})$	$20{\cdot}\log_{10}(S_{6x})$	$\arg(S_{6x})$	$20{\cdot}\log_{10}(S_{7x})$	$\arg(S_{7x})$
1	-9.92	56.1°	-9.54	-123.2°	-9.65	56.0°
2	-9.77	-124.9°	-9.64	-122.4°	-9.77	56.7°
3	-9.71	-123.4°	-9.85	60.8°	-9.65	58.4°
4	-9.53	57.8°	-9.89	63.4°	-9.69	60.7°

Table 5: The measured magnitudes and phases of the hybrid network at 1500 MHz. The indices of the ports are shown in green text in Figure 30 (b). Note that the front-end frequency was later changed from 1500 MHz to 1000 MHz.

The input signals to the signal processing units (see Section 5.1.2) must be in baseband (BB), thus in the 0 - 50 MHz range. Therefore, the wideband signals delivered from the hybrid network have to be downconverted to that span. This is done by heterodyning the BPM signals together with a harmonic of the main RF frequency in a front-end unit, as illustrated in Figure 31. The wideband BPM signal is first filtered in a band-pass filter so that its frequency span is in the 950-1050 MHz range, and then mixed with the 10th RF harmonic. The signal at the mixer RF input (see green text in Figure 31) can be approximated as $v_{\mathrm{R}}(t) = A(t)\cos(10\omega_{\mathrm{RF}}t+\phi(t))$, where $A(t)$ is an amplitude function which mainly depends on the transverse motion

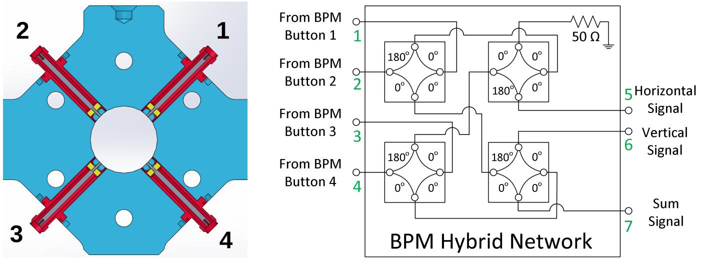

(a) (b)

Figure 30: (a) shows a 2D cross section of the BPM chamber and the indices of the four buttons. (b) shows a circuit diagram of the hybrid network where the horizontal, vertical, and sum signals are created.

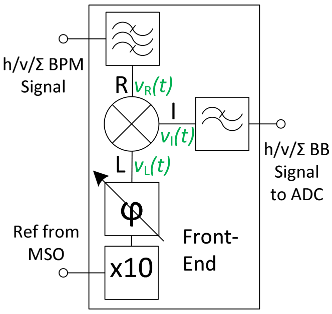

Figure 31: A simplified block diagram of a front-end.

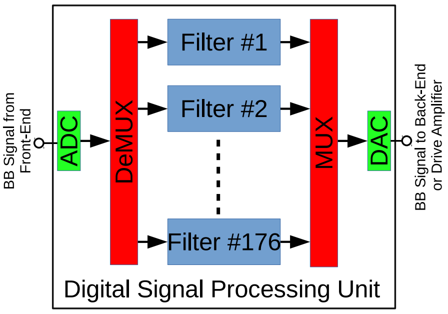

Figure 32: A simplified block diagram of a digital signal processing unit.

of the beam, and $\phi(t)$ is a phase function which is caused by longitudinal bunch oscillations. The signal at the LO input is $v_{\mathrm{L}}(t) = \cos(10\omega_{\mathrm{RF}}t + \varphi_0)$, where φ_0 is a phase constant that is set by the phase shifter in Figure 31.

If we are monitoring the horizontal, or vertical differential signal, the amplitude is proportional to the beam displacement in the corresponding plane. If we set $\varphi_0 = 0$, the output signal at the IF port, $v_{\mathrm{I}}(t) = v_{\mathrm{R}}(t)v_{\mathrm{L}}(t)$, becomes

$$v_{\mathrm{I}}(t) = \frac{1}{2}A(t)\{\cos(\phi(t)) + \cos(20\omega_{\mathrm{RF}}t + \phi(t))\} \approx \frac{1}{2}A(t)\{1 + \cos(20\omega_{\mathrm{RF}}t + \phi(t))\} \quad (5.1)$$

Here, it is assumed that $\phi(t) \ll 1$, thus the beam is stable in the longitudinal plane. The second high-frequency term is then removed by the low-pass filter (see Figure 31), and we see that the output signal of the front-end is proportional to the amplitude of the transverse motion $A(t)$. Signal detection in the horizontal and vertical planes are therefore known as amplitude detection.

When we monitor the longitudinal plane, the sum signal from the hybrid network is used. This signal is not sensitive to transverse beam oscillations, which makes the

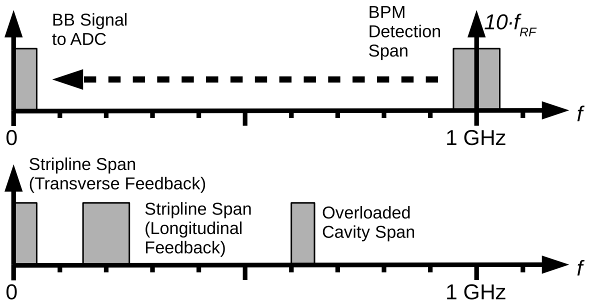

Figure 33: The heterodyning in the front-end (upper), and the span of the feedback signals that are applied to the striplines and to the cavity (lower).

approximation $A(t) = A_0$ relevant, where A_0 is a constant. By setting $\varphi_0 = -\pi/2$, the voltage $v_{\mathrm{I}}(t) = v_{\mathrm{R}}(t)v_{\mathrm{L}}(t)$, becomes

$$v_{\mathrm{I}}(t) = \frac{1}{2}A_0\{\sin(\phi(t)) + \sin(20\omega_{\mathrm{RF}}t + \phi(t))\} \approx \frac{1}{2}A_0\{\phi(t) + \sin(20\omega_{\mathrm{RF}}t + \phi(t))\} \quad (5.2)$$

Again, the second term is removed by the low-pass filter, and the front-end output signal is therefore proportional to $\phi(t)$. Signal detection in the longitudinal plane is therefore known as phase detection. Note that it is assumed in (5.1)-(5.2) that the mixers are ideal and that they are operating in their linear region.

Figure 33 (upper) shows how the detected BPM signals around $10 \cdot f_{\mathrm{RF}}$ are downconverted to BB. A commercial front-end unit delivered by Dimtel [11] is used, and this unit has three separated front-end channels, one for each plane. The Dimtel front-end unit also contains a back-end that will be used for upconverting the BB feedback signal for the overloaded cavity (see Section 5.1.3).

5.1.2 Signal Processing Units

The BBB feedback system is equipped with iGp12 FPGA based signal processing units delivered by Dimtel. Each plane requires its own unit. The three iGp12 units for the 3 GeV ring can be seen in Figure 38.

The signal processing chain consists of a high-speed 12-bit ADC, an FPGA, and a high-speed DAC. The ADC is clocked by f_{RF}, and it samples the turn-by-turn BB signal from the front-end (see Section 5.1.1) of each single bunch. Note that the synchrotron frequency is much lower than the betatron frequencies, so downsampling has to be used in the longitudinal plane. The sampled signal is then demultiplexed into 176 channels (one for each bunch), where each channel is processed with an adjustable digital FIR (Finite Impulse Response) filter. The digital filters are described in detail in [30], and they determine the correction signal (amplitude and phase) for each bunch. Finally, the correction signals from each channel are multiplexed to a DAC that is also clocked by f_{RF}. The analogue correction signal is then amplified and sent to an actuator (via a back-end if needed, as described in Section 5.1.3). Figure 32 shows a simplified block diagram of a digital signal processing unit.

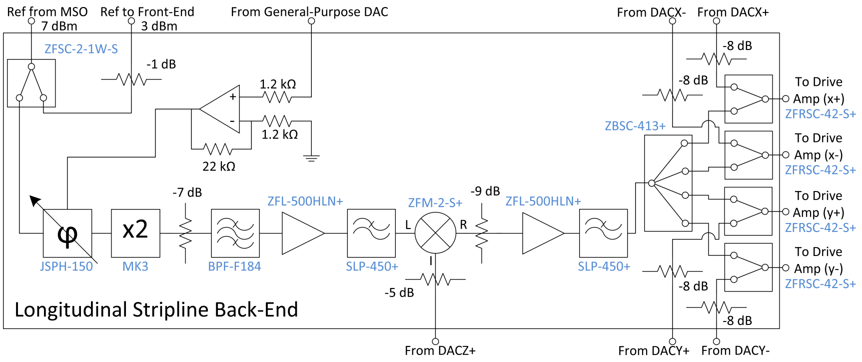

Figure 34: The circuit diagram of the longitudinal stripline back-end. All part numbers are from the Mini-Circuits' catalogue.

The FPGA also has integrated data acquisition memories which makes it possible to analyse the turn-by-turn data (see Section 6.1). Each unit also contains an integrated Linux based computer that controls the FPGA and provides the communication with the outside world via ethernet. The controls are performed via EPICS, and an EPICS-to-Tango gateway makes it possible to control the units via the MAX IV control system.

5.1.3 Back-End

The BB DAC output signals from the three iGp units are differential (each unit has two output ports, with the opposite signal polarity relative to each other). They are named DAC(X/Y/Z)(+/-) depending on which plane, (X/Y/Z), and which polarity, (+/-). The striplines have high transverse shunt impedances, $R_{\perp}(\omega)$, in the 0-50 MHz BB span (see Figure 9), and the transverse feedback signals, DAC(X/Y)(+/-), can therefore be fed directly to the striplines in differential-mode via drive amplifiers.

$R_{||}(\omega)$ is however weak in the BB span, and the DACZ+ signal must therefore be upconverted to a span where $R_{||}(\omega)$ is higher (DACZ- is not needed since the striplines are fed in common-mode when applying longitudinal feedback). A back-end that upconverts the DACZ+ signal to the $f = (2 \pm 0.5)f_{\mathrm{RF}}$ range with heterodyning was therefore constructed. Figure 34 shows a block diagram of the longitudinal stripline back-end, and Figure 35 shows the components assembled in a standard 19" rack case. The heterodyning occurs in a mixer where the BB signal is mixed with the second harmonic of f_{RF}. $2 \cdot f_{\mathrm{RF}}$ is generated in a frequency doubler, and its phase is adjusted by a voltage controlled phase shifter. The control signal

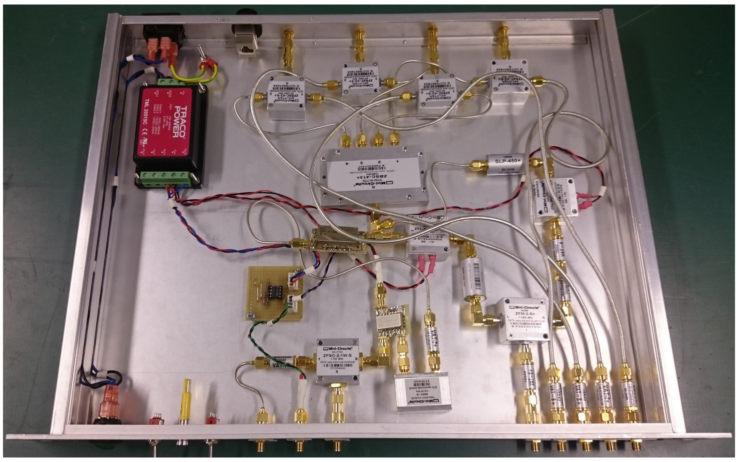

Figure 35: The longitudinal stripline back-end assembled inside a standard 19" rack case.

to the phase shifter is provided by a channel from the general-purpose DAC of one of the iGp units (this is not the same high-speed DAC that is used to generate the feedback signals). This signal is amplified by an OP amplifier to the phase shifter's operational input range of 0-15 V. The upconverted signal is then split into four signals and fed to the four strips via the amplifiers in common-mode. Before feeding these upconverted signals to the amplifiers, they are combined with the DACX+, DACX-, DACY+, and DACY- signals using four resistive splitters. This is shown in Figure 34, and makes it possible to provide longitudinal and transverse feedback with both striplines simultaneously.

Figure 36 shows the power spectrum of one of the output signals of the longitudinal stripline back-end. Here, a 25 MHz CW signal at the maximum DACZ+ output of +2 dBm is applied, and one can see that the isolation between the 25 MHz sidebands of 200 MHz to the highest unwanted peak is more than 30 dB. These neighbouring peaks are a combination of mixer products and harmonics created in the frequency multiplier and in the amplifiers. Figure 37 shows the two output signals when driving 3 bunches ($3 \cdot 10$ ns). As seen, the rise and fall times at 0 and 30 ns respectively are quite short which ensures good bunch-to-bunch isolation during excitation.

The commissioning of the overloaded cavity will start in the autumn of 2017. The DACZ+ signal will then instead be upconverted to the 600-650 MHz range in the Dimtel front/back-end unit. Figure 33 (lower) shows the feedback spans that are applied to the overloaded cavity and to the two striplines when they are operating as transverse and longitudinal actuators.

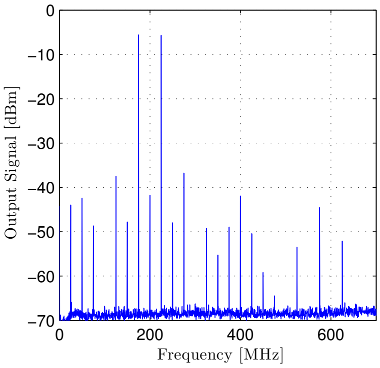

Figure 36: The power spectrum of one of the output signals from the longitudinal stripline back-end measured with a spectrum analyser. Here, a +2 dBm 25 MHz CW signal from DACZ+ is applied.

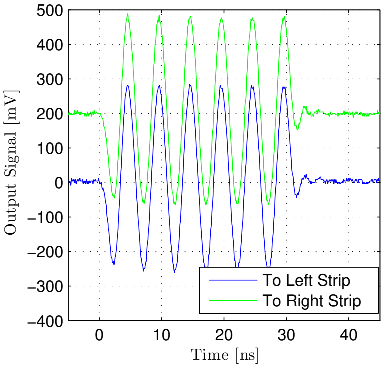

Figure 37: The two output signals to the horizontal stripline from the longitudinal stripline back-end when driving 3 bunches with a 1 kHz signal from DACZ+. The vertical offset of the green curve is 200 mV.

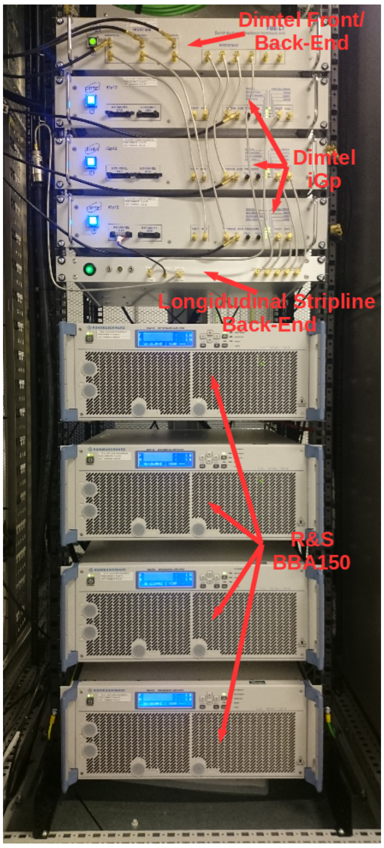

Figure 38: The BBB electronics in a cabinet above Achromat 08 with the Dimtel front/back-end unit, the Dimtel iGp12 signal processing units, the longitudinal stripline back-end, and the R&S BBA150 amplifiers.

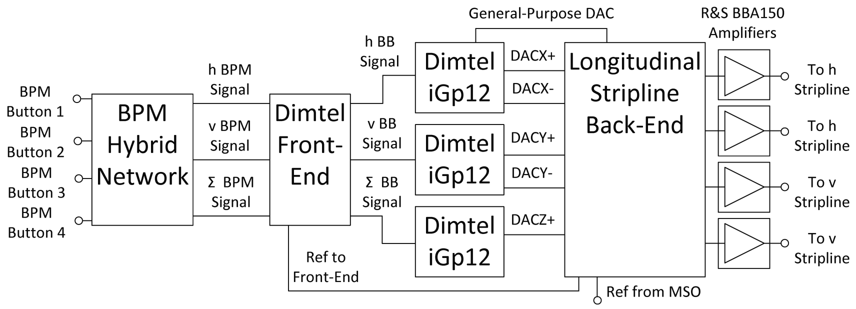

Figure 39: A somewhat simplified block diagram of the BBB feedback system in the 3 GeV ring. Note that this set-up is used when applying longitudinal feedback with the striplines, and not with the overloaded cavity.

5.1.4 Complete Set-up

Figure 39 shows a block diagram of the BBB feedback set-up in the 3 GeV ring. Figure 30, 31, 32, and 34 show the block/circuit diagrams of the sub components. The feedback signals to the striplines are amplified by four Rohde & Schwarz BBA150 wideband amplifiers [22]. These amplifiers can deliver an rms RF power of at least 200 W in a frequency span from 9 kHz to 250 MHz. Thus they can be used for both providing transverse feedback in the BB range and for longitudinal feedback in the 150 - 250 MHz range (see Figure 33). This is the set-up that has been used this far. After the 2017 summer shut-down, the longitudinal feedback will be provided by the cavity, and the longitudinal stripline back-end will no longer be needed. The transverse feedback signals, DAC(X/Y)(+/-), are then fed directly to the striplines via the amplifiers. The longitudinal common-mode feedback signal, DACZ+, will be upconverted to the 600-650 MHz range in the Dimtel front/back-end unit and fed to the cavity as shown in Figure 17. Commercial UHF amplifiers will be used to drive the cavity.

The two striplines and the button BPM are installed in Achromat 08 (the 3 GeV ring has 20 achromats in total). They are shown in the ring tunnel in Figure 40. The overloaded cavity has recently been installed in Achromat 11, as seen in Figure 41. Figure 38 shows the BBB electronics installed in a cabinet just above Achromat 08.

5.2 BBB Feedback in the 1.5 GeV Ring

The 1.5 GeV ring is equipped with the same Dimtel signal processing units as in the 3 GeV ring. The Dimtel front/back-end unit is here operating at 1.5 GHz compared to 1 GHz in the 3 GeV ring. While the front-end has been connected to a BPM, no actuators have yet been connected to the system. Thus, it is possible to monitor the beam motion with the system, but not applying any feedback. However, it has been

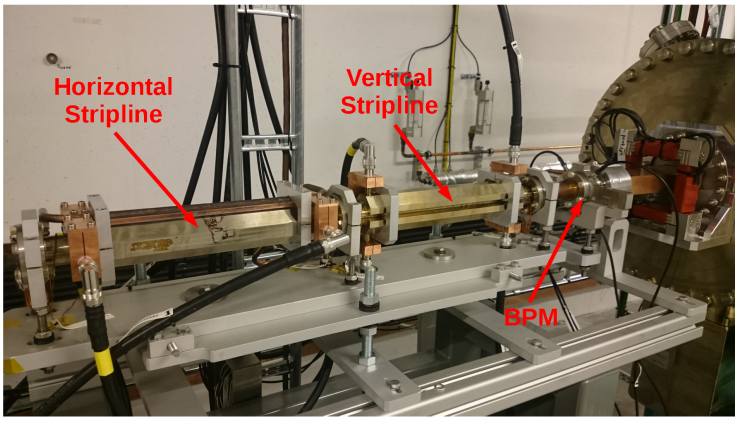

Figure 40: The two striplines and the button BPM installed in Achromat 08.

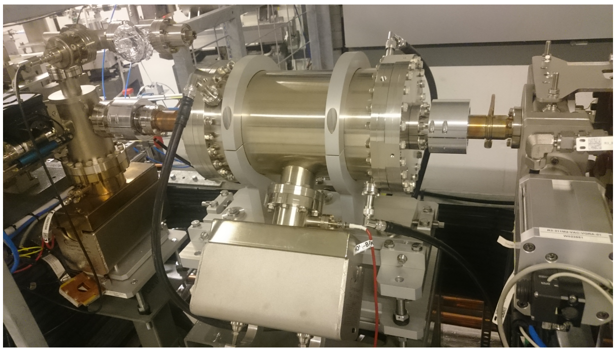

Figure 41: The cavity when it is installed in Achromat 11.

possible to keep the beam stable at beam currents above 150 mA in the longitudinal plane, even without feedback. This was achieved by injecting with an unstable beam up to approximately 150 mA with the Landau cavities tuned in. At this current, the induced fields in the Landau cavities are large enough to provide enough bunch lengthening and Landau damping to make the beam longitudinally stable. This is only possible at certain cavity temperatures where the dangerous HOMs are shifted away from the spectrum of the CBMs. It has not yet been possible to use the same technique in the 3 GeV ring to keep a longitudinal stable beam at high currents. One explanation can be that the harmonic number is 176 in the 3 GeV ring and 32 in the 1.5 GeV ring, giving a 5.5 denser CBM spectrum in the former (see Section 2.1). Another explanation is that the longitudinal CBMIs are driven by HOMs in the main and Landau cavities, and there are at date twice as many cavities in the 3 GeV ring.

It has this far not been possible to keep the beam stable in the horizontal and vertical plane at higher currents in the 1.5 GeV ring, so feedback will eventually be needed. After the 2017 summer shut-down, feedback will be applied in all three planes via the diagnostic stripline [20]. Here, the longitudinal BB signal has to be upconverted, and a back-end for that purpose has to be constructed.

6 Beam Measurements

In this section, some measurements on the electron beam are presented where different applications of the BBB feedback system are being used.

6.1 Diagnostic Measurements

Since the signal processing units record the beam motion over several turns, the BBB feedback system can be used as a comprehensive diagnostic tool. This can even be done in parallel with feedback operation. An an example, the transverse tunes are obtained as an FFT of the beam motion and monitored by the MAX IV control system during operation.

The BBB feedback system can also create transients in the oscillation amplitudes of the bunches, which makes it possible to measure growth and damp times. The transients are generated by switching the filter settings in the feedback system. An example of a grow/damp transient measurement in the horizontal plane is shown in Figure 42. Here, the beam is horizontally unstable without feedback but stable when the feedback is running, thus $D - G < 0$ and $D + D_{\text{fb}} - G > 0$ in (2.7). The grow transient is generated when the feedback is turned OFF at $t = 0$. As seen in Figure 42 (a), the oscillation amplitudes of all the 176 bunches grow exponentially until $t = 25$ ms when the feedback is turned ON again. After that, the oscillation amplitudes of the bunches are damped exponentially. Since the oscillations of each single bunch are recorded during the grow/damp transient, it is possible to do a mode analysis to find which of the CBMs that are driving the instability. This is shown in Figure 42 (b), where the mode spectrum is plotted. As seen, CBM #152 is driving the instability, and this mode is excited by a cavity HOM. During this measurement, the growth rate measured when $0 < t < 25$ ms was $D - G = -0.29$ 1/ms, while the damping rate when $t > 25$ ms was $D + D_{\text{fb}} - G = 2.50$ 1/ms.

Grow/damp measurements have been particularly useful when suppressing longitudinal CBMs by shifting the frequencies of the cavity HOMs, as described in Section 2.3.4. If instead the beam is naturally stable ($D - G > 0$), one can drive the bunches with positive feedback ($D_{\text{fb}} < 0$) until they oscillate with a relatively large amplitude, and then turn OFF the feedback and measure the damping time as the oscillations decay. This is knowns as a drive/damp measurement.

More diagnostic applications for a BBB feedback system are described in [17].

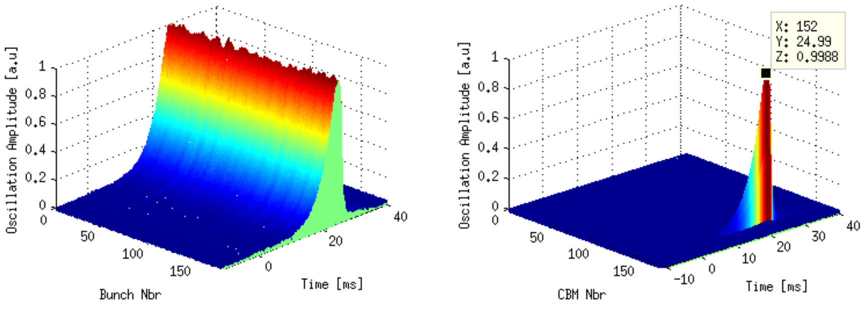

(a) (b)

Figure 42: (a) shows the evolution of the oscillation amplitude for each bunch during a horizontal grow/damp measurement. The horizontal feedback is turned OFF at $t = 0$ ms, and turned ON again at $t = 25$ ms. (b) shows the evolution of the CBMs during the measurement. As seen, the instability is caused by CBM #152.

6.2 Bunch Cleaning

As mentioned in Section 2.3.5, there are several advantages of operating with non-uniform filling pattern. The BBB feedback system can perform bunch cleaning where individual bunches are driven at their betatron frequency until they oscillate with so large amplitudes that they hit the physical boundaries of the beam chambers and are lost. At MAX IV, the bunch cleaning is often performed in the verical plane, and the unwanted bunches are dumped at a vertical scraper that is inserted close the to beam. As an example, Figure 43 shows the measured filling pattern for the uniform filled ring, and when 8 populations, each with 11 bunches, are kept. In [10], it is reported that bunch cleaning has been used to perform single-bunch experiments.

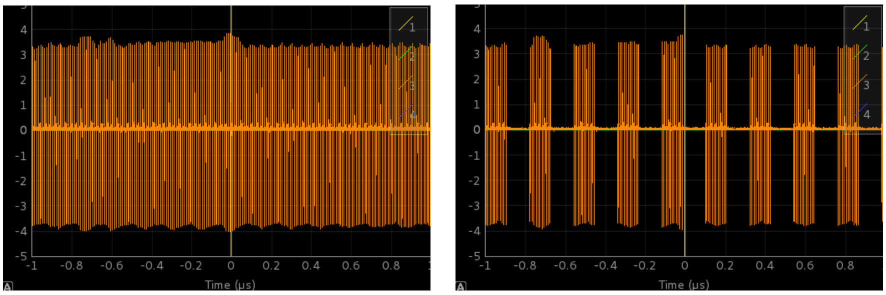

(a) (b)

Figure 43: The filling pattern measured from the bi-polar BPM signal with an oscilloscope. (a) shows an almost uniform filling pattern, while (b) shows the filling pattern when 8 populations, each with 11 bunches, are kept.

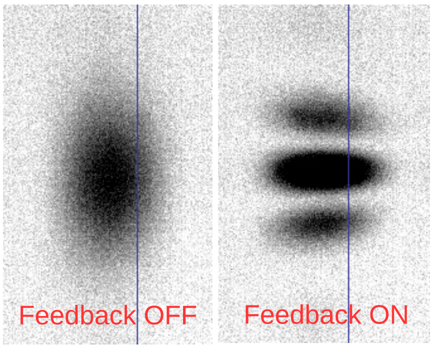

Figure 44: The diffracted transverse beam profile measured at the diagnostic beamline when the vertical feedback is turned ON and OFF. The CBMIs are here driven by ions.

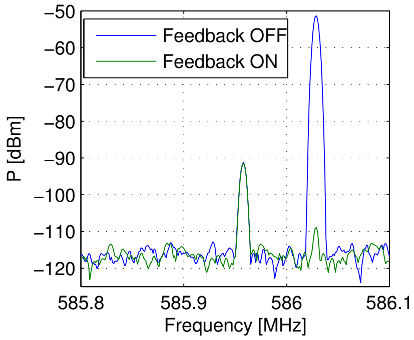

Figure 45: The horizontal beam spectrum around the 1032:nd revolution harmonic, with the horizontal feedback ON and OFF. CBM #152 is excited which is driven by a cavity HOM.

6.3 Feedback Effect on Beam Quality

As mentioned, the BBB feedback system is a comprehensive diagnostic tool that can be used for many types of beam studies. However, in the end, its most important task is to suppress CBMIs and thereby make sure that the effective emittance and energy spread of the beam are kept at their design values. Some examples where the beam properties are measured, with and without, feedback are now presented.

6.3.1 Transverse Feedback

During the early commissioning of the 3 GeV ring, ion-induced instabilities in both the horizontal and in the vertical plane were detected at beam currents as low as 30-40 mA. These CBMIs have this far been relatively weak, and it has been possible to suppress them with feedback. Figure 44 shows the transverse beam profile measured at the diagnostic beamline in Achromat 20, with and without feedback, when a vertical ion-driven CBMI is excited. The beam profile is here obtained from the synchrotron light radiating from a dipole magnet that is projected on a CCD camera [8]. As seen, the vertical beam size, and thereby the effective vertical emittance, is blown up when the feedback is turned OFF. The threshold where the ion-driven CBMIs appear has steadily moved towards higher beam currents as the quality of the vacuum has improved. They were rarely seen at currents below 100 mA in June 2017.

CBMIs that are driven by trapped transverse high-Q eigenmodes in the cavities, have also been observed. As an example, Figure 45 shows the horizontal beam spectrum around the 1032:nd ($5 \cdot 176 + 152$) revolution harmonic when the feedback is turned ON and OFF. The spectrum is obtained with a spectrum analyser and the BPM receiving network described [20]. The CBM is found at 586.0289 MHz, and its spectrum line is suppressed by more than 50 dB when the feedback is running. Note that the magnitude of the revolution harmonic at 585.9582 MHz is unchanged by the feedback (as it should). The RF frequency and horizontal fractional tune during the measurement were $f_{\mathrm{RF}} = 99.9308$ MHz and $\nu = 0.1246$, respectively, and we see from (2.6) that it is CBM #152 ($m = 152$) that is excited. Note that this is the same mode that was excited during the grow/damp measurement in Figure 42.

6.3.2 Longitudinal Feedback

The longitudinal CBMIs have this far been driven by HOMs in the cavities, and it has been necessary to operate with feedback in this plane in order to keep the beam stable at higher currents. It is possible to measure the longitudinal bunch profile at the diagnostic beamline by measuring the temporal distribution of the dipole light with an optical sampling oscilloscope. As an example, Figure 46 shows the measured bunch profile at 70 mA, with and without longitudinal feedback [3]. The Landau cavities are here completely detuned, and do not contribute to any bunch lengthening. The bunch profile should therefore be rather Gaussian which can be seen when the feedback is ON. When the feedback is turned OFF, the Gaussian-shaped bunches are oscillating in the longitudinal plane around their energy equilibrium which also results in an increased energy spread of the beam. Thus, the wider bunch profile measured with feedback OFF is not a result of any notable bunch lengthening, but mainly due to an oscillating beam and to the fact that the oscilloscope is unable to capture data from a single bunch at a single turn. The centroid of the unstable bunch is oscillating with a magnitude of approximately $\Delta T = \pm 200$ ps. This corresponds to $\Delta\phi = \pm 7.2$ degrees relative to the 100 MHz RF system. The synchrotron frequency, f_s during the measurement was 1.00 kHz, and with this parameter known, we can estimate that the dipole oscillation of the centroid corresponds to a relative energy oscillation, $\Delta W/W_0$, of

$$\frac{\Delta W}{W_0} = \frac{2\pi f_s}{\alpha}\Delta T = \pm 0.0041 \tag{6.1}$$

where $\alpha = 3.06 \cdot 10^{-4}$ is the momentum compaction factor of the ring. The natural energy spread of the bare lattice is $7.7 \cdot 10^{-4}$, so the dipole oscillations introduced by the longitudinal CBMI result in an additional energy spread of the beam that is several times greater than that of a stable beam.

While measurements of the beam profile and beam spectrum show that CBMIs have a degrading effect on the beam quality, the ultimate measurement would be on the spectral lines at the beamlines since they comprise the light delivered to the users. Spectral measurements with longitudinal stable and unstable beams have been performed at the BioMAX beamline[4]. BioMAX is an X-ray macromolecular crystallography beamline where the photon energy range is 5-25 keV [5]. The X-ray source is an in-vacuum undulator with a magnetic length of 2 m, and with a minimum magnet gap of 4.2 mm.

---

[3] The measurement was assisted by Jens Sundberg

[4] The measurements at BioMAX were assisted by Roberto Appio and Thomas Ursby

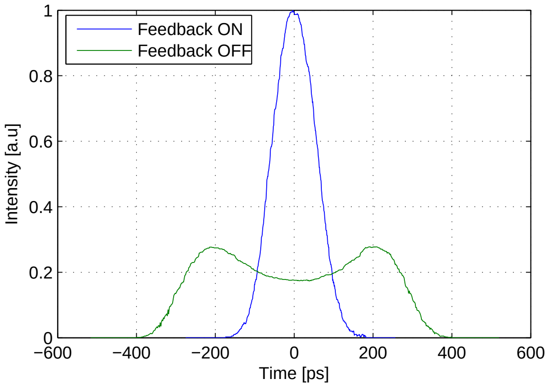

Figure 46: The bunch profile measured at the diagnostic beamline at a 70 mA, with longitudinal feedback ON and OFF. Note that the wider profile measured with feedback OFF is mainly a result of the bunches oscillating around their energy equilibrium, and not due to bunch lengthening.

One measurement series was performed in April 2017 around the 7:th harmonic spectral line. The beamline configuration was the same that has been used during beam delivery to some of the first users. Figure 47 shows the measured photon flux at a beam current of 37 mA with longitudinal feedback ON and OFF. As seen, the spectral line is wider and the peak flux is decreased when the beam is unstable in the longitudinal plane due to the increased effective energy spread. A simulation of the photon flux with the same beamline parameters was performed in SPECTRA [23]. The simulation results can also been seen in Figure 47 where the peak flux has been normalized to that of the stable beam. There is an excellent agreement to the measurement. The spectrum was also measured at a beam current of 3.3 mA (see Figure 47), and the current is here so low that the beam remains stable even without feedback. The normalized flux for the stable beam at 37 mA and 3.3 mA are plotted in Figure 48. As seen, the line widths look very similar for the two curves, and one can therefore conclude that the properties of a beam that is stabilized with feedback is very similar to that of a beam that is naturally stable.

The magnitude of the dipole oscillations for the unstable beam in Figure 47 is not as large as during the bunch profile measurements shown in Figure 46. A measurement series at BioMAX, with larger dipole oscillations, was performed in November 2016. The results can be seen in Figure 49. Here, the 5:th harmonic spectral line is measured at a beam current of 12 mA. The reason why the oscillations are larger during this measurement, despite that the beam current is a factor three lower, is mainly because more dangerous cavity HOMs are here overlapping the spectrum of the CBMs (see Section 2.3.4). The two peaks of the unstable beam are found at approximately ±0.06 keV from the 5:th harmonic spectral line of 8.92 keV.

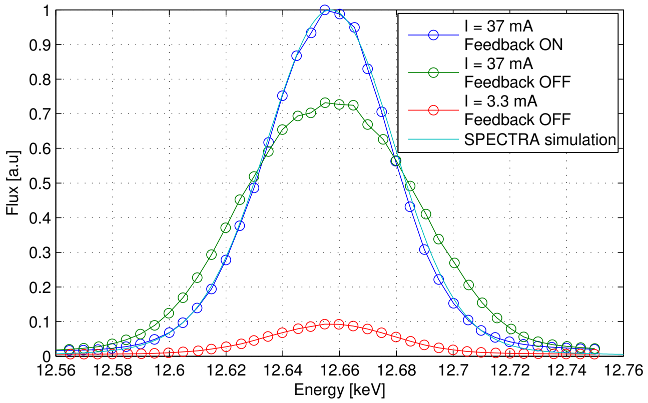

Figure 47: The photon flux around the 7:th harmonic spectral line at the BioMAX beamline measured in April 2017. The results are compared to a SPECTRA simulation.

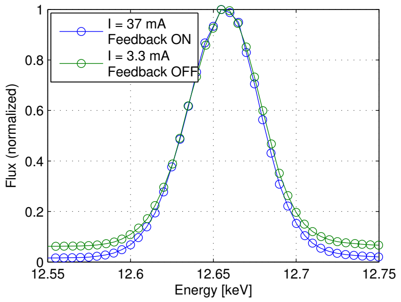

Figure 48: The normalized photon flux around the 7:th harmonic spectral line of a naturally stable beam at 3.3 mA and of a stabilized beam at 37 mA. It is the same measurement as in Figure 47.

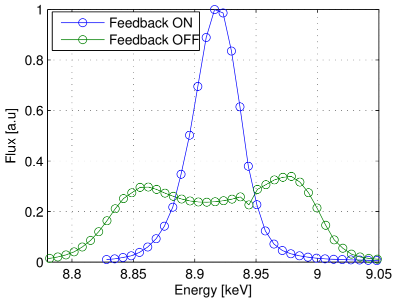

Figure 49: The measured photon flux around the 5:th harmonic spectral line. The measurement was performed at the BioMAX beamline in November 2016 at a beam current of 12 mA.

The photon wavelength of the k:th harmonic spectral line can be approximated as

$$\lambda_k = \frac{\lambda_u}{2k\gamma^2}\left(1 + \frac{K^2}{2} + \gamma^2\vartheta^2\right) \tag{6.2}$$

where λ_u is the undulator magnetic period, γ the Lorentz factor, K is the undulator/wiggler parameter, and ϑ is the observation angle from the forward direction of the emitted synchrotron radiation [28]. The photon energy is then given by $E = \hbar c_0/\lambda_k$, where c_0 is the speed of light and $\hbar$ is the Planck constant. We can see that the sizes of the collimators used during the measurements are very small since the spectral lines of the stable beams in Figure 47-49 look quite symmetrical. Thus, the spectrum is close to that of a pin-hole spectrum, and the red-shift due to the Doppler effect (ϑ is small in (6.2)) has little effect on the observed spectrum. The corresponding relative energy oscillation of the bunch centroid during the measurement is estimated to approximately $\Delta W/W_0 = \pm 0.0034$ when using (6.2). Here, $\lambda_w = 1.8$ cm, $k = 5$, and $K = 1.825$. It is also assumed that $\vartheta = 0$ (the horizontal and vertical design dispersion at the undulator is zero).

7 Conclusions and Future Work

It has been observed that the CBMIs have a degrading effect on the quality of the beam in the two MAX IV storage ring. A BBB feedback system has been installed in the 3 GeV ring for suppression of CBMIs, and it has this far been possible to keep a stable beam at currents above 100 mA. Two stripline kickers have been manufactured, and they have provided feedback in all three planes. A WG overloaded cavity kicker that is dedicated for longitudinal feedback has also been deigned and manufactured, but has not yet been commissioned.

After the 2017 summer shut-down, the WG overloaded cavity will be commissioned, and this will hopefully make it easier to achieve a longitudinally stable beam at higher currents. The BBB feedback system in the 1.5 GeV ring will also be commissioned during the autumn of 2017. The ultimate goal is to deliver light to the users in both storage rings with stable beams at the design current of 500 mA.

Acknowledgements

The authors would like to thank Karl Åhnberg for doing the mechanical design of the striplines and the cavities. Thanks to Henrique de Oliveira Caiafa Duarte and Sergio Rodrigo Marques at LNLS, Nikolas Heurich at ELSA, and Alun Morgan at Diamond for sharing ideas on the mechanical design of the cavity. Thanks to Eshraq Al Dmour, Marek Grabski, Mathieu Leme, and Esa Paju in the vacuum group for the support and expertise in the design and assembly phase of the cavity. Thanks to Anders Bjermo, Lars Christiansson, and Dirk Winnat for the workshop support. Thanks to Jens Sundberg for his support at the diagnostic beamline. Thanks to Roberto Appio, Hamed Tarawneh, and Thomas Ursby for their help during the measurements at BioMAX. Also big thanks to Dmitry Teytelman at Dimtel for all the support with the BBB feedback system.

Finally, a special thanks to Åke Andersson, Francis Cullinan, and Pedro Fernandes Tavares for all the help during the commissioning of the BBB feedback system and for all the hours spent in the control room, fighting those damn cavity HOMs!

References

[1] N. P. Abreu, R. H. A. Farias, and P. F. Tavares. “Longitudinal dynamics with rf phase modulation in the brazilian electron storage ring”. *Physical Review Special Topics: Accelerators and Beams* 9 (2006).

[2] Å. Andersson et al. “The 100 mhz rf system for the max iv storage rings”. In: *2nd International Particle Accelerator Conference*. 2011, pp. 193–195.

[3] J. Andersson and D. Olsson et al. “New features of the max iv thermionic pre-injector”. *Nuclear Instruments and Methods in Physics Research* 855 (2017), pp. 65–80.

[4] C. Belver-Aguilar et al. “Stripline design for the extraction kicker of compact linear collider damping rings”. *Physical Review Special Topics: Accelerators and Beams* 17 (2014).

[5] *BioMAX website.* https://www.maxiv.lu.se/accelerators-beamlines/beamlines/biomax/.

[6] J. Björklund-Svensson. “Master thesis: characterization of higher order modes in the max iv active 100 mhz cavities” (2015).

[7] R. Boni et al. “A waveguide overloaded cavity as longitudinal kicker for the daphne bunch-by-bunch feedback system”. In: *Particle Accelerators.* 1996, pp. 95–113.

[8] J. Breunlin and Å. Andersson. “Emittance diagnostics at the max iv 3 gev storage ring”. In: *7th International Particle Accelerator Conference.* 2016, pp. 2908–2910.

[9] *COMSOL Multiphysics website.* http://www.comsol.com/.

[10] F. J. Cullinan et al. “Impedance characterization and collective effects in the max iv 3 gev ring”. In: *North American Particle Accelerator Conference.* 2016.

[11] *Dimtel website.* http://www.dimtel.com/.

[12] *FMB Berlin website.* http://www.fmb-berlin.de.

[13] *GdfidL website.* http://www.gdfidl.de.

[14] D. A. Goldberg and G. R. Lambertson. “Dynamic devices a primer on pickups and kickers”. In: *AIP Conference Proceedings.* 1992, pp. 537–600.

[15] N. Heurich et al. “A longitudinal kicker cavity for a bunch-by-bunch feedback system at elsa”. In: *2nd International Particle Accelerator Conference.* 2011, pp. 480–486.

[16] Y. M. Kang and R. L. Kustom. “Hom damping with coaxial dampers in the storage ring cavities of the advanced photon source”. In: *4th European Particle Accelerator Conference.* 1994.

[17] M. Lonza and H. Schmickler. “Multi-bunch feedback systems”. In: *CAS-CERN: Advanced Accelerator Physics, Trondheim, Norway.* 2014, pp. 503–546.

[18] A. F. D. Morgan and G. Rehm. “Design for the diamond longitudinal bunch-by-bunch feedback cavity”. In: *5th International Beam Instrumentation Conference*. 2016, pp. 340–343.

[19] K. Y. Ng. *Physics of Intensity Dependent Beam Instabilities*. World Scientific Publisher, 2005.

[20] D. Olsson, A. Karlsson, and L. Malmgren. *Design of Striplines for the MAX IV and SOLARIS Storage Rings*. Tech. rep. LUTEDX/(TEAT-7254)/(2017). Lund Institute of Technology, 2017.

[21] *R. Lindvall, priv. comm. (June 2017).*

[22] *Rohde & Schwarz website.* http://www.rohde-schwarz.com.

[23] *SPECTRA website.* http://wwww.radiant.harima.riken.go.jp/spectra/.

[24] *T. Günzel, priv. comm. (Oct 2016).*

[25] M. Takao et al. “Observation of ion effects at the spring-8 storage ring”. In: *8th European Particle Accelerator Conference*. 2002, pp. 1562–1564.

[26] P. F. Tavares et al. “The max iv storage ring project”. *Journal of Synchrotron Radiation* 21 (2014), pp. 862–877.

[27] H. Wang and J. Guo. “Bead-pulling measurement principle and technique used for the srf cavities at jlab”. In: *USPAS Education in Beam Physics and Accelerator Technology, SRF Practices and Hands-on Measurements, Thomas Jefferson Lab, USA*. 2015.

[28] H. Wiedemann. *Particle Accelerator Physics*. Third. Springer-Verlag, 2007.

[29] W. Z. Wu et al. “Development and commissioning of bunch-by-bunch longitudinal feedback system for duke storage ring”. In: *23rd Particle Accelerator Conference*. 2009, pp. 4117–4119.

[30] W. Wu. “Ph.d. thesis: feedback systems for control of coupled-bunch instabilities in the duke storage ring” (2012).

Appendix A Stripline S-parameter Measurements

Figure 50-57 show the measured mixed-mode S-parameters of the two striplines. The measurement set-up with the physical and logical ports are the same as described in [20]. Here, all the 2x16 parameters are not shown since $S_{\mathrm{dc11}} \approx S_{\mathrm{cd11}}$, $S_{\mathrm{dc22}} \approx S_{\mathrm{cd22}}$, $S_{\mathrm{dd21}} \approx S_{\mathrm{dd12}}$, $S_{\mathrm{cc21}} \approx S_{\mathrm{cc12}}$, $S_{\mathrm{dc21}} \approx S_{\mathrm{cd12}}$, and $S_{\mathrm{dc12}} \approx S_{\mathrm{cd21}}$.

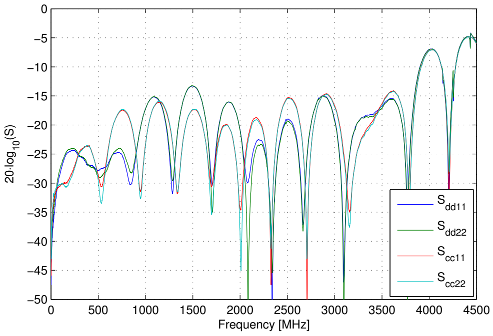

Figure 50: Differential and common-mode reflection coefficients of the horizontal stripline.

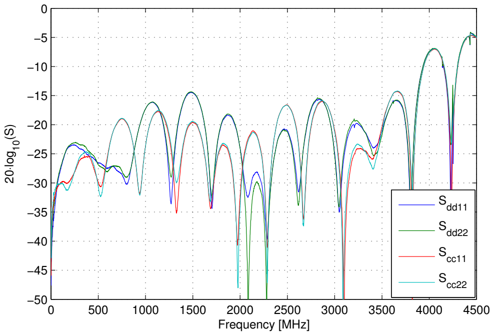

Figure 51: Differential and common-mode reflection coefficients of the vertical stripline.

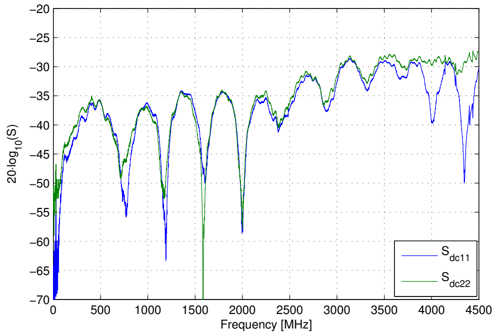

Figure 52: Cross-mode reflection coefficients of the horizontal stripline.

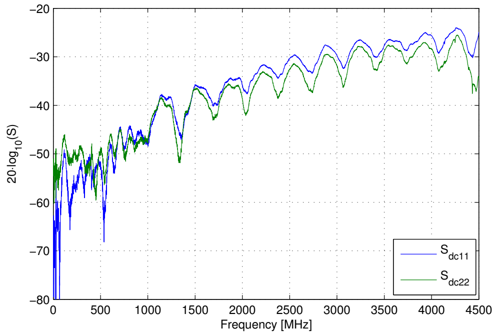

Figure 53: Cross-mode reflection coefficients of the vertical stripline.

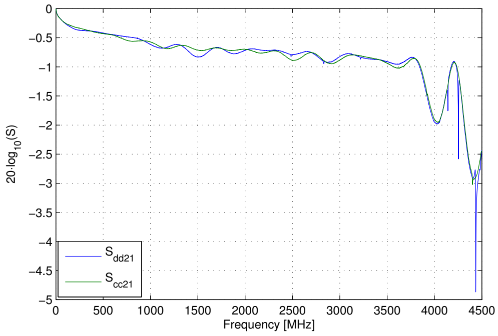

Figure 54: Differential and common-mode transmission coefficients of the horizontal stripline.

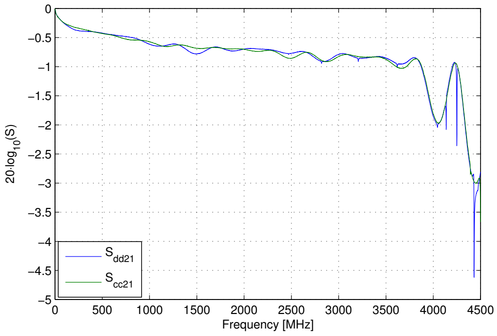

Figure 55: Differential and common-mode transmission coefficients of the vertical stripline.

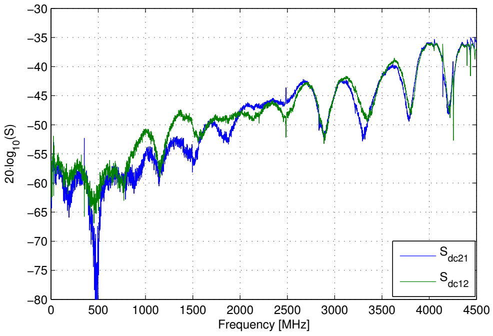

Figure 56: Cross-mode transmission coefficients of the horizontal stripline.

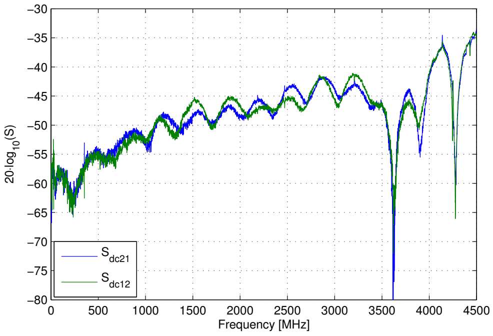

Figure 57: Cross-mode transmission coefficients of the vertical stripline.

PAPER V

Design and Implementation of Stripline Feedback Kickers in the MAX IV 3 GeV Ring

D. Olsson, L. Malmgren and K. Åhnberg.

pp THPIK086 (2017) *Proceedings of IPAC17, Copenhagen, Denmark.*

Proceedings of IPAC2017, Copenhagen, Denmark **THPIK086**

DESIGN AND IMPLEMENTATION OF STRIPLINE FEEDBACK KICKERS IN THE MAX IV 3 GeV STORAGE RING

D. Olsson*, L. Malmgren, K.Åhnberg
MAX IV Laboratory, Lund, Sweden

Abstract

Commissioning of the Bunch-By-Bunch (BBB) feedback system in the MAX IV 3 GeV storage ring was started in early 2016. At the moment, the actuators are two stripline kickers oriented in the horizontal and in the vertical plane, respectively. Apart from providing feedback in the transverse plane, they are simultaneously operating as longitudinal actuators. This is done by upconverting the longitudinal 0 - 50 MHz baseband signal to the 150 MHz - 250 MHz range where the longitudinal shunt impedance of the striplines is higher. The upconverted signal is then fed to the stripline electrodes in common-mode. The design of the stripline kickers and the layout of the BBB feedback system in the 3 GeV ring are presented in this report. Results from instability studies in this ring are also discussed.

INTRODUCTION

The MAX IV facility in Lund, Sweden consists of two storage rings for production of synchrotron radiation, and a Short-Pulse-Facility (SPF) [1]. The two rings are designed for 3 GeV and 1.5 GeV, respectively, where the initial beam commissioning of the former has recently been completed, and commissioning of the latter was started in September 2016. Both rings will be operating with top-up injections delivered by a full-energy injector [2].

The two rings have been equipped with BBB feedback systems, where the signal processors are delivered by Dimtel [3]. In the 3 GeV ring, two stripline kickers that are dedicated for BBB feedback have been installed and commissioned. Apart from applying transverse feedback, the striplines are also simultaneously operating as weak longitudinal actuators and applying feedback in that plane too. The commission of the BBB feedback system in the 1.5 GeV has not yet been started.

The 3 GeV ring has been delivering synchrotron light to users since November 2016, and it has been observed that both longitudinal and transverse Coupled-Bunch-Mode-Instabilities (CBMIs) have a degrading effect on the quality of the light if they are not suppressed.

STRIPLINE DESIGN

The feedback stripline design is based on the diagnostic stripline used for tune measurements [4], and the cross-section and the dimensions of the geometry can be seen in Figure 1 and in Table 1, respectively. The main difference to the design in [4] is that the feedback striplines only have two electrodes, each with a length of $L = 300$ mm (feedthrough-to-feedthrough). Each electrode has also two tapered sections of $L_t = 25$ mm. The tapered sections reduce the impedance mismatch between the electrodes and the coaxial feedthroughs, but they also suppress the beam impedance at higher frequencies as shown in [5]. The tapered sections can be seen in Figure 2. Both the vacuum chamber and the electrodes are made of stainless steel. The electrodes are welded to the inner conductors of the coaxial feedthroughs.

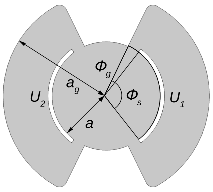

Figure 1: A transverse cross-section of the geometry.

Table 1: Parameters of the stripline geometry.

Parameter	
a	13.5 mm
a_g	25.2 mm
L	300 mm
L_t	25 mm
ϕ_s	107.20°
ϕ_g	12.75°

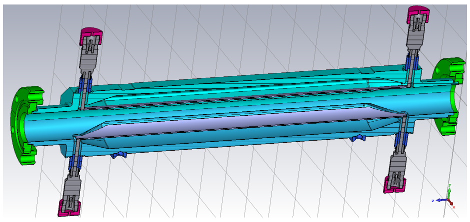

Figure 2: A cut-through of the stripline.

One can analytically obtain the electric scalar potential $\Phi(\rho, \phi)$ in the region $0 \leq \rho \leq a$ of the first propagating TEM modes by solving Laplace equation in 2D by using the methods presented in [6]. $\Phi(\rho, \phi)$ is given by (1), and the electric field is then obtained as $\mathbf{E}(\rho, \phi) = -\nabla\Phi(\rho, \phi)$. Here we assume that the electric field in the four gaps between the electrodes and the zero-potential chamber walls at $\rho = a$ is constant and purely azimuthal, thus $\mathbf{E}(a, \phi) = \pm \frac{U_1}{a\phi_g}\hat{\phi}$. The potential of the two electrodes (see Figure 1) for the odd and even mode are $U_1 = -U_2$ and $U_1 = U_2$, respectively. The odd mode is excited when driving the stripline in differential-mode and applying transverse feedback, while the even mode is excited when driving the stripline in common-mode and applying longitudinal feedback. Figure 3 shows $\Phi(\rho, \phi)$ ob-

---

[*] email: david.olsson@maxiv.lu.se

ISBN 978-3-95450-182-3

$$\Phi(\rho,\phi) = \frac{\phi_g+\phi_s}{2\pi}(U_1+U_2) + \frac{4}{\pi\phi_g}\sum_{n=1}^{\infty}\left(\frac{\rho}{a}\right)^n \frac{\sin\left(n\frac{\phi_g}{2}\right)\sin\left(n\frac{\phi_s+\phi_g}{2}\right)}{n^2}\left(U_1\cos(n\phi)+U_2\cos(n(\phi-\pi))\right) \quad (1)$$

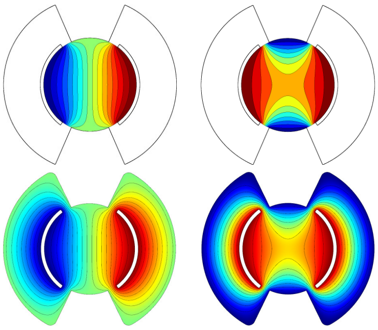

Figure 3: $\Phi(\rho,\phi)$ obtained analytically from (1) (upper), and numerically from COMSOL (lower). The left figures show the odd mode, and the right ones show the even mode.

tained from (1) and from electrostatic simulations in COMSOL Multiphysics [7].

The width of the two electrodes ϕ_s are optimized for on-axis field homogeneity when operating in differential mode, and a_g is set to obtain a characteristic impedance close to 50 Ω. The characteristic impedance of a single electrode when operating in differential and common-mode are $Z_{0,\perp} = 47.2\ \Omega$ and $Z_{0,||} = 52.9\ \Omega$, respectively, and they are chosen so that $\sqrt{Z_{0,\perp}Z_{0,||}} = 50\ \Omega$. The transverse and longitudinal shunt impedances, $R_\perp(\omega)$ and $R_{||}(\omega)$, of a stripline can be approximated as

$$R_\perp(\omega) = 2Z_{0,\perp}\left(\frac{g_\perp c_0}{a}\right)^2 \frac{\sin^2\left(\frac{\omega(L-L_t)}{c_0}\right)}{\omega^2}\frac{\sin^2\left(\frac{\omega L_t}{c_0}\right)}{\left(\frac{\omega L_t}{c_0}\right)^2} \quad (2)$$

$$R_{||}(\omega) = 2Z_{0,||}g_{||}^2\sin^2\left(\frac{\omega(L-L_t)}{c_0}\right)\frac{\sin^2\left(\frac{\omega L_t}{c_0}\right)}{\left(\frac{\omega L_t}{c_0}\right)^2} \quad (3)$$

where $g_\perp = a|\mathbf{E}(\rho=0)|/U_1 = 1.10$ and $g_{||} = \Phi(\rho=0)/U_1 = 0.67$ are the transverse and longitudinal geometry factors obtained for the odd and even mode, respectively as defined in [8]. $R_\perp(\omega)$ and $R_{||}(\omega)$ obtained analytically and from frequency domain simulations in COMSOL are shown in Figure 4.

Figure 5 - 6 show the differential ($S_{\mathrm{dd}x1}$) and common mode ($S_{\mathrm{cc}x1}$) S-parameters, respectively obtained from COMSOL and from measurements with a 4-port vector network analyser. In the mixed-mode measurements, the two physical downstream ports form the first logical port, while the two physical upstream ports form the second logical port.

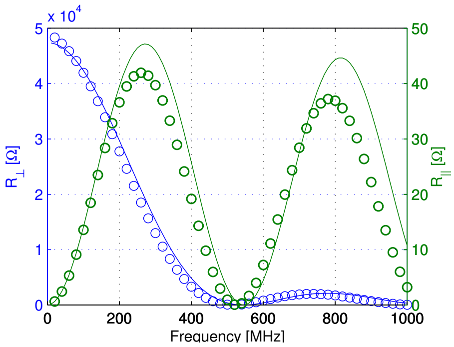

Figure 4: $R_\perp(\omega)$ and $R_{||}(\omega)$ obtained from (2)-(3) (solid lines) and from COMSOL (circles).

The dominant source for impedance mismatch and transmission losses are the ceramic feedthroughs. Note that three narrow-band notches are visible in the measured data above 4 GHz in Figure 5 but not in Figure 6. These are eigenmodes with dipole components (hence only excited in differential mode) that are trapped inside the structure.

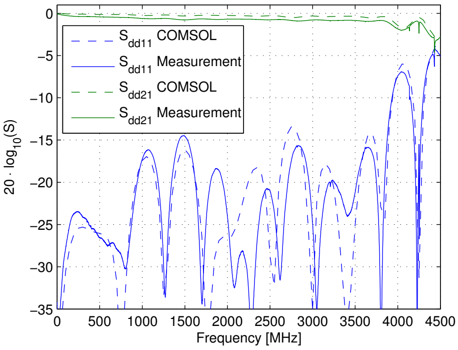

Figure 5: The measured and simulated differential-mode S-parameters.

The main ring RF system in MAX IV is operating at 100 MHz [9], so the span of the BBB feedback baseband signals is 0-50 MHz. Both striplines are simultaneously operating as weak longitudinal actuators. This is possible by feeding the longitudinal baseband signal, upconverted to the 150 MHz-250 MHz range, in common-mode to the electrodes. As seen

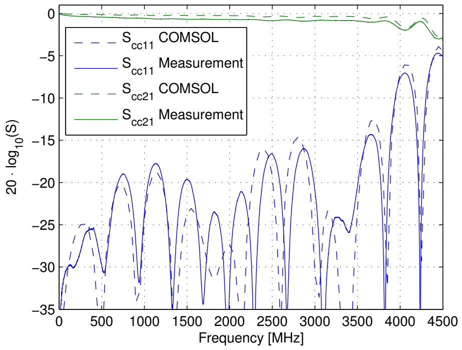

Figure 6: The measured and simulated common-mode S-parameters.

in Figure 4, $R_{||}(\omega)$ is quite low, and an overloaded cavity that will operate as a permanent longitudinal actuator is being constructed, and it will be installed in June 2017 [10]. Figure 7 shows a simplified circuit diagram of the upconverting back-end, where BB(x/y/z)(+/-) are the differential-mode baseband signals from the signal processors. The four output signals are fed to the four stripline electordes via broad-band R&S BBA150 drive amplifiers [11].

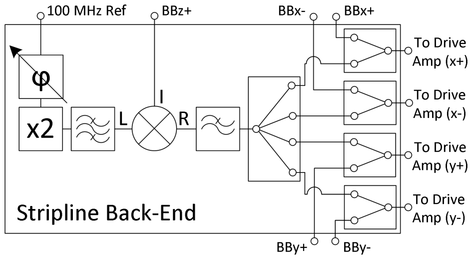

Figure 7: A simplified circuit diagram of the stripline back-end.

COUPLED-BUNCH INSTABILITIES IN THE 3 GeV RING

The longitudinal CBMIs in the 3 GeV ring are driven by Higher-Order Modes (HOMs) in the main and in the 3:rd harmonic (Landau) cavities, and it has been possible to suppress them with feedback at currents well above 100 mA this far even with the Landau cavities completely detuned (without any bunch lengthening). This was, however, only possible after mapping the dangerous HOMs in the cavities and by tuning their resonance frequencies away from the frequencies of the nearby coupled-bunch modes that are driving the instabilities. Figure 8 shows the longitudinal bunch profile measured with a sampling oscilloscope at the diagnostic beamline [12] with longitudinal feedback ON and OFF. The Landau cavities are here detuned, so the profile of the stable bunch is rather Gaussian. The much wider profile observed without feedback is mainly due to longitudinal dipole oscillations of the bunches and due to the fact that the sampling oscilloscope is unable to capture data from a single bunch at a single turn. The centroid of the unstable bunches are here oscillating with a magnitude of approximately ±200 ps which corresponds to ±7.2° relative to the 100 MHz RF system.

The observed CBMIs in the transverse plane have this far mainly been driven by ions, and the threshold where they appear has moved towards higher beam currents as the quality of the vacuum has improved. The transverse feedback voltage provided by the striplines has this far been more than enough to suppress them.

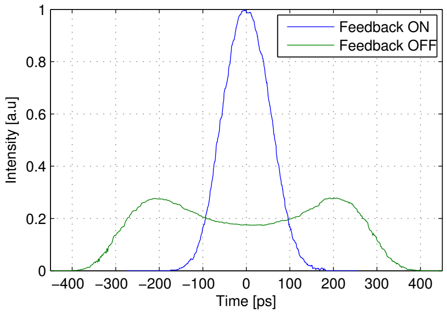

Figure 8: The longitudinal bunch profile measured at the diagnostic beamline at a beam current of 70 mA.

CONCLUSIONS AND FUTURE WORK

This far, the BBB feedback system has been able to suppress the transverse and longitudinal CBMIs in the 3 GeV ring at currents above 100 mA, and it has made it possible to deliver a stable beam to the first users at MAX IV. More powerful feedback can soon be applied in the longitudinal plane when the overloaded cavity is installed during the summer of 2017. Commissioning of the BBB feedback system in the 1.5 GeV ring will be carried out in the second half of 2017.

ACKNOWLEDGEMENTS

The authors would like to thank Åke Andersson, Francis Cullinan, Pedro Fernandes Tavares, and Jens Sundberg for their help during the measurements and during the commissioning of the BBB feedback system. Also big thanks to Dmitry Teytelman at Dimtel for all the support.

REFERENCES

[1] P. F. Tavares *et al.*, “The MAX IV storage ring project”, *Jour. of Synch. Rad.*, 21, pp. 862–877, 2014.

[2] S. Thorin *et al.*, “The MAX IV LINAC”, in *Proc. 27:th Linear Acc. Conf. (LINAC’14)*, Geneva, Switzerland, Sep. 2014, paper TUIOA03, pp. 400–403.

[3] Dimtel, `http://www.dimtel.com/`.

[4] D. Olsson, “Design of Stripline Kicker for Tune Measurements in the MAX IV 3 GeV Ring”, in *Proc. 34:th Progress in Electromagnetic Research Symp. (PIERS’13)*, Stockholm, Sweden, Aug. 2013, pp. 1095–1099.

[5] C. Belver-Aguilar *et al.*, “Stripline design for the extraction kicker of Compact Linear Collider damping rings”, *Phys. Rev. ST Acc. Beams*, 17, 071003, 2010.

[6] J. D. Jackson, in *Classical Electrodynamics Third Edition*, Chapter 2-3, John Wiley & Sons, 1998.

[7] COMSOL Multiphysics, `http://www.comsol.com/`.

[8] D. A. Goldberg and G. R. Lambertson, “Dynamic Devices A Primer on Pickups and Kickers”, in *AIP Conf. Proc. Series - Phys. of Part. Acc.*, 1992.

[9] Å. Andersson *et al.*, “The 100 MHz RF system for the MAX IV storage rings”, in *Proc. 2:nd Int. Part. Acc. Conf. (IPAC’11)*, San Sebastian, Spain, Sep. 2011, paper MOPC05, pp. 193–195.

[10] D. Olsson *et al.*, “A Waveguide Overloaded Cavity Kicker for the MAX IV Bunch-by-Bunch Feedback System", in *Proc. 8:th Int. Part. Acc. Conf. (IPAC’17)*, Copenhagen, Denmark, May. 2017, paper THPIK087.

[11] Rohde & Schwarz, `http://www.rohde-schwarz.com`.

[12] J. Breunlin *et al.*, “Emittance diagnostics at the MAX IV 3 GeV storage ring”, in *Proc. 7:th Int. Part. Acc. Conf. (IPAC’16)*, Busan, Korea, May. 2016, paper WEPOW034, pp. 2908–2910.

Paper VI

A Waveguide Overloaded Cavity Kicker for the MAX IV Bunch-by-Bunch Feedback System

D. Olsson, L. Malmgren and K. Åhnberg.

pp THPIK087 (2017) *Proceedings of IPAC17, Copenhagen, Denmark.*

A WAVEGUIDE OVERLOADED CAVITY KICKER FOR THE MAX IV BUNCH-BY-BUNCH FEEDBACK SYSTEM

D. Olsson[*], L. Malmgren, K. Åhnberg
MAX IV Laboratory, Lund, Sweden

Abstract

The Higher-Order Modes (HOMs) in the main and the 3:rd harmonic cavities are driving longitudinal Coupled-Bunch Mode Instabilities (CBMIs) in the MAX IV 3 GeV storage ring. This far, negative feedback has been applied in the longitudinal plane by two stripline kickers. However, the maximum longitudinal feedback voltage provided by the striplines is rather weak, and a Waveguide (WG) overload cavity was therefore designed. Due to the long bunch length in the MAX IV storage rings, a relatively low center frequency of 625 MHz is selected. The new cavity kicker is being manufactured, and will be installed in the 3 GeV ring in June 2017. In this paper, the RF and mechanical design of the cavity is presented.

INTRODUCTION

The MAX IV facility in Lund, Sweden consists of two storage rings for production of synchrotron radiation, and a Short-Pulse-Facility (SPF) [1]. The two rings are designed for 3 GeV and 1.5 GeV, respectively, where the initial beam commissioning of the former has recently been completed, and commissioning of the latter was started in September 2016. Both rings will be operating with top-up injections delivered by a full-energy injector [2].

The 3 GeV ring is operating with a Bunch-By-Bunch (BBB) feedback system, where the signal processors are delivered by Dimtel [3]. In this ring, there is one horizontal and one vertical stripline installed, and they are dedicated as actuators for feedback in the transverse plane. At the moment, the two striplines are simultaneously operating as longitudinal actuators as well, as described in [4]. However, the longitudinal voltage provided by the striplines is rather weak, and a WG overloaded cavity based on the original DAΦNE design [5] that is dedicated for longitudinal feedback has therefore been designed. The new cavity will be installed in the 3 GeV ring in June 2017.

The commissioning of the BBB feedback system in the 1.5 GeV ring will start in the second half of 2017.

KICKER REQUIREMENTS

The first step when designing the cavity is to determine its center frequency f_c and its Bandwidth (BW). The minimum required BW in order to suppress all CBMIs is $f_{\mathrm{RF}}/2 = 50$ MHz if f_c is chosen so that $f_c = f_{\mathrm{RF}}(1/4 + n/2)$, $n \in \mathbb{N}$. $f_{\mathrm{RF}} = 100$ MHz is the operating frequency of the MAX IV ring RF system. f_c in similar cavities might vary between 900 MHz [6] and 1900 MHz [7], and is often carefully chosen and optimized for the conditions at the facility where it is installed. Choosing a high f_c has several advantages such as a more compact cavity and a higher achievable shunt impedance, $R_{||}$. Another advantage with a higher f_c is that all the potentially harmful HOMs are shifted upwards in frequency as well. The shunt impedance is defined as $R_{||} = |V_{||}|^2/2P_{\mathrm{rms}}$, where P_{rms} is the rms power supplied to the cavity by the amplifiers. The voltage gain, $V_{||}$, is defined as

$$V_{||} = \int_{-L}^{L} |E_z(z)| e^{j(kz+\varphi)} \mathrm{d}z \qquad (1)$$

where $E_z(z)$ is the on-axis longitudinal electrical field, $k = \omega/c_0$ is the wave number, $2L \rightarrow \infty$ is the integration length, and φ is an arbitrary phase.

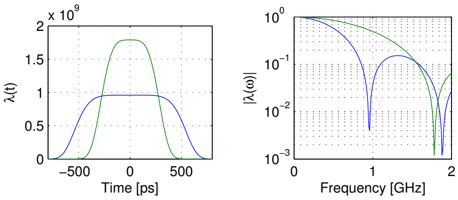

(a) (b)

Figure 1: (a) shows the normalized longitudinal profile of a bunch in time domain, $\lambda(t)$, and (b) shows the same profile in frequency domain, $|\lambda(\omega)|$. The green curves are for a double (100 MHz + 300 MHz) and the blue curves are for a triple (100 MHz + 300 MHz + 500 MHz) RF system during ideal bunch lengthening.

When selecting f_c, one also has to consider the long ring bunches at MAX IV. Currently, both rings have double RF systems with passive 3:rd harmonic (Landau) cavities for bunch lengthening. There are also future plans to operate with a triple RF system in the 3 GeV ring in order to increase the bunch lengthening further by adding 5:th harmonic cavities as well. If the filling pattern is uniform, each bunch has a normalized longitudinal profile in time domain, $\lambda(t)$, so that $\int \lambda(t)\mathrm{d}t = 1$. $\lambda(\omega)$ is the same bunch profile in frequency domain, and $\lambda_z(z)$ is the normalized spatial profile where $c_0\lambda_z(c_0 t) = \lambda(t)$. Figure 1 shows $\lambda(t)$ and $\lambda(\omega)$ during ideal bunch lengthening with a double and a triple RF system. If f_c is too high, the head of the bunch obtains a kick with a different direction compared to its tail, and the net kick over the bunch can be zero in a worst-case scenario. The average voltage gain over the normalized electron bunch V_{avg} is

---

[*] email: david.olsson@maxiv.lu.se

$$
\begin{aligned}
V_{\text{avg}} &= \int_{-L}^{L} \lambda_z(z') \left\{ \int_{-L}^{L} |E_z(z)| e^{j(k(z-z')+\varphi)} \mathrm{d}z \right\} \mathrm{d}z' \\
&= V_{||} \int_{-L/c_0}^{L/c_0} \lambda_z(c_0 t') e^{-j\omega t'} c_0 \mathrm{d}t' = \lambda(\omega) V_{||} \qquad (2)
\end{aligned}
$$

As seen in Figure 1 (b), f_c must be relatively low in order to keep a high kick efficiency. A good compromise between a compact cavity geometry and fairly high V_{avg} is to set f_c = 625 MHz. Here, $|\lambda(\omega)|$ is 0.77 and 0.40 for a double and a triple RF system, respectively.

CAVITY DESIGN

A simple pillbox cavity with f_c = 625 MHz would have a radius of 184 mm. However, it was decided to decrease the cavity radius so that a standard steel pipe with an inner radius of 100 mm can be used as the cavity lateral surface. f_c is therefore shifted downwards with a coaxial loaded structure with long nose cones. The nose cones also increase the geometry factor, $R_{||}/Q$, due to field focusing. Initially, the optimization of the 2D rotation-symmetrical unloaded cavity volume was performed in a MATLAB [8] with livelink to COMSOL [9]. Here, $R_{||}/Q$ was optimized for the fundamental mode while it was kept as low as possible for the first rotation-symmetrical HOMs. Four ridged WGs are added to the unloaded cavity, and they are optimized to achieve the necessary BW of the fundamental mode, but also to damp unwanted HOMs.

Figure 2 shows a 3D model of the assembled cavity. The nose cones and the ridged WGs are milled into two copper bodies. Each copper body is braced to a steel flange and then attached to the flanges that are welded to the outer steel pipe. In order to improve the vacuum in the vicinity of the cavity, an ion pump is added to the design, where the pumping occur via grids on the outer pipe (see Figure 2). The grids are parallel to the surface currents, $\mathbf{J} = \hat{\mathbf{n}} \times \mathbf{H}$, on the cavity inner lateral surface of the fundamental mode, and their presence has a neglectable effect on the cavity performance.

Proper electrical contact between the outer tube and the copper bodies are provided by contact springs as in the ELSA design [10], where the springs are placed in grooves in the copper body. Contact between the inner conductor of the coaxial feedthrough and the copper body is provided by gold plated socket connectors that are screwed to the latter as seen in Figure 2. These socket connectors are the same type as the female inner pin at the N-type connector of the feedthroughs.

SIMULATIONS

As mentioned above, the first step was to optimize the unloaded cavity, and $R_{||}/Q$ of the rotation-symmetrical eigenmodes up to 4.5 GHz can be seen in Figure 3. $R_{||}/Q = 162\,\Omega$ for the fundamental mode.

In order to reduce the requirements on mechanical tolerances and to improve the gain flatness, a somewhat larger −3 dB BW of 70 MHz (590 MHz - 660 MHz) was chosen.

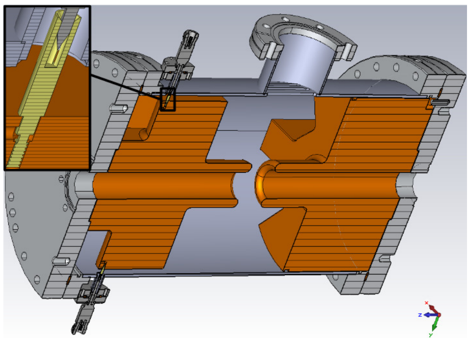

Figure 2: A 3D model of the cavity. The socket connector can be seen in the zoomed area.

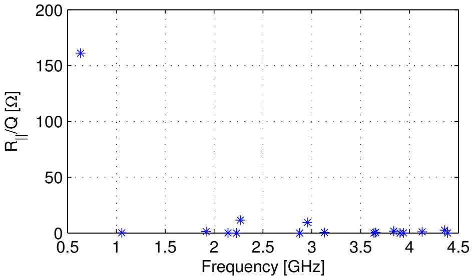

Figure 3: The simulated values of $R_{||}/Q$ for the rotation-symmetrical eigenmodes of the unloaded cavity up to 4.5 GHz.

Figure 4 shows the simulated common-mode S-parameters when the four WGs have been added. Here, the two physical downstream ports form the first logical port, while the two physical upstream ports form the second logical port. As seen, f_c has been shifted slightly downwards in frequency in order to keep the desired BW. Figure 5 shows $R_{||}(\omega)$ obtained in COMSOL. $R_{||}(\omega)$ decreases more rapidly at higher frequencies which is mainly because the transit time factor decreases with frequency.

Figure 6 shows the real part of the longitudinal beam impedance, $\Re(Z_{||}(\omega))$, obtained in GdfidL [11]. As seen, the WGs are effectively damping the HOMs up to ≈ 3 GHz. At higher frequencies, the eigenmodes are more narrow-banded up to ≈ 8 GHz where the broadband region starts due to the TM_{01} cut-off frequency of the beam pipe. For optimum bunch lengthening with the double RF system, the power lost in the structure by the beam is ≈ 460 W when the filling pattern is uniform at a beam current of 500 mA. Because of the narrow bunch spectrum in Figure 1 (b), almost all power lost by the beam is induced in the fundamental mode, and it is dissipating in the external coaxial terminations, and not in the cavity itself. Since the loaded quality factor, $Q_L = 8.9$, of the fundamental mode is very low, contributions from coherent multi-turn wakefield superposition are neglectable.

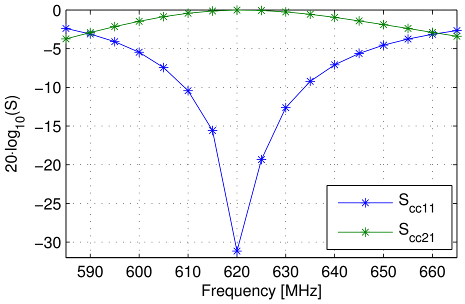

Figure 4: The simulated common-mode S-parameters of the cavity.

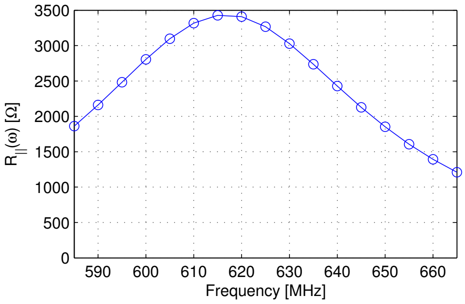

Figure 5: The longitudinal shunt impedance $R_{||}(\omega)$ obtained in COMSOL.

CONCLUSIONS AND FUTURE WORK

This far, the longitudinal BBB feedback in the MAX IV 3 GeV ring has been provided by two striplines. However, the striplines are very weak longitudinal actuators, and in order to increase the kick voltage, a waveguide overloaded cavity has been designed and is being constructed. Due to the long bunches at MAX IV, a relatively low cavity center frequency of 625 MHz was chosen in order to keep a high kick efficiency. The cavity will be installed in June 2017.

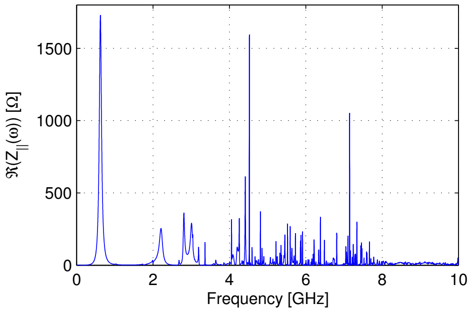

Figure 6: The longitudinal beam impedance $\Re(Z_{||}(\omega))$ obtained in GdfidL.

ACKNOWLEDGMENTS

The authors would like to thank Henrique de Oliveira Caiafa Duarte and Sergio Rodrigo Marques at LNLS, Nikolas Heurich at ELSA, and Alun Morgan at Diamond for sharing ideas on the mechanical design. A special thanks to Eshraq Al Dmour, Marek Grabski, and Esa Paju in the vacuum group for the support and expertise in the design and assembly phase.

REFERENCES

[1] P. F. Tavares *et al.*, "The MAX IV storage ring project", *Jour. of Synch. Rad.*, 21, pp. 862–877, 2014.

[2] S. Thorin *et al.*, "The MAX IV LINAC", in *Proc. 27:th Linear Acc. Conf. (LINAC'14)*, Geneva, Switzerland, Sep. 2014, paper TUIOA03, pp. 400–403.

[3] Dimtel, `http://www.dimtel.com/`.

[4] D. Olsson *et al.*, "Design and Implementation of Stripline Feedback Kickers in the MAX IV 3 GeV Ring ", in *Proc. 8:th Int. Part. Acc. Conf. (IPAC'17)*, Copenhagen, Denmark, May. 2017, paper THPIK086

[5] R. Boni *et al.*, "A waveguide overloaded cavity as longitudinal kicker for the DAΦNE bunch-by-bunch feedback system", in *Part. Acc*, 52, pp. 95–113, 1996.

[6] W. Z. Wu *et al.*, "Development and commissioning of bunch-by-bunch longitudinal feedback system for Duke storage ring", in *Proc. 23:rd Part. Acc. Conf. (PAC'09)*, Vancouver, Canada, May. 2009, paper TH6REP070, pp 4117–4119.

[7] A. F. D. Morgan *et al.*, "Design for the Diamond Longitudinal Bunch-by-Bunch Feedback Cavity", in *Proc. 23:rd Int. Beam Inst. Conf. (IBIC'16)*, Barcelona, Spain, Sep. 2016, paper TUPG12.

[8] MATLAB, `http://www.mathworks.com/`

[9] COMSOL Multiphysics, `http://www.comsol.com/`

[10] N. Heurich *et al.*, "A longitudinal kicker cavity for a bunch-by-bunch feedback system at ELSA", in *Proc. 2:nd Int. Part. Acc. Conf. (IPAC'14)*, San Sebastian, Spain, Sep. 2011, paper MOPO004, pp. 484–486.

[11] GdfidL, `http://www.gdfidl.de/`

Paper VII

Design of Striplines for the MAX IV and SOLARIS Storage Rings

D. Olsson, A. Karlsson and L. Malmgren.

LUTEDX/(TEAT-7254)/(2017) *Technical Report, Department of Electromagnetic Theory, Lund University.*

CODEN:LUTEDX/(TEAT-7254)/1-60/(2017)

Design of Striplines for the MAX IV and SOLARIS Storage Rings

David Olsson, Lars Malmgren, and Anders Karlsson

Electromagnetic Theory
Department of Electrical and Information Technology
Lund University
Sweden

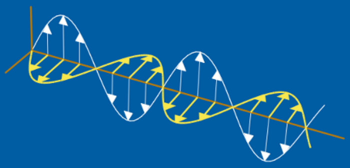

(TEAT-7254)/1-60/(2017): D. Olsson *et al.*, Design of Striplines for the MAX IV and SOLARIS Storage Rings

David Olsson
david.olsson@maxiv.lu.se

MAX IV Laboratory
Lund University
P.O. Box 118
SE-221 00 Lund
Sweden

Lars Malmgren
lars.malmgren@maxiv.lu.se

MAX IV Laboratory
Lund University
P.O. Box 118
SE-221 00 Lund
Sweden

Anders Karlsson
anders.karlsson@eit.lth.se

Department of Electrical and Information Technology
Electromagnetic Theory
Lund University
P.O. Box 118
SE-221 00 Lund
Sweden

This is an author produced preprint version as part of a technical report series from the Electromagnetic Theory group at Lund University, Sweden. Homepage `http://www.eit.lth.se/teat`

Editor: Mats Gustafsson

Abstract

MAX IV and SOLARIS are two synchrotron light sources located in Lund and in Krakow, respectively. A stripline is a standard multi-purpose component that is used in many accelerators and consists of one or multiple electrodes. The currents that are induced by the Lorentz contracted fields of the electron beam at the electrodes can be used for beam diagnostics, or one can excite the electrodes in order to manipulate the properties of the beam. The design and initial measurements of the MAX IV/SOLARIS striplines are presented in this report. Different design considerations and possible applications for the striplines are also presented.

Contents

1 Introduction

The MAX IV facility is a national Swedish research facility located in Brunnshög outside Lund [12]. The facility consists of two electron storage rings that are operated at 3 GeV and 1.5 GeV [20], respectively, where the former is optimized for production of high-brilliance hard X-ray synchrotron light, and the latter will produce light in the IR to the soft X-ray spectral range. The rings will be operated with *top-up injections* where the electron losses are compensated by injections at short intervals. The full-energy injector consists of a 39 S-band LINAC structures [21], and will also operate as a driver for a Short Pulse Facility (SPF) where X-ray pulses with durations down to tens of fs are produced. The LINAC might also be the driver for a future Free Electron Laser (FEL) [3], and in this case it is likely that more LINAC structures are added in order to reach higher energies. The 3 GeV ring has recently started delivering light to the first users, while the 1.5 ring is under beam commissioning.

The SOLARIS Synchrotron is a national Polish research facility located in Krakow, and consists of an injector and a storage ring [19]. The storage ring is basically a replica of the MAX IV 1.5 GeV ring. One key difference compared to MAX IV is that the SOLARIS injector has an energy gain of 550 MeV, and the electrons are therefore injected and stored at this energy before the beam energy is increased by the accelerating cavities, and by synchronously increasing the magnetic fields. This process is known as *ramp-up*.

The design parameters of the MAX IV and SOLARIS storage rings are listed in Table 1, and these parameters will be further explained in the following sections. However, the focus in this report is on the design and measurements of the stripline, and its related RF components, that are installed in the MAX IV 3 GeV ring.

Several diagnostic devices are needed for the operation of an electron storage ring. In this paper we describe a stripline can be used for two different types of

Parameter	3 GeV Ring (MAX IV)	1.5 GeV Ring (MAX IV / SOLARIS)
Beam energy	3.0 GeV	1.5 GeV
Maximum beam current	500 mA	500 mA
RMS bunch length	56 mm	56 mm
Main radio frequency	99.931 MHz	99.931 MHz
Harmonic number	176	32
Ring circumference	528 m	96 m
Betatron tune (horizontal/vertical)	42.20/16.28	11.22/3.15
BPM pick-up frequency	500 MHz	500 MHz

Table 1: The design parameters of the MAX IV and SOLARIS storage rings.

beam diagnostics. It can act as a passive device that monitors the longitudinal and transverse motion of the beam. It can also be an active device that excites the beam and by that makes it possible to measure several parameters of the accelerator. Aside from being used as a purely diagnostic device, a stripline can also be used to excite the beam in a way that gives it properties that some users would benefit from or to damp unwanted beam oscillations that are driven by instabilities.

In Section 2, different applications for the stripline are listed. Here, a brief review of the transverse beam dynamics in a circular accelerator is also given. The geometry and manufacturing method of the stripline vacuum chamber is presented in Section 3. An analysis of the transmission line properties and the electromagnetic fields inside the chamber are presented in Section 4. The ability of the stripline to kick the beam and to monitor the motion of the beam are discussed in Section 5 and 6, respectively. When a charged beam propagates inside a vacuum chamber it induces mirror currents on the walls of the chamber. These mirror current generate electromagnetic fields which act back on the beam itself. Such phenomena are known as *collective effects* and are further described in Section 7. In Section 8 the scattering parameters of the manufactured stripline are presented. The design and measurements of an RF distribution network that is feeding the stripline, and an RF receiving network that is monitoring the beam motion are presented in Section 9. Finally, some initial measurements from the commissioning of the MAX IV 3 GeV ring are presented in Section 10 where the beam is excited using the stripline.

2 Applications for the Stripline

A stripline is a multi-purpose tool that can both excite and monitor the electron beam. In this section three possible applications of the stripline are listed.

2.1 Tune measurements

The main purpose of the stripline is to excite the beam during measurements of the betatron tunes. Here, a brief review is given on transverse beam dynamics in a circular accelerator, and it is shown why monitoring the transverse beam motion provides valuable information about the status of the accelerator.

2.1.1 Transverse Beam Dynamics in a Circular Accelerator

In order to understand the concept tune measurements, one has to understand the basic principles of transverse beam dynamics. In this report, only a brief review is given on the subject. For further reading, [22] and [23] are recommended.

The ideal orbit of a particle with a nominal energy in a circular accelerator is defined by the magnet layout (the *lattice*). The trajectory of a single particle that moves in the vicinity of the orbit can be described by using a co-moving cartesian coordinate system $K(x, y, s)$ whose origin moves along the orbit with the longitudinal position s. $x(s)$ and $y(s)$ are the horizontal and vertical displacement at the longitudinal position s, respectively. For a particle with nominal energy $x(s)$ satisfies Hill's differential equation

$$\frac{\mathrm{d}^2 x(s)}{\mathrm{d}s^2} + k(s)x(s) = 0 \tag{2.1}$$

where $k(s)$ is an L periodic focusing function determined mainly by the quadrupole magnets, and L is the circumference of the ring. The solution to (2.1) is the horizontal oscillating function around the ideal orbit known as the *betatron oscillation*

$$x(s) = \sqrt{\epsilon_x \beta_x(s)} \cos(\psi_x(s) + \varphi_x) \tag{2.2}$$

$$\psi_x(s) = \int_0^s \frac{\mathrm{d}s'}{\beta_x(s')} \tag{2.3}$$

where ϵ_x is the *emittance*, $\beta_x(s)$ is the *beta function*, $\psi_x(s)$ is the *phase advance function*, and φ_x is a constant. Analogously, the vertical displacement from the ideal orbit is given by $y(s) = \sqrt{\epsilon_y \beta_y(s)} \cos(\psi_y(s) + \varphi_y)$. The number of (horizontal/vertical) betatron oscillations performed by a particle travelling once around the ring is called the *betatron tune*, $Q_{x/y}$, and is given by

$$Q_{x/y} = \frac{1}{2\pi} \int_s^{s+L} \frac{\mathrm{d}s'}{\beta_{x/y}(s')} \tag{2.4}$$

There is a chance of resonance growth of the betatron oscillations if Q_x or Q_y are integers or simple fractions. These instabilities are known as *optical resonances*, and they may even result in beam loss. However, it is not sufficient to choose Q_x and Q_y individually so that they are not integers or simple fractions since the field strength in one plane depends on the displacement in the other plane for multipole fields of higher order. A coupled optical resonance has the order $|m| + |n|$, with the resonance condition $mQ_x + nQ_y = p,\ \{m, n, p\} \in \mathbb{Z}$. Generally, the strength of an optical resonance decreases with its order. As seen in Table 1, the optical resonances of the operation points have the order 5 ($m = \pm 5,\ n = 0$) in the 3 GeV ring, and order 11 ($m = \pm 5,\ n = \pm 6$) in the two 1.5 GeV rings. This pair of values for Q_x and Q_y is called the *working point* of the machine.

The amplitude function $\sqrt{\epsilon_x \beta_x(s)}$ in (2.2) is called the horizontal *beam envelope*. A single particle might have different displacement from its ideal orbit when passing the same longitudinal position in a storage ring. However, the magnitude of this displacement is never greater than the beam envelope, as seen in (2.2). The beta function is determined by the lattice. In (2.2), ϵ_x is a single particle constant of motion, and $\pi\epsilon_x$ is the area of the ellipse of particle motion in the x-x' phase space, where $x' = \mathrm{d}x/\,\mathrm{d}s$. However, a beam consists of many particles oscillating with different amplitudes. One can show that the transverse distributions of an electron beam in a storage ring are nearly Gaussian distributions with rms beam sizes σ_x and σ_y. It is therefore more customary to define ϵ_x as the emittance corresponding to the emittance of electrons travelling at exactly one STD, σ_x, from the ideal orbit. By doing so, the amplitude function $\sqrt{\epsilon_x \beta_x(s)} = \sigma_x(s)$ can be referred to as the horizontal rms *beam size* at the longitudinal position s. ϵ_x can be seen as the horizontal "temperature" of the beam.

2.1.2 Obtaining the Tunes

When operating the machine, it is vital to monitor its betatron tunes and to confirm that it is operating far away from any strong optical resonances. Deviations from the working point might imply misaligned magnets or drift in the magnet power supplies.

Consider a single particle with charge q that is propagating with velocity v on the design orbit in a circular machine. The charge density $\lambda(t)$ of the particle can be described as a Fourier series of the revolution frequency ω_0

$$\lambda(t) = \frac{q}{v} \sum_{n=-\infty}^{\infty} \delta(t - nT_0) = \frac{q}{L} \sum_{n=-\infty}^{\infty} \cos(n\omega_0 t) \tag{2.5}$$

where T_0 is the revolution period. The transverse dipole moment $d(t)$ of the particle is defined as the product of its charge and its transverse displacement from the orbit, thus the horizontal displacement becomes $d(t) = q \cdot x(t)$. From here on, the horizontal/vertical indices of the parameters listed above are dropped since it should be obvious from the content which index to use. The horizontal displacement of the particle is $x(t) = x_0 + \hat{x}\cos(Q\omega_0 t)$, where x_0 is a constant offset due to a closed orbit distortion. Here, a smooth approximation is applied on the phase advance function in (2.3) where $\psi(s) \approx \frac{2\pi Q}{L} s$. One can measure the displacement at a single point in the machine with, for example, a standard button BPM by combining the signals from two opposite located buttons with a 180° hybrid combiner (see Figure 1). By using this set-up, the obtained signal is proportional to the dipole moment of the particle (higher multipole components are discarded in the analysis). Note that a misalignment of the BPM device results in an additional component to the offset of the measured signal, similar to x_0. However, the measured offset can be rejected by calibration, and by dropping this term the dipole density becomes

$$d(t) = \frac{q\hat{x}}{L} \sum_{n=-\infty}^{\infty} \cos((n+Q)\omega_0 t) = \frac{q\hat{x}}{L} \left(\cos(Q_f \omega_0 t) + \sum_{n=1}^{\infty} \cos((n \pm Q_f)\omega_0 t) \right) \quad (2.6)$$

where Q_f is the fractional part of Q. Apart from the first term in (2.6) at $Q_f \omega_0$, the spectrum consist of frequency components separated $\pm Q_f \omega_0$ from each harmonic of ω_0. The integer part of Q in the measured signal is however lost which is known as the *stroboscope effect.* One method of measuring the integer part is to perform a position measurement along the machine with the offsets at each BPM rejected by calibration. A small dipole field is then applied somewhere in the machine which results in a a small closed orbit distortion, and the number of betatron oscillations per turn can then be counted by taking the difference between the new orbit and the calibrated orbit.

A particle in a circular machine also performs a longitudinal oscillation, or a *synchrotron oscillation*, due to the gradient of the fields in the accelerating cavities when the particle is accelerated off-crest. This is known as *phase focusing*, and the oscillation occurs around the nominal phase (relative to the phase of the accelerating fields) of an ideal particle known as the the *synchronous phase.* Due to the synchrotron oscillation, the particle receives a different momentum gain every turn when it passes the accelerating cavities. Note that the momentum gain per turn is equal to the momentum loss per turn when the phase of the particle is equal to the synchronous phase. The momentum deviation from the nominal momentum p_0 results in a deviations from the nominal revolution period $T_0 = 2\pi/\omega_0$ which relation is

$$\frac{\mathrm{d}T}{T_0} = \eta_c \frac{\mathrm{d}p}{p_0} \quad (2.7)$$

where η_c is the *phase slip factor.* The momentum deviation also causes a shift in the betatron tune since the L-periodic focusing function $k(s)$ in (2.1) has a different magnitude for a particle with an non-nominal momentum. This tune shift is described by the *chromaticity* of the lattice, and given by

$$\xi = \frac{\mathrm{d}Q/Q_0}{\mathrm{d}p/p_0} \quad (2.8)$$

where Q_0 is the nominal betatron tune.

When including the phase focusing into the transverse spectrum, the dipole moment of a single particle can be written as in (2.9), where J_m is the Bessel function of the first kind with index m, Ω_s is the angular frequency of the synchrotron oscillation, φ is a phase constant, and τ_s is the maximum amplitude of the oscillation of the revolution time [18].

$$d(t) = \frac{q\hat{x}}{L} \sum_{n=-\infty}^{\infty} \sum_{m=-\infty}^{\infty} j^{-m} J_m \left(\left(n + Q - \frac{\xi Q}{\eta_c} \right) \omega_0 \tau_s \right) e^{jm\varphi} e^{j((n+Q)\omega_0 + m\Omega_s)t} \quad (2.9)$$

As seen in (2.9), there is an infinite number of synchrotron satellites at $\pm m\Omega_s$ around the betatron lines that were found in (2.6). All these spectral lines are also amplitude and phase modulated. There will be a momentum spread among the electrons in the beam which results in a spread in their betatron tunes and their revolution frequencies. The spectral lines in (2.9) are therefore smeared out in a signal from a real electron beam. Transverse wakefields (see Section 7) result in a shift of the betatron tunes, which means that the position of the spectral lines also depends on the total stored current. Measurements of the beam spectrum are presented in Section 10.

Since the individual electrons also oscillate with different phases, they all perform betatron oscillations around the ideal orbit incoherently. Therefore, in order to measure the betatron tunes one has to excite the beam so that the electrons perform transverse oscillations coherently. This excitation can be made by applying an external driving force to the beam (via for example the stripline), or the beam can be excited by itself due to an instability. The latter case is undesired, and will not be considered in this report. In the 3 GeV ring, three different methods of exciting transverse oscillations and measuring the betatron tunes are implemented.

The first method includes the stripline which excites the beam when it is swept with a sinusoidal signal. The transverse beam position is then monitored by a button BPM where the differential signals between opposite located buttons are measured. Figure 1 shows a simplified illustration of the measurement set-up. A more detailed overview of the RF distribution in the measurement set-up is presented in Section 9. The frequency of the exciting signal is generated by the tracking generator of a spectrum analyzer, and the differential signal at the BPM is monitored by the same instrument. Coherent transverse oscillations are excited when the frequency of the tracking generator is close to the frequency components of the Fourier series in (2.9), and are therefore displayed as spectrum lines by the spectrum analyzer.

In the second method, the beam is excited by a fast transverse kick which has a duration that is less than the revolution period of a bunch. For this purpose, fast pinger magnets are installed in the rings that can kick the beam both in the horizontal and vertical plane. The beam position is then measured at the positions of the button BPMs along the ring. This method is not as accurate as the first method.

A third method is to use the bunch-by-bunch feedback system. Here, an external excitation signal is swept in the vicinity of the betatron frequency (just as in the first method), and the beam spectrum is then obtained as an FFT of the signal from a single button BPM. The bunch-by-bunch feedback system is described in [16].

2.2 Pick-up Device

The stripline will intercept fractions of the mirror current induced by the electron beam. This results in induced signals at the stipline ports which can be used for estimating the total charge, the transverse and longitudinal motion, and the charge distribution of each ring bucket. Even though the storage ring already has several diagnostics tools such as capacitive buttons (button BPMs), current transformers,

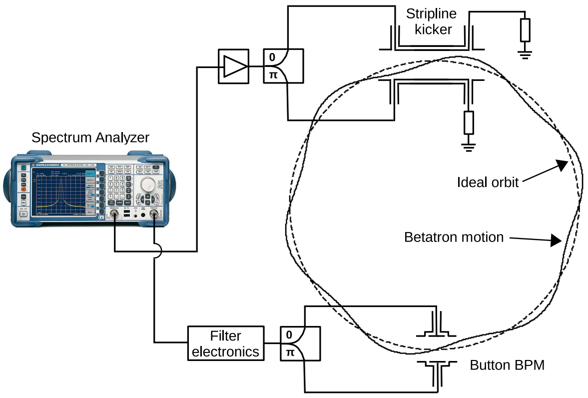

Figure 1: A simplified block diagram that shows the set-up of the betatron tune measurements in FD.

and diagnostic beam lines for these type measurements, the stripline can be used as a complementary pick-up device. The pick-up characteristics of the stripline is investigated in Section 6.

2.3 Feedback Kicker

There are bunch-by-bunch feedback systems installed in both MAX IV storage rings [16]. At the moment, there are no dedicated feedback kickers installed in the 1.5 GeV ring. The stripline that is installed in this ring will therefore operate as a temporary feedback kicker in all three planes when the commissioning of the feedback system starts in this ring during the autumn of 2017.

3 Stripline Geometry

The stripline vacuum chamber consists of a main body, four stripline electrodes, 8 coaxial feedthroughs, and connectors needed for water cooling. A 3D CAD model of the stripline can be seen in Figure 2, and Figure 4 shows the strips and the inner boundaries of the main body in the xy-plane.

Four stripline electrodes are needed since the design target is to construct a device that is able to excite the beam in both transverse planes independently of each other. The stripline electrodes are hereby referred to as "strips", and the complete component is referred to as the "stripline" in this report. The main body and the strips are made of 316LN and 316L, respectively, that are two stainless steel alloys. As seen in Figure 4, tracks are milled in the main body, and the strips are placed inside the cavities. The reason for doing so is to minimize the discontinuity of the inner chamber walls since a beam that passes such discontinuities induces EM fields that act back on the beam itself which might result in instabilities. More on that in Section 7. The strips are rotated 45 degrees relative to the two transverse planes in order to protect them from synchrotron radiation that is emitted from an upstream dipole magnet. If the synchrotron radiation would hit one of the strips, it becomes heated, and since it is a thin component that is difficult to cool, it might become damaged. Bursts of radiation that hit the strip would also induce noise in the measured signal if the stripline is used as a pick-up device. With the rotation of 45 degrees, the synchrotron radiation hits the main body instead which is the reason why it is cooled by water (see Figure 2). The coaxial feedthroughs that provide the electrical contact between the external feeding network and the strips have N-type connectors and ceramic vacuum insulators. The outer connectors of the feedthroughs are welded to the main body, and the inner conductors are welded to the strips. In order to connect the stripline to the neighboring vacuum chambers, two CF flanges are attached to the upstream and downstream ends of the main body.

In Figure 4, $a = 14.00$ mm, $a_g = 19.04$ mm, $\phi_s = 45.00$ degrees, and $\phi_g = 8.19$ degrees. The length of each strip L is 150 mm (measured between its two welding points to the feedthroughs). The total length of the stripline is 250 mm (flange-to-flange). The dimensions chosen for the stripline are further explained in the following sections.

A total number of four striplines are manufactured; one for each ring in MAX IV and SOLARIS, and one unit is kept as a spare part. One of the completed striplines is shown in Figure 3.

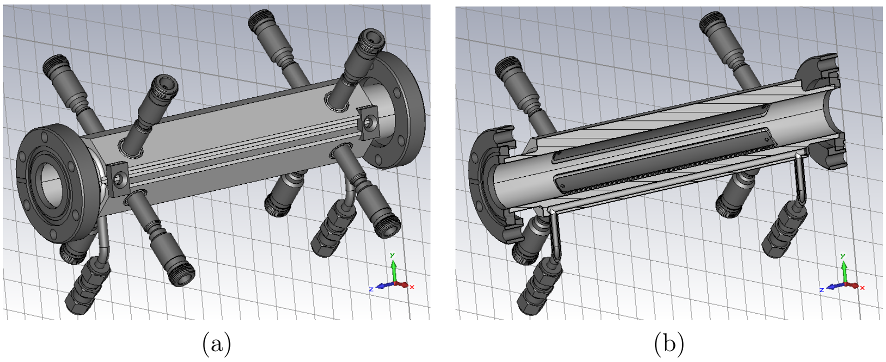

(a)

(b)

Figure 2: The CAD model of the stripline, where (a) shows the complete model and (b) shows a cut through in the yz-plane. Note the water cooling channel at the bottom of the main body in (b).

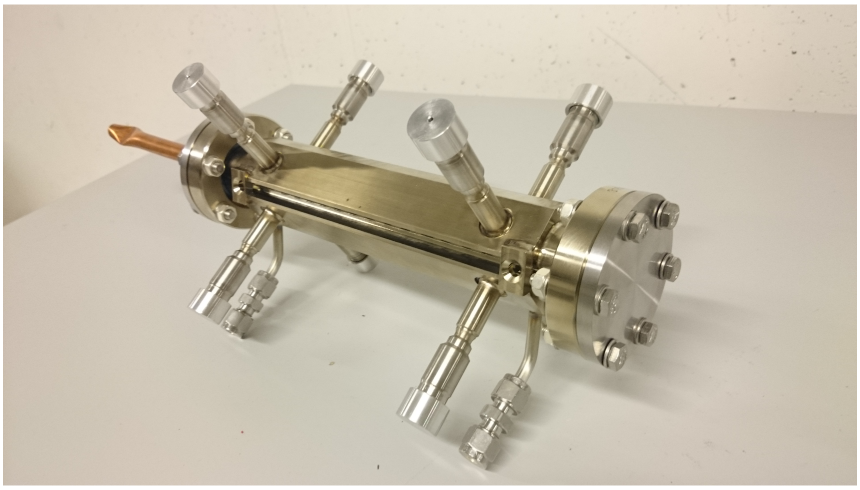

Figure 3: One of the four manufactured striplines.

4 Field and Transmission Line Analysis

The main purpose of the stripline is to excite the beam in the transverse plane. One should be able perform these transverse excitations in the horizontal and vertical planes independently of each other, but also in both planes simultaneously (in the "diagonal plane"). For the beam excitation described above, one needs to operate the stripline in the three different modes that are listed in Table 2. Here, U_n is the applied RF potential to the n:th strip (see Figure 4), where a negative potential is due to a phase shift of 180 degrees compared to the strip with positive potential. The sum mode is not for beam excitation, but describes the potential distribution when a beam that is centered in the beam pipe excites the four strips. This is further explained in Section 6.1. The RF signals are applied to the feedthroughs that are located downstream relative to the electron beam. This is due to the directional properties of a stripline which are explained more in detail in Section 5.1.

4.1 Impedance Matching

Each strip forms a coaxial waveguide, and transmission line theory can therefore be applied in order to obtain the signal along the strip [10]. The analysis is here limited to a transverse cross section of the stripline far away from the feedthroughs. In FD, the voltage propagating along a strip, $U(z)$, is the solution to the transmission line equation

$$\frac{\mathrm{d}^2U(z)}{\mathrm{d}z^2} - \gamma^2 U(z) = 0 \tag{4.1}$$

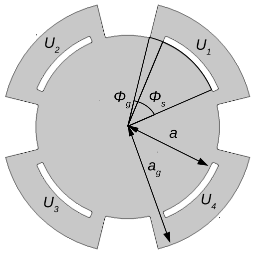

Figure 4: The 2D cross section of the stripline kicker.

Mode of operation	U_1	U_2	U_3	U_4	$Z_s[\Omega]$
Diagonal (d)	V_0	0	$-V_0$	0	50.0
Horizontal (h)	V_0	$-V_0$	$-V_0$	V_0	50.0
Vertical (v)	V_0	V_0	$-V_0$	$-V_0$	50.0
Sum (Σ)	V_0	V_0	V_0	V_0	53.4

Table 2: The modes of operation and their cha teristic impedances.

where $\gamma = \sqrt{(R + j\omega L)(G + j\omega C)}$ is the *propagation constant.* R, G, L, and C are the resistance, conductance, inductance and capacitance per unit length, respectively. The analysis is simplified by assuming that the strips are lossfree, thus $R = G = 0$, and phenomena such as attenuation and distortion are therefore not taken into account. Anyway, the losses in the 15 cm strips due to R and G are insignificant below 10 GHz, especially when comparing to the losses introduced by the ceramic vacuum insulators in the feedthroughs. For a lossfree transmission line in vacuum, the *phase velocity* is $v_p = 1/\sqrt{LC} = c_0$. Hence, the propagation constant can now be written as $\gamma = j\omega/c_0 = jk_z$, where k_z is the longitudinal wave number. The voltage $V(z)$ and current $I(z)$ that are propagating along the strip are

$$U(z) = V_0 e^{jk_z z} \tag{4.2}$$

$$I(z) = \frac{V_0}{Z_s} e^{jk_z z} \tag{4.3}$$

since the signal of excitation is travelling in the direction opposite to the electrons (in negative z direction). V_0 is a constant and $Z_s = \sqrt{L/C}$ is the *characteristic impedance* of the strip.

It is necessary that the strips have 50 Ω impedance to minimize mismatch to the feeding system. Since $c_0 = 1/\sqrt{LC}$ and $Z_s = \sqrt{L/C}$, the characteristic impedance of each strip can be obtained as $Z_s = (c_0 C)^{-1}$.

The electric field for the fundamental TEM mode in a coaxial transmission line is obtained by solving the electrostatic field over a transverse cross section (more on that in Section 4.2). C for a strip is given by the electrostatic definition of a capacitor

$$C = \frac{Q_{\text{tot}}}{U} = \frac{1}{U} \oint\limits_{\Gamma} \hat{\boldsymbol{n}} \cdot \boldsymbol{D}(\boldsymbol{r})\, \mathrm{d}l \tag{4.4}$$

where Q_{tot} and $\boldsymbol{D}(\boldsymbol{r})$ are the total charge per unit length and the electric flux density, respectively. In (4.4), the closed line integration is performed on the curve Γ which is defined by the transverse boundaries of the strip, and $\hat{\boldsymbol{n}}$ is the normal vector that is directed outward from the strip. Note that Z_s of an individual strip depends on the charge distribution in the surrounding structure, and thereby on the excitation of the other strips. Z_s is obtained numerically in the electrostatic solver in COMSOL Multiphysics for the different modes, and can be seen in Table 2. As seen, there is a slight mismatch in sum mode. COMSOL is a software which can perform numerical simulations within several different disciplines in electrical, mechanical, fluid, and chemical physics [2]. It is also able to solve coupled physics phenomena of different disciplines simultaneously, i.e., pure multiphysics. Besides from using the electrostatic solver in COMSOL, the Frequency Domain solver is used to obtain the S-parameters and the eigenmodes in this report.

Figure 5 shows S_{11} and S_{21} for one strip obtained for the diagonal mode of operation in COMSOL. Even though the strips and the coaxial feedthroughs have impedances close to 50 Ω, there will still be a mismatch in the region where the feedthroughs are welded to the strip. This mismatch becomes more distinctive at higher frequencies as seen from Figure 5. One way to improve the matching is to taper the strips to make the transit region more smooth, but since the main purpose of the stripline is beam excitation and monitoring at frequencies below 1 GHz, this was not implemented. A tapered structure would also complicate the manufacturing process.

4.2 Field Analysis

Solving $\boldsymbol{E}(\boldsymbol{r})$ in Helmholtz equation for the propagating TEM modes is equivalent to solving $\boldsymbol{E}_{\perp}(\rho,\phi)$ in a two dimensional electrostatic problem. One can therefore analytically obtain the electric scalar potential, $\Phi(\rho,\phi)$, of the (first) propagating TEM modes by solving Laplace equation over a cross section of the stripline. $\boldsymbol{E}_{\perp}(\rho,\phi)$ is then obtained as $-\nabla\Phi(\rho,\phi)$. The analysis is here limited to the region where $0 \leq \rho \leq a$, and requires that the stripline is evaluated far away from its end gaps. Between the excited strips and the ground at $\rho = a$ the electric field is approximated by $\boldsymbol{E}(a,\phi) = \pm\frac{V_0}{R\phi_g}\hat{\boldsymbol{\phi}}$. By applying the conditions of full azimuthal periodicity, finite $\Phi(\rho = 0)$, and the potential at $\rho = a$ described above and in Table 2, one obtains $\Phi(\rho,\phi)$ as the Fourier series in (4.5). The complete expansion of $\Phi(\rho,\phi)$ is presented in Appendix A.

$$\Phi(\rho,\phi) = \sum_{m=1}^{4}\frac{U_m}{\pi}\left(\frac{\phi_s+\phi_g}{2} + \frac{4}{\phi_g}\sum_{n=1}^{\infty}\left(\frac{\rho}{a}\right)^n \frac{\sin\left(n\frac{\phi_g}{2}\right)\sin\left(n\frac{\phi_s+\phi_g}{2}\right)}{n^2}\cos\left(n\left(\phi - \frac{m\pi}{2} + \frac{\pi}{4}\right)\right)\right) \tag{4.5}$$

Figure 6 shows $\Phi(\rho,\phi)$ in the diagonal, vertical, and sum mode obtained in (4.5) (upper figure) together with electrostatic simulations of the same modes in COMSOL (lower figure).

For the modes of operation, it is convenient to define a *transverse geometry factor* $g_{\perp} = a|\boldsymbol{E}(\rho = 0)|/V_0$ in order to compare different designs. Thus, a higher value of $g_{\perp}$ means a stronger electric field at the origin for a given radius a. The *longitudinal geometry factor* in sum mode is defined as $g_{||} = \Phi(\rho = 0)/V_0$. Here, the definitions

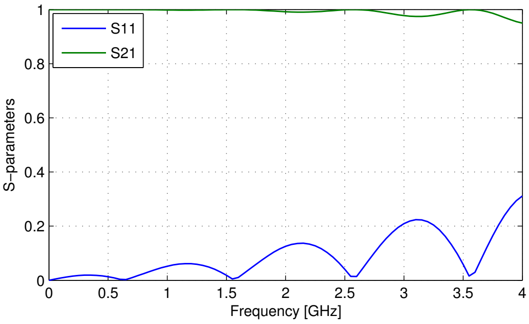

Figure 5: The S-parameters for one strip obtained for the diagonal mode of operation in COMSOL. Note that the vertical scale is linear.

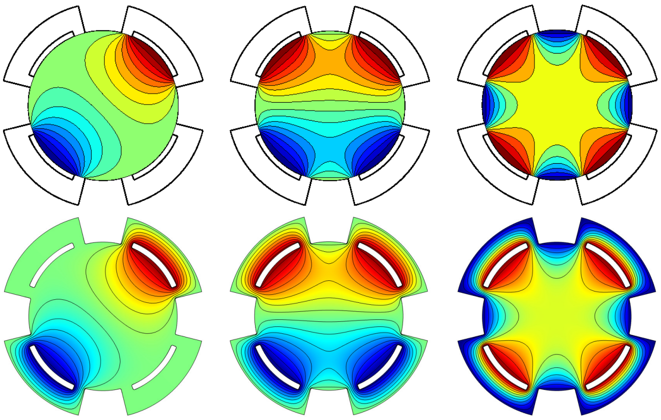

Figure 6: $\Phi(\rho, \phi)$ obtained analytically in (4.5) (upper) and numerically in COMSOL (lower). Here, (from the left) the diagonal, vertical, and sum mode are shown.

of $g_\perp$ and $g_{||}$ described in [6] are used. g for diagonal (d), horizontal/vertical (h/v), and sum mode (Σ) can be derived from (4.5), and are listed in (4.6)-(4.8). For this geometry, $g_{\perp,d} = 0.57$ and $g_{||,\Sigma} = 0.59$. The geometry factors obtained in COMSOL are identical to those obtained analytically when using an accuracy of two decimals. As seen, g_Σ and $g_\perp$ are obtained from the monopole term of $\Phi(\rho, \phi)$ and from the dipole term of $\boldsymbol{E}_\perp(\rho, \phi)$, respectively. Since the beam propagates very close to the z-axis, it is often sufficient to describe the fields in the vicinity of the beam without including any higher order multipole terms in the analysis.

$$g_{\perp,d} = \frac{8}{\phi_g \pi} \sin\left(\frac{\phi_g}{2}\right) \sin\left(\frac{\phi_s + \phi_g}{2}\right) \tag{4.6}$$

$$g_{\perp,h/v} = \sqrt{2} g_{\perp,d} \tag{4.7}$$

$$g_{||,\Sigma} = 2\frac{\phi_s + \phi_g}{\pi} \tag{4.8}$$

The electric and magnetic fields have the same z dependence as the voltages and currents in (4.2) and (4.3). $\boldsymbol{E}(\rho = 0, \phi, z)$ and $\boldsymbol{H}(\rho = 0, \phi, z)$ when the strips are diagonally excited can therefore be written as in (4.9) and (4.10), where the latter is obtained by using Ampere's law .

$$\boldsymbol{E}(\rho = 0, \phi, z) = \frac{V_0 g_{\perp,d}}{a} e^{jk_z z}\left(-\frac{\hat{\boldsymbol{x}} + \hat{\boldsymbol{y}}}{\sqrt{2}}\right) \tag{4.9}$$

$$\boldsymbol{H}(\rho = 0, \phi, z) = \frac{j}{\mu_0 \omega}\nabla \times \boldsymbol{E}(\rho = 0, \phi, z) = \frac{V_0 g_{\perp,d}}{\mu_0 c_0 a} e^{jk_z z}\left(\frac{-\hat{\boldsymbol{x}} + \hat{\boldsymbol{y}}}{\sqrt{2}}\right) \tag{4.10}$$

For the horizontal (vertical) mode of operation, $\boldsymbol{E}(\rho = 0, \phi, z)$ and $\boldsymbol{H}(\rho = 0, \phi, z)$ have the normal vectors $-\hat{\boldsymbol{x}}$ $(\hat{\boldsymbol{y}})$ and $-\hat{\boldsymbol{y}}$ $(-\hat{\boldsymbol{x}})$, respectively. The magnitude of the fields are also a factor $\sqrt{2}$ stronger compared to the diagonal mode of operation due to (4.7).

5 Kick Efficiency

Here, the electromagnetic fields obtained in the previous chapter are used to study how the excited strips affect the beam motion. It will be shown that the deflection of the beam is a function of both the power and frequency of the exciting signals.

5.1 Shunt Impedance and Kick Angle

If the stripline is operating in diagonal mode and the coaxial ports of two opposite strips are excited with voltage signals $\pm V_0 e^{j\omega t}$, the voltage along each strip becomes $U(z, t) = \pm V_0 e^{j(k_z z + \omega t + \varphi)}$, where φ is an arbitrary phase. An ultrarelativistic electron with the velocity $\boldsymbol{v} \approx c_0 \hat{\boldsymbol{z}}$ that propagates inside the excited stripline will obtain a *transverse voltage gain* $V_\perp$ that is given by (5.1). Here, $\boldsymbol{E}(z)$ and $\boldsymbol{B}(z)$ are the on-axis EM fields obtained in (4.9) - (4.10), and $k = \omega/|\boldsymbol{v}| \approx k_z$ is the wavenumber of the beam. Note that $V_\perp$ is not a real voltages strictly speaking, but the transverse work per unit charge since some of the force is a result of the magnetic field. In (5.1), one makes the approximation that $\boldsymbol{E}(z)$ and $\boldsymbol{B}(z)$ only exist in the spatial range of the strips, $-L/2 \leq z \leq L/2$, and have constant magnitudes (but different phases) on that interval. This is not true since there are fringing fields at the ends of the strips, but it gives a good approximation of $V_\perp$. A straight-line approximation is also made. Thus, the deflection provided by the stripline is small. Also note that since $\boldsymbol{v} = c_0 \hat{\boldsymbol{z}}$, $\boldsymbol{E}(z) = \boldsymbol{v} \times \boldsymbol{B}(z)$. On the other hand, if $\boldsymbol{v} = -c_0 \hat{\boldsymbol{z}}$, then $\boldsymbol{E}(z) = -\boldsymbol{v} \times \boldsymbol{B}(z)$, and the particle would obtain no voltage gain. This explains the directional properties of a stripline.

$$V_\perp = \left(\int_{-L/2}^{L/2} (\boldsymbol{E}(z) + \boldsymbol{v} \times \boldsymbol{B}(z)) e^{j(kz+\varphi)} \, \mathrm{d}z \right)_\perp \approx \frac{2V_0 g_{\perp,d} c_0}{a} e^{j\varphi} \left(\frac{\sin(\omega L/c_0)}{\omega} \right) \tag{5.1}$$

A figure of merit of a stripline is the *transverse shunt impedance* $R_\perp$ which measures its effectiveness to produce a transverse voltage gain for a given input power, P_{rms} . When operating in diagonal mode, two strips are excited and the total rms power becomes $P_{\text{rms}} = 2 \cdot V_0^2/2Z_s$. $R_\perp$ is then given by

$$R_\perp = \frac{V_\perp {V_\perp}^*}{2P_{\text{rms}}} \approx 2Z_s \left(\frac{g_{\perp,d} c_0}{a} \right)^2 \left(\frac{\sin(\omega L/c_0)}{\omega} \right)^2 \tag{5.2}$$

where ${V_\perp}^*$ is the complex conjugate of $V_\perp$. Note that $V_\perp$ depends on the phase φ of the applied RF signal (or equivalent, of the time of arrival of the particle). The product $V_\perp {V_\perp}^*$ is real and independent of φ. In vertical and horizontal mode of operation, the magnitude of $V_\perp$ becomes a factor $\sqrt{2}$ greater compared to the diagonal excitation. However, $R_\perp$ is unchanged since horizontal and vertical mode of operation have four excited strips instead of two, and the required power for the excitation in Table 2 is therefore twice as high. In Figure 7 values obtained from (5.2) are compared to values obtained from COMSOL. At the excitation frequency of 500 MHz, the analytical and numerical values of $R_\perp$ are 1509 Ω and 1457 Ω, respectively. Note that dielectric and ohmic losses in the complete system are not included in the analysis above. As seen from (5.2), $R_\perp$ is maximized if the length of the strips is $L = \lambda/4$. At our BPM monitoring frequency $f = 500$ MHz, $L = 15$ cm is optimum.

Instead of terminating the upstream ports, one can recirculate the RF signal through several strips, as in [17]. That decreases the required power since it increases $R_\perp$. However, this solution is not chosen since it would also make the feeding network (see Section 9.1) more complicated due to the requirements of being able to kick the beam in several transverse planes.

When an electron passes the excited stripline, the transverse voltage gain results in a deflection with a *kick angle* Θ. For small deflections ($\Theta \ll 1$), the maximum kick angle is given by

$$\Theta_{\text{max}} \approx \frac{|eV_\perp|}{W} = \frac{|e|\sqrt{2R_\perp P_{\text{rms}}}}{W} \tag{5.3}$$

where W and e are the energy and charge of the electron, respectively.

6 Pick-up Characteristics

As mention above, the stripline can be used for monitoring several properties of the beam, and the pick-up characteristics are presented in this section. Both the transient response in TD and the response in FD are studied.

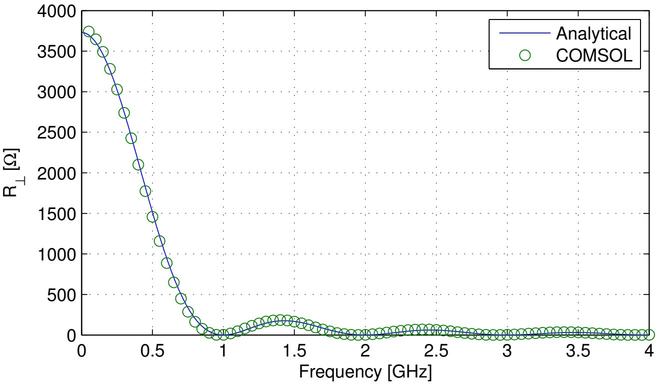

Figure 7: $R_\perp$ obtained from (5.2), and numerically in COMSOL.

6.1 Longitudinal

An electron bunch that propagates inside a vacuum chamber induces image currents on the chamber walls. Due to relativistic effects the EM field of an ultra-relativistic particle is confined to a sector in the transverse direction with angle $\gamma^{-1} = \sqrt{1-(v/c_0)^2}$. The longitudinal distribution of the image currents is therefore approximately the same as for the bunch itself. When a bunch with the current distribution $i_b(t)$ reaches the upstream gap of the stripline at $t = 0$, current pulses are induced on the strips. The intercepted mirror current at each strip is $i_b(t)g_{||,\Sigma}/4$, and it sees an impedance of $Z_s/2$ since the strip consists of two parallel port terminations of Z_s. Hence, the current pulse splits into two equal parts, where the first part propagates to the upstream port, and the second part propagates along the strip where it reaches the downstream port at $t = L/c_0$. When the bunch reaches the downstream end of the stripline at $t = L/c_0$, a negative current pulse is induced. This pulse also splits into two equal parts that propagate in two different directions toward the two terminations. However, the new pulse that propagates to the downstream termination cancels the pulse that was induced at the upstream port at $t = 0$ since they have different polarities. The second half of the new pulse reaches the upstream port at $t = 2L/c_0$. Hence, an ideal stripline BPM is a directional device, where a bi-polar pulse whose two lobes are separated by $t = 2L/c_0$ are induced at the upstream port, and where no signal is induced at the downstream port. Figure 8 shows a circuit model of a strip. The induced voltage, $u_{\text{port}}(t)$, at a single upstream port is given by (6.1). Note that this circuit model is an approximation and requires that the strips are perfectly matched to the external loads. We will therefore from here on assume that $Z_s = Z_L$ in the analysis. This approximation is quite accurate in the lower frequency region. For higher frequencies the characteristic impedance Z_s of the strips may deviate from Z_L, depending on the how the strips are excited. The circuit model approximation is also not valid when reaching the first trapped eigenmodes of the structure itself.

In storage rings, it is often more convenient to express the pick-up characteristics of a device in terms of a *transfer impedance* in FD. Thus, one set the beam current to $i_b(t) = I_b e^{j\omega t}$ and defines the *longitudinal transfer impedance* $Z_p(\omega)$ as the ratio of the induced voltage to the beam current. (6.2) shows $Z_p(\omega)$ where the induced voltage is obtained from the combined signal of the four upstream ports (note that $Z_p(\omega)$ can also be defined from the voltage at a single upstream port and is then a factor 2 lower).

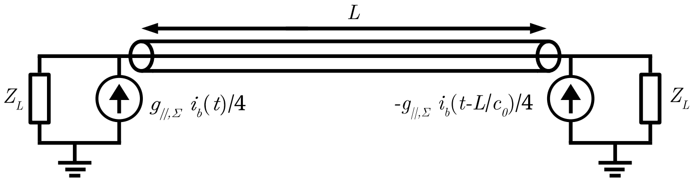

Figure 8: Circuit model of a strip.

$$u_{\text{port}}(t) = \frac{1}{2} Z_s \frac{g_{||,\Sigma}}{4} \left(i_b(t) - i_b(t - 2L/c_0) \right) \tag{6.1}$$

$$Z_p(\omega) = \frac{Z_s g_{||,\Sigma}}{2} e^{j(\pi/2 - \omega L/c_0)} \sin\left(\frac{\omega L}{c_0}\right) \tag{6.2}$$

6.2 Transverse

The induced voltage at an upstream port due to a beam with a offset relative to the z-axis can also be calculated. If the offset is diagonal ($x_{\text{offset}} = y_{\text{offset}}$), an additional dipole field is induced in the structure as in Figure 6 (left). Of course, other higher order fields are also induced, but they can be neglected in a first order approximation for small beam offsets. The induced voltage at the upstream ports of two opposite strips that are located in the same plane as the beam displacement can now be written as

$$u_{\text{port}}(t) = \frac{1}{2} Z_s \left(\frac{g_{||,\Sigma}}{4} \pm \frac{g_{\perp,d}}{2a} \Delta r \right) \left(i_b(t) - i_b(t - 2L/c_0) \right) \tag{6.3}$$

where Δr is the magnitude of the diagonal beam displacement. Note that for a small offset, the induced voltage in the two strips that are orthogonal to the beam displacement are still approximately given by (6.1). The *transverse transfer impedance* $Z_p'(\omega)$ can now be written as in (6.4) and defines the sensitivity of the BPM to transverse beam displacements. In this definition, the voltage in the numerator is obtained as the signal difference between the two ports [6]. The unit of $Z_p'(\omega)$ is Ω/m.

$$Z_p'(\omega) = \frac{Z_s g_{\perp,d}}{a\sqrt{2}} e^{j(\pi/2 - \omega L/c_0)} \sin\left(\frac{\omega L}{c_0}\right) \tag{6.4}$$

6.3 Simulations

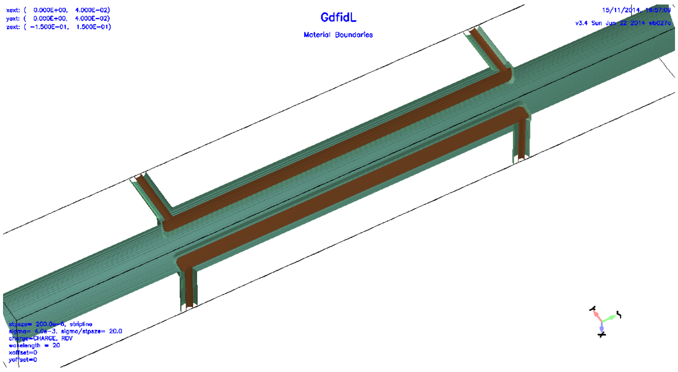

Figure 9: The stripline boundaries in the GdfidL environment when 1/4 of the model is simulated.

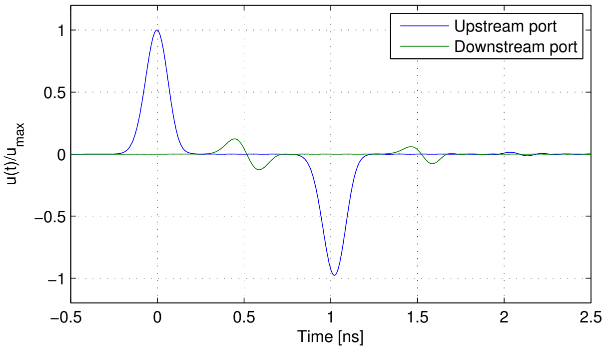

Figure 10: The induced voltage $u(t)$ at an upstream and downstream port obtained in GdfidL. The current source is a Gaussian charge distribution of length $\sigma_z = 20$ mm.

The port response from the electron beam is simulated in GdfidL which is an FDTD based 3D electromagnetic code written in FORTRAN, and developed by Warner Bruns [4]. In these simulations, the source of excitation is an ultra-relativistic Gaussian charge distribution that is propagating through the beam pipe, with and without a transverse displacement. The same simulations are also used to obtain the wake function and the beam impedance in Section 7. GdfidL is also capable of simulating the S-parameters of the ports in TD, and the eigenmodes in FD. However, in this report, COMSOL is used for those simulations. Figure 9 shows the stripline boundaries in the GdfidL environment when 1/4 of the model is simulated.

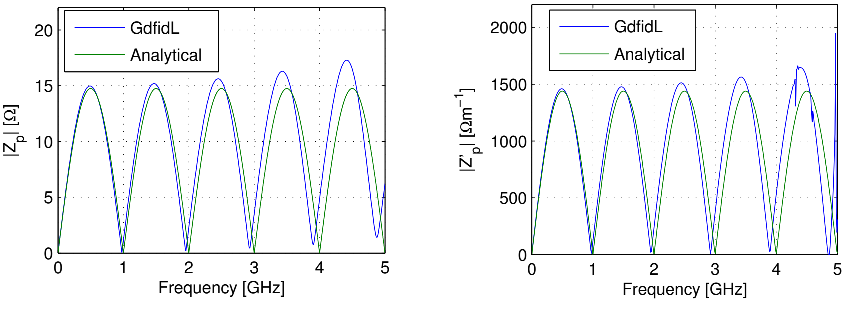

(a) (b)

Figure 11: (a) $Z_p(\omega)$ obtained in GdfidL and in (6.2), (b) $Z'_p(\omega)$ obtained in GdfidL and in (6.4). Note the impact of the trapped eigenmodes in $Z'_p(\omega)$.

Note that only 1/4 of the volume has to be simulated when obtaining $Z_p(\omega)$ since the xz and yz-planes are planes of symmetry where $\hat{\boldsymbol{n}} \times \boldsymbol{H} = 0$.

To illustrate the directional properties of the stripline, the induced voltage in TD at the upstream and downstream ports are plotted in Figure 10. Here, the source of excitation is a Gaussian bunch with $\sigma_z = 20$ mm, and a bi-polar pulse can be seen at the upstream port, while the signal is (almost) cancelled out at the downstream port. As seen, there are some reflected signals at the upstream port around 1 ns after the second lobe arrives. These reflections are caused by mismatch in the regions between the strip and its feedthroughs.

The absolute values of the simulated transfer impedances $|Z_p(\omega)|$ and $|Z'_p(\omega)|$ defined in (6.2) and (6.4) are shown in Figure 11 together with the analytical results. At 500 MHz, which is the operating frequency of the BPM electronics, $|Z_p| = 15.0\ \Omega$ and $|Z'_p| = 1458\ \Omega\text{m}^{-1}$. As expected, the simulated transfer impedances in Figure 11 agree better with the analytical approximations at lower frequencies. The spikes seen above 4 GHz in $|Z'_p(\omega)|$ are caused by trapped transverse eigenmodes. These transverse eigenmodes are investigated further in Section 7.4.2.

7 Collective Effects

In this section, it is studied how the induced mirror currents on the stripline chamber walls act back on the beam itself. Such collective effects are very important to study in an accelerator since they might result in various instabilities.

7.1 Wake Fields

In this section, the particles are assumed to be ultra-relativistic. Such a particle induces *wake fields* in the vacuum structure. Due to causality these fields only exist in a wake behind the exciting particle. It is important to consider the wake fields in the design of a storage ring. The wake fields can give rise to beam instabilities and unacceptable heating of sensitive components. It might make the storage ring operational only at beam currents levels below the design specifications.

It is often more convenient to study the integrated effect of the wake fields in a structure than the excited EM fields at each point in time and space inside the boundaries of the structure. The integrated effect of the wake field is given by the *wake function.* Consider two test charges q_1 and q travelling parallel to the axis of a vacuum chamber. Both charges have velocity $\boldsymbol{v}$, their transverse displacements from the axis are $\boldsymbol{r}_1$ and $\boldsymbol{r}$. Charge q_1 is the leading charge and is a time τ ahead of q_2. The *longitudinal wake function* $G_{||}(\boldsymbol{r}, \boldsymbol{r}_1, \tau)$ is defined as the energy lost by the trailing charge per unit of both charges q_1 and q as a function of $\boldsymbol{r}$, $\boldsymbol{r}_1$, and τ. Thus, a positive value of $G_{||}$ means a decelerating integrated electric field, and the energy gain of the charge is therefore $\Delta W(\tau) = -qq_1 G_{||}(\tau)$. Here, it is assumed that only the kinetic energy of the charges, and not their trajectories and velocities are altered due to the wake fields excited by the test charge. The wake function has the units V/C.

$$G_{||}(\boldsymbol{r}, \boldsymbol{r}_1, \tau) = -\frac{1}{q_1} \int\limits_{-\infty}^{\infty} E_z(\boldsymbol{r}, \boldsymbol{r}_1, z, \frac{z}{v} + \tau)\, \mathrm{d}z \tag{7.1}$$

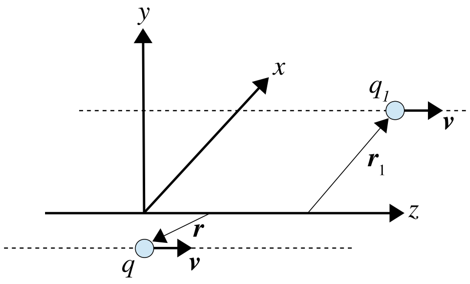

Figure 12: The test and trailing charges with their corresponding coordinates.

Consequently, one can define the *transverse wake function* $\boldsymbol{G}_{\perp}(\boldsymbol{r}, \tau)$ as in (7.2) which is the integrated transverse force along a straight path at the time τ after the test charge divided by q_1. From here on, it is assumed that the test and the trailing charge have the same offset $\boldsymbol{r}_1 = \boldsymbol{r}$. This is often a valid approximation in most storage rings since the transverse envelope of the beam is much smaller than the cross section of the vacuum chambers.

$$\boldsymbol{G}_{\perp}(\boldsymbol{r}, \tau) = -\frac{1}{q_1} \int\limits_{-\infty}^{\infty} (\boldsymbol{E}_{\perp}(\boldsymbol{r}, z, \tau) + \boldsymbol{v} \times \boldsymbol{B}_{\perp}(\boldsymbol{r}, z, \tau))\, \mathrm{d}z \tag{7.2}$$

One can find different definitions of the transverse wake function in the literature, we prefer (7.2) since it is valid for all structures, with and without any symmetry planes. However, many vacuum structures have symmetry in the xz and in the yz planes. For such structures, $\boldsymbol{G}_{\perp}(\boldsymbol{r},\tau)$ is zero at the origin, and the most dominant deflecting force is the dipole component of $\boldsymbol{G}_{\perp}(\boldsymbol{r},\tau)$ which is proportional to the beam displacement. It is therefore common to define the dipole transverse wake function $\boldsymbol{G}'_{\perp}(\tau)$ as (7.2) divided by the displacement, thus $\boldsymbol{G}'_{\perp}(\tau) = \boldsymbol{G}_{\perp}(\boldsymbol{r},\tau)/r$. The unit of $\boldsymbol{G}'_{\perp}(\tau)$ is [V/Cm].

The wake functions defined in (7.1) and (7.2) are Green functions where the fields are excited by a single point charge. One can also define the wake function, $\boldsymbol{W}(\tau)$, excited by the normalized longitudinal current distribution $\lambda(t)$ of the bunch, where $\int \lambda(t)\,\mathrm{d}t = 1$. The characteristics of $\lambda(t)$ in the storage rings are further discussed in Section 7.2. $\boldsymbol{W}(\tau)$ is then defined as the convolution of $\boldsymbol{G}(\tau)$ and $\lambda(\tau)$, and is given by (7.3) and (7.4). Sometimes in the literature, $W_{||}(\tau)$ and $\boldsymbol{W}'_{\perp}(\tau)$ are referred to as the longitudinal and the (dipole) transverse wake potential, respectively. Note that $\boldsymbol{W}(\tau) \to \boldsymbol{G}(\tau)$ when $\lambda(t) \to \delta(t)$, where $\delta(t)$ is the Dirac delta distribution.

$$W_{||}(\tau) = \int\limits_0^{\infty} G_{||}(\tau')\lambda(\tau-\tau')\,\mathrm{d}\tau' \tag{7.3}$$

$$\boldsymbol{W}'_{\perp}(\tau) = \int\limits_0^{\infty} \boldsymbol{G}'_{\perp}(\tau')\lambda(\tau-\tau')\,\mathrm{d}\tau' \tag{7.4}$$

One can obtain the wake function $\boldsymbol{W}(\tau)$ for any arbitrary bunch distribution $\lambda(t)$ once $\boldsymbol{G}(\tau)$ is known. However, most vacuum structures are quite complex, so the wake function has to be obtained numerically. Since the bunch length of the exciting bunch must be a multiple of the mesh size, it is not possible to use $\delta(t)$ as the source of excitation. The wake function is therefore often obtained in a simulation code for a very short charge distribution, and $\boldsymbol{G}(\tau)$ is then approximated as $\boldsymbol{W}(\tau)$. Of course, this limits the accuracy, especially when studying $\boldsymbol{G}(\tau)$ close to the the origin ($\tau \approx 0^{+}$) [24].

Just like the pick-up characteristics, it is sometimes more convenient to express the wake properties in the FD since it relates the induced beam voltage to the spectrum of the beam current. The *beam impedance*, $\boldsymbol{Z}(\omega)$, is defined as the Fourier transform of the wake function, and its longitudinal and the transverse (dipole) components are given by (7.5) and (7.6), respectively. Unlike the wake function, which is real, the beam impedance is a complex function, where $\mathrm{Re}(Z_{||}(\omega))$ and $\mathrm{Im}(\boldsymbol{Z}'_{\perp}(\omega))$ are even, and $\mathrm{Im}(Z_{||}(\omega))$ and $\mathrm{Re}(\boldsymbol{Z}'_{\perp}(\omega))$ are odd functions of ω. The resistive part of the beam impedance relates to the beam voltage that is in phase with the oscillations of the source of excitation, $I(\omega)$, while the reactive part is related to the voltage that is in quadrature with $I(\omega)$. This is the reason for including the imaginary unit j in (7.6). The numerical errors when approximating $\boldsymbol{G}(\tau)$ as $\boldsymbol{W}(\tau)$ in a simulation code does also reduce the accuracy of $\boldsymbol{Z}(\omega)$, which becomes more profound at higher frequencies. $Z_{||}(\omega)$ and $\boldsymbol{Z}'_{\perp}(\omega)$ have the units [Ω] and [Ω/m], respectively.

$$Z_{||}(\omega) = \int_{0}^{\infty} G_{||}(\tau)e^{-j\omega\tau}\,\mathrm{d}\tau \tag{7.5}$$

$$\boldsymbol{Z}'_{\perp}(\omega) = j\int_{0}^{\infty} \boldsymbol{G}'_{\perp}(\tau)e^{-j\omega\tau}\,\mathrm{d}\tau \tag{7.6}$$

The beam impedance that is analysed below is the *geometrical impedance* which only depends on the geometry of structures. Hence, material parameters such as finite conductivity of different materials are not included the analysis. There are definitions of other beam related impedances such as the *resistive wall impedance*, which describes the decelerating field seen by the beam due to the finite conductivity of the structure walls, the *space charge impedance*, which describes the impact of the deflecting forces between the charges in the bunches, and the *synchrotron radiation impedance*, which describes the losses when the bunches move along a curved trajectory. However, these impedances are not treated in this report.

As mentioned, the energy loss of a single trailing charge q is $\Delta W(\tau) = -qq_1G_{||}(\tau)$. The energy lost for a charge distribution with the total charge q can be written as $\Delta W = -q^2\kappa_{||}$ where $\kappa_{||}$ is called the (longitudinal) *loss factor* and is defined in (7.7). As seen $\kappa_{||}$ depends on the bunch shape and can be defined for a single vacuum component or for the whole accelerator. $\kappa_{||}$ has the unit [V/C]. The power lost in the structure, P_{loss}, is given by (7.8), where I_0 is the total stored current, and f_{RF} is the RF frequency of the accelerating cavities. Note that (7.8) requires that the buckets in the storage ring are uniformly filled, otherwise the expression has to modified. Other "exotic" filling patterns have been discussed for the MAX IV rings, but it is assumed in the calculation below that the buckets are uniformly filled. This power loss has to be compensated by the voltage in the accelerating cavities. However, the majority of the power loss in a storage ring is due to synchrotron radiation in the optics and in the insertion devices (undulators/wigglers). Since the bunch loses energy, some of its energy is transformed to currents and lost in the resistive walls of the structure, and some energy propagates as EM waves to the surrounding structures if the frequency is above or close to the cut-off frequency of the beam pipe. However, it will be shown that in the stripline, almost all of the lost power leaves the structure via the coaxial feedthroughs and dissipates in the 50 Ω terminations.

$$\kappa_{||} = \frac{1}{\pi}\int_{0}^{\infty} \mathrm{Re}(Z_{||}(\omega))\lambda(\omega)\lambda^{*}(\omega)\,\mathrm{d}\omega \tag{7.7}$$

$$P_{\mathrm{loss}} = \frac{I_0^2}{f_{\mathrm{RF}}}\kappa_{||} \tag{7.8}$$

In a similar way, one can define the (dipole) *kick factor* (also called the *transverse loss factor* in the literature), $\boldsymbol{\kappa}'_{\perp}$, as the transverse voltage gain over the total charge in the bunch and the beam displacement which is given by (7.9). Hence, $\boldsymbol{\kappa}'_{\perp}$ has the units [V/Cm]. The bunch then obtains a transverse kick Θ per displacement each time it passes the component. Θ is given by (7.10). Θ has the unit [rad/m].

$$\boldsymbol{\kappa}'_{\perp} = \frac{1}{\pi}\int_{0}^{\infty} \mathrm{Im}(\boldsymbol{Z}'_{\perp}(\omega))\lambda^{*}(\omega)\,\mathrm{d}\omega\lambda(\omega) \tag{7.9}$$

$$\Theta = \frac{eI_0}{f_{\mathrm{RF}}W}|\boldsymbol{\kappa}'_{\perp}| \tag{7.10}$$

The wakefields are simulated in TD for different beam offsets, and the trapped eigenmodes are obtained in FD simulations. The TD simulations are performed in GdfidL, where the wakelength is set to, $s_{\mathrm{max}} = 20$ m, the length of the charge distribution to $\sigma_z = 4$ mm, and the mesh size to 0.2 mm. As mentioned above, a shorter bunch length results in a wake function that is closer to the ideal Green's function, but it increases the computation time and the memory usage. A longer wakelength improves the accuracy of the beam impedance, since it increases the integration span in (7.5) and (7.6). This is most notable in larger structures with many trapped eigenmodes where the excited electromagnetic energy in the structure has a slower decay rate. Note that in [15], the TD simulations were performed in CST Particle Studio. The eigenmode simulations in FD are performed in COMSOL with proper material parameters. Here, the ports can not be terminated with 50 Ω as in the TD simulations, so they must be shorted. Therefore, eigenmodes that couple to the coaxial structure at the ports or to the ends of the beam pipe are unphysical and are therefore discarded.

7.2 Bunch Structure

The MAX IV and SOLARIS storage rings have third harmonic (Landau) cavities installed [1]. Unlike the 100 MHz main accelerating cavities, the Landau cavities operate at 300 MHz and are passive. Thus, their accelerating fields are induced by the electron beam itself by wakefields. The accelerating voltage for one revolution in the rings is given by the superposition of the fields in the main and the Landau cavities, and the result is that the accelerating voltage gradient seen by the beam is flattened out when the fields from the Landau cavities are added. This causes a longitudinal bunch lengthening, which decreases the charge density in the bunches. The current distribution, $i(s)$, within each bunch in a storage ring with third order harmonic cavities has a quartic distribution when operating with a flat potential, and is given by

$$i(s) = \frac{4\pi\sqrt{2\pi}}{\sqrt{2}\Gamma^2(1/4)}\frac{RI_0}{h\sigma_z}e^{-\frac{2\pi^2}{\Gamma(1/4)}\left(\frac{s}{\sigma_z}\right)^4} \tag{7.11}$$

where Γ is the gamma function, and $s = \tau/c_0$ is the distance behind the bunch center [8]. R, I_0, h, and σ_z are the radius of the ring, the average ring current, the harmonic number, and the rms bunch length after the bunch lengthening, respectively (see Table 1). Without the Landau cavities installed, the bunch shape would be close to

Gaussian with $\sigma_z = 12$ mm instead of quartic with $\sigma_z = 56$ mm. Figure 13 shows the current distribution λ in TD and in FD, with and without the Landau cavities in operation. The main advantages of the bunch lengthening are; reduced Touschek scattering, reduced intrabeam scattering, increased longitudinal tune spread, and that it decouples the bunch spectrum from the high-frequency part of the impedance spectrum of the machine.

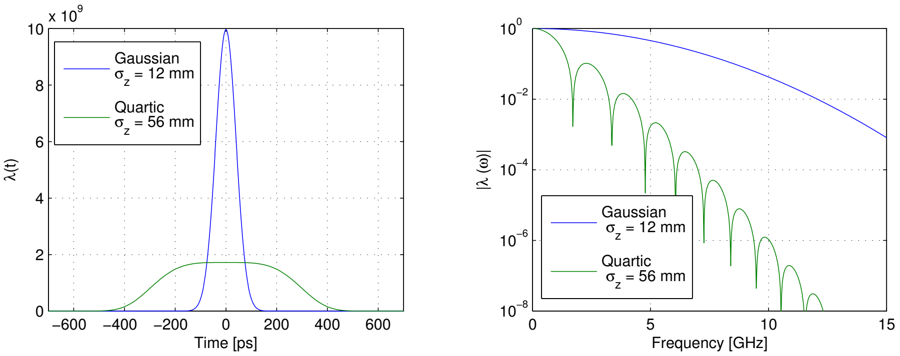

(a) (b)

Figure 13: The normalized current distribution λ in TD (a) and in FD (b), with and without the Landau cavities in operation.

As mentioned in Section 2.1.1, the beam performs transverse betatron oscillations around a closed ideal orbit, which is described by (2.2). When two electrons collide, their transverse momenta can be transformed into longitudinal momenta. If the electrons after the collision have longitudinal momenta that are outside the window of the longitudinal momentum acceptance in the RF-bucket, they are lost. This is called the *Touschek scattering* and is the limiting factor of the stored electron beam life time in modern storage ring. While Touschek scattering describes a process of collisions that result in an immediate beam loss, there are other collisions where the exchange of momenta is too small to result in beam loss. This is called *intrabeam scattering* (IBS). Longitudinal collisions can also result in a transformation of longitudinal momenta into transverse momenta. The result is IBS since the ratio of the longitudinal momenta of the synchrotron motion to the transverse momentum acceptance is too small for beam loss. IBS is a rather slow process and results in higher equilibrium emittance [22]. The increase in emittance due to IBS can be significant for ultra-low emittance storage rings such as the MAX IV 3 GeV ring [20]. By lengthening the bunches, their charge density decrease, and thereby the effects of Touschek and intrabeam scattering.

The spread of the synchrotron tune among the electrons within each bunch increases when the bunches are elongated. This tune spread increases with the nonlinearity of the total RF voltage seen by the bunches. The tune spread has a damping effect on coupled-bunch mode instabilities that are explained more in detail in [16].

As seen in Figure 13 (b), the quartic distribution has a more narrow frequency spectrum compared to the Gaussian one. This shows another advantage of implementing Landau cavities since according to (7.7)-(7.10), only the low frequency part of the impedance spectrum gives a significant contribution to the heat load and kick factor introduced by the vacuum chambers. Hence, the high-frequency part of the machine impedance spectrum, $Z(\omega)$, has little effect on the beam.

7.3 Longitudinal Impedance

7.3.1 Time Domain

As explained in Section 6.1, only a fraction $g_{||,\Sigma}/4$ of the mirror current sees the (geometrical) impedance of each strip if the bunch is propagating on-axis. The result is an induced voltage $U_{\text{port}}(\omega)$ at the upstream gap of the strip which is given by (6.1). This voltage acts back on the beam which sees a potential of $U_b(\omega) = (g_{||,\Sigma}/4)U_{\text{port}}(\omega)$. The total longitudinal beam impedance $Z_{||}(\omega)$ for the four strips is therefore $4U_b(\omega)/I_b(\omega)$ and can be written as

$$Z_{||}(\omega) = \frac{Z_s g_{||,\Sigma}^2}{8}\left(2\sin^2\left(\frac{\omega L}{c_0}\right) + j\sin\left(\frac{2\omega L}{c_0}\right)\right) \tag{7.12}$$

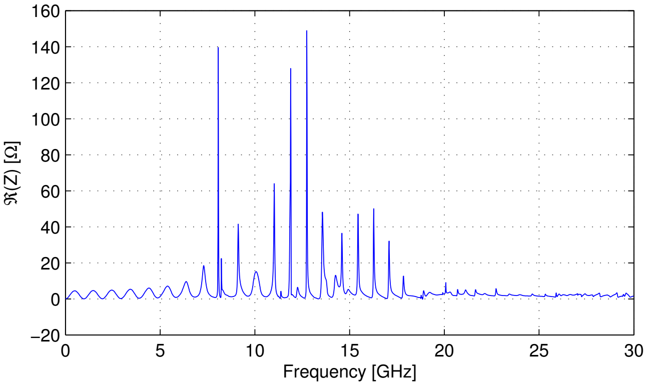

Figure 14: Re($Z_{||}$) obtained in GdfidL.

Figure 14 and 15 show Re($Z_{||}$) and Im($Z_{||}$) up to 30 GHz obtained in GdfidL, and Figure 16 shows the impedance obtained in (7.12) together with the simulation results up to 4 GHz. Here, we also see that the theoretical circuit model has a better agreement with the simulations at low frequencies. When examining Figure 14 and 15, one can distinguish three different regions in the spectrum. In the first region, where $f \lesssim 8$ GHz, the impedance behaves as in the circuit model with a more significant mismatch at higher frequencies. In the second region, where 8 GHz $\lesssim f \lesssim 18$ GHz, the resonance peaks of trapped and semi propagating modes

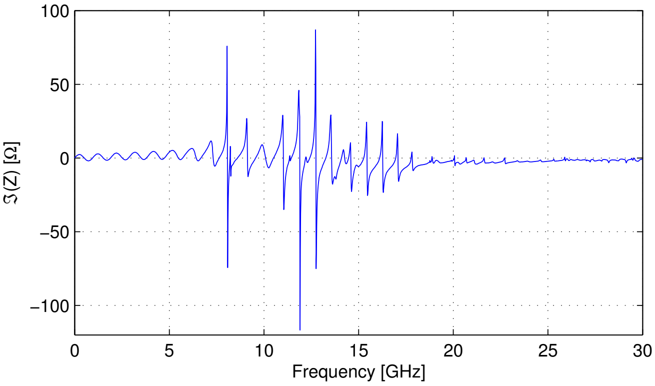

Figure 15: Im($Z_{||}$) obtained in GdfidL.

dominate the spectrum. The spectrum in the third region, where $f \gtrsim 18$ GHz, is called the *broad-band impedance* region. In this region, the higher order resonance modes of the structure get denser which results in a smeared out spectrum. Since all these overlapping modes are well above the cut-off frequency of the beam pipe, many of them radiate their power into the surrounding structures which is the explanation to why no significant resonance peaks are found in this region.

By performing an inverted Fourier transform on (7.12), the longitudinal wake function $G_{||}(\tau)$ can be written as in (7.13), where $\delta(\tau)$ is the Dirac delta distribution. Figure 17 shows $G_{||}(s)$ obtained in (7.13) and $W_{||}(s)$ obtained in GdfidL where the 4 mm Gaussian bunch is the source of excitation. Here, the mismatch at higher frequencies is quite notable in form of oscillations, and shows the limitations of the simplified circuit model. One can also see that the second pulse appears at a distance slightly longer than $s = 2L$. This is because L is defined as the distance between the origins of the two coaxial inner conductors that are attached to each strip. Therefore, the "effective length" of each strip is actually somewhat longer. The phenomenon can also be seen in Figure 11 and 16 where the analytical transfer and beam impedances have longer periods in the spectrum compared to when they are obtained in simulations.

$$G_{||}(\tau) = \frac{Z_L g_{||,\Sigma}^2}{8} \left(\delta(\tau) - \delta(\tau - 2L/c_0)\right) \tag{7.13}$$

The loss factors in (7.7) and dissipated power in (7.8) for the 12 mm Gaussian and for the 56 mm quartic distributions are listed in Table 3. As seen, the bunch lengthening that is enabled by the Landau cavities, decreases the power loss by more than a factor 5. Note that when using Re($Z_{||}$) from (7.12) to calculate the dissipated power we get $P_{\text{loss}} = 8.42$ W for the 56 mm quartic distribution. When comparing to the other ring components, the dissipated power is quite high for a non-cavity shaped structure. However, most of the power will dissipate in the 50 Ω

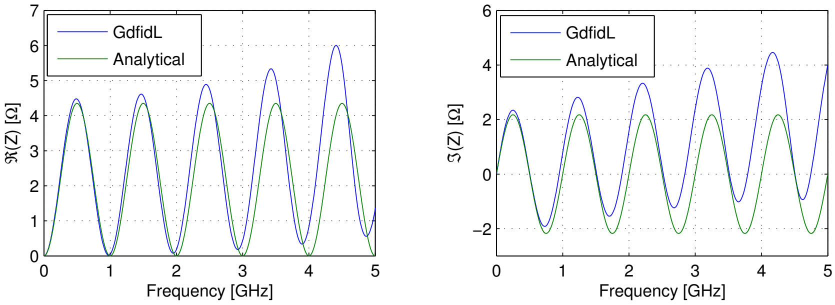

Figure 16: Re($Z_{||}$) and Im($Z_{||}$) obtained in GdfidL and in (7.12).

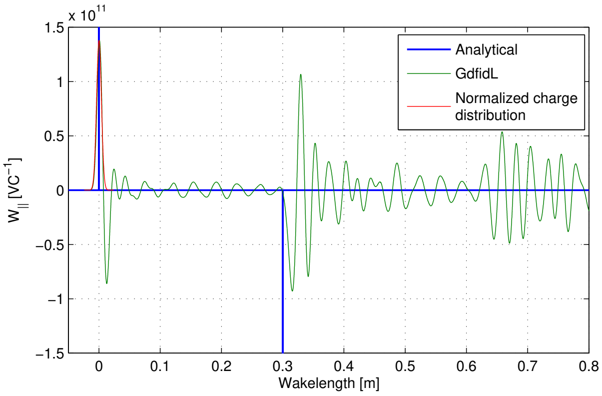

Figure 17: $G_{||}(s)$ obtained in (7.13) and $W_{||}(s)$ obtained in GdfidL. The charge distribution, $\lambda(s)$, normalized to $\max(W_{||}(s))$, is the source of the excitation, and can also be seen.

terminations that are connected to the feedthroughs, and not in the structure itself. Since the longitudinal transfer impedance $Z_p(\omega)$ is known, one can obtain the power lost in the ports P_{port} as

$$P_{\text{port}} = \frac{I_0^2}{f_b \pi} \int_0^\infty \frac{Z_p^2(\omega)}{Z_L} \lambda(\omega)\lambda^*(\omega)\, \mathrm{d}\omega \tag{7.14}$$

By using $Z_p(\omega)$ obtained in GdfidL (see Section 6.1) with the quartic 56 mm distribution, $P_{\text{port}} = 8.14$ W. Thus, the power that is lost in the structure or propagating as EM waves to the surrounding structures is approximately $P_{\text{loss}} - P_{\text{port}} =$ 10 mW, assuming that the ports are perfectly matched to 50 Ω. Note that in the ideal circuit model presented above, $P_{\text{loss}} = P_{\text{port}}$.

Guassian $\sigma_z = 12$ mm		Quartic $\sigma_z = 56$ mm	
$\kappa_{\|\|}$ [mV/pC]	P_{loss} [W]	$\kappa_{\|\|}$ [mV/pC]	P_{loss} [W]
18.33	45.86	3.26	8.15

Table 3: The loss factor and dissipated power obtained in GdfidL.

7.3.2 Frequency Domain

As seen in Figure 14, there exist several trapped eigenmodes in the structure. If one uses the parallel RLC-circuit model of the the cavity, one can obtain the longitudinal beam impedance $Z_{||,n}$ of the n:th eigenmode as in (7.15) [24], where $Q_{0,n}$ is the unloaded quality factor of that mode. $R_{\text{s},n}$ is the *longitudinal modal shunt impedance* and is defined as (7.16), where V_n is the voltage obtained by integrating the longitudinal electric field seen by the beam, $V_n = \int E_z(z)e^{jkz}\,\text{d}z$, and V_n^* its complex conjugate. P_{wall} is the power lost in the cavity walls of the corresponding electric field distribution. Since there exist an infinite number of eigenmodes in a cavity, (7.15) is of course only valid in a region close to the particular mode, and requires that the mode is sufficiently separated in frequency from the neighbouring modes. The *modal loss factor* $\kappa_{||,n}$ can then be obtained by using (7.7) and (7.15), and if $Q_{0,n}$ is large, it can be approximated as (7.17). The total loss factor is then obtained as $\kappa_{||} = \Sigma_n \kappa_{||,n}$. In the stripline where almost all of the power dissipates in the port terminations, $\kappa_{||}$ can of course not be obtained as the sum of the modal loss factors. However, for a component with many eigenmodes that have high shunt impedances that are located below the cut-off frequency off the beam pipe, $\kappa_{||}$ obtained in TD and FD are approximately the same. The main and Landau cavities are good examples of such components.

$$Z_{||,n}(\omega) = \frac{R_{\text{s},n}}{1 + jQ_{0,n}(\omega/\omega_{0,n} - \omega_{0,n}/\omega)} \tag{7.15}$$

$$R_{\text{s},n} = \frac{V_n V_n^*}{2P_{\text{wall},n}} \tag{7.16}$$

$$\kappa_{||,n} = \frac{\omega_{0,n}}{2}\left(\frac{R_{\text{s}}}{Q_0}\right)_n \lambda(\omega_{0,n})\lambda^*(\omega_{0,n}) \tag{7.17}$$

Even though $Q_{0,n}$ and $R_{\text{s},n}$ depend on the conductivity of the cavity walls (both terms are inversely proportional to $P_{\text{wall},n}$), the factor $(R_{\text{s}}/Q)_n$ does not. Thus, (7.17) is independent of the material properties, and we are therefore still dealing with the geometrical impedance. In fact, $(R_{\text{s}}/Q)_n$ depends only on the shape of the cavity, and is therefore often called the *geometrical factor* of the cavity.

In the eigenmode simulations, the first trapped longitudinal mode is the TM$_{010}$-like mode that is found at 8.069 GHz. This mode can also be seen in the TD simulations as the sharp peak at the same frequency in Figure 14. Figure 18 shows $|E_z(\boldsymbol{r})|$ of the mode in the COMSOL environment, and $|E_z(z)|$ in the pipe center of the corresponding mode. As seen, there are two lobes in $|E_z|$ caused by the potential difference between the end gaps of the strips and the surrounding structure. Only

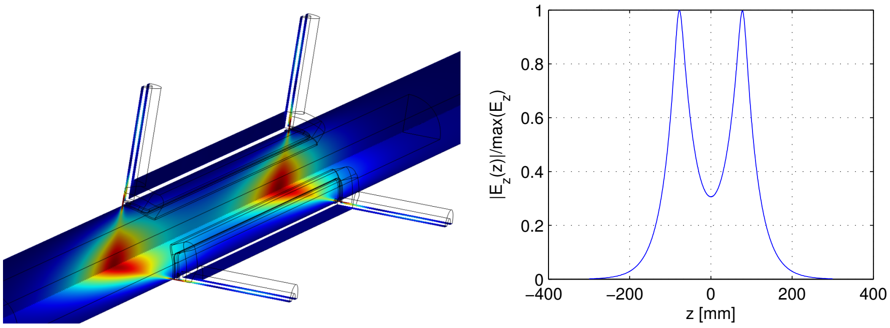

(a) (b)

Figure 18: (a) $|E_z(\boldsymbol{r})|$ of the first longitudinal eigenmode in the COMSOL environment, and (b) $|E_z(x=0, y=0, z)|$ of the same mode.

	f_0 [GHz]	Q_0	R_s [Ω]	$\kappa_{\|\|}$ [mV/pC]	P_loss [W]
FD	8.069	939	269	$3.84 \cdot 10^{-9}$	$\mathbf{9.61 \cdot 10^{-9}}$
TD	8.071	-	-	$4.05 \cdot 10^{-9}$	$\mathbf{10.13 \cdot 10^{-9}}$

Table 4: Results obtained for the TM_{010}-like mode in FD and in TD for the 56 mm quartic distribution.

1/4 of the volume is simulated since the boundary conditions of $\boldsymbol{n}\times\boldsymbol{H} = 0$ is true for the mode in the xz and yz planes. Note that it would also be possible to implement a boundary condition of $\boldsymbol{n} \times \boldsymbol{E} = 0$ in the xy plane (at $z = 0$) for this mode and thereby only simulate 1/8 of the volume. Table 4 shows the properties of the mode obtained in FD together with a comparison of the loss factor and dissipated power obtained in TD. In the latter case, $\kappa_{||,n}$ is obtained by integrating $\mathrm{Re}(Z_{||}(\omega))$in the spectrum close to the resonance frequency f_0. As seen, the power lost by the first longitudinal mode is insignificant compared to the power lost in the feedthroughs. The longitudinal mode analysis does not extend further up in frequency since there are many higher-order modes that are semi-propagating and therefore difficult to isolate. Besides, since the other eigenmodes are located even higher up in frequency their contribution to the total power loss is negligible due to the narrow frequency spectrum of $\lambda(\omega)$.

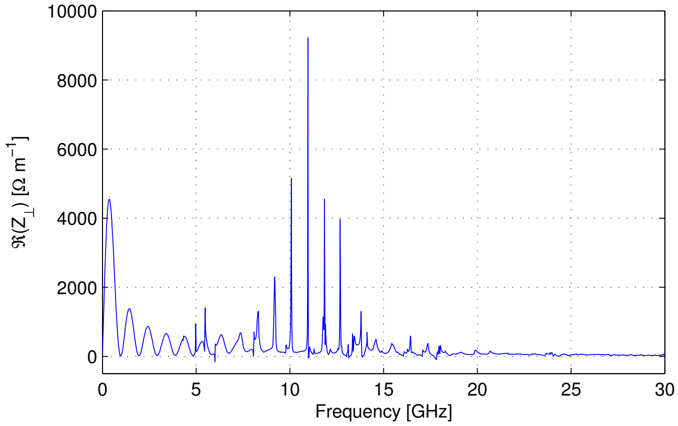

Figure 19: Re($Z'_\perp$) obtained in GdfidL.

7.4 Transverse Impedance

7.4.1 Time Domain

The transverse dipole impedance, $\boldsymbol{Z'}_\perp(\omega)$ is obtained analytically in [14][1]. For a diagonal displacement, $\boldsymbol{Z'}_\perp(\omega)$ becomes

$$\boldsymbol{Z'}_\perp(\omega) = \frac{c_0 Z_s g^2_{\perp,d}}{4a^2}\frac{1}{\omega}\left(2\sin^2\left(\frac{\omega L}{c_0}\right) + j\sin\left(\frac{2\omega L}{c_0}\right)\right)\hat{\boldsymbol{e}}_\perp \tag{7.18}$$

where $\hat{\boldsymbol{e}}_\perp$ is the diagonal unit vector.

Figure 19 and 20 show Re($Z_\perp$) and Im($Z_\perp$) obtained in GdfidL, and Figure 21 shows the analytical impedance obtained in (7.18) together with the simulated one up to 5 GHz. Figure 21 is yet another example on how the accuracy of the circuit model decreases at higher frequencies.

$\boldsymbol{Z'}_\perp(\omega)$ in (7.18) is obtained for a displacement in the diagonal plane. However, in a storage ring, it is often more convenient to express the transverse impedance as Z'_x and Z'_y. If one consider a vertical displacement, $\hat{\boldsymbol{e}}_\perp = \hat{\boldsymbol{y}}$, the induced vertical electric potential is similar to the one in Figure 6 (middle). However, if one compare with the potential induced due to a diagonal displacement in Figure 6 (left), the induced potential at the two upper strips in Figure 6 (middle) is only a factor $1/\sqrt{2}$ compared to the upper right strip in Figure 6 (left) assuming that the magnitude of the horizontal and diagonal displacements are the same. Since the vertical and diagonal geometry factors, $g_{\perp,v}$ and $g_{\perp,d}$, in (4.6)-(4.7) are defined when the strips are held at positive and negative unit potentials, the magnitude of the deflecting electric field in the origin, $|\boldsymbol{E}_\perp|$, is identical for a vertical and for diagonal beam displacement because $(1/\sqrt{2})g_{\perp,v} = g_{\perp,d}$. Hence, the transverse impedance $|\boldsymbol{Z}'_\perp(\omega)|$

---

[1] In [14], the transverse geometry factor is approximated as $g_{\perp,d} = (4/\pi)\sin(\phi_s/2)$.

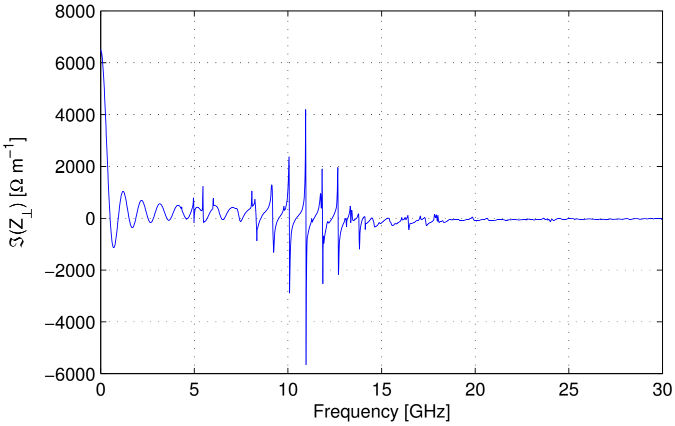

Figure 20: $\mathrm{Im}(Z'_\perp)$ obtained in GdfidL.

Guassian $\sigma_z = 12$ mm		Quartic $\sigma_z = 56$ mm	
$\kappa_\perp$ [mV/pCm]	Θ [μrad/m] (1.5 GeV / 3 GeV)	$\kappa_\perp$ [mV/pCm]	θ [μrad/m] (1.5 GeV / 3 GeV)
4542	15.15 / 7.575	3288	10.97 / 5.483

Table 5: Kick factor $\kappa_\perp$ and kick angles Θ for the 12 mm Gaussian and 56 mm Quartic distributions obtained from the transverse simulations. Θ is listed for energies of 3 GeV and 1.5 GeV.

is identical for a vertical (or horizontal) and a diagonal displacement. Simulations confirm this.

The transverse dipole wake function $G'_\perp(\tau)$ is given by (7.19) and can be obtained by performing an inverted Fourier transform on (7.18) and by using the integral representation of the Heaviside step function $\theta(\tau)$.

$$G'_\perp(\tau) = -\frac{c_0 Z_s g^2_{\perp,d}}{4a^2}\left(\theta(\tau) - \theta\left(\tau - \frac{2L}{c_0}\right)\right) \tag{7.19}$$

Figure 22 shows $G'_\perp(s)$ obtained analytically in (7.19), and $W'_\perp(s)$ obtained in GdfidL, where the source of excitation in the latter is the 4 mm Gaussian test bunch. Note the oscillations around $s = 0.3$ m in $W'_\perp(\tau)$ due to the mismatch explained above.

Table 5 shows the kick factors and kick angles obtained in the TD simulations. Here, Θ is calculated for a uniform filling pattern and $I_{\text{tot}} = 0.5$ A. Note that $\kappa_\perp = 3054$ mV/pCm for the 56 mm quartic distribution when using the transverse impedance in (7.18).

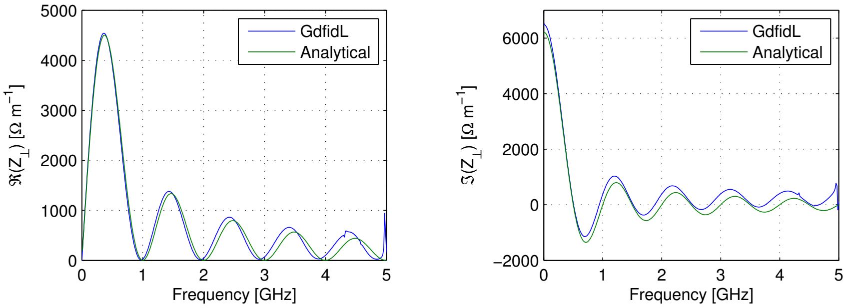

Figure 21: $\mathrm{Re}(Z'_\perp)$ and $\mathrm{Im}(Z'_\perp)$ obtained in GdfidL and in (7.18).

7.4.2 Frequency Domain

There are several trapped TE modes in the structure. These are very similar to those found in a cavity magnetron, and for this reason we adopt the same notation as in [5]. The TE modes have longitudinal magnetic field components in the cavity volumes between the strips and the main chamber. The phase difference of H_z in such a cavity to H_z in one of its neighbouring cavities determines the name of the transverse mode. The $\pi/2$, π, and 0 modes are the fist TE modes that are found in a 2D cross section, and these have indices $m = 1, 2, 3$, respectively. Figure 23 shows $H_z(\boldsymbol{r})$ and $\boldsymbol{E}_\perp(\boldsymbol{r})$ of the mentioned 2D modes in the COMSOL environment, and Table 6 lists their resonance frequencies $f_{\perp,m}$. Note that the $\pi/2$ mode is a degenerate mode, and there are therefore two $\pi/2$ modes with the the same resonance frequency whose transverse electric field are orthogonal to each other.

$f_{\perp,m}$ [GHz]	Index	ID
4.250	$m = 1$	$\pi/2$ (x2)
5.064	$m = 2$	π
6.479	$m = 3$	0

Table 6: The resonance frequencies, $f_{\perp,m}$, of the first three transverse eigenmodes found in a 2D cross section of the stripline.

Since $\boldsymbol{H} \cdot \hat{\boldsymbol{n}} = 0$ at the metallic surfaces in the cavities, we can obtain an approximation of the corresponding 3D modes as

$$f_{m,n} \approx \sqrt{f_{\perp,m}^2 + \left(\frac{nc_0}{2L_c}\right)^2}, \ (m,n) \in \mathbb{Z}^+ \tag{7.20}$$

where $f_{\perp,m}$ is the resonance frequency of the m:th transverse mode found in the 2D cross section. Table 7 lists the 3D modes obtained in COMSOL, and Figure 24 shows $H_z(\boldsymbol{r})$ of the TE_{21} mode (the first π-mode). Note that $\pi/2$-modes where $n > 4$ are not listed since their frequencies are above the cut-off frequency of the

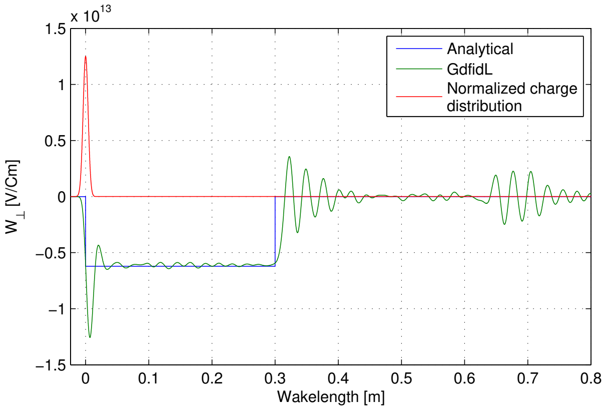

Figure 22: $G'_{\perp}(s)$ obtained in (7.19) and $W'_{\perp}(s)$ obtained in GdfidL. The charge distribution, $\lambda(s)$, normalized to $\max(W'_{\perp}(s))$, which is the source of excitation in the simulation is also included.

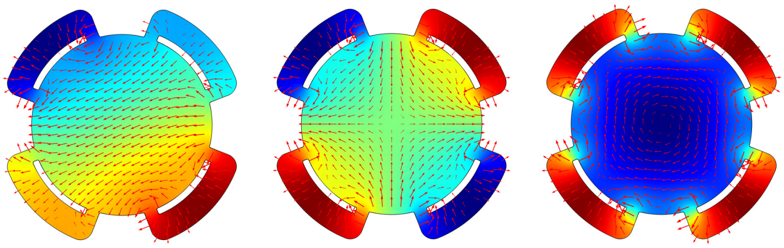

Figure 23: (from left to right) the $\pi/2$, π, and 0 mode in a 2D cross section of the stripline. The color scale shows $H_z(\boldsymbol{r})$, and the red arrows show $\boldsymbol{E}_{\perp}(\boldsymbol{r})$.

TE_{11} mode of the pipe. Also note that the TE_{11}, TE_{12}, and TE_{13} modes are visible as glitches in Figure 21.

8 Stripline S-parameter Measurements

The purpose of these measurements is to study the impedance matching and to confirm that no severe mismatches exist. The input port of a strip is matched to 50 Ω when the input port of the opposite located strip is excited with a signal that has the same potential but is phase shifted 180° as described in Table 2 and Figure 6 (left). Therefore, it is relevant to produce the same distribution of signal potentials during the measurements. This can be done with a *differential-mode* measurement using a 4-port *Vector Network Analyzer* (VNA).

The most common way of transmitting a signal in transmission lines is by us-

$f_{m,n}$ [GHz]	Q_0	Index	ID
4.336	660	$m = 1, n = 1$	$\pi/2$ (x2)
4.595	612	$m = 1, n = 2$	$\pi/2$ (x2)
4.981	697	$m = 1, n = 3$	$\pi/2$ (x2)
5.136	624	$m = 2, n = 1$	π
5.366	612	$m = 2, n = 2$	π
5.473	736	$m = 1, n = 4$	$\pi/2$ (x2)
5.729	601	$m = 2, n = 3$	π
6.202	594	$m = 2, n = 4$	π
6.529	994	$m = 3, n = 1$	0
6.707	937	$m = 3, n = 2$	0
6.760	595	$m = 2, n = 5$	π
6.996	869	$m = 3, n = 3$	0

Table 7: f_c, Q_0, and indices of the trapped transverse eigenmodes up to 7 GHz obtained in COMSOL.

ing *single-ended* or *unbalanced* transmission lines such as coaxial, microstrip, and coplanar lines. In single-ended transmission lines, the signal is represented as the voltage between the signal conductor and ground. The drawback is that the ground potential might vary along the transmission line due to currents in the ground plane that might interfere with the measured signal. These current can be caused by the external interferences or by the signal itself, and result in potential differences because of the finite conductivity and parasitic inductances in the conductors. Besides from interfering with the signal itself, a single-ended transmission line might also act as an antenna and can therefore interfere other electrical system.

One way of reducing the interference caused by ground currents is to use a *balanced* transmission line with two symmetrical conductors that are separated from ground. The signal in a balanced transmission line in differential-mode is represented as the voltage between the two conductors without using ground as a signal reference. In theory, the potential of the surrounding ground becomes irrelevant for a balanced transmission line. The stripline excited in diagonal mode in Figure 6 (left) is a good example of a balanced transmission line in differential-mode.

Besides from differential-mode signals, *common-mode* signals where the two conductors have the same potentials and phases can also propagate along a balanced transmission line. Common-mode signals are often unwanted, but in an ideal balanced transmission line, a common mode interference would not degrade the signal quality since it is easy to distinguish it from the differential mode signal. However, *cross-mode* conversion between common-mode and differential-mode signals (and vice verse) might exist, which results in interference. This can happen if the symmetry of the two conductors is not perfect. Differential and common-mode are also known as odd and even mode, respectively.

A 4-port VNA can perform *mixed-mode* measurements where the differential, common, and cross-mode S-parameters of a balanced transmission line are obtained by using *modal decomposition* [7]. Here, the four physical VNA ports are represented

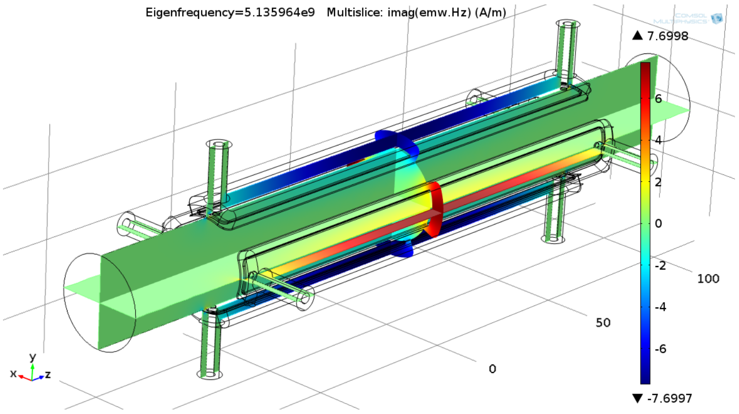

Figure 24: $H_z(\boldsymbol{r})$ (color scale) of the first π-mode ($m = 2,\ n = 1$) in the COMSOL environment.

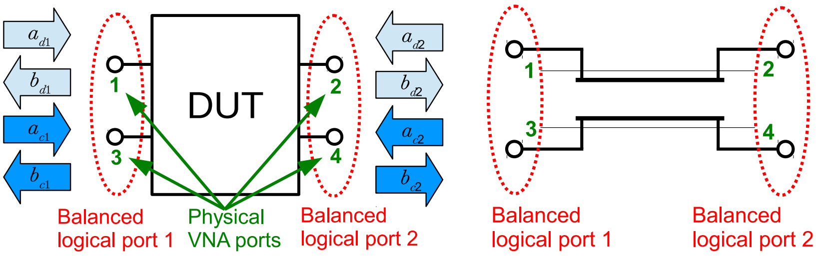

(a) (b)

Figure 25: (a) A physical four-port DUT (Device Under Test) during mixed-mode measurements, and (b) the port configuration during the stripline measurements.

as two logical ports which are shown in Figure 25 (a). The mixed-mode S-matrix is defined as

$$\boldsymbol{S} = \begin{bmatrix} S_{\mathrm{dd11}} & S_{\mathrm{dd12}} & S_{\mathrm{dc11}} & S_{\mathrm{dc12}} \\ S_{\mathrm{dd21}} & S_{\mathrm{dd22}} & S_{\mathrm{dc21}} & S_{\mathrm{dc22}} \\ S_{\mathrm{cd11}} & S_{\mathrm{cd12}} & S_{\mathrm{cc11}} & S_{\mathrm{cc12}} \\ S_{\mathrm{cd21}} & S_{\mathrm{cd22}} & S_{\mathrm{cc21}} & S_{\mathrm{cc22}} \end{bmatrix} \tag{8.1}$$

where

- $S_{\mathrm{dd}ij}$ is the differential-mode reflection/transmission parameter at logical port i when the logical port j is excited with a differential-mode signal.
- $S_{\mathrm{cc}ij}$ is the common-mode reflection/transmission parameter at logical port i when the logical port j is excited with a common-mode signal.

- $S_{\mathrm{cd}ij}$ is the differential-mode reflection/transmission parameter at logical port i when the logical port j is excited with a common-mode signal.
- $S_{\mathrm{dc}ij}$ is the common-mode reflection/transmission parameter at logical port i when the logical port j is excited with a differential-mode signal.

As an example, the cross-mode parameter S_{cd21} is defined as $\frac{b_{\mathrm{c2}}}{a_{\mathrm{d1}}}\big|_{a_{\mathrm{c1}}=a_{\mathrm{d2}}=a_{\mathrm{c2}}=0}$ in Figure 25 (a).

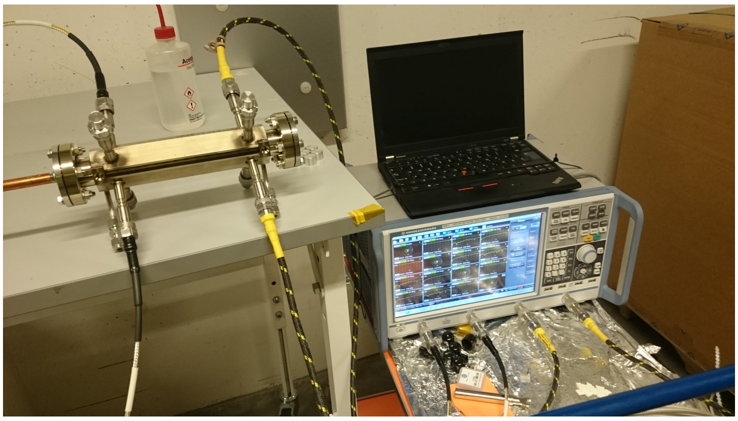

Figure 26: The test set-up during the mixed-mode S-paramater measurements.

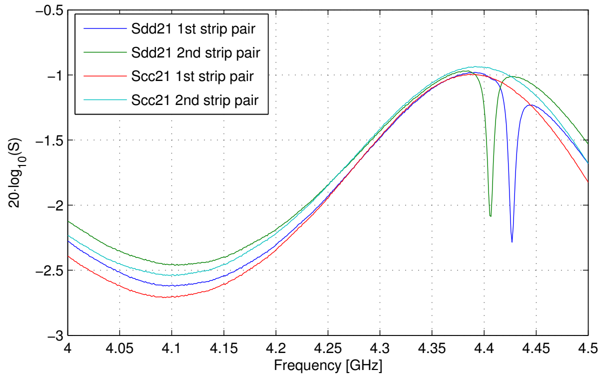

Figure 27: S_{dd21} and S_{cc21} of the two strip pairs in the range 4 to 4.5 GHz.

It is also possible to perform balanced transmission line measurement with single-ended VNA ports by using a balanced-unbalanced (*balun*) transformer network.

However, the accuracy of such measurements are limited by the phase/amplitude unbalance and by the bandwidth limitation of the network.

Two measurements per stripline are performed, where a single opposite located strip pair are characterized in each measurement. In each such measurement, the downstream stripline port of the upper strip is connected to the physical VNA port 1, while the upstream stripline port is connected to the the physical VNA port 2. Consequently, the downstream and upstream port of the lower strip are connected to the physical VNA ports 3 and 4, respectively. The four ports of the stripline pair that are not measured are terminated with 50 Ω loads. The test set-up is shown in Figure 26, and Figure 25 (b) shows a diagram of the port configuration during the measurements. The mixed-mode S-parameters of the two strip pair in the stripline that is located in the 3 GeV ring are shown in Figure 36-43 in Appendix B.

As expected, the matching becomes worse at higher frequencies as shown in the differential and common-mode reflection parameters depicted in Figure 36 and 37. This can also be seen in the differential and common-mode transmission parameters in Figure 40 and 41. However, ceramic losses in the coaxial feedthroughs also increase with frequency, so impedance mismatch is not the only reason why the throughput is lower at higher frequencies. The cross-mode parameters in Figure 42 and 43 show that the phase/amplitude balance is better for the second strip pair since $S_{\mathrm{dc21}} = S_{\mathrm{dc12}} = S_{\mathrm{cd21}} = S_{\mathrm{cd12}} = 0$ if the strips would be identical and with the same dielectric losses in the feedthroughs.

Figure 27 shows S_{dd21} and S_{cc21} of the two strip pairs in the range 4 to 4.5 GHz. Note that there is a glitch found at 4.427 GHz in the otherwise quite smooth S_{dd21} curve of the first strip pair. A similar glitch is found at 4.407 GHz when measuring the second strip pair. These glitches are the resonance responses of the first trapped $\pi/2$ mode (the TE_{11} mode) pair, listed in Table 7. As mentioned, the $\pi/2$ modes are degenerate modes and exist in orthogonal pairs. However, due to mechanical tolerances, the two-plane transverse symmetry is not perfect, which seems to have resulted in a mode separation of 20 MHz. The mechanical tolerances might also explain why the measured resonance frequencies differ 1.6 % and 2.1 %, respectively from the simulated one. Also note that the response of the trapped eigenmodes can only be seen in the S_{dd21} curves, and not in the S_{cc21} curves. This indicates that the eigenmodes are dipole modes since they are only excited when the two strips pairs are fed in differential-mode. $\boldsymbol{E}_{\perp}(r)$ in Figure 23 shows why the $\pi/2$ modes can only be excited when the strips are fed in differential-mode.

The upper bandwidth limit of the VNA is 4.5 GHz, so it was not possible to map any higher order eigenmodes during the measurements of the S-parameters.

9 RF Distribution

In this section, the design and measurements of the RF feeding network for the stripline and the receiving network for the diagnostic BPM are presented. This is for the RF networks in the MAX IV 3 GeV ring when the stripline is used for tune measurements.

The feeding network distributes the RF power delivered by an amplifier to the strips. This distribution is adjusted to the plane where the excitation occurs. The receiving network combines the signals from the four BPM buttons so that the horizontal, vertical and longitudinal motions of the beam can be monitored. The control of the feeding and receiving networks are integrated into the MAX IV control system. Unlike the S-parameter measurements described in Section 8, the measurements of the feeding and receiving networks are single-ended.

9.1 Feeding Network

Basically, the feeding network consists of three 180° 2-way splitters, eight 2-way electromechanical switches, and four adjustable phase shifters (line stretchers). A circuit diagram of the feeding network can be seen in Figure 28. The control signals to the electromechanical switches are 24 V logic and are delivered by an external PLC system. A logic diagram of the two switch control signals, Sw1-2, and how they correspond to the three modes of operation can be seen in Table 8. The numbering of the output ports and the modes of operation are the same as in Table 2 and Figure 4, respectively. The logic table is selected so that all the control signals are low when exciting the beam in the diagonal mode of operation. Thus it is possible to excite the beam so that both the horizontal and vertical tunes can be measured in case of a PLC system failure.

The bandwidth and maximum input power at Port 0 are 100 MHz - 500 MHz and 200 W, respectively. These limits are set by the specifications of the splitters [13], while the electromagnetic switches and line stretchers are more broadband and can handle higher power levels. During the initial tests, it was discovered that the switches could not be placed as close to each other as planned. The reason was that they did not switch back to the "low" state after being put in the "high" state. This is most likely because there still exists a magnetic field around the electromagnet in the neighbouring switch due to magnetic remanence. This remaining magnetic field prevents a neighbouring switch from being switched back to the "low" state. This problem was eliminated by placing sheets of mu-metal (an alloy with very high permeability) between each neighbouring pair of switches in order to provide magnetic shielding. The components of the feeding network are mounted in a standard 19” rack case, see Figure 29.

The amplifier is feed by the tracking generator of the spectrum analyzer. Both the amplifier and the spectrum analyzer are placed in a cabinet room on top of the 3 GeV ring where they are protected from radiation. The feeding network is less sensitive to radiation and is therefore placed inside the enclosure of the ring, about 1 m from the stripline. Four phase matched N-type cables are connecting the feeding network to the stripline, and the short length of the cables maximizes the delivered power to the strips. The 8 coaxial terminations (4 for the feeding network and 4 for the upstream ports of the stripline) are connected via N-type cables, and their cooling flanges are attached to a water cooling pipe in order to minimize the heat exchange to the storage ring enclosure.

It would be possible to construct a simpler network with less switches by using

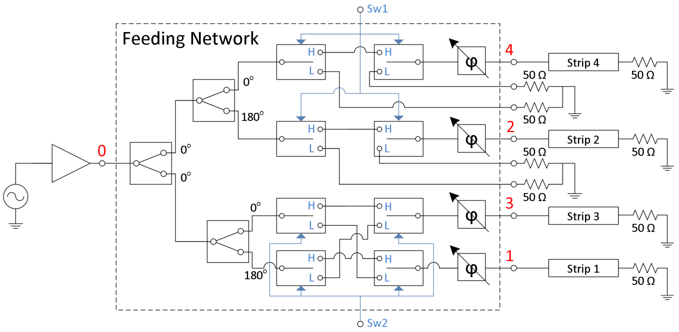

Figure 28: A circuit diagram of the stripline feeding network. The tracking generator of the spectrum analyzer is the AC source. The red numbers show the port indices during the S-parameter measurements.

Figure 29: The feeding network mounted in a standard 19" rack case. Note that half of the switches are not visible since they are shielded by sheets of mu-metal.

180° hybrid junctions as in the receiving network (see Section 9.2). However, it was decided to use a single in-house designed amplifier as the source of excitation, and we were only able to find wide-band 180° hybrid junctions that could handle much less power than the splitters used in the design described above. It would of course be possible to feed a low-power RF signal to the hybrid junctions and then add four amplifiers (one for each strip), but it would be harder to obtain a good phase and amplitude match between the four strips with this layout since the amplitude/phase unbalance between four amplifiers would be much larger than in the feeding network alone. A system with only one amplifier (and a spare unit) is also considered more reliable.

Since the amplifier is optimized for 500 MHz, the line stretchers were adjusted for that frequency. Table 9 lists the magnitudes and phases of the S_{x0} parameters at 500 MHz. The measured phase and amplitude unbalance originate mainly from

Mode of operation	Sw1	Sw2
Diagonal	L	L
Horizontal	H	L
Vertical	H	H

Table 8: The PLC logic diagram of the three modes of operation of the feeding network. Here, H (High) and L (Low) correspond to 24 V and 0 V, respectively.

the splitters. The complete S-parameters measurement results are presented in Appendix C.

	Diagonal		Horizontal		Vertical	
Port, x	$20 \cdot \log_{10}(S_{x0})$	$\arg(S_{x0})$	$20 \cdot \log_{10}(S_{x0})$	$\arg(S_{x0})$	$20 \cdot \log_{10}(S_{x0})$	arg(S_{x0}
1	-7.57	-107.1°	-7.57	70.4°	-7.74	-107.3°
2	< -100	-	-7.72	-108.4°	-7.72	-108.4°
3	-7.83	70.3°	-7.83	-107.0°	-7.65	70.3°
4	< -100	-	-7.54	71.7°	-7.54	71.7°

Table 9: The magnitudes and phases of the S_{x0} parameters of the feeding network at 500 MHz when the switches are set to excite the beam in the diagonal, horizontal, and vertical plane. The port indices can be seen in Figure 28.

9.2 Receiving Network

This network produces the horizontal differential, the vertical differential, and the sum signal of the induced signals from four BPM electrodes. Basically, the receiving network consists of four 180° hybrid junctions. A circuit diagram of the network can be seen in Figure 30. The hybrid junctions have a large specified bandwidth of 2-2000 MHz [11], but S-paramter measurements show that the network can be used for monitoring signals up to at least 3.5 GHz. However, the phase and magnitude unbalance becomes worse outside the specified bandwidth. The specific signal that one wants to monitor is selected by four electromechanical switches. The switches also make sure that the two signals that are not monitored are terminated. The switches are controlled by three 24 V-logic signals (Sw1-3) that are provided by a PLC system which can be controlled from the MAX IV control system. Table 10 shows the logic diagram of the three switch signals. The components are mounted inside a standard 19” rack case seen in Figure 31. The rack case is larger than needed and is therefore prepared for future modifications such as adding low-noise amplifiers, etc. Three SMA jumpers are mounted on the front of the case, and if one wants to monitor the three different signals simultaneously, one can bypass the four switches by disconnecting the jumpers and connect the instrument(s) directly to the three outputs.

The four input ports seen in Figure 30 are connected to the output ports of the diagnostic BPM chamber which have the port indices seen in Figure 32. This diagnostic BPM chamber is located in the first achromat directly after the transport line from the LINAC. While the standard BPM chambers in the 3 GeV ring have circular cross sections, this cross section is hexagonal. Note that there is no symmetry in the yz-plane of vacuum chamber. The reason for this is that the electron pulse that is injected has an orbit that is left of the origin in the BPM chamber, while the stored beam is centered in the chamber. The "Switch Output" port is connected to the input port of the spectrum analyzer.

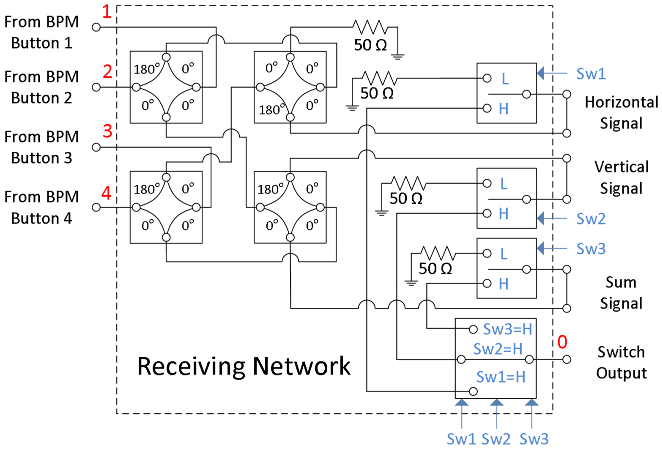

Figure 30: A circuit diagram of the receiving network. The red numbers show the port indices during the S-parameter measurements.

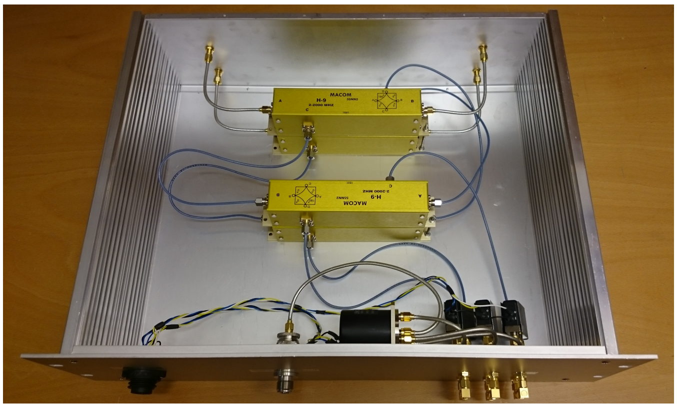

Figure 31: The receiving network mounted inside a standard 19" rack case.

Table 11 lists the magnitudes and phases of the S_{0x} parameters at 500 MHz. As seen, the measured phase and amplitude unbalance at this frequency is quite low.

Signal	Sw1	Sw2	Sw3
Horizontal	H	L	L
Vertical	L	H	L
Sum	L	L	H

Table 10: The PLC logic diagram of the receiving network when the horizontal, vertical and sum signals are monitored. Here, H (High) and L (Low) correspond to 24 V and 0 V, respectively.

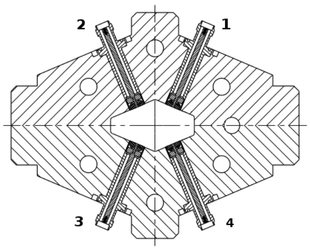

Figure 32: The 2D cross section of the diagnostic BPM chamber and the indices of the four buttons.

The complete S-parameters measurements, up to 1 GHz are presented in Appendix D.

	Horizontal		Vertical		Sum	
Port, x	$20{\cdot}\log_{10}(S_{0x})$	$\arg(S_{0x})$	$20{\cdot}\log_{10}(S_{0x})$	$\arg(S_{0x})$	$20{\cdot}\log_{10}(S_{0x})$	$\arg(S_{0x}$
1	-8.49	-17.6°	-8.31	142.9°	-8.41	-37.2°
2	-8.39	163.5°	-8.33	144.1°	-8.43	-36.0°
3	-8.41	163.5°	-8.34	-36.7°	-8.35	-37.1°
4	8.35	-15.9°	-8.36	-36.0°	-8.38	-36.2°

Table 11: The magnitudes and phases of the S_{0x} parameters of the receiving network at 500 MHz, when the switches are set to monitor the horizontal, vertical, and sum signal of the four BPM buttons. The port indices can be seen in Figure 30.

10 Initial Beam Measurements in MAX IV

Figure 33 and 34 show the power spectrum obtained at the diagnostic BPM when the stripline is exciting the beam in the horizontal and vertical plane, respectively. In each figure, the receiving network is switched to monitor the corresponding plane. The measurements were performed in the MAX IV 3 GeV ring during the initial state of beam commissioning in October 2015, and only 8 following ring buckets were filled. The total ring current during the measurements was approximately 5 mA. The peaks found at 498.51 MHz, 499.08 MHz, and 499.65 MHz are the 878:th, 879:th, and 880:th harmonic of the revolution frequency ω_0, respectively. Note that if the ring would be filled with a perfectly even filling pattern, the revolution harmonics would not be visible in the spectrum (but the RF harmonics would). The horizontal and vertical betatron oscillations can be seen as sidebands of each revolution harmonic at ±178 kHz and ±130 kHz, respectively.

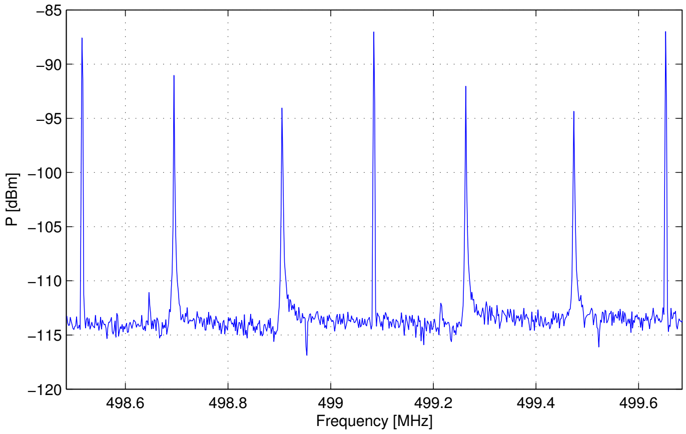

Figure 33: The power spectrum obtained at the diagnostic BPM when the beam is excited by the stripline in the horizontal plane. The peaks at 498.51 MHz, 499.08 MHz, and 499.65 MHz are harmonics of the revolution frequency. The horizontal betatron oscillations can be seen as sidebands of each revolution harmonics at ±178 kHz.

As already mentioned in Section 2.1.2, the integer part of the betatron tunes are lost due to the stroboscope effect. Therefore, the integer parts of the tunes during the measurements were obtained by counting the number of horizontal/vertical oscillations registered by the BPM system for a distorted orbit around the ring. The horizontal and vertical integers of the tunes are 42 and 16, respectively. According to (2.6), one can not determine if the fractional part of the tunes are higher or lower than 0.5 by looking at the spectrum alone. However, by sweeping one of the quadrupole magnets and observing the tune shift, it was found that $Q_f < 0.5$ in both planes. Hence, the betatron tunes during the measurements were $Q_x = 42.31$ and $Q_y = 16.23$. These values differ somewhat from those specified in Table 1. However, the measurements were performed in the initial state of beam commissioning, and numerous adjustments have been done to the optics since.

The receiver network is switched to sum mode when monitoring the longitudinal beam motion. This is very useful when measuring the synchrotron frequency Ω_s when the phases between the accelerating cavities are adjusted. Due to the longitudinal phase focusing, the electrons inside a ring bucket reach an energy equilibrium where the mean energy gain per turn $e\hat{U}\sin(\Psi_s)$ is equal to the mean energy loss

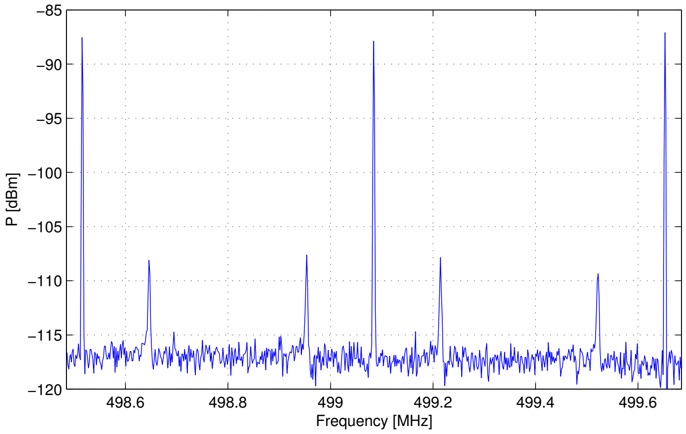

Figure 34: The power spectrum obtained at the diagnostic BPM when the beam is excited by the stripline in the vertical plane. The peaks at 498.51 MHz, 499.08 MHz, and 499.65 MHz are harmonics of the revolution frequency. The vertical betatron oscillations can be seen as sidebands of each revolution harmonics at ±130 kHz.

per turn W_0. Therefore, the relative phase of the bucket (the *synchronous phase* Ψ_s) to the fields in the accelerating cavities changes if the total peak voltage of the cavities $\hat{U}$ changes so that W_0 remains constant. Note that we define Ψ_s so that $\pi/2 < \Psi_s < \pi$ for a stored beam. The synchrotron frequency increases with the magnitude of the accelerating gradient so that $\Omega_s \propto (-\hat{U}\cos(\Psi_s))^{1/2}$. Hence, Ω_s is maximized when the fields in all the accelerating cavities have the same phase relative to the beam. Note that this relation between Ω_s, $\hat{U}$, and Ψ_s is different when the fields induced by Landau cavities are present.

Since the beam commissioning of the 3 GeV ring began in the autumn of 2015, the stripline with its RF distribution networks have been used almost on daily basis to monitor the transverse and longitudinal tunes.

11 Conclusions

In this report, the design of the striplines that are used in the MAX IV and SOLARIS storage rings is presented. The EM fields inside a stripline when the strips are excited in different modes, and their action on the beam have been analyzed. The signals that are induced at the strips by the beam via mirror currents, and their action on the beam via wakefields have also been investigated. Overall, there is a good correlation between the analysis and the simulations.

The scattering parameters of the manufactured striplines have been measured, and the result is acceptable. Two distribution networks that are feeding the stripline and selecting the plane to monitor at the diagnostic BPM have been constructed and installed in the 3 GeV ring. The amplitude and phase balance between the ports of these networks have also been verified. Finally, initial measurements have been performed in the MAX IV 3 GeV ring where coherent transverse beam oscillations have been excited using a stripline.

Acknowledgments

We thank Jonny Ahlbäck, Eshraq Al-Dmour, Åke Andersson, Simon C. Leemann, Robert Lindvall, Magnus Sjöström, Jens Sundberg, and Pedro Fernandes Tavares for their expertise and help during the process.

Appendix A The Scalar Potential in the Stripline

The scalar potential over a cross section of the stripline is obtained by solving Laplace equation in two dimensions, cf. [9]. The analysis is here limited to the region where $0 \leq \rho \leq a$.

Since the geometry is circular, it is more convenient to use polar coordinates. Laplace equation reads

$$\nabla^2 \Phi = \frac{1}{\rho}\frac{\partial}{\partial \rho}\left(\rho \frac{\partial \Phi}{\partial \rho}\right) + \frac{1}{\rho^2}\frac{\partial^2 \Phi}{\partial \phi^2} = 0 \tag{A.1}$$

By using the method of separating of variables and denoting $\Phi(\rho, \phi) = R(\rho)\Psi(\phi)$, and multiplying (A.1) by ρ^2/Ψ we have

$$\frac{\rho}{R}\frac{\partial}{\partial \rho}\left(\rho \frac{\partial R}{\partial \rho}\right) + \frac{1}{\Psi}\frac{\partial^2 \Psi}{\partial \phi^2} = 0 \tag{A.2}$$

The two terms in (A.2) must be constant since they are functions of ρ and ϕ respectively. If the first term equals ν^2 and the second term $-\nu^2$, the general solution becomes

$$\begin{cases} R(\rho) = c_0 + d_0 \ln(\rho) + c\rho^{\nu} + d\rho^{-\nu} \\ \Psi(\phi) = C_0 + D_0\phi + Ce^{j\nu\phi} + De^{-j\nu\phi} \end{cases} \tag{A.3}$$

where the terms with indices 0 are for the special case when $\nu = 0$.

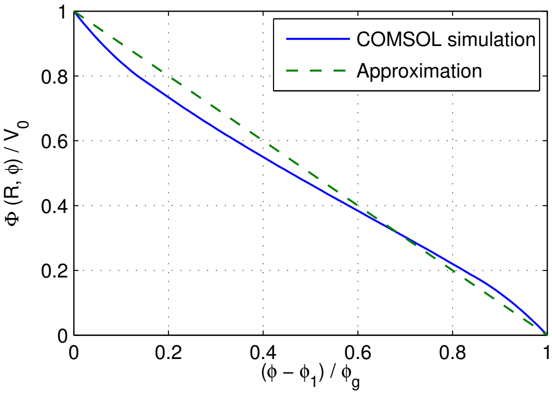

Figure 35: The simulated and approximated potential in the upper gap between the strip and the extended ground.

Consider a stripline as in Figure 4 but with only one strip that is centered at the right side with the angular extension ϕ_s and an angular gap ϕ_g to the extended ground regions. The potential of the strip is V_0 and 0 at the extended ground. The potential in the two gaps are unknown, but a good approximation is that the azimuthal electric field is constant and the radial electric field is zero, i.e. $\boldsymbol{E}(a,\phi) = \pm\frac{V_0}{a\phi_g}\hat{\boldsymbol{\phi}}$. This implies that the potential increases/decreases linearly with ϕ in the gaps. Figure 35 shows the simulated and the approximated value of $\Phi(a,\phi)$ in the upper gap. The potential at $\rho = a$ can now be written as

$$\Phi(a,\phi) = \begin{cases} \frac{V_0}{\phi_g}(\phi_2+\phi) & , -\phi_2 \le \phi - \le \phi_1 \\ V_0 & , -\phi_1 \le \phi \le \phi_1 \\ \frac{V_0}{\phi_g}(\phi_1-\phi) & , \phi_1 \le \phi \le \phi_2 \\ 0 & , \text{elsewhere} \end{cases} \tag{A.4}$$

where $\phi_1 = \phi_s/2$ and $\phi_2 = \phi_s/2+\phi_g$. Three boundary conditions can now be stated.

$$\begin{cases} \text{(1) Full azimuthal periodicity, i.e. } \Phi(\rho,\phi) = \Phi(\rho,\phi+2\pi). \\ \text{(2) Finite potential at the origin.} \\ \text{(3) } \Phi(a,\phi) \text{ as denoted in (A.4).} \end{cases}$$

(1) implies that ν is an integer, and that D_0 must vanish. d_0 and d must also vanish due to (2). $\Phi(\rho,\phi)$ can now be written as the following series

$$\Phi(\rho,\phi) = C_0 + \sum_{n=1}^{\infty} \rho^n \left(C_n e^{jn\phi} + D_n e^{-jn\phi}\right) \tag{A.5}$$

C_0 is obtained by integrating both sides over one azimuthal period when $\rho = a$.

$$\text{LHS} = \int_{-\pi}^{\pi} \Phi(a,\phi)\,\mathrm{d}\phi = V_0(\phi_1+\phi_2)$$

$$\text{RHS} = \int_{-\pi}^{\pi} C_0\,\mathrm{d}\phi + \sum_{n=1}^{\infty} a^n \int_{-\pi}^{\pi} \left(C_n e^{jn\phi} + D_n e^{-jn\phi}\right)\mathrm{d}\phi = 2\pi C_0$$

Thus,

$$\boxed{C_0 = \frac{V_0}{2\pi}(\phi_1+\phi_2) = \frac{V_0}{2\pi}(\phi_s+\phi_g)} \tag{A.6}$$

C_n is obtained by multiplying (A.5) by $e^{-jn'\phi}$ and then integrating over one azimuthal period when $\rho = a$.

$$
\begin{aligned}
\mathrm{LHS} &= \int\limits_{-\pi}^{\pi} \Phi(a,\phi) e^{-jn'\phi}\,\mathrm{d}\phi \\
&= \frac{V_0}{\phi_g}\int\limits_{-\phi_2}^{-\phi_1} (\phi+\phi_2) e^{-jn'\phi}\,\mathrm{d}\phi + V_0 \int\limits_{-\phi_1}^{\phi_1} e^{-jn'\phi}\,\mathrm{d}\phi + \frac{V_0}{\phi_g}\int\limits_{\phi_1}^{\phi_2} (\phi_2-\phi) e^{-jn'\phi}\,\mathrm{d}\phi \\
&= 2V_0 \int\limits_{0}^{\phi_1} \cos(n'\phi)\,\mathrm{d}\phi + \frac{2V_0\phi_2}{\phi_g}\int\limits_{\phi_1}^{\phi_2} \cos(n'\phi)\,\mathrm{d}\phi - \frac{2V_0}{\phi_g}\int\limits_{\phi_1}^{\phi_2} \phi\cos(n'\phi)\,\mathrm{d}\phi \\
&= \frac{2V_0}{n'}\sin(n'\phi_1) + \frac{2V_0\phi_2}{n'\phi_g}\left(\sin(n'\phi_2) - \sin(n'\phi_1)\right) \\
&\quad - \frac{2V_0}{n'\phi_g}\left(\phi_2\sin(n'\phi_2) - \phi_1\sin(n'\phi_1)\right) - \frac{2V_0}{n'^2\phi_g}\left(\cos(n'\phi_2) - \cos(n'\phi_1)\right) \\
&= \frac{2V_0}{n'^2\phi_g}\left(\cos(n'\phi_1) - \cos(n'\phi_2)\right) \\
&= \frac{4V_0}{n'^2\phi_g}\sin\left(n'\frac{\phi_g}{2}\right)\sin\left(n'\frac{\phi_s+\phi_g}{2}\right) \\
\mathrm{RHS} &= \int\limits_{-\pi}^{\pi} C_0 e^{-jn'\phi}\,\mathrm{d}\phi + \sum_{n=1}^{\infty} a^n \int\limits_{-\pi}^{\pi}\left(C_n e^{j(n-n')\phi} + D_n e^{-j(n+n')\phi}\right)\mathrm{d}\phi \\
&= 2\pi\sum_{n=1}^{\infty} a^n C_n \delta_{n,n'} = 2\pi a^{n'} C_{n'}
\end{aligned}
$$

Thus,

$$
\boxed{C_n = \frac{2V_0}{\pi\phi_g} a^{-n} \frac{\sin\left(n\frac{\phi_g}{2}\right)\sin\left(n\frac{\phi_s+\phi_g}{2}\right)}{n^2}} \tag{A.7}
$$

D_n is obtained in the same way as C_n, except by multiplying both side in (A.5) by $e^{jn'\phi}$ instead of $e^{-jn'\phi}$. Due to symmetry, we have that

$$
\boxed{D_n = C_n} \tag{A.8}
$$

By inserting (A.6), (A.7), and (A.8) into (A.5), $\Phi(\rho,\phi)$ can finally be written as

$$
\Phi(\rho,\phi) = \frac{V_0(\phi_s+\phi_g)}{2\pi} + \frac{4V_0}{\pi\phi_g}\sum_{n=1}^{\infty}\left(\frac{\rho}{a}\right)^n \frac{\sin\left(n\frac{\phi_g}{2}\right)\sin\left(n\frac{\phi_s+\phi_g}{2}\right)}{n^2}\cos(n\phi) \tag{A.9}
$$

We can now calculate the potential for an arbitrary rotated strip by adding its rotation angle α to (A.9), thus $\cos(n\phi) \to \cos(n(\phi-\alpha))$. We superimpose the potentials from the four strips, and the potential of the excitation modes listed in Table 2 can be written as

$$\boxed{\Phi(\rho,\phi)=\sum_{m=1}^{4}\frac{U_m}{\pi}\left(\frac{\phi_s+\phi_g}{2}+\frac{4}{\phi_g}\sum_{n=1}^{\infty}\left(\frac{\rho}{a}\right)^n\frac{\sin\left(n\frac{\phi_g}{2}\right)\sin\left(n\frac{\phi_s+\phi_g}{2}\right)}{n^2}\cos\left(n\left(\phi-\frac{m\pi}{2}+\frac{\pi}{4}\right)\right)\right)}$$

where U_m is the potential of the m:th electrode.

Appendix B Stripline S-parameter Measurement

The S-parameters from the measurements described in Section 8 can be seen in Figure 36-43. Here, all the 2x16 parameters are not shown since $S_{\mathrm{dc11}} \approx S_{\mathrm{cd11}}$, $S_{\mathrm{dc22}} \approx S_{\mathrm{cd22}}$, $S_{\mathrm{dd21}} \approx S_{\mathrm{dd12}}$, and $S_{\mathrm{cc21}} \approx S_{\mathrm{cc12}}$.

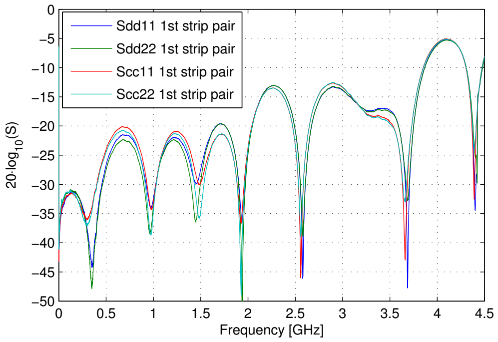

Figure 36: Differential and common-mode reflection coefficients of the first strip pair.

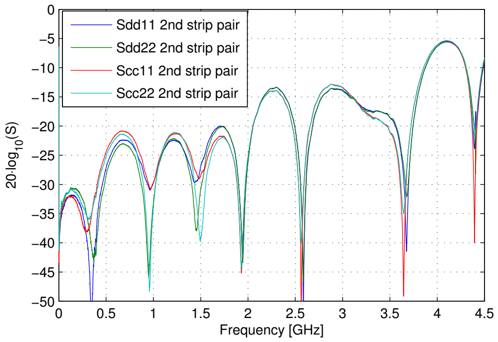

Figure 37: Differential and common-mode reflection coefficients of the second strip pair.

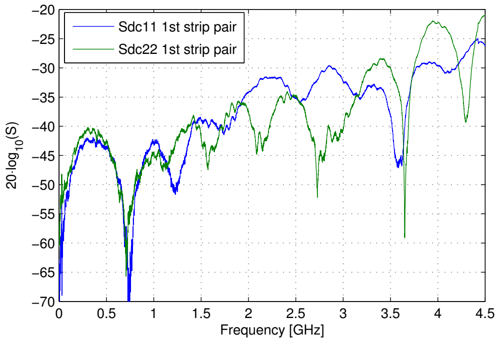

Figure 38: Cross-mode reflection coefficients of the first strip pair.

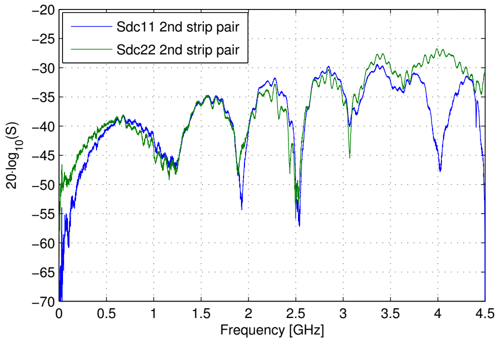

Figure 39: Cross-mode reflection coefficients of the second strip pair.

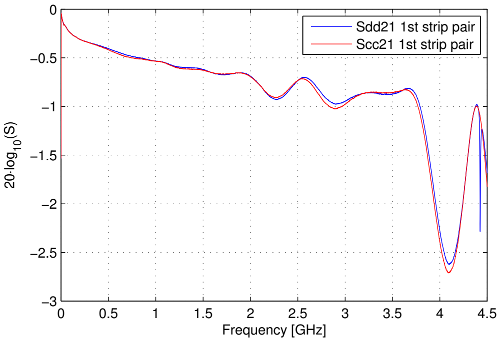

Figure 40: Differential and common-mode transmission coefficients of the first strip pair.

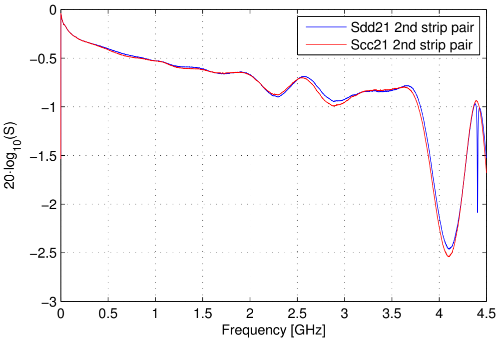

Figure 41: Differential and common-mode transmission coefficients of the second strip pair.

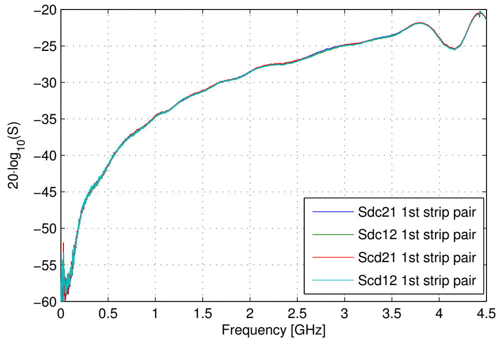

Figure 42: Cross-mode transmission coefficients of the first strip pair.

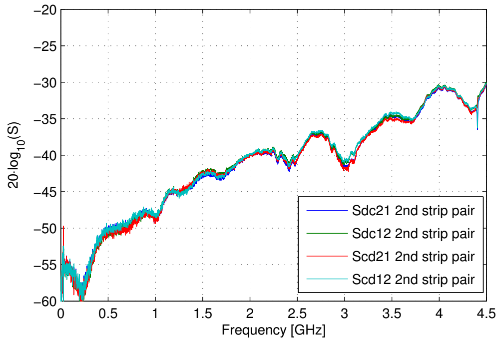

Figure 43: Cross-mode transmission coefficients of the second strip pair.

Appendix C Feeding Network S-parameter Measurements

Here, the S-parameter measurements of the feeding network in Section 9.1 are presented. The port numbering in Figure 28 are used. The transmission coefficients of the network can be seen in Figure 44-49, and Figure 50 shows S_{00}.

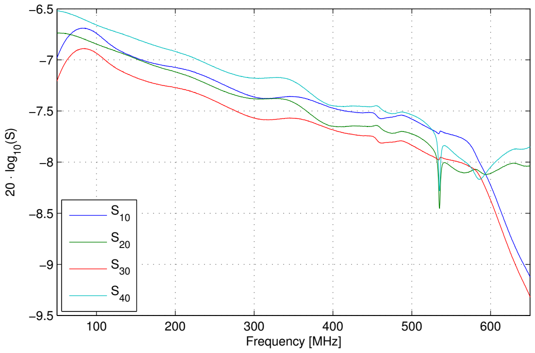

Figure 44: S_{x0} of the feeding network in the horizontal mode.

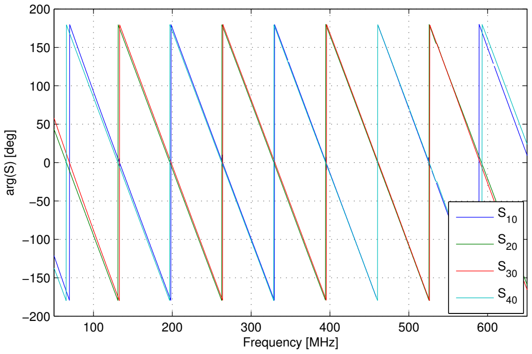

Figure 45: S_{x0} of the feeding network in the horizontal mode.

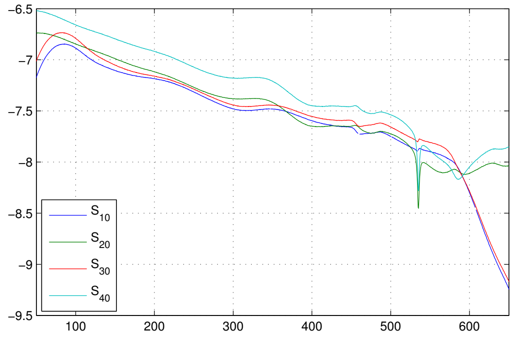

Figure 46: S_{x0} of the feeding network in the vertical mode.

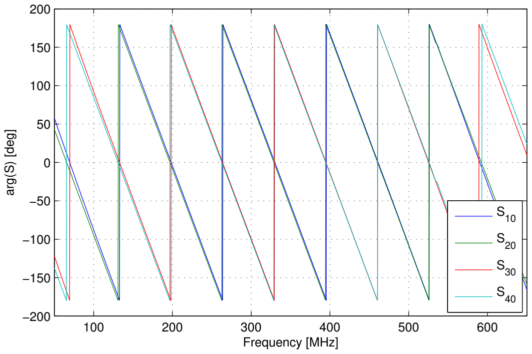

Figure 47: S_{x0} of the feeding network in the vertical mode.

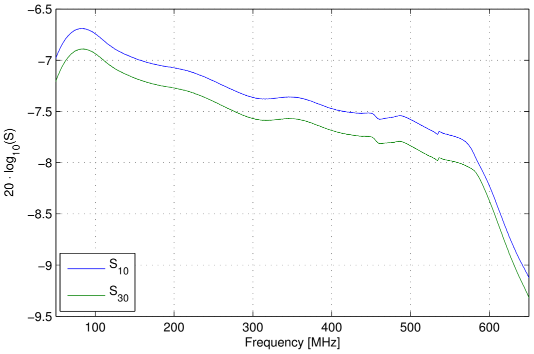

Figure 48: S_{x0} of the feeding network in the diagonal mode.

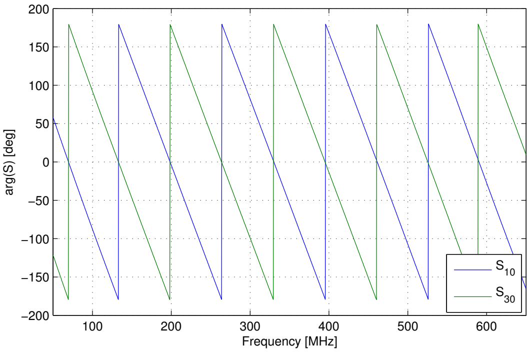

Figure 49: S_{x0} of the feeding network in the diagonal mode.

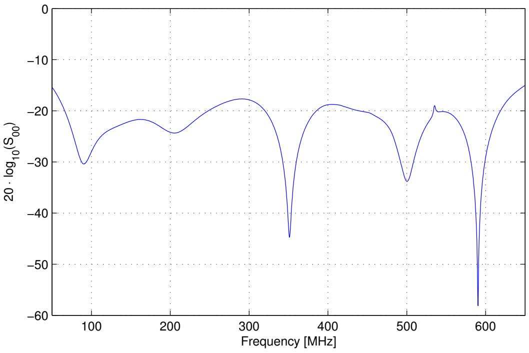

Figure 50: S_{00} of the feeding network in the diagonal mode. Note that S_{00} does not differ much in the horizontal and vertical mode of operation.

Appendix D Receiving Network S-parameter Measurements

Here, the S-parameter measurements of the receiving network in Section 9.2 are presented. The four input ports can be seen in Figure 30 and correspond to the button indices in Figure 32. Port 0 is the "Switch Output" port in Figure 30. The spectrum of the transmission coefficients can be seen in Figure 51-56.

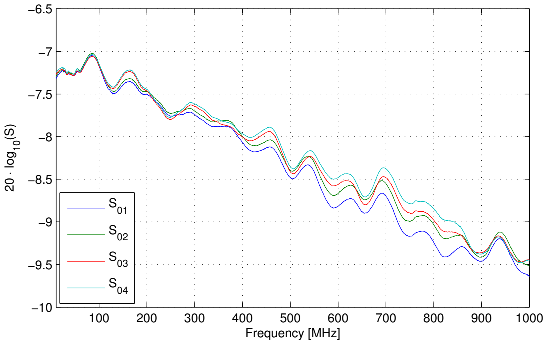

Figure 51: S_{0x} of the receiving network when monitoring the horizontal signal.

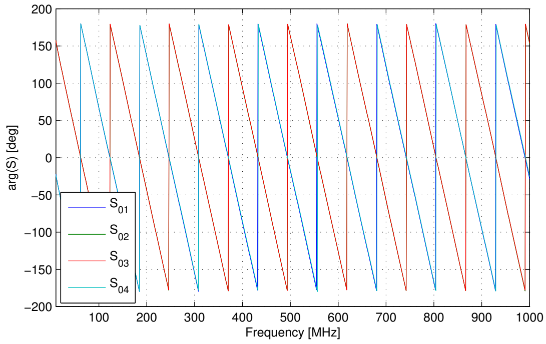

Figure 52: S_{0x} of the receiving network when monitoring the horizontal signal.

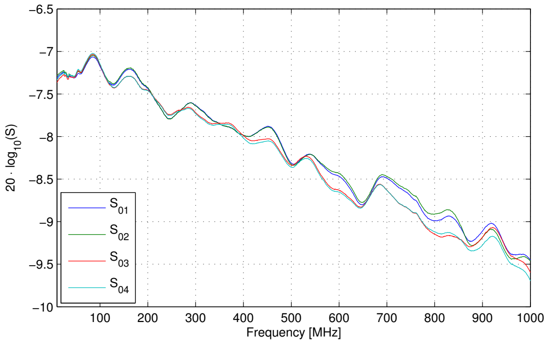

Figure 53: S_{0x} of the receiving network when monitoring the vertical signal.

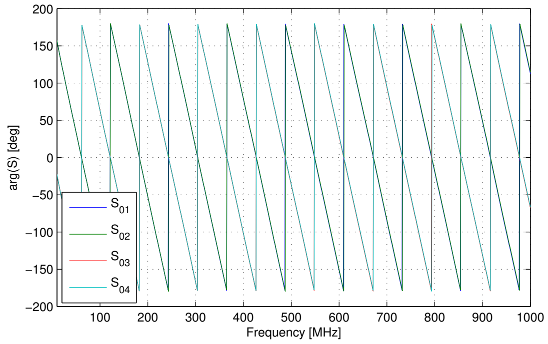

Figure 54: S_{0x} of the receiving network when monitoring the vertical signal.

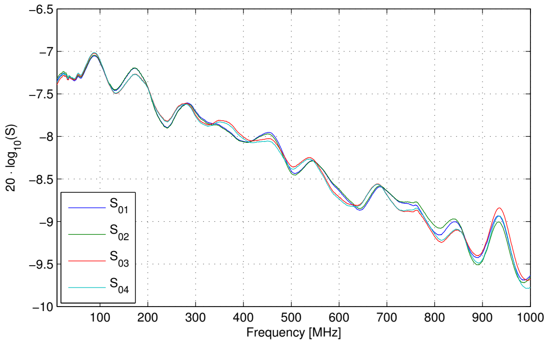

Figure 55: S_{0x} of the receiving network when monitoring the sum signal.

58

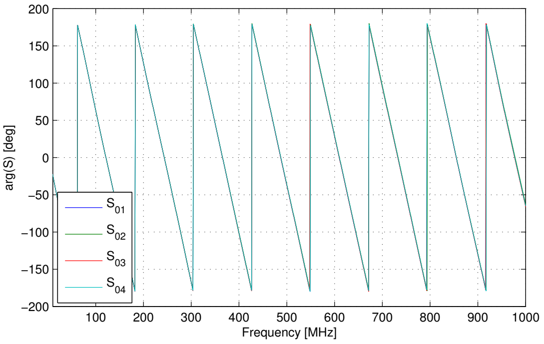

Figure 56: S_{0x} of the receiving network when monitoring the sum signal.

Appendix References

[1] Å. Andersson et al. "The 100 mhz rf system for the max iv storage rings". In: *2nd International Particle Accelerator Conference*. 2011, pp. 193–195.

[2] *COMSOL Multiphysics website.* http://www.comsol.com.

[3] F. Curbis et al. "Extension of the max iv linac for a free electron laser in the x-ray region". In: *International Particle Accelerator Conference (IPAC), Shanghai, China*. 2013, pp. 1244–1246.

[4] *GdfidL website.* http://www.gdfidl.de.

[5] A. S. Gilmour. *Klystrons, Traveling Wave Tubes, Magnetrons, Crossed-Field Amplifiers, and Gyrotrons.* Artech House, 2011.

[6] D. A. Goldberg and G. R. Lambertson. "Dynamic devices a primer on pickups and kickers". In: *AIP Conference Proceedings*. 1992, pp. 537–600.

[7] M. Hiebel. *Fundamentals of Vector Network Analysis.* Rohde&Schwarz GmbH & Co, 2008.

[8] A. Hofmann and S. Myers. "Beam dynamics in a double rf system". In: *11th International Conference on High-energy Accelerators*. 1980, pp. 610–614.

[9] J. D. Jackson. *Classical Electrodynamics.* Third. John Wiley & Sons, 1999.

[10] A. Karlsson and G. Kristensson. *Mikrovågsteori.* KFS AB, 2003.

[11] *MACOM H-9 180° hybrid junction product specifications.* http://cdn.macom.com/datasheets/H-9.pdf.

[12] *MAX IV Laboratory website.* https://www.maxlab.lu.se/maxiv.

[13] *MCLI splitter product specifications.* http://mcli.com/documents/hcd-12.pdf http://mcli.com/documents/hcd-19.pdf.

[14] K. Y. Ng. "Impedance of stripline beam-position monitors". *Particle Accelerators* 23 (1988), pp. 93–102.

[15] D. Olsson. "Design of stripline kicker for tune measurements in the max iv 3 gev ring". In: *Progress In Electromagnetics Research Symposium Proceedings (PIERS)*. 2013, pp. 1095–1099.

[16] D. Olsson, A. Karlsson, and L. Malmgren. *The Bunch-by-Bunch Feedback System in the MAX IV 3 GeV Ring.* Tech. rep. LUTEDX/(TEAT-7253)/(2017). Lund Institute of Technology, 2017.

[17] D. Olsson et al. "A chopper system for the max iv thermionic pre-injector". *Nuclear Instruments and Methods in Physics Research* 759 (2014), pp. 29–35.

[18] M. Serio. "Transverse betatron tune measurements". *Frontiers of Particle Beams; Observation, Diagnosis and Correction Lecture Notes in Physics* 343 (1989), pp. 65–93.

[19] *SOLARIS Synchrotron website.* http://www.synchrotron.uj.edu.pl.

[20] P. F. Tavares et al. “The max iv storage ring project”. *Journal of Synchrotron Radiation* 21 (2014), pp. 862–877.

[21] S. Thoorin et al. “Design of the max iv ring injector and spf/fel driver”. In: *Particle Accelerator Conference (PAC), New York, NY, USA*. 2011, pp. 2447–2449.

[22] H. Wiedemann. *Particle Accelerator Physics*. Third. Springer-Verlag, 2007.

[23] K. Wille. *The Physics of Particle Accelerators*. Oxford University Press, 2000.

[24] B. W. Zotter and S. Kheifets. *Impedances and Wakes in High-Energy Particle Accelerators*. World Scientific Publisher, 1998.

PAPER VIII

Design of Stripline Kicker for Tune Measurements in the MAX IV 3 GeV Ring

D. Olsson.

(2013) *Proceedings of PIERS13, Stockholm, Sweden.*

Progress In Electromagnetics Research Symposium Proceedings, Stockholm, Sweden, Aug. 12-15, 2013 1095

Design of Stripline Kicker for Tune Measurements in the MAX IV 3 GeV Ring

D. Olsson
MAX IV Laboratory, Lund University, Sweden

Abstract— During commissioning and routine operation of the MAX IV 3 GeV storage ring, the ability to measure the betatron tunes is important. For these measurements a shaker such as a stripline kicker is needed to excite coherent transverse oscillations of the beam within a narrow range of frequencies. In this paper, the design of this stripline kicker is described. Besides from operating as an active device during tune measurements, the stripline will also work as a BPM pick-up during normal operation.

1. INTRODUCTION

MAX IV will be Sweden's next-generation synchrotron radiation light source, and will consist of two storage rings and a full energy injector LINAC. The larger 3 GeV ring will have a circumference of 528 m, and the smaller 1.5 GeV ring a circumference of 96 m. In the 3 GeV ring, a stripline kicker will be used as a shaker during tune measurements. The beam oscillation is then monitored by a standard button BPM. However, the stripline kicker should also be used as a passive BPM pick-up during normal operation. The relevant parameters of the 3 GeV ring are given in Table 1 [1].

Beam energy	3.0 GeV
Maximum beam current	500 mA
RMS bunch length	5.6 cm
Main radio frequency	99.931 MHz
Harmonic number	176
Ring circumference	528 m
Betatron tune (horizontal/vertical)	42.20/14.28
Excitation frequency for tune measurements	500 MHz
BPM pick-up frequency	500 MHz

Table 1: Parameters of the MAX IV 3 GeV storage ring.

2. STRIPLINE DESIGN

We need four stripline electrodes since we like to shake the beam independently in the vertical and horizontal direction. Often the beam should be shaken in a direction tilted 45 degrees from the horizontal direction. For this reason, the strips are oriented accordingly at 45, 135, 225, and 315 degrees, as seen in Figure 1. The radius of curvature, R, is the same as the radius of the beam pipe, i.e., 13.5 mm. This value minimizes the unwanted effect of the beam impedance. Each strip has an angular extension of $\varphi_s = 45$ degrees and a thickness of 1 mm. The optimum stripline length L when considering kicker performance is $\lambda/4$, where λ is the RF excitation wavelength. Therefore, a length of $L = 15$ cm is chosen. Between each strip there is a region of extended (raised) ground. The angular gap φ_g between a strip and the extended ground region is 8.6 degrees. All the stripline components are made of Stainless Steel 316 L.

For the beam excitation described above, we need to operate the stripline kicker in the three different modes that are described in Table 2. Here, U_x is the applied RF amplitude of the corresponding strip (see Figure 1), where a negative amplitude is due to a phase shift of 180 degrees compared to the strip with positive potential. The sum mode is not actually a mode for beam excitation, but describes the potential distribution from the excitation of the beam itself assuming the beam is centered on the pipe. The characteristic impedance, Z_L, of each mode is obtained from electrostatic simulations in COMSOL Multiphysics and the results are seen in Table 2. It is possible to achieve an impedance closer to 50 Ω near the coaxial feedthroughs by using tapered strips, but since the purpose of the stripline is beam excitation and beam monitoring in a narrow frequency range, there are no requirements for bandwidth. Therefore, the coaxial feedthroughs are just welded to the strips as shown in Figure 3.

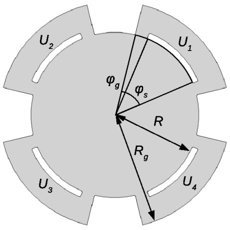

Figure 1: The 2D geometry of the stripline kicker.

Mode of operation	U_1	U_2	U_3	U_4	Z_L [Ω]
Diagonal (d)	V_0	0	$-V_0$	0	50.0
Horizontal (h)	V_0	$-V_0$	$-V_0$	V_0	50.0
Vertical (v)	V_0	V_0	$-V_0$	$-V_0$	50.0
Sum (Σ)	V_0	V_0	V_0	V_0	53.4

Table 2: The modes of operation.

We can analytically obtain the electric scalar potential, $\Phi(\rho, \varphi)$, of the (first) propagating TEM modes along the stripline by solving Laplace equation in two dimensions. This is in the region where $0 \leq \rho \leq R$ and requires that we evaluate the striplines far away from their end-gaps. Here, we make an approximation by assuming that the azimuthal electric field in the gaps between the strips and the extended ground at $\rho = R$ is constant and that the radial component is zero, i.e., $\mathbf{E}(R, \varphi) = \pm \frac{V_0}{R\varphi_g}\hat{\varphi}$. By applying the conditions of full azimuthal periodicity, finite $\Phi(\rho = 0)$, and the potential at $\rho = R$ described above and in Table 2, we get $\Phi(\rho, \varphi)$ as the following Fourier series, cf. [2].

$$\Phi(\rho,\varphi)=\sum_{m=1}^{4}\frac{U_m}{\pi}\left(\frac{\varphi_s+\varphi_g}{2}+\frac{4}{\varphi_g}\sum_{n=1}^{\infty}\left(\frac{\rho}{R}\right)^n\frac{\sin\left(n\frac{\varphi_g}{2}\right)\sin\left(n\frac{\varphi_s+\varphi_g}{2}\right)}{n^2}\cos\left(n\left(\varphi-\frac{m\pi}{2}+\frac{\pi}{4}\right)\right)\right) \quad (1)$$

Figure 2 shows $\Phi(\rho, \varphi)$ in the diagonal, vertical, and sum mode obtained from (1) (upper figure) together with electrostatic simulations of the same modes in COMSOL (lower figure). The stripline geometry factor g described in [3] can be obtained from (1), and is shown in (2)–(4) for diagonal, horizontal/vertical, and sum mode. The transverse geometry factor is defined as $g_\perp = |\mathbf{E}(\rho = 0)|R$, and the longitudinal as $g_\parallel = \Phi(\rho = 0)$. Here, the excitation voltage V_0 is held at unit potential. In this case, $g_{\perp,d} = 0.57$ and $g_{\parallel,\Sigma} = 0.59$.

$$g_{\perp,d} = \frac{8}{\varphi_g\pi}\sin\left(\frac{\varphi_g}{2}\right)\sin\left(\frac{\varphi_s+\varphi_g}{2}\right) \quad (2)$$

$$g_{\perp,h/v} = \sqrt{2}g_{\perp,d} \quad (3)$$

$$g_{\parallel,\Sigma} = 2\frac{\varphi_s+\varphi_g}{\pi} \quad (4)$$

The cut-off frequency for the beam pipe is 6.5 GHz for the TE_{11} mode and 8.5 GHz for the TM_{01} mode. The 3D structure is simulated using the eigenmode solver in COMSOL. There are TE modes with frequencies below 6.5 GHz, but these can be neglected since they have a longitudinal shunt impedance close to zero and hence they do not affect the beam.

3. KICKER STRENGTH

The transverse shunt impedance Z_{sh} is the ratio of the square of the change in transverse beam voltage to the input power. When operating the striplines in diagonal mode, Z_{sh} is obtained from (5) [3], where c_0 is the speed of light and ω the angular frequency. Here, we assume that the line impedance and the termination impedance are the same as the stripline characteristic impedance, Z_L. Note that Z_{sh} is the same in horizontal/vertical mode as in (5) since the shunt impedance is inversely proportional to the input power, which has to be twice as high according to Table 2, and since $g_{\perp,h/v} = \sqrt{2}g_{\perp,d}$. At the excitation frequency of 500 MHz, the transverse shunt impedance is 1.6 kΩ.

$$Z_{sh} = 2Z_L\left(\frac{g_{\perp,d}c_0}{\omega R}\right)^2\sin^2\left(\frac{\omega L}{c_0}\right) \quad (5)$$

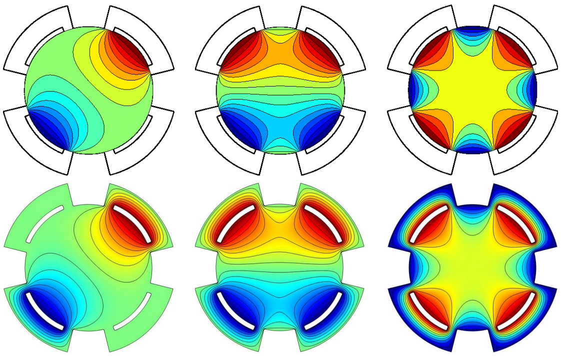

Figure 2: $\Phi(\rho, \varphi)$ obtained from (1) (upper) and from COMSOL simulations (lower). Here, (from the left) the diagonal, vertical, and sum mode are shown.

The maximum kick in radians, $\Delta\alpha$, for one passage is given by (6), where e is the elementary charge, P the applied RMS power, and E the beam energy.

$$\Delta\alpha = \frac{e\sqrt{2Z_{sh}P}}{E} \tag{6}$$

4. BEAM COUPLING AND PICK-UP CHARACTERISTICS

The longitudinal beam impedance $Z_{\parallel}$ is defined as the Fourier transform of the wake potential. For a stripline kicker, $Z_{\parallel}$ is given by (7) [3, 4]. This formula is only a valid approximation at lower frequencies where the RF mismatch at the stripline ends is negligible, and the wakes caused by the discontinuity of the surrounding structure are minor. In order to get a more accurate estimation of $Z_{\parallel}$, the whole geometry was simulated in CST Particle Studio using the wakefield solver. Here, all the coaxial feedthroughs are terminated with ports, and all metal surfaces have the same parameters as Stainless Steel 316 L ($\sigma = 1.32\,\mathrm{MSm}^{-1}$). Figure 3 shows the stripline in the CST Particle Studio environment, and Figure 4 shows $\mathrm{Re}(Z_{\parallel})$ obtained from the simulation and from (7).

$$Z_{\parallel} = \frac{Z_L}{8} g_{\parallel,\Sigma}^2 \left(2\sin^2\left(\frac{\omega L}{c_0}\right) + j\sin\left(\frac{2\omega L}{c_0}\right) \right) \tag{7}$$

The longitudinal beam impedance behaves like the circuit impedance when considering the dissipated power, P_{loss}, in the structure. P_{loss} is given by (8), where $\lambda(t)$ is the normalized charge distribution, I_0 the average beam current, and f_b the bunch repetition frequency. Since no resonance modes with considerable longitudinal shunt impedance exist below the cut-off frequency of the pipe, these mode currents have not been included in the calculations of P_{loss}. The storage ring will have third harmonic (Landau) cavities for bunch stretching, so the bunch distribution will be non-Gaussian. Therefore, a bunch shape described in [5] is used with values from Table 1.

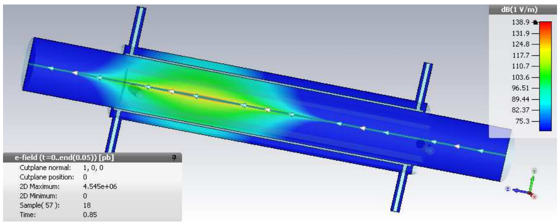

e-field (t=0..end(0.05)) [pb]

Cutplane normal: 1, 0, 0
Cutplane position: 0
2D Maximum: 4.545e+06
2D Minimum: 0
Sample(57): 18
Time: 0.85

Figure 3: The electric field of a Gaussian bunch in CST particle studio.

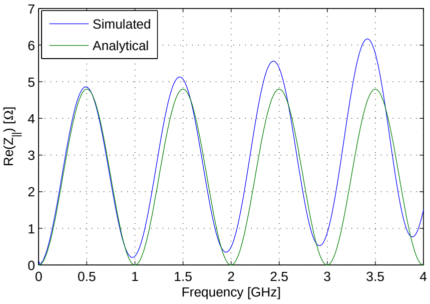

Figure 4: $\mathrm{Re}(Z_\parallel)$ obtained from CST Particle studio, and from (7).

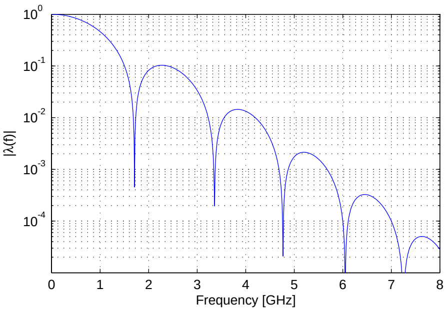

Figure 5: The charge distribution of the bunch in the frequency domain.

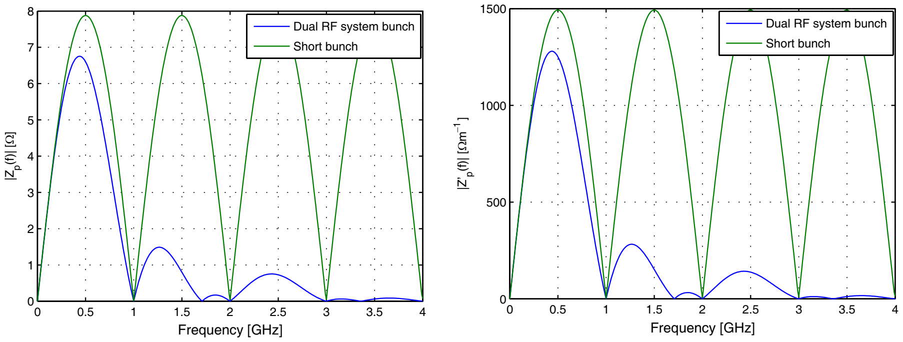

(a) (b)

Figure 6: (a) $|Z_p|$ and (b) $|Z'_p|$ for the MAX IV bunch and for a much shorter bunch.

Figure 5 shows the normalized bunch, $\lambda(f)$, in the frequency domain. With uniform filling and at the maximum beam current (500 mA), the dissipated power is 8.9 W. Here, $Z_\parallel$ obtained from CST is used. However, most of the power will dissipate in the stripline terminations, so only a fraction will be transformed into heat inside the stripline.

$$P_{loss} = \frac{I_0^2}{\pi f_b} \int_0^\infty \mathrm{Re}(Z_\parallel(\omega))\lambda^2(\omega)d\omega \tag{8}$$

The longitudinal and transverse transfer impedances, Z_p and Z'_p, are important parameters when evaluating the performance of the stripline as a BPM. Z_p is defined as the ratio of the output port voltage to the beam current. If we only consider the ratio of the induced voltage at one port to the total beam current, we get Z_p given by (9). Z'_p is defined as the ratio of the output port voltage to the dipole moment of the beam. If we take the difference of the induced port voltage of two opposite located strips, and if the transverse beam deviation is diagonal, then Z'_p given by (10) and has the dimension $\Omega\mathrm{m}^{-1}$. Note that Z_p and Z'_p are often defined without the $\lambda(\omega)$ term in the literature.

$$Z_p = \frac{Z_L g_{\parallel,\Sigma}}{4}\lambda(\omega)e^{j(\pi/2-\omega L/c_0)}\sin\left(\frac{\omega L}{c_0}\right) \tag{9}$$

$$Z'_p = \frac{Z_L g_{\perp,d}}{R\sqrt{2}}\lambda(\omega)e^{j(\pi/2-\omega L/c_0)}\sin\left(\frac{\omega L}{c_0}\right) \tag{10}$$

We see from (9) and (10) that $\lambda(\omega)$ makes the transfer impedance decay faster for longer bunches. This is due to destructive interference between the two traveling pulses that are induced at the stripline ends (the pulses have different signs). Figure 6 shows $|Z_p|$ and $|Z'_p|$ for the MAX IV bunch shown in Figure 5 and for a much shorter bunch. At 500 MHz, Z_p is 6.6 Ω, and Z'_p is 1.25 $\mathrm{k\Omega m^{-1}}$.

5. CONCLUSION

The stripline kicker design for the MAX IV 3 GeV ring described in this paper has sufficient performance in terms of line matching, kick efficiency, beam impedance, and power dissipation. It will also work as a pick-up, and will be a good complement to the standard button BPMs in the ring during normal operation. There is also a good agreement between simulation results from COMSOL and CST and results obtained analytically.

REFERENCES

1. Leemann, S. C., Å. Andersson, M. Eriksson, L.-J. Lindgren, E. Walléen, J. Bengtsson, and A. Streun, "Beam dynamics and expected performance of Sweden's new storage-ring light source: MAX IV," *Physical Review Special Topics — Accelerators and Beams*, Vol. 12, 120701, 1–15, 2009.
2. Jackson, J. D., *Classical Electrodynamics*, 3rd Edition, Chapters 2–3, John Wiley & Sons, 1998.
3. Goldberg, D. A. and G. R. Lambertson, "Dynamic devices a primer on pickups and kickers," *AIP Conference Proceedings Series —Physics of Particle Accelerators*, 1992.
4. Chao, A. W. and M. Tigner, *Handbook of Accelerator Physics and Engineering*, 3rd Printing, Chapter 3.2, World Scientific, 2009.
5. Hofmann, A. and S. Myers, "Beam dynamics in a double RF system," *XIth International Conference on High Energy Accelerators CERN*, Genevea, 1980.